




University of "G. D'Annunzio" Chieti-Pescara

School of Advanced Studies "G. D'Annunzio"

Department of Medical, Oral and Biotechnological Sciences

PhD course in Biomolecular and Pharmaceutical Sciences

Curriculum: Molecular Medicine

XXXVIII° cycle

EV20/Omomyc and 1959-sss/DM4: Preclinical Development and Analytical Characterization of Immunoconjugates for Targeted Cancer Therapy

PhD Student

Dr. Giulio Lovato

Coordinator

Prof. Assunta Pandolfi, PhD

Tutor

Prof. Gianluca Sala, PhD

Academic Years 2022-2025

INDEX

ABSTRACT **4**

BACKGROUND **5**

ANTIBODY–DRUG CONJUGATES IN ONCOLOGY: RATIONALE, EVOLUTION, AND CORE MECHANISMS 5

Historical context and rationale *5*

Current clinical landscape *5*

Mechanism of action *5*

ARCHITECTURE OF ADCS 7

ADCs as engineered systems *7*

The antibody and target axis *7*

Payload and Linker Selection *7*

Conjugation and Drug Antibody Ratio *9*

ADC CONJUGATION CHEMISTRY 11

Classical conjugation *11*

Site-specific conjugation *12*

Next-generation linker architectures *14*

CURRENT CLINICAL LANDSCAPE 15

ADC in Hematologic malignancies *17*

ADC in Solid tumors *17*

AIMS **21**

CHAPTER ONE **22**

HER3-TARGETING ANTIBODY AND MYC INHIBITION: FROM EV20 TO EV20/OMOMYC IMMUNOCONJUGATE 22

1.1 HER3 biology and clinical relevance in cancer therapy *22*

1.2 From MP-RM-1 to EV20 *23*

1.3 EV20-derived immunoconjugates *24*

1.4 MYC as an oncogenic driver *25*

1.5 Omomyc *26*

1.6 EV20/Omomyc immunoconjugate as treatment for Neuroblastoma *27*

EV20/Omomyc: a novel dual MYC/HER3 targeting immunoconjugate 29

CHAPTER 2 **48**

1959-Based Non-Internalizing Antibody–Drug Conjugates Targeting Secreted LGALS3BP 48

2.1 LGALS3BP *48*

2.2 1959-sss/DM4 ADC *51*

2.3 1959-sss/DM4 ADC based combination therapy *52*

LGALS3BP antibody-drug conjugate enhances tumor-infiltrating lymphocytes and synergizes with immunotherapy to restrain neuroblastoma growth 54

CHAPTER 3 **75**

Analytical Characterization of Antibody–Drug Conjugates: DAR, Linker Stability, and Payload Quantification in Biological Matrices 75

3.1 How to analyse an ADC *75*

3.2 Chromatographic and Mass Spectrometric Techniques for ADCs characterization *76*

3.3 Analytical methods applied to ADC Preclinical Evaluation *77*

HPLC-DAD validated method for DM4 and its metabolite S-Me-DM4 quantification in biological matrix for clinical and pharmaceutical applications 78

Evaluation of Antibody-Drug Conjugate Performance Using a Novel HPLC-DAD Method for Tumor-Specific Detection of DM4 and S-Methyl-DM4 95

CHAPTER 4 **115**

LGALS3BP as a Cancer Biomarker in Liquid Biopsy 115

4.1 Potential Diagnostic Biomarker Across Tumor Types *115*

4.2 LGALS3BP as early Biomarker in Bladder Cancer *116*

Glycosylated LGALS3BP is highly secreted by bladder cancer cells and represents a novel urinary disease biomarker 118

CHAPTER 5 **136**

Methods development 136

5.1 EV20/Omomyc conjugation method development *136*

5.2 1959-sss/DM4 conjugation method optimization *137*
5.3 DM4 and S-Met-DM4 extraction and quantification method development *138*
5.5 ELISA assay development *140*

DISCUSSION **141**

REFERENCES **146**

ABBREVIATIONS AND ACRONYMS **159**

ABSTRACT

Antibody–drug conjugates (ADCs) represent an advanced class of targeted therapeutics designed to improve the therapeutic index of anticancer agents by selectively delivering bioactive payloads to tumor cells. Despite significant clinical progress, conventional ADCs remain largely restricted to cytotoxic small molecules and internalizing targets, highlighting the need for innovative strategies that expand both payload diversity and targeting mechanisms.

This PhD thesis investigates the design, development, and analytical characterization of two distinct antibody-based conjugate platforms aimed at overcoming these limitations: the EV20/Omomyc immunoconjugate and the 1959-sss/DM4 ADC targeting LGALS3BP.

The first part of the work focuses on EV20/Omomyc, a novel antibody–protein conjugate combining a humanized anti-HER3 antibody (EV20) with Omomyc, a dominant-negative MYC inhibitor. This approach was developed to extend ADC technology beyond cytotoxic payloads toward intracellular targeting of oncogenic transcription factors. The conjugate retained HER3 binding affinity, demonstrated efficient internalization and nuclear delivery of Omomyc, and showed antigen-dependent accumulation in HER3-positive tumors. In preclinical neuroblastoma models, EV20/Omomyc exhibited enhanced antitumor activity compared to free Omomyc, supporting the concept that antibody-mediated delivery can improve the efficacy and specificity of protein-based therapeutics.

The second part of the thesis investigates a non-internalizing ADC strategy based on the 1959-sss/DM4 conjugate targeting the secreted glycoprotein LGALS3BP. This work demonstrates that extracellular tumor-associated antigens can be effectively exploited for selective drug release within the tumor microenvironment. The 1959-sss/DM4 ADC showed significant antitumor activity in preclinical neuroblastoma models and enhanced tumor-infiltrating lymphocytes, with evidence of synergistic effects when combined with immunotherapy.

In parallel, substantial effort was devoted to the development of robust analytical methodologies for ADC characterization, including drug-to-antibody ratio (DAR) assessment, linker stability evaluation, and quantitative measurement of payloads (DM4 and its metabolites) in biological matrices using HPLC-DAD. These methods enabled accurate pharmacokinetic and biodistribution studies, representing essential tools for preclinical evaluation and translational development.

Finally, the thesis explores LGALS3BP as a potential liquid biopsy biomarker, demonstrating its elevated presence in cancer patients and supporting its relevance as both a diagnostic marker and therapeutic target.

Overall, this work provides proof-of-concept for two complementary innovations in antibody-based therapeutics: (i) the use of antibodies to deliver non-cytotoxic, protein-based inhibitors to intracellular oncogenic targets, and (ii) the exploitation of non-internalizing mechanisms to target extracellular tumor components. These findings contribute to expanding the design space of next-generation ADCs and support the development of more versatile and effective targeted cancer therapies.

BACKGROUND

Antibody–Drug Conjugates in Oncology: Rationale, Evolution, and Core Mechanisms

Historical context and rationale

The development of antibody–drug conjugates (ADCs) exemplify the "magic bullet" paradigm, which aims to deliver cytotoxic agents selectively to diseased cells while minimizing harm to healthy tissues. Paul Ehrlich originally described this principle as the foundation for targeted therapy (1). In oncology, the rationale for ADCs stems from a key therapeutic challenge: while many cytotoxic agents are effective against malignant cells, their systemic administration is constrained by narrow therapeutic indices and significant toxicities. Monoclonal antibodies (mAbs) offer high target selectivity and favourable pharmacokinetics but often lack sufficient potency as monotherapies in advanced disease (2,3). ADCs overcome these limitations by integrating the tumor-targeting and pharmacokinetic advantages of antibodies with the potent cytotoxicity of specialized payloads (3,4). These agents are complex, multicomponent therapeutics whose pharmacological properties depend on the interplay among antigen biology, antibody characteristics, conjugation chemistry, linker stability and cleavage, payload mechanism, and the tumor microenvironment (5). This complexity introduces both opportunities and challenges, as even minor modifications in linker design, conjugation site, drug-to-antibody ratio (DAR), or payload physicochemical properties can substantially affect pharmacokinetics, tumor penetration, efficacy, and toxicity (3,5).

Current clinical landscape

The field of ADCs is experiencing rapid clinical growth, with ongoing innovations in target selection, linker chemistries, payload classes, and conjugation techniques (3,5). Recent studies demonstrate a consistent increase in the number of ADCs approved worldwide (6). Clinical development encompasses a wide array of targets, including HER2, TROP2, Nectin-4, CD19, and CD79b, and has benefited from advances in safety engineering and improved patient-selection strategies, which have enabled the targeting of previously inaccessible antigens. However, toxicity remains a major factor influencing clinical outcomes, frequently limiting dose intensity and narrowing the therapeutic window 5). ADC-associated toxicity arises from several mechanisms, including on-target binding in normal tissues expressing the antigen, off-target uptake and catabolism via Fc receptor–mediated pathways, and premature payload release in circulation due to linker instability or deconjugation. (7) Additionally, adverse event profiles often correlate with specific linker–payload combinations, underscoring the significance of payload pharmacology and systemic exposure to free drug as key determinants of dose-limiting toxicity (3,7).

Mechanism of action

Despite a wide heterogeneity, most ADCs share a common mechanism of action, as shown in Figure 1. Initially, the ADC binds to a specific antigen on the surface of cancer cells. This complex is internalized through endocytosis and transported within intracellular compartments. Inside the cell,

the cytotoxic payload is released via enzymatic cleavage of the linker, chemical conditions, or antibody degradation. The released payload then interacts with intracellular targets, such as microtubules or DNA, thereby inhibiting cell proliferation and inducing cell death. This process may also induce cancer cells to emit signals that enhance immune-mediated tumor destruction in a mechanism called Antibody-Dependent Cell-mediated Cytotoxicity (ADCC) (3, 5).

Two more principles guide current ADC design. The first is the bystander effect, where membrane-permeable payloads diffuse from antigen-positive cells to adjacent antigen-negative or antigen-low tumor cells, potentially enhancing efficacy in heterogeneous tumors (5). This effect is primarily determined by the physicochemical properties of the payload and is further influenced by linker type and tumor architecture. However, it necessitates balancing increased intratumoral activity with the risk of off-tumor toxicity if the payload escapes the tumor microenvironment (3). The second principle involves non-internalizing ADC strategies that do not rely on antigen-mediated endocytosis but instead utilize extracellular payload-release mechanisms, such as disulfide-bridge reduction, favored by the reductive tumor microenvironment when targeting extracellular components (8). These approaches broaden the spectrum of viable targets and may provide therapeutic options for tumors with limited internalization or stromal-dominant characteristics, although they require rigorous conjugate design to ensure tumor-specific activation (8).

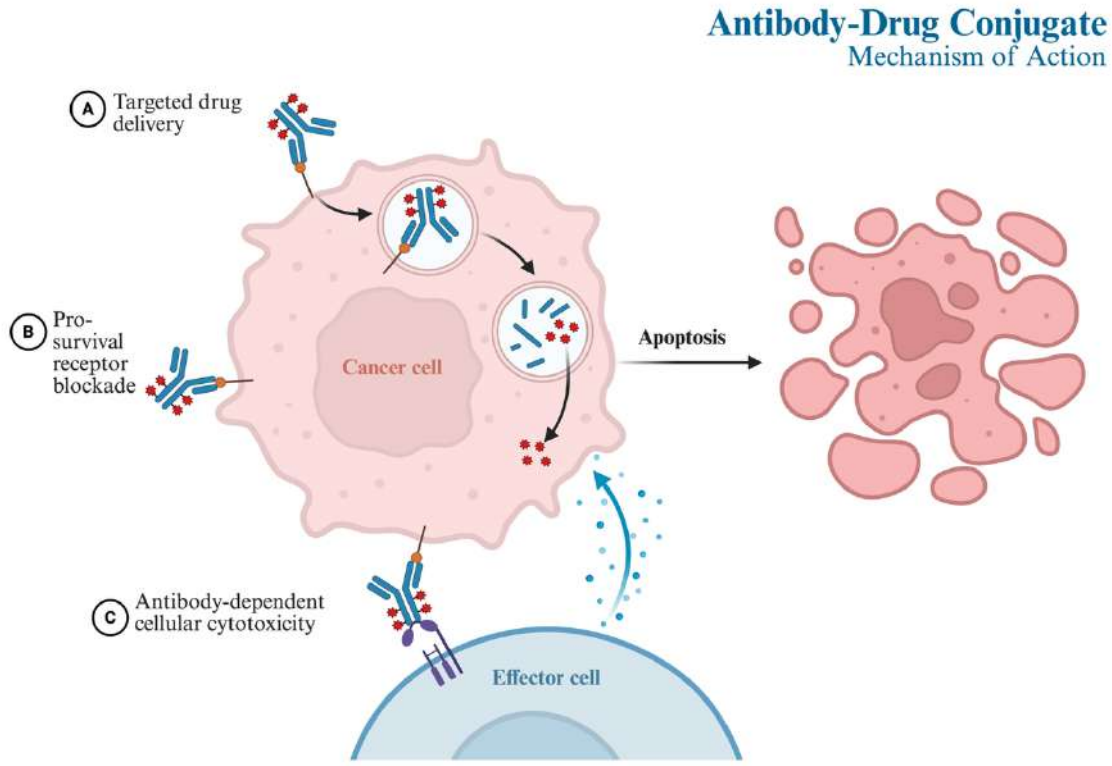


Figure 1. Schematic representation of the mechanism of action of antibody–drug conjugates (ADCs). Upon specific binding to a target receptor on the cancer cell surface, the ADC is internalized and releases its cytotoxic payload, ultimately inducing apoptosis (A, targeted drug delivery). In parallel, antibody binding may inhibit pro-survival signaling pathways mediated by the receptor (B, pro-survival receptor blockade) and activate immune effector functions, such as antibody-dependent cellular cytotoxicity (ADCC) (C), thereby contributing to tumor cell elimination. *Image realized with Biorender online tool.*

Architecture of ADCs

ADCs as engineered systems

Although antibody-drug conjugates (ADCs) are often described as "antibodies carrying cytotoxics," they are better seen as integrated prodrug systems. Here, antigen binding, cellular processing, payload chemistry, and stability together determine tumor exposure and toxicities (9). The therapeutic window relies on optimizing antibody or target biology, linker and conjugation chemistry, and payload properties, including potency, permeability, and activity (9,10). Each component can enhance or limit the others, so a holistic design is required. By this way, Drug-to-antibody ratio (DAR) is a key parameter. Higher DAR increases potency but also hydrophobicity, aggregation, clearance, and nonspecific uptake. These changes affect efficacy and safety (3). As a result, ADC development now emphasizes controlled conjugation and rigorous analytical methods to ensure consistent quality and predictable clinical results (3).

The antibody and target axis

The antibody component confers selectivity, an extended half-life, and a biodistribution profile typical of IgG scaffolds. However, it also limits target accessibility, affects internalization kinetics, and mediates Fc interactions with immune effectors and FcRn recycling (9). From a drug-design perspective, the antibody can be both a targeting ligand and a macromolecular carrier that influences pharmacokinetics and pharmacodynamics. It also must tolerate chemical modification without losing its structure. Fc functions are retained when needed for biological activity or manufacturability (9,10). Target biology determines ADC efficacy by controlling the delivery of the payload to tumor cells. Key factors are antigen density, internalization, trafficking, and antigen expression in normal tissues (9). For example, blood cancers provide easy access to targets, whereas solid tumors create barriers like poor perfusion and antigen diversity, limiting ADC delivery. Even with selective antibodies, poor penetration or rapid clearance can reduce the therapeutic index—a limitation that can be offset by optimizing linker stability, payload potency, and DAR. Recent advances in ADC development have expanded the perspective on internalization, shifting from considering it a requirement to recognizing multiple tumor-selective mechanisms for payload release. (9, 10, 11, 12).

Payload and Linker Selection

Because tumors absorb only a part of the administered dose, ADC payloads must be very potent, working at lower concentrations than standard chemotherapies (9). Figure 2 shows the most used and clinically successful payload classes. Clinical ADCs often use tubulin inhibitors such as auristatins (MMAE, MMAF) and maytansinoids (DM1, DM4), chosen for potency, manufacturability, and linker compatibility (11,12). Early studies with auristatin conjugates showed that linker and payload chemistry directly affect ADC stability, release, and tolerability (11). Potency is important, but the mechanism of action also shapes tumor response. Tubulin inhibitors kill cells quickly, while DNA-damaging agents may be effective against slow-growing cells but can cause broader toxicity if not tightly controlled. Payload membrane permeability is crucial: drugs must reach both antigen-positive cells and nearby cells to exert a bystander effect. Thus, payload choice is closely linked to cytotoxic potential, linker release, and active catabolite form (9, 11, 15).

At the same time, Linkers choose is foundamental. They can be cleavable or non-cleavable; both connect tumor-specific triggers—like pH or proteases—to antibody degradation (13). Cleavable

linkers such as Val–Cit motifs are stable in blood and release payloads after internalization and lysosomal breakdown. The anti-CD30 auristatin system shows this: a valine–citrulline linker provides plasma stability and efficient MMAE drug release after uptake (12,15). However, "protease cleavability" is complicated. Cathepsin B was thought to be key for processing Val–Cit linkers, but multiple lysosomal proteases can help, so one enzyme doesn't predict performance. Linker stability and processing also depend on the conjugation site, local microenvironment, and the ADC's structure (16). Non-cleavable linkers are meant to maximize systemic stability. They rely on complete lysosomal degradation of the antibody to produce an active drug-containing catabolite (13). Trastuzumab–DM1 (T-DM1) is an example. Preclinical studies showed that a non-cleavable thioether linkage can maintain antitumor activity while reducing premature drug release (16). Non-cleavable linkers usually yield more polar catabolites than freely diffusible payloads. This can reduce bystander effects but may lower toxicity from extracellular payload diffusion (13,16).

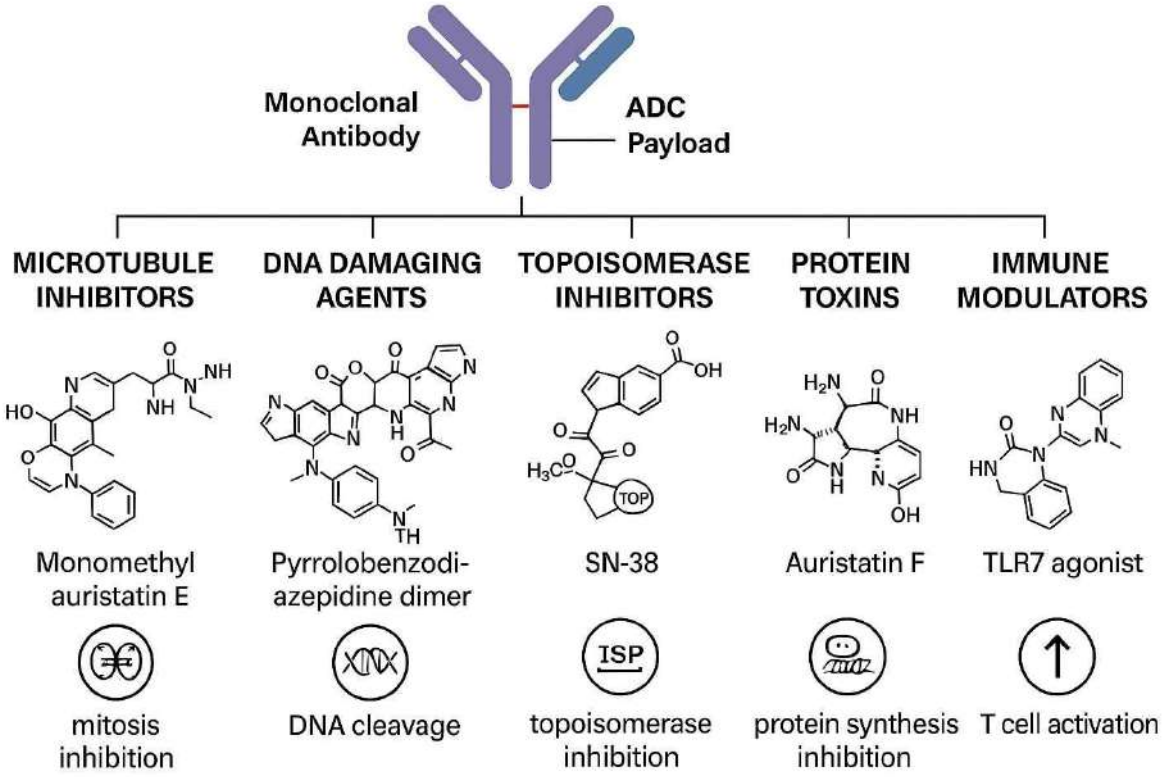


Figure 2. Overview of the main classes of payloads used in antibody–drug conjugates (ADCs). Following conjugation to a monoclonal antibody, different cytotoxic or immunomodulatory agents can be delivered to target cells, including microtubule inhibitors (e.g., monomethyl auristatin E) that disrupt mitosis, DNA-damaging agents (e.g., pyrrolobenzodiazepine dimers) that induce DNA cleavage, topoisomerase inhibitors (e.g., SN-38) that interfere with DNA replication, protein toxins (e.g., auristatin F) that inhibit protein synthesis, and immune modulators (e.g., TLR7 agonists) that promote T cell activation. Image taken from the BOC Sciences ADC Technology website. *Image source: https://adc.bocsci.com/resource/optimize-adc-drug-payload-selection-for-maximum-efficacy.html*

Conjugation and Drug Antibody Ratio

Antibodies have many chemical sites for drug attachment. Originally, drugs were randomly attached to lysines or cysteines, producing mixtures with different DARs and attachment sites. This impacts aggregation, FcRn binding, and clearance. Such complexity makes analysis and quality control more difficult, leading to site-specific conjugation methods, that allows more predictable products. (9,10). Maleimide–thiol chemistry is standard for cysteine conjugation, but it can undergo exchange or retro-Michael addition under physiological conditions, potentially leading to deconjugation. Self-hydrolysing maleimides improved this by stabilizing the linkage and enhancing ADC stability and function (17).

The drug-to-antibody ratio (DAR) is often seen as a simple measure of ADC potency. In practice, more drugs do not always lead to better results. High loading can increase hydrophobicity, aggregation, and clearance (9,18). Studies with anti-CD30 auristatin conjugates showed that higher drug-to-antibody ratios (DARs) increased *In Vitro* potency, but intermediate DARs yielded similar results in animal studies with better safety (18). So, DAR should be balanced—not simply maximized—to optimize efficacy and minimize toxicity. A schematic description of common DAR distribution based on different conjugation site is reported in Figure 3.

Site-specific conjugation strategies address the challenges of variable DAR (9,10). Engineering defined cysteine sites for conjugation has improved the therapeutic index over less controlled methods. This shows that precise control of attachment sites and DAR improves efficacy and safety (19). Other innovations include enzymatic conjugation via sortase or transglutaminase, and the use of orthogonal reactive handles, such as unnatural amino acids or engineered aldehyde tags (10,20). Unnatural amino acids support precise conjugation and modular, homogeneous ADC synthesis (20). Enzymatic methods use mild conditions and offer defined stoichiometry (10). Both sortase- and transglutaminase-mediated approaches have enabled the production of site-specific ADCs with robust *In Vitro* and *In Vivo* potency (21, 22) These platforms expand ADC design by enabling systematic comparisons of payloads and linkers at fixed sites. This improves understanding of pharmacokinetics, pharmacodynamics, and toxicity (10,20,22). Site specificity also supports multifunctional constructs, such as dual site-specific conjugates for separate or sequential cargo delivery, anticipating new dual- or multi-payload ADC strategies (23,24).

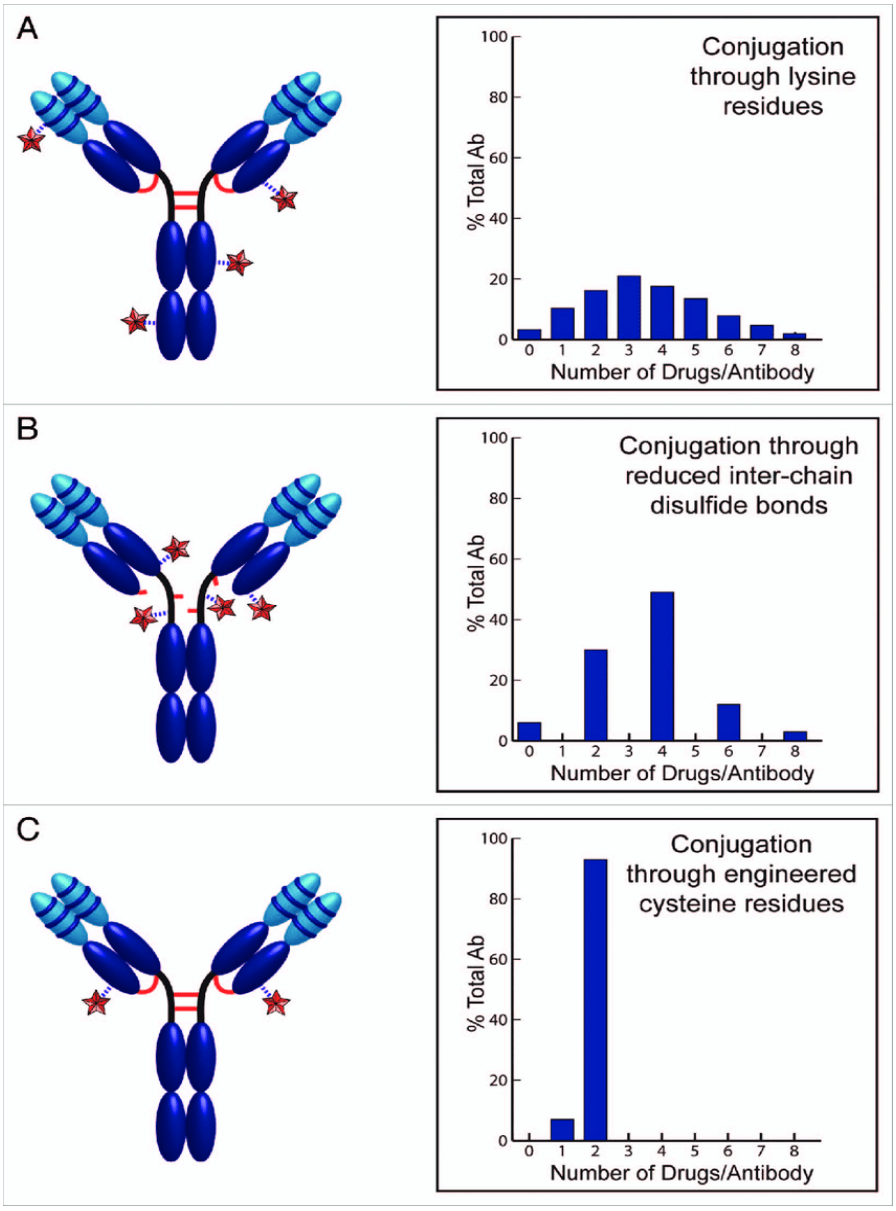


Figure 3. Antibody conjugation methods include (a) cysteine-reactive, and (b) lysine-reactive chemistries which generate heterogeneous mixtures of drug-antibody-ratio (DAR), while (c) site specific conjugation methods deliver more homogeneous product with defined DAR using engineered residues, modified specific glycans, enzymatic ligations, and chemical cross-linkers. Schematic representation of antibody heavy chains and light chains are colored light blue and dark blue respectively. Complementarity determining regions (CDRs) and conjugation sites are depicted as blue lines and red stars respectively. Approximate DAR distribution for stochastic cysteine and lysine conjugations is presented as bar charts.

Image source: Panowski et Al. 2014 (25).

ADC Conjugation chemistry

The method used to link a toxic payload to an antibody determines the drug-to-antibody ratio (DAR) and the stability of covalent bonds during storage and *In Vivo* circulation. Consequently, conjugation chemistry plays a central role in establishing critical quality attributes (CQAs) and the therapeutic index. It exerts a significant impact on systemic clearance, tissue distribution, tolerability, and efficacy, even when the target, antibody, and payload are constant (9,25,26).

Classical conjugation

Historically, clinical ADCs have been produced using conjugation strategies that exploit nucleophilic residues on native immunoglobulins, most commonly lysines or cysteines exposed after partial reduction of interchain disulfides (Figure 4). Although these methods are robust and scalable, they inherently generate polydisperse products, resulting in distributions of conjugation sites and DAR states rather than a single, defined chemical species. Lysine-directed conjugation, due to the abundance of accessible ε-amines, produces extensive positional microheterogeneity and broad DAR distributions. Cysteine-directed conjugation offers improved control over the number of reactive sites, but it still yields mixtures. Additionally, disulfide reduction can introduce structural perturbations depending on the extent of reduction, re-oxidation, and re-bridging (9,25).

The impact of conjugation methods is shown by anti-CD30–MMAE conjugates enriched to discrete DAR states. Increased drug loading enhances *In Vitro* potency but also elevates plasma clearance and reduces tolerability *In Vivo* (18). These observations established that DAR is a parameter that should be optimized to balance potency, clearance, and toxicity, rather than simply maximizing drug loading. Higher-DAR species exhibit greater hydrophobicity, increasing their propensity for aggregation and accelerated uptake by the mononuclear phagocyte system. In contrast, lower-DAR species may be better tolerated but may deliver insufficient payload (9,18). These observations also highlight why “average DAR” is an incomplete descriptor of ADC behavior. (9,25) Therefore, average DAR alone does not fully characterize ADC behavior, as preparations with identical mean DAR can behave differently when different DAR species and aggregated hydrophobic subpopulations are present (9,25).

Controlling conjugation heterogeneity is essential, as it links manufacturing processes to clinical variability through measurable changes in exposure and safety. The stability of new covalent bonds formed during conjugation is also critical for tumor-selective delivery (9,25) In many cysteine-linked ADCs, thiol addition to maleimide-functionalized drug-linker forms a thiosuccinimide linkage (17). Although efficient, this linkage can be unstable *In Vivo* due to deconjugation or thiol exchange (9, 18). Hydrolysis of the succinimide ring stabilizes this linkage, as demonstrated by self-hydrolyzing maleimides that improve *In Vivo* stability and pharmacological properties, including increased antitumor activity and reduced neutropenia in models (18).

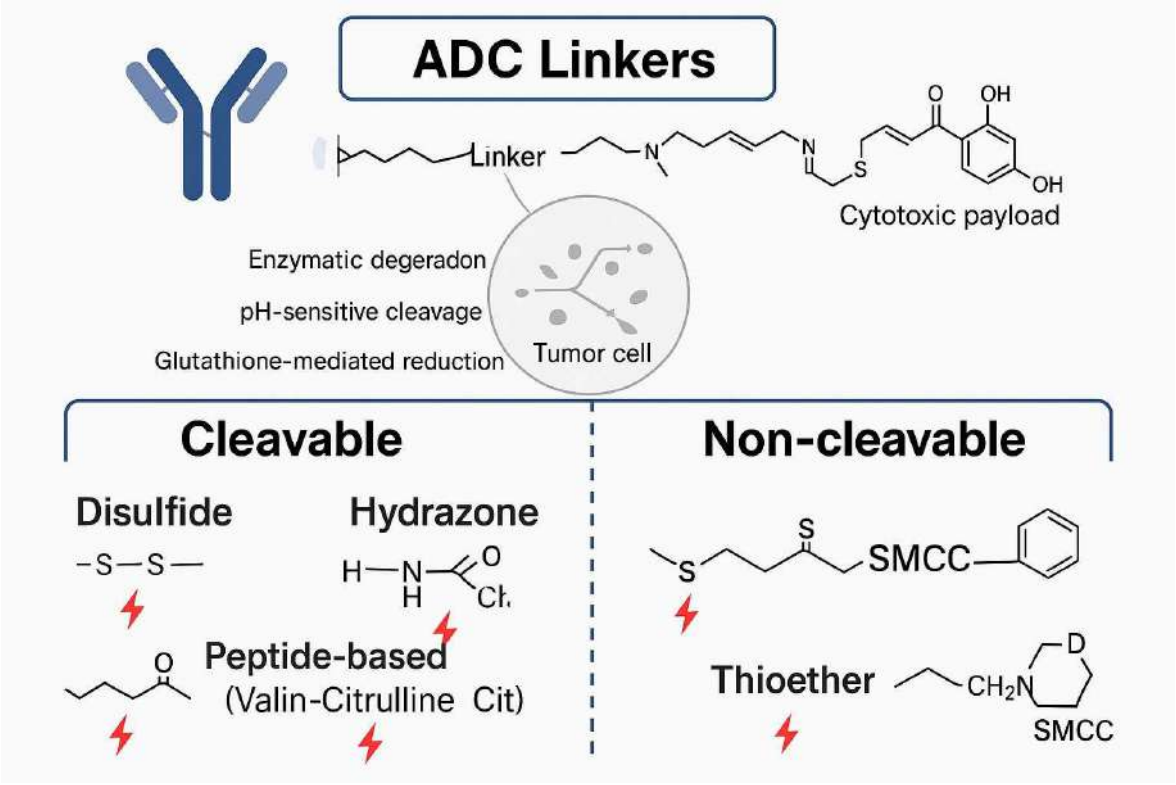


Figure 4. Schematic representation of commonly used linkers for Antibody - Drug conjugation: (**Left**) Linkers can be broadly classified as cleavable linker (the payload can dissociate from the mAb at the tumor site) or (**right**) non-cleavable linker (the payload remains bound to the mAb). Common cleavable linkers include chemically active linkers, acid-cleavable linkers, reducible chain linkers and enzyme-cleavable linkers.

Image taken from the BOC Sciences ADC Technology website.
Image source: https://adc.bocsci.com/products/antibody-drug-conjugates-adcs-7387.html

Site-specific conjugation

To overcome the limitations of classical conjugation, site-specific strategies have been developed as described in Figure 5. These approaches generate a narrow set of ADC species and improve the therapeutic index by minimizing subpopulations (9,18,25). A common site-specific conjugation method involves introducing engineered cysteine residues at selected positions, which preserves protein folding and antigen binding while enabling conjugation at predefined locations (n.d. TIOMAB) (9, 12). This strategy yields near-homogeneous products with controlled stoichiometry, often achieving a DAR of approximately 2 in typical two-site designs and reducing both DAR dispersion and positional isomerism (9). Consequently, site-specific conjugation has improved the therapeutic index compared to less controlled methods, supporting the principle that reducing the number of attachment sites and DAR can maintain efficacy while enhancing tolerability (19).

Expanding upon site-specific strategies, another approach uses non-natural amino acids with orthogonal reactive groups, enabling chemoselective ligations at defined positions (9,20). For instance, a ketone-bearing amino acid facilitates oxime ligation, producing homogeneous ADCs with defined conjugation sites and stoichiometry, and supporting strong target-dependent cytotoxicity and

robust *In Vivo* antitumor activity (20). Orthogonal ligations address persistent limitations of classical conjugation, such as uncontrolled positional isomerism and chemically fragile linkages at broadly reactive residues, by encoding the conjugation site within the antibody sequence itself (9, 20). Alternatively, the conserved Fc N-glycan (Asn297) can serve as a chemically addressable feature that is enzymatically remodelled and functionalized, providing positional control without introducing backbone mutations (9,27). In this context, glycoengineering enables the installation of reactive groups on the glycan, which are then coupled to payloads via chemo selective reactions, resulting in well-defined product profiles and target-dependent antitumor activity in preclinical models (27).

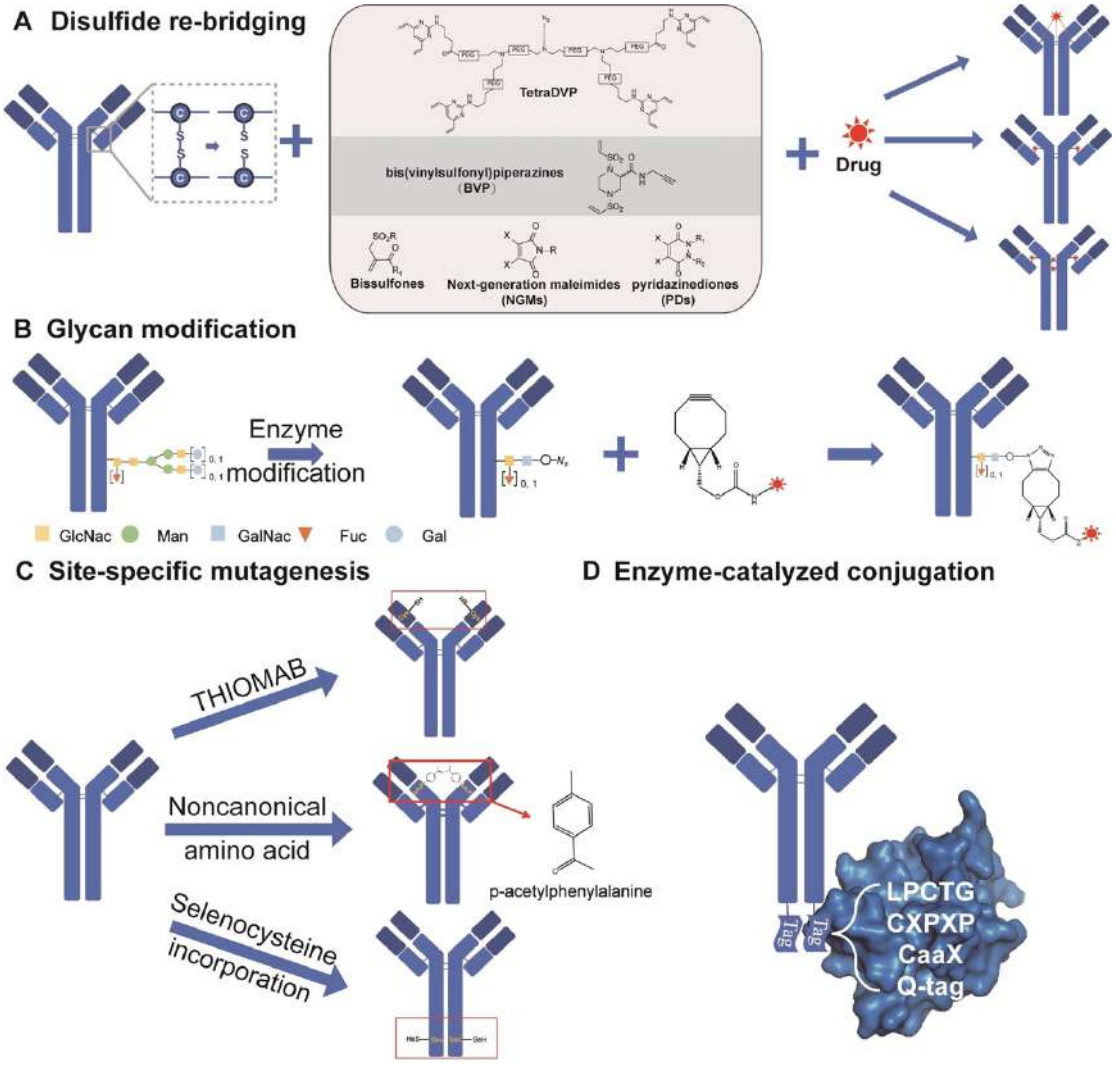


Figure 5. Figure. Strategies for site-selective antibody–drug conjugation. (A) Disulfide re-bridging approaches exploit the reduction of interchain disulfide bonds followed by re-linking with bifunctional reagents (e.g., TetraDVP, BVPs, bissulfones, next generation maleimides, and pyridazinediones) to enable controlled drug attachment. (B) Glycan modification relies on enzymatic remodeling of Fc N-glycans to introduce reactive handles for subsequent conjugation. (C) Site-specific mutagenesis strategies include engineered cysteines (THIOMAB), incorporation of noncanonical amino acids (e.g., p-acetylphenylalanine), or selenocysteine insertion to achieve precise conjugation sites. (D) Enzyme-catalyzed conjugation employs peptide tags (e.g., LPXTG, CXpXP, CaaX, Q-tag) recognized by specific enzymes to mediate highly selective drug attachment. *Image source: Dong et Al. 2024 (28)*

Next-generation linker architectures

Linker design has advanced beyond the basic distinction between “cleavable” and “non-cleavable” connectors and is now considered a systems-level engineering element. Linker architecture can modulate hydrophobicity, drug loading, colloidal stability, systemic exposure, and the spatial distribution of payload activity within tumors (29,30). As a result, linker architectures are now designed to separate efficacy-driving parameters, such as payload class, DAR, release chemistry, and bystander-killing capacity, from developability challenges, including aggregation, accelerated clearance, premature deconjugation or release, and limited tolerability margins (29,30). Moreover, solid tumors often require effective intratumoral drug delivery despite heterogeneous antigen expression and limited tissue penetration (29,30).

The rationale for high-DAR ADCs (commonly DAR ≥ 6) is to increase the number of cytotoxic molecules delivered, thereby enhancing cytotoxicity within tumor tissue (30,31). High DAR is particularly advantageous when payload potency is reduced to improve safety, when antigen density is moderate, when internalization is slow or heterogeneous, or when antibody access is restricted by microregional barriers (30,31). However, increasing DAR also increases hydrophobicity and aggregation propensity, which enhance non-specific interactions, accelerate clearance, compromise exposure, and narrow tolerability. Therefore, the design objective is to balance drug loading with hydrophilicity, stability, and controlled-release kinetics to prevent adverse pharmacokinetics or tolerability issues as drug loading increases (30,31). A direct, broadly applicable strategy to achieve higher DAR is to incorporate hydrophilic motifs into the drug–linker module. These motifs mask payload-driven hydrophobicity and enhance colloidal stability (29,32). For example, systematic studies with monodisperse PEG-containing linkers demonstrate that PEG presence alone is insufficient. The topology and positioning, such as pendant versus linear placement, as well as the nature of the antibody–linker bond, for instance, amide versus carbamate, can significantly influence aggregation under stress and alter *In Vivo* clearance in mice (31).

Building on this approach, polysarcosine (PSAR) has emerged as a prominent “PEG-like” hydrophilic masking entity. PSAR can be synthesized in monodisperse, well-defined formats and incorporated into drug–linker platforms (31,32). For instance, monodisperse PSAR-based drug–linker conjugation enables the generation of highly loaded, homogeneous ADCs with improved physicochemical properties, pharmacokinetics, and *In Vivo* antitumor efficacy, consistent with PSAR functioning as a hydrophobicity-buffering element (31). The PSAR strategy has also been applied to clinically relevant payload classes, such as camptothecin-derived topoisomerase I inhibitors. In these cases, PSAR incorporation reduced overall hydrophobicity and enabled high drug loading with pharmacokinetics like those of the unconjugated antibody in preclinical models (32,33). Collectively, PEG- and PSAR-based designs demonstrate that hydrophilic masking can expand the feasible DAR range without proportionally increasing aggregation or clearance, thereby broadening the design space for payload selection and dosing strategies (29,32).

Current Clinical Landscape

Recent reviews report that about 15 antibody-drug conjugates (ADCs) have FDA approval for clinical use. The exact number varies by region and by whether historically withdrawn approvals are included (3,34,35). Approvals include both hematologic malignancies and solid tumors, in addition, clinical efficacy has been established across multiple tumor types and payload classes. ADCs use various payloads, such as auristatin-based agents (e.g., monomethyl auristatin E, a microtubule inhibitor), maytansinoid-based agents (e.g., DM1/DM4), calicheamicin derivatives (DNA-damaging agents), and topoisomerase I inhibitors (e.g., SN-38, DXd). Each payload class needs specific consideration of linker design, catabolite profiles, bystander effect, and tolerability (5,34,35), as summarized in Table 1.

Table 1: Descriptive table of all 2025 FDA commercially approved ADCs.

ADC	Target	Linker type	Linker motif / trigger	Payload (class)	Payload (molecule)	Conjugation chemistry	Typical DAR	Key tumor indications	Key source (Ref)
Gemtuzumab ozogamicin (Mylotarg)	CD33	Cleavable	Acid-labile hydrazone + reducible disulfide (bifunctional AcBut linker)	DNA-damaging enediyne	N-acetyl-γ-calicheamicin derivative	Lysine conjugation	≈2–3	CD33+ acute myeloid leukemia (AML)	(36)
Inotuzumab ozogamicin (Besponsa)	CD22	Cleavable	Acid-labile / disulfide	DNA-damaging enediyne	N-acetyl-γ-calicheamicin derivative	Lysine conjugation	≈5-6	Relapsed/refractory B-cell precursor acute lymphoblastic leukemia	(37)
Brentuximab vedotin (Adcetris)	CD30	Cleavable	Protease-cleavable dipeptide (valine–citrulline) + PABC self-immolative spacer	Microtubule inhibitor (auristatin)	MMAE	Cysteine conjugation	≈4	Hodgkin lymphoma; systemic anaplastic large cell lymphoma; other CD30+ lymphomas	(38)
Polatuzumab vedotin (Polivy)	CD79b	Cleavable	Protease-cleavable dipeptide (vedotin platform)	Microtubule inhibitor (auristatin)	MMAE	Cysteine conjugation	≈3–4	Diffuse large B-cell lymphoma (DLBCL)	(39)
Enfortumab vedotin (Padcev)	Nectin-4	Cleavable	Protease-cleavable dipeptide (vedotin platform)	Microtubule inhibitor (auristatin)	MMAE	Cysteine conjugation	≈3–4	Urothelial carcinoma (± combination with pembrolizumab)	(40)
Tisotumab vedotin (Tivdak)	Tissue factor (TF)	Cleavable	Protease-cleavable dipeptide (vedotin platform)	Microtubule inhibitor (auristatin)	MMAE	Cysteine conjugation	≈4	Recurrent/metastatic cervical cancer	(41)

Trastuzumab emtansine (T-DM1; Kadcyla)	HER2 (ERBB2)	Non-cleavable	Thioether linker (SMCC/MCC) requiring lysosomal degradation of antibody	Microtubule inhibitor (maytansinoid)	DM1	Lysine conjugation	≈3.5	HER2+ breast cancer (metastatic) / non-squamous NSCLC	(42)
Trastuzumab deruxtecan (T-DXd; Enhertu)	HER2 (ERBB2)	Cleavable	Protease-cleavable peptide linker	Topoisomerase I inhibitor (exatecan derivative)	DXd	Cysteine conjugation	≈8	HER2+ and HER2-low breast cancer; HER2+ gastric; non-squamous NSCLC	(43)
Sacituzumab govitecan (Trodelvy)	Trop-2	Cleavable	Hydrolyzable CL2A linker (pH-sensitive release in tumor)	Topoisomerase I inhibitor (irinotecan metabolite)	SN-38	Click Chemistry, Cysteine conjugation	≈8	Metastatic triple-negative breast cancer; HR+/HER2− breast cancer; non-squamous NSCLC	(44)
Loncastuximab tesirine (Zynlonta)	CD19	Cleavable	Protease-cleavable dipeptide linker	DNA crosslinker	PBD dimer (SG3199)	Cysteine conjugation	≈2.3	Relapsed/refractory large B-cell lymphoma (LBCL)	(45)
Mirvetuximab soravtansine-gynx (Elahere)	Folate receptor alpha (FRα/FOLR1)	Cleavable	Hydrophilic disulfide linker (sulfo-SPDB); reducible / disulfide exchange	Microtubule inhibitor (maytansinoid)	DM4	Lysine conjugation	≈3.4	FRα-high platinum-resistant ovarian cancer	(46)
Datopotamab deruxtecan (Dato-DXd; Datroway)	Trop-2	Cleavable	Protease-cleavable tetrapeptide linker	Topoisomerase I inhibitor (exatecan derivative)	DXd	Cysteine conjugation	4	Breast cancer (HR+/HER2) non-squamous NSCLC	(47)
Telisotuzumab vedotin (Teliso-V; Emrelis)	c-Met (MET)	Cleavable	Protease-cleavable linker, (vedotin platform)	Microtubule inhibitor (auristatin)	MMAE	Cysteine conjugation	3.1	c-Met–high, EGFR-wildtype non-squamous NSCLC	(48)
Moxetuzumab Pasudotox (Lumoxiti)	CD22	Linkerless	Linkerless	Elongation factor-2 inhibitor	PE38 (38 kDa fragment of Pseudomonas exotoxin A)	Fused protein	1	Relapsed or Refractory Hairy Cell Leukemia (HCL)	(49)
Belantamab Mafodotin-blmf (Blenrep)	BCMA	Non-Cleavable	Thioether linker (SMCC/MCC) requiring lysosomal degradation of antibody	Tubulin polymerization inhibitor	MMAF	Cysteine conjugation	≈4	Multiple Myeloma	(50)

ADC in Hematologic malignancies

Hematologic malignancies provided the first evidence for ADC efficacy, partly because malignant cells are more accessible and present more specific targets than those in solid tumors (5,34,35). In Hodgkin lymphoma, the CD30-targeting ADC brentuximab vedotin achieved high response rates in heavily pretreated patients, and the ECHELON-1 study showed that adding brentuximab vedotin to first-line chemotherapy improved outcomes in advanced disease. Long-term follow-up confirmed continued therapeutic benefit and a favourable safety profile (51–54).

Clinical experience with ADCs in acute leukemias highlights the importance of dosing and exposure. In acute myeloid leukemia (AML), recent studies show that the CD33-targeting ADC gemtuzumab ozogamicin improves outcomes when given in split doses with standard chemotherapy; notably, the ALFA-0701 trial improved survival and helped clinicians develop strategies to balance efficacy with hepatic toxicity (55). For certain relapsed leukemias, the CD22-targeting ADC inotuzumab ozogamicin outperformed standard chemotherapy, suggesting that targeted cytotoxic delivery can increase remission rates and facilitate progression to potentially curative interventions, such as stem cell transplantation. However, these studies also found specific risks, including hepatotoxicity, which clinicians must manage carefully through individualized patient care and treatment planning (56).

ADC in Solid tumors

Solid tumors present additional challenges for ADC therapy.: vascular delivery is heterogeneous, interstitial pressure and stromal barriers impede penetration, antigen expression can be mosaic, and payload diffusion may be required to kill antigen-low/negative neighboring cells. (5,34,35) These challenges led to the development of drugs and linkers that allow payload diffusion to neighboring cells while keeping stability in circulation (5, 33). Clinically, payloads such as topoisomerase inhibitors and microtubule inhibitors have demonstrated strong efficacy, even in tumors with mixed target expression. Each class, however, has its own adverse effect profile (3, 5, 34).

Careful monitoring is required, especially in breast cancer. Trastuzumab emtansine (T-DM1) established ADCs as a durable treatment. The EMILIA study showed T-DM1 improved outcomes compared to lapatinib plus capecitabine in previously treated HER2-positive metastatic breast cancer. This proved that antibody-delivered cytotoxic payloads can outperform traditional targeted therapy plus chemotherapy (57,58). HER2-targeted ADCs advanced further in the DESTINY-Breast03 trial, where trastuzumab deruxtecan (T-DXd) outperformed T-DM1 in HER2-positive metastatic breast cancer. This result highlighted the effectiveness of a membrane-permeable topoisomerase I payload combined with an ADC design that enables high intracellular drug delivery and a clinically relevant bystander effect (59,60). Longer-term follow-up analyses have further clarified the survival impact and safety associated with sustained exposure. DESTINY-Breast04 also demonstrated that T-DXd was superior to chemotherapy in HER2-low metastatic breast cancer. This redefined HER2 as a critical biomarker here (61).

Gastric and gastro-oesophageal junction cancers provided further validation of HER2-ADC therapeutic efficacy beyond breast cancer. In the DESTINY-Gastric01 trial, trastuzumab deruxtecan improved outcomes compared to chemotherapy in patients with previously treated HER2-positive disease. This finding led to regulatory approval and demonstrated that ADCs maintain efficacy across different epithelial tumors, even when HER2 expression and amplification remain more heterogeneous than in breast cancer (62).

Beyond HER2, TROP2-directed ADCs have shown progress in metastatic triple-negative breast cancer. The ASCENT trial showed that sacituzumab govitecan improved progression-free and overall survival compared with standard chemotherapy, establishing ADCs as a standard of care in a subtype with few targeted therapies (63,64). ADCs not only outperform chemotherapy in sensitive tumors but also offer a distinct and manageable toxicity profile that varies by payload class and systemic exposure; for example, neutropenia and diarrhea are associated with SN-38–based constructs (3,5,35,64).

In bladder cancer, the Nectin-4-targeting ADC enfortumab vedotin improved outcomes in patients who had received other therapies. Specifically, the EV-301 study found that enfortumab vedotin provided better survival than chemotherapy in patients with advanced disease after platinum-based and checkpoint inhibitor therapies (65). Building on this, combining enfortumab vedotin with immunotherapy pembrolizumab in the EV-302/KEYNOTE-A39 study recently led to improved outcomes compared with chemotherapy in untreated advanced bladder cancer. Together, these results demonstrate the potential for ADCs to work effectively with immunotherapy, perhaps by enhancing immune recognition of cancer cells and altering the tumor environment. Nonetheless, managing these combinations requires care because overlapping toxicities—including skin, nerve, and metabolic effects—can occur (66).

In gynecologic oncology, the tissue factor–directed ADC tisotumab vedotin showed meaningful activity in recurrent or metastatic cervical cancer in the innovaTV 204 trial, providing a therapeutic option in a situation with limited second-line efficacy. This result supports the idea that ADC targets do not need to be strictly tumor-specific if expression and dosing give a suitable therapeutic index (67). Similarly, in platinum-resistant ovarian cancer, the folate receptor-α–targeted ADC mirvetuximab soravtansine did better than chemotherapy in the MIRASOL trial, with patients with high FRα expression seeing improvements in progression-free survival, overall survival, and response rate (68).

The examples described, along with other antibody-drug conjugates (ADCs) in development against a wide range of malignancies (see Table 2), highlight several key considerations. First, target density and distribution are critical determinants of ADC efficacy; however, their effects are not always linear or predictable. Some targets enable efficient internalization, while others allow slower uptake but maintain clinical utility due to high antigen density, sustained binding, or compensatory payload mechanisms such as bystander killing (5,34,35). Second, the clinical significance of the bystander effect is context dependent. This effect may be beneficial in tumors with heterogeneous antigen expression, but it can also increase toxicity when normal tissues express low levels of the antigen or when the payload's catabolites diffuse extensively (3,5,35). Third, achieving efficacy in solid tumors often requires balancing systemic stability with effective payload release within the tumor microenvironment. Highly stable ADC constructs may exhibit reduced efficacy if intratumoral payload release is insufficient, whereas less stable ADCs are prone to premature release and systemic toxicity (3,5,25,26). These pharmacodynamic properties are reflected in adverse events such as lung disease with T-DXd, neutropenia and diarrhea with SN-38–based ADCs, neuropathy with MMAE-based ADCs, and ocular toxicity with maytansinoid. These toxicities necessitate vigilant monitoring and may require interventions such as treatment delays, dose reductions, or discontinuation. These challenges emphasize the need for ongoing optimization of linker design, dosing strategies, and scheduling (3,5,35,60,68).

Table 2: Descriptive table of some advanced or promising ADCs in clinical phases.

ADC (code name)	Target	Linker type	Linker motif / trigger	Payload (molecule /class)	Conjugation chemistry	Typical DAR (reported)	Most advanced phase	Key tumor indications	Key source(s) (DOI)
Patritumab deruxtecan (HER3-DXd; U3-1402)	HER3 (ERBB3)	Cleavable	Protease-cleavable peptide linker	DXd (TOP1 inhibitor)	Cysteine conjugation	≈7-8	Phase II/III program in EGFR-mutant NSCLC	EGFR-mutant NSCLC after EGFR-TKI; other HER3+ tumors	(69)
DS-7300a (Ifinatamab deruxtecan; I-DXd)	B7-H3 (CD276)	Cleavable	Protease-cleavable peptide linker	DXd (TOP1 inhibitor)	Cysteine conjugation	≈4	Phase I/II	B7-H3+ solid tumors (e.g., SCLC and others)	(70)
Raludotatug deruxtecan (R-DXd; DS-6000a)	Cadherin-6 (CDH6)	Cleavable	Deruxtecan platform	DXd (TOP1 inhibitor)	Cysteine conjugation	8	Phase I	Ovarian cancer; renal cell carcinoma; other CDH6+ tumors	(71)
Trastuzumab duocarmazine (SYD985)	HER2 (ERBB2)	Cleavable	Protease-cleavable peptide linker + self-immolative p-aminoethylcarbamoyl (PABC) spacer	seco-DUBA (duocarmycin analog; DNA-alkylating)	Cysteine conjugation	≈2.8	Phase III (breast cancer program; global)	HER2+ / HER2-low breast cancer; other HER2-expressing tumors	(72)
Tusamitamab ravtansine (SAR408701)	CEACAM5	Cleavable	SPDB bifunctional cleavable linker	DM4 (maytansinoid; tubulin inhibitor)	Lysine conjugation to the antibody, disulphide bond with DM4	≈3.8	Phase II/III program in CEACAM5+ NSCLC (global)	CEACAM+ non-squamous NSCLC; other CEACAM5 + tumors	(73)
MGC018 (vobramitamab duocarmazine)	B7-H3 (CD276)	Cleavable	Protease-cleavable peptide linker	seco-DUBA (duocarmycin analog; DNA-alkylating)	Cysteine conjugation	≈2.7	Phase I/II	Advanced solid tumors (multiple); prostate cancer and others	(74)
SGN-B6A	Integrin β6 (ITGB6)	Cleavable	Vedotin platform (protease-cleavable)	MMAE (auristatin; tubulin inhibitor)	Cysteine conjugation	≈4	Phase I	ITGB6+ solid tumors (NSCLC, pancreatic, etc.)	(75)
Zilovertamab vedotin (ZV; VLS-101)	ROR1	Cleavable	Protease-cleavable peptide linker	MMAE (auristatin; microtubule inhibitor)	Cysteine conjugation	≈4	Phase I (first-in-human)	Lymphoid cancers (e.g., mantle cell lymphoma, DLBCL); other ROR1+ malignancies	(76)

Pivekimab sunirine (IMGN632)	CD123	Cleavable	Protease-cleavable mc-val-cit-PABC linker	Indolinobenzodiazepine (IGN) pseudodimer (DNA-alkylating)	Cysteine conjugation	≈4	Phase I/II	AML; blastic plasmacytoid dendritic cell neoplasm (BPDCN); other CD123+ malignancies	(77)
Camidanlumab tesirine (ADCT-301)	CD25	Cleavable	Protease-cleavable linker	PBD dimer (SG3199-like DNA crosslinker class)	Cysteine conjugation	2.3	Phase I/II	Hodgkin lymphoma; T-cell lymphomas	(78)
Praluzatamab ravtansine (CX-2009; Probody drug conjugate)	CD166 (ALCAM)	Cleavable	SPDB bifunctional disulfide cleavable linker + peptide mask (tumor-activated)	DM4 (maytansinoid)	Lysine conjugation to the antibody, disulphide bond with DM4	3.5	Phase I/II	Advanced solid tumors (incl. HR+ breast cancer)	(79)
CX-2029 (Probody drug conjugate)	CD71 (transferrin receptor 1)	Cleavable	Protease-activated peptide mask;	MMAE (auristatin)	Cysteine conjugation	≈2	Phase I	Advanced solid tumors	(80)
Farletuzumab ecteribulin (MORAb-202)	Folate receptor alpha (FRα/FOLR1)	Cleavable	maleimido-PEG2–valine–citrulline–PABC (cathepsin-cleavable)	Eribulin derivative (microtubule inhibitor)	Cysteine conjugation	4.0	Phase I	FRα+ solid tumors (ovarian, TNBC, gastric, etc.)	(81)
Luveltamab tazevibulin (STRO-002)	Folate receptor alpha (FRα/FOLR1)	Cleavable	Cleavable 3-aminophenyl hemiasterlin linker-warhead (SC239)	SC209 (hemiasterlin-derived tubulin inhibitor)	Site-specific nonnatural amino acid (para-azidomethyl-L-phenylalanine);	4	Phase I	Ovarian; endometrial; FRα+ tumors	(82)
AZD8205 (puxitatug samrotecan)	B7-H4 (VTCN1)	Cleavable	Protease-cleavable linker Val-Ala-PEG8 linker	TOP1 inhibitor (AZ14170133); TOP1i class	Cysteine conjugation	8	Phase I	B7-H4+ solid tumors (e.g., breast/ovarian/endometrial; others)	(83)
XMT-1660 (emiltatug ledadotin)	B7-H4 (VTCN1)	Cleavable	Cleavable ester linker	Auristatin hydroxypropylamide AF-HPA (Dolasynthen payload class)	Site-specific conjugation remodeled glycans on Asn297 residue (heavy chain) GlycoConnect™ click chemistry	6	Phase I	B7-H4+ breast, ovarian, endometrial cancers	(84)

AIMS

This PhD thesis aimed to design, validate, and analytically interpret antibody-based conjugate strategies that expand targeted cancer therapy beyond the conventional paradigm of internalizing, cytotoxic antibody-drug conjugates (ADCs). By integrating multiple conjugate formats with comprehensive bioanalytical and pharmacological characterization, this research examines how antibody-guided delivery of anticancer agents can be adapted to various biological contexts and therapeutic goals.

These projects leverage and expand upon the extensive research expertise that our laboratory has developed over the years. Previously, the group developed antibody platforms targeting three clinically relevant proteins:

1. HER3 (ERBB3): a cell-surface receptor involved in signaling and cell growth.
2. LGALS3BP (90K or Mac-2 binding protein): a secreted glycoprotein associated with cancer progression.
3. TEM1/Endosialin: an antigen expressed on tumor-associated endothelial cells (85).

Three humanized antibodies were generated and subsequently used to create their respective antibody–drug conjugates (ADCs).

This research focuses on the design, development, and analytical characterization of two antibody-based anticancer conjugates: EV20/Omomyc and 1959sss/DM4, presented across five chapters:

Development of a dual MYC/HER-3 targeting immunoconjugate

The initial objective of this project was to develop and characterize EV20/Omomyc, a novel antibody–protein conjugate. This construct combines the humanized anti-HER3 therapeutic antibody EV20 with Omomyc, a MYC-inhibitory mini-protein. The strategy was designed to evaluate whether antibody-guided delivery platforms can be expanded beyond traditional cytotoxic small-molecule payloads to include protein-based inhibitors that target intracellular oncogenic signaling pathways.The primary goal was to determine whether this targeted delivery approach could achieve measurable antitumor efficacy in relevant neuroblastoma models, thereby establishing proof of concept for HER3-directed intracellular MYC inhibition.

Development and analytical characterization of a non-internalizing linkerless antibody drug-conjugate targeting circulating LGALS3BP

The second objective of this thesis project focused on optimizing the manufacturing processes of the non-internalizing antibody–drug conjugate (ADC) 1959sss/DM4, which targets the circulating protein LGALS3BP.In parallel, an analytical method was developed to quantify serum and tissue levels of the payload DM4, a potent inhibitor of tubulin polymerization that is already clinically validated as a cytotoxic component in other ADCs. Finally, the antitumor activity of 1959sss/DM4 was evaluated in a syngeneic preclinical neuroblastoma model, including assessment in combination with immunotherapy, to explore potential therapeutic synergy.

This thesis also explored LGALS3BP as a potential urinary biomarker and therapeutic target in bladder cancer. A preliminary study was conducted to analyze urinary and serum levels of circulating LGALS3BP in patients with bladder cancer compared to age-matched healthy controls. Finally, preclinical bladder cancer models were used to evaluate the therapeutic potential of the ADC 1959sss/DM4 in this context.

CHAPTER ONE

HER3-Targeting Antibody and MYC Inhibition: From EV20 to EV20/Omomyc immunoconjugate

This chapter examines the EV20/HER3 axis (the interaction between the EV20 antibody and the HER3 receptor) and the scientific rationale for the EV20/Omomyc immunoconjugate, an engineered construct that combines tumor targeting of HER3 with suppression of the MYC pathway (a signaling pathway involved in cell growth and proliferation).

1.1 HER3 biology and clinical relevance in cancer therapy

The human epidermal growth factor receptor (HER/ERBB) family includes EGFR (HER1/ERBB1), HER2 (ERBB2), HER3 (ERBB3), and HER4 (ERBB4). These receptors regulate cell growth, survival, and differentiation through ligand-induced dimerization and downstream signaling. HER3 is unique within this family. Despite impaired intrinsic kinase activity, HER3 is a central signaling hub, forming heterodimers—primarily with HER2—that efficiently activate PI3K/AKT via multiple phosphotyrosine docking sites on its cytoplasmic tail (86,87). In cancer, HER3 amplifies signals in ERBB-driven tumors and acts as an adaptive escape node when pathways are inhibited, maintaining PI3K/AKT signaling even when upstream targets are blocked (86,87), as shown in Figure 6. HER3 is linked to progression, metastasis, and therapy resistance in various solid tumors, including breast, lung, colorectal, ovarian, melanoma, and head and neck cancers. Its effects depend on ligand availability (such as neuregulins), receptor coexpression (notably HER2), and pathway crosstalk (54,55). HER3 activity often exploits after EGFR- or HER2-targeted therapy, underscoring its role as a dynamic mediator of resistance (86,87).

HER3 offers both opportunities and challenges for therapeutic development. As a cell-surface protein involved in cancer-promoting signaling, HER3 is overexpressed in many tumors. This makes it a promising target for antibody-based drugs and conjugates (86,87). Several strategies have been investigated: blocking ligand binding, promoting down-regulation, inhibiting dimerization with related receptors, and using HER3 for targeted delivery of toxic or inhibitory substances to cancer cells. Each approach's effectiveness depends on tumor type (86,87).

Over the past decade, clinical validation of HER3 as a therapeutic target has advanced with the development of HER3-directed antibody–drug conjugates (ADCs). Patritumab deruxtecan (HER3-DXd) exemplifies this; it is an anti-HER3 antibody linked to a topoisomerase I inhibitor via a cleavable peptide linker, enabling intracellular drug release. Early-phase trials showed antitumor activity in EGFR-mutant non-small-cell lung cancer (NSCLC) resistant to EGFR inhibitors, and later studies confirmed these results (88). In the phase II HERTHENA-Lung01 trial, patritumab deruxtecan was assessed in EGFR-mutant NSCLC after prior EGFR tyrosine kinase inhibitor and platinum-based chemotherapy.

Anti-HER3 antibody platforms can be engineered as modular vehicles to deliver various therapeutic functions, including cytotoxic, inhibitory, or immunomodulatory effects, depending on the payload and conjugation strategy. The laboratory’s HER3 antibody platform, EV20, and its derivative

immunoconjugates represent a systematic approach to investigating HER3 targeting for receptor inhibition and delivery of biologically active agents (82,83).

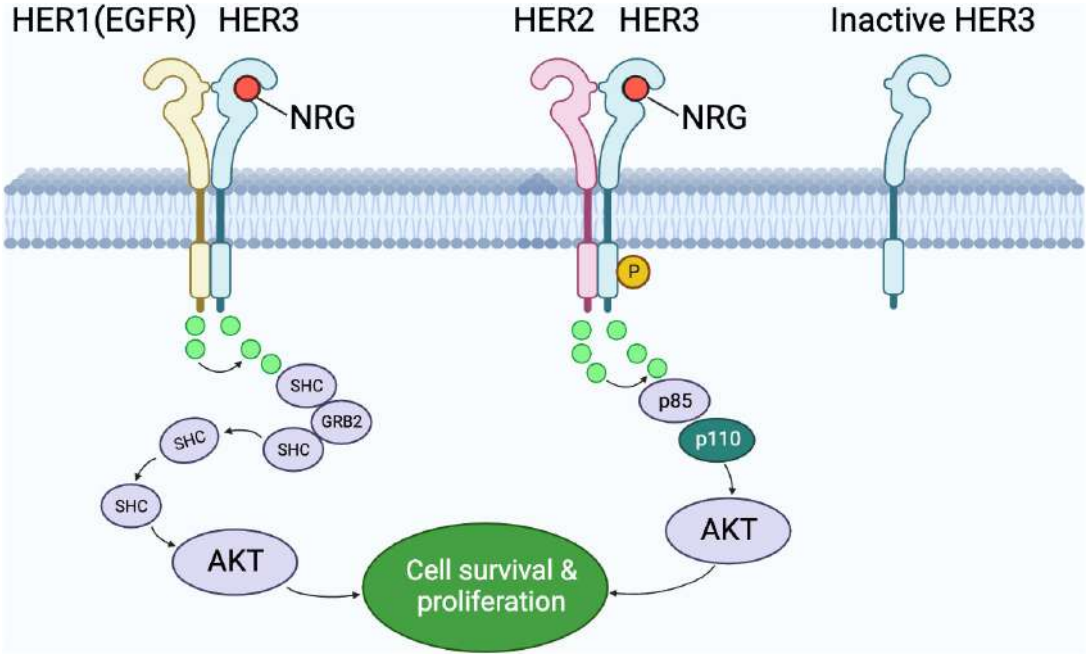


Figure 6. The interplay of HER family members in cell signaling pathways. This graphic depicts the dimerization interactions between HER1 (EGFR) and HER3, as well as between HER2 and HER3. The emphasis is on HER3's significance in both its operational and dormant states. An operational HER3 forms dimer with fellow members to convey signals through intermediaries like SHC, p85, and p110, whereas a dormant HER3 remains detached. Notably, the interaction of HER2 and HER3, when the ligand NRG is present, results in the AKT pathway's activation, promoting cell survival and proliferation. *Image source: Chen et Al. 2024* (91)

1.2 From MP-RM-1 to EV20

HER3 is a critical component of ERBB signaling networks, and therapeutic strategies targeting HER3 are supported by the fact that it induces direct inhibition of survival signaling and increased responsiveness to other treatments (86,87). Based on this rationale, the laboratory initiated an early-phase program to generate and characterize anti-HER3 monoclonal antibodies. The objective was to identify candidates that can disrupt HER3-dependent signaling in tumor models. A significant result was the development of MP-RM-1, a murine anti-ErbB3 antibody evaluated for its capacity to inhibit ErbB3-dependent signaling and tumor growth. In preclinical studies, MP-RM-1 effectively suppressed HER3 activation and downstream signaling. This provided evidence that HER3 blockade can impair tumor survival pathways in relevant models (89). Building upon these results, the program progressed to EV20, a humanized anti-HER3 antibody engineered for clinical development. EV20 maintained functional activity in HER3-dependent tumor models (90,91). Published studies indicate that EV20 induces HER3 downregulation and inhibits tumor cell proliferation and growth in xenograft models. This demonstrates effective receptor engagement and signaling suppression (92). In the context of HER3 biology, downregulation is particularly significant because HER3 signaling

relies on surface availability for heterodimer formation and PI3K recruitment. Consequently, reducing surface expression can result in more sustained suppression of downstream signaling in susceptible models. The EV20 program progresses along two development strategies. Initially, EV20 was developed as a therapeutic antibody targeting HER3 that inhibits tumor-promoting signaling pathways. Later, EV20 served as a targeting agent that, upon HER3 recognition, enables the delivery of therapeutic agents beyond receptor blockade. This strategy included conjugating cytotoxic agents or other effectors to EV20, which can directly induce tumor cell death or more effectively inhibit oncogenic signaling (86,87,93).

Studies indicate that HER3 frequently contributes to treatment resistance in cancer cells through feedback mechanisms and alternative signaling pathways. Consequently, durable therapeutic outcomes may require broader pathway inhibition than antibody blockade alone, or alternative strategies such as antibody-mediated delivery of cytotoxic agents to overcome resistance. This was possible through optimized conjugation chemistry and payload selection. Within this context, the laboratory employed EV20 as a scaffold to develop a series of EV20-based immunoconjugates. Each was designed to test specific therapeutic hypotheses in HER3-expressing cancers (90,94).

1.3 EV20-derived immunoconjugates

The development of EV20-based conjugates entailed a systematic investigation of how payload class, conjugation strategy, and mechanism of action influence therapeutic outcomes in HER3-positive tumor models. The initial strategy employed a protein-toxin format. Researchers engineered EV20 into an immunotoxin by coupling it to saporin, a ribosome-inactivating protein that is highly cytotoxic upon internalization. In melanoma models, the EV20–saporin immunotoxin demonstrated potent antitumor activity, including against HER3-expressing cells. This supported the feasibility of using EV20 for intracellular delivery of potent protein payloads (94). Subsequently, EV20 was evaluated as an ADC-like platform carrying small-molecule cytotoxins. EV20 was conjugated to monomethyl auristatin F (MMAF), a microtubule-inhibitor payload (Figure 7). In preclinical melanoma models, EV20–MMAF demonstrated greater antitumor efficacy than the unconjugated antibody, amplify the therapeutic effects of EV20 (95). Beyond conventional ADC payloads, EV20 was also utilized to deliver non-traditional anticancer agents. For example, one study described an EV20 conjugate delivering NMS-P945, a duocarmycin-like payload–linker, thereby expanding the pharmacologic potential and enabling antitumor activity through mechanisms distinct from microtubule disruption, for example with potent antitumour antibiotics as in this case (96). The platform also progressed toward more defined conjugation formats using engineered strategies, such as disulfide-based designs or chemically controlled linkages. These formats resolved some issues regarding stability, release, and intracellular delivery. In hepatocellular carcinoma models, an EV20-based conjugate carrying MMAF, designated EV20-sss-vc/MMAF, demonstrated antitumor activity. This further supported the versatility of EV20 as a targeting scaffold beyond melanoma (90). Collectively, these studies exemplify an iterative process. EV20 was adapted into multiple immunoconjugate architectures, each representing a step toward maximizing the therapeutic potential of HER3 targeting (90,94).

Situating these efforts within the broader HER3 therapeutic landscape highlights their translational significance. Patritumab deruxtecan (HER3-DXd, a leading clinical HER3-targeted antibody-drug conjugate) is currently the most clinically advanced HER3-targeted ADC. Its success demonstrates

that HER3 is an effective entry point for payload delivery. Clinical benefit is achieved by aligning HER3-targeting with the specific payload mechanism and tumor context (88).

Within this context, this chapter focuses on EV20/Omomyc and advances the research in a new direction. Instead of employing HER3 targeting to deliver a cytotoxic agent or microtubule inhibitor, EV20/Omomyc utilizes HER3 targeting to deliver an inhibitory protein of the key oncogenic transcription factor, MYC.

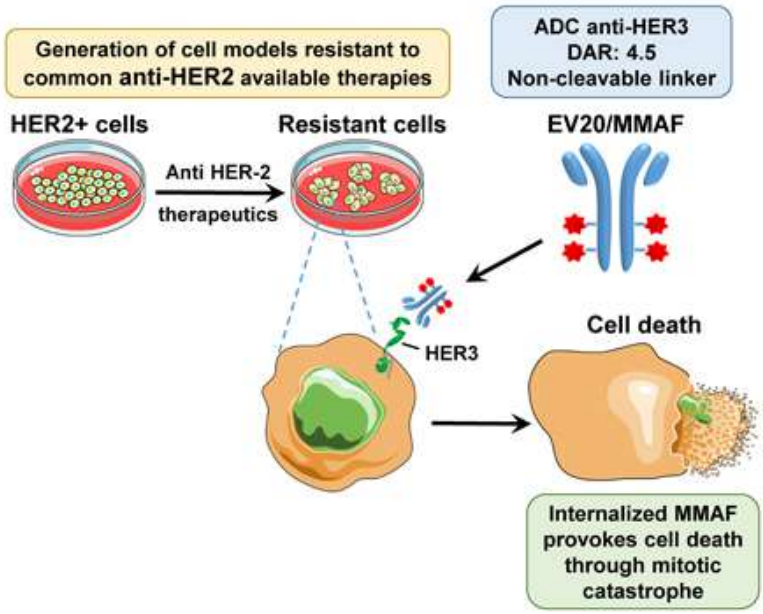


Figure 7. Therapeutic value of EV20/MMAF, a HER3-targeted antibody-drug conjugate loaded with monomethyl auristatin F, for the treatment of breast tumors refractory to conventional anti-HER2 therapies. HER3 was expressed in HER2 positive breast cancer cells with (acquired) resistance to anti-HER2 therapies. The antibody drug conjugate EV20/MMAF, which targets HER3, exerted a strong antitumoral action in several models of primary and secondary resistance to commonly used anti-HER2 therapies. *Image source: Gandullo-Sánchez et Al. 2020* (97)

1.4 MYC as an oncogenic driver

The MYC family of transcription factors is central to cancer biology. It regulates genes for cell growth, metabolism, ribosome biogenesis, stress response, and survival. MYC dysregulation is strongly linked to aggressive tumors across cancers (98,99), as shown in Figure 8. However, MYC is difficult to target due to its nuclear location, lack of enzymatic activity, and disordered transactivation domains (89,90). Evidence shows MYC is not just a cancer marker but is essential for tumor maintenance. Preclinical studies show that inactivating MYC can shrink tumors. Transient or reversible MYC inhibition is well tolerated by normal tissues, suggesting a therapeutic window (98,99). As a result, several MYC inhibition strategies are being developed, including disrupting MYC/MAX dimerization, blocking DNA binding, altering MYC transcription or stability, and creating dominant-negative MYC variants (98,99).

Interest in MYC inhibition has grown because many tumors depend on complex, redundant signaling pathways. Targeting a single receptor or kinase often causes other pathways to compensate. In contrast, MYC inhibition disrupts gene expression programs regulated by multiple oncogenic

pathways simultaneously (98,99). Unfortunately, MYC inhibition alone may not always fully suppress tumors, so the use of combination therapies and advanced delivery methods are fundamental to make MYC pathway targeting more effective and selective (98,100).

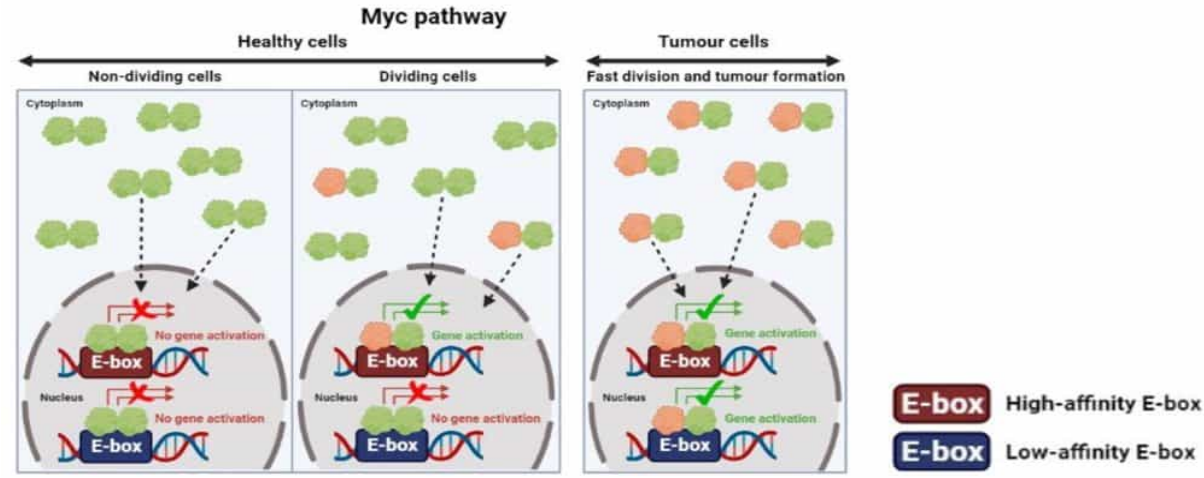


Figure 8. Level of activity of the Myc pathway in healthy (left) and tumour cells (right). Myc protein is absent in non-dividing cells, where Max dimers act as repressors of cell division. In dividing cells, low levels of Myc are enough to infiltrate into the nucleus and activate high-affinity (but not low-affinity) E-boxes in the DNA for an organised cell division. In tumour cells, excessively high Myc-Max levels activate both high-affinity and low-affinity E-boxes, activating an uncontrolled cell division and various tumoral characteristics.

Image taken from Enric Arasanz Picher "Omomyc for cancer treatment - Making the impossible become possible?", 2022, posted on the Society of Spanish Researchers in the United Kingdom (SRUK/CERU) website. *Image source: https://sruk.org.uk/omomyc-for-cancer-treatment-making-the-impossible-become-possible/*

1.5 Omomyc

Omomyc, made by *Peptomyc* company*, i*s a dominant-negative MYC variant. It blocks MYC by altering MYC-MAX interactions and gene regulation, as shown in Figure 9. Early studies showed Omomyc counteracts MYC-driven traits and alters MYC-activated genes (100). Further experiments showed Omomyc is effective and well-tolerated in living organisms. A key study found that reversible, whole-body MYC inhibition led to rapid shrinkage of Ras-driven lung tumors in mice, showing MYC inhibition can strongly affect established cancers (98). These results changed MYC from undruggable to a viable target for engineered proteins or peptides, provided they are delivered effectively (98,99).

At first, Omomyc was mainly used for genetic or intracellular research. This raised concerns about its use as a therapy. The view changed when purified Omomyc was shown to enter cells on its own, enabling delivery without genetic modification. One important study showed that purified Omomyc miniprotein could enter cancer cells, inhibit MYC, and have antitumor effects in mice while keeping a good safety profile (101). The first clinical trial of OMO-103 evaluated its administration, pharmacokinetics, and safety in patients with solid tumors (100). Protein-based therapies like

Omomyc often need repeated intravenous administration at milligram-per-kilogram doses to be effective. If high and frequent dosing is needed, it becomes important to improve tumor targeting and delivery to evoid off-target effects. One strategy is to conjugate the drug to antibodies that guide it to tumors with the target antigen. This approach can make treatment safer and more effective, reducing the amount of Omomyc administered (88,100).

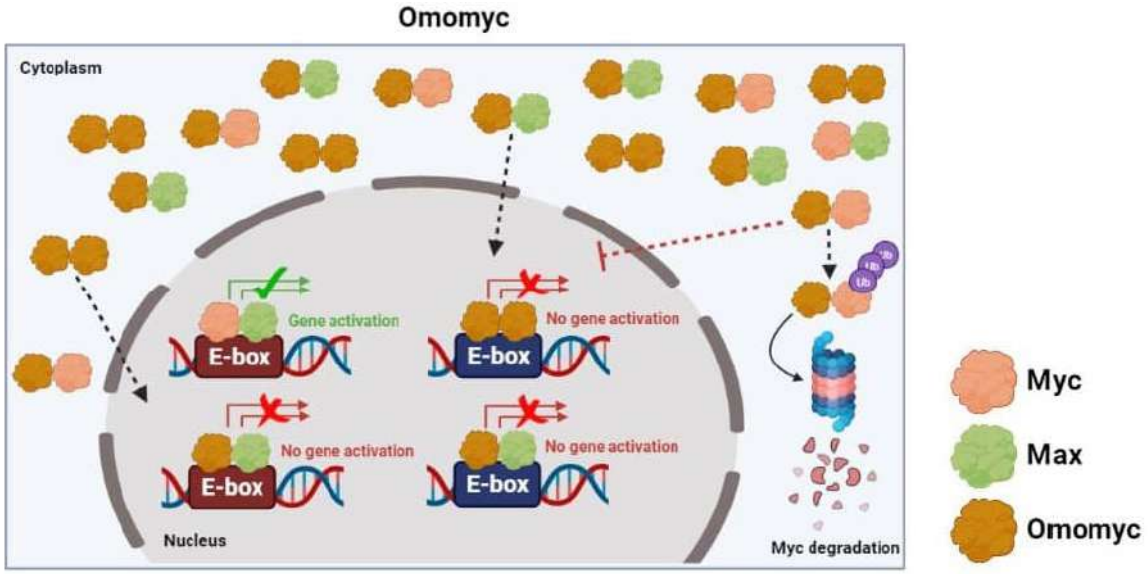


Figure 9. Mechanism of action of Omomyc in the inhibition of Myc activity in preclinical models. Omomyc blocks the pro-tumoral potential of Myc by 1) sequestering Max, avoiding the formation of Myc-Max complexes, and inducing Myc degradation; and 2) binding to E-boxes in the DNA in Omomyc-Omomyc or Omomyc-Max inactive dimers to prevent the binding of Myc, as well as the activation of genes promoting tumour growth. Omomyc cannot displace Myc-Max complexes when they are already bound to the DNA,

Image taken from Enric Arasanz Picher "Omomyc for cancer treatment - Making the impossible become possible?", 2022, posted on the Society of Spanish Researchers in the United Kingdom (SRUK/CERU) website. *Image source: https://sruk.org.uk/omomyc-for-cancer-treatment-making-the-impossible-become-possible/*

1.6 EV20/Omomyc immunoconjugate as treatment for Neuroblastoma

Neuroblastoma (NB) is the most common extracranial solid tumor in children. It accounts for a large share of pediatric cancer deaths. High mortality is due to early spread, heterogeneity, and frequent relapse after intensive therapy (102,103). Advances in risk stratification and standard treatments—such as chemotherapy, surgery, radiation, stem cell transplant, and immunotherapy—have improved care. Still, long-term outcomes for high-risk neuroblastoma remain poor. Relapsed disease is especially hard to cure (103). These challenges require better-targeted therapies to control tumors and reduce side effects. This is crucial for children because both short- and long-term toxicity must be minimized (103).

Neuroblastoma insurgence and progession often depends on MYC-family signaling. MYCN amplification and related gene programs define a large group of high-risk neuroblastomas. These are

linked with fast disease progression and poor outcomes, supporting the idea of targeting MYC/MYCN as therapy (104,105) Neuroblastoma also relies on pro-survival receptor tyrosine kinase signaling, especially the PI3K/AKT pathway, which helps tumor cell survival and resistance to treatment (106). These features make neuroblastoma a good model for testing drugs that target oncogenic transcriptional dependencies, such as the MYC axis and cell-surface receptor pathways involved in survival, growth, and therapy adaptation (103,106). The HER/ERBB network is involved in neuroblastoma, with evidence for ERBB-family overexpression and ERBB signaling affecting neuroblastoma cells (107). Studies show that ERBB3/HER3 expression is linked to neuroblastic transcriptional states, suggesting that HER3 can be targeted in some cases of neuroblastoma (108). Together, these findings show that targeting HER3 can disrupt survival mechanisms and deliver therapeutics selectively to tumor cells. This is important in pediatric oncology, where sparing healthy tissues is crucial (103,107,108).

Neuroblastoma is thus a reliable model to test HER3-targeting mediated MYC inhibition. The development of the EV20/Omomyc immunoconjugate aims to inhibit MYC in tumors by delivering the MYCN inhibitor Omomyc via the HER3-targeting ability of the EV20 mAb, thereby improving the therapeutic index and providing a new therapeutic option for high-risk pediatric neuroblastoma. The goal is to improve drug efficacy so that robust MYC pathway suppression occurs at lower doses than those required by the high-dose regimens used for unconjugated Omomyc.
This approach aligns with a broader trend in antibody–conjugate engineering. In this field, antibodies deliver not only toxic drugs but also targeted inhibitors of cell signaling or gene regulation. The next sections present and discuss the published work which I've contributed:

Bibbò, S., et al. (2024). EV20/Omomyc immunoconjugate targeting HER3 with MYC inhibition for enhanced anticancer activity. Journal of Translational Medicine. https://doi.org/10.1186/s12967-024-05535-y (109)

EV20/Omomyc: A novel dual MYC/HER3 targeting immunoconjugate

Sandra Bibbo [a, b, 1, 2], Emily Capone [a,b,2], Giulio Lovato [a, b], Sara Ponziani [c], Alessia Lamolinara [b, c, d], Manuela Iezzi [b, d], Rossano Lattanzio [a, b], Katia Mazzocco [e], Martina Morini [e], Francesco Giansanti [c], Vincenzo De Laurenzi [a, b], Jonathan Whitfield [h], Stefano Iacobelli [f], Rodolfo Ippoliti [c], Marie-Eve Beaulieu [g], Laura Soucek [g, h, I, j], Arturo Sala [k] , Gianluca Sala [a, b,]

[a] Department of Innovative Technologies in Medicine & Dentistry, University "G. D'Annunzio" of Chieti-Pescara, Chieti, Italy

[b] Center for Advanced Studies and Technology (CAST), University "G. D'Annunzio" of Chieti-Pescara, Chieti, Italy

[c] Department of Life, Health and Environmental Sciences, University of L'Aquila, Coppito, Italy

[d] Department of Neurosciences, Imaging and Clinical Sciences, University "G. D'Annunzio" of Chieti-Pescara, Chieti, Italy

[e] Laboratory of Experimental Therapies in Oncology, IRCCS Istituto Giannina Gaslini

[f] MediaPharma s.r.l., Via Colonnetta 50/A, Chieti, Italy

[g] Peptomyc S.L., Barcelona 08035, Spain

[h] Vall d'Hebron Institute of Oncology (VHIO), Barcelona 08035, Spain

[i] Department of Biochemistry and Molecular Biology, Universitat Autonoma de Barcelona, Bellaterra 08193, Spain

[j] Institucìo Catalana de Recerca i Estudis Avançats (ICREA), Barcelona, Spain

[k] Centre for Inflammation Research and Translational Medicine (CIRTM); College, of Health, Medicine and Life Sciences, Brunel University London, Uxbridge UB8 3PH, United Kingdom,

Abstract

MYC is one of the most important therapeutic targets in human cancer. Many attempts have been made to develop small molecules that could be used to curb its activity in patients, but most failed to identify a suitable direct inhibitor. After years of preclinical characterization, a tissue-penetrating peptide MYC inhibitor, called Omomyc, has been recently successfully used in a Phase I dose escalation study in late-stage, all-comers solid tumour patients. The study showed drug safety and positive signs of clinical activity, prompting the beginning of a new Phase Ib combination study currently ongoing in metastatic pancreatic adenocarcinoma patients. In this manuscript, we have explored the possibility to improve Omomyc targeting to specific cancer subtypes by linking it to a therapeutic antibody. The new immunoconjugate, called EV20/Omomyc, was developed by linking a humanised anti-HER3 antibody, named EV20, to Omomyc using a bifunctional linker. EV20/Omomyc shows antigen-dependent penetrating activity and therapeutic efficacy in a metastatic model of neuroblastoma. This study suggests that directing Omomyc into specific cell types using antibodies recognising tumour antigens could improve its therapeutic activity in specific indications, like in the paediatric setting.

1. Introduction

The MYC family of transcription factors is composed of 3 members: MYC, MYCN and L-MYC. They form an essential signalling hub in most human malignancies: about 70% of all cancers display excessive MYC function as a consequence of genetic, metabolic or transcriptional deregulation in transformed cells [1]. This leads to the robust dependency of a variety of human malignancies on

MYC signalling, which has been documented in both solid and haematologic cancers [2]. MYC exerts its transforming function by regulating gene expression. Evidence suggests that increased expression of MYC family members can activate specific target genes required for transformation but can also induce generalised transcriptional amplification by a phenomenon called enhancer invasion [3]. In each case, MYC activity is dependent on the interaction with a MYC-like protein called MAX. Only the MYC-MAX heterodimer can bind to DNA, promoting transcriptional activation. A mini-protein therapeutic, called Omomyc, was developed to target MYC. Omomyc is a 91-aminoacid protein derived from the MYC basic Helix-Loop-Helix leucine zipper (bHLHZ) domain that acts as a dominant negative molecule, inhibiting MYC/MYCN/L-MYC association with MAX, with positive therapeutic effects in cancer models [4]. It has been shown that systemic transgenic expression or intravenous injection of recombinant Omomyc in mice can impair the growth of different types of tumours, with only marginal effects on normal tissue homeostasis [4–6]. The same excellent safety has been recently confirmed in humans in a Phase I clinical trial (https: //clinicaltrials.gov/ct2/show/NCT04808362). A notable feature of Omomyc is its cell penetrating ability [5]. However, while its preclinical biodistribution following intra- venous (i.v.) administration supported its use for the majority of solid tumours, the drug's distribution into harder-to-reach tissues (eg. Brain or nerves) has not been studied yet and could limit its clinical application. To overcome these potential issues, we have explored the idea of using Omomyc as a payload of a new immunoconjugate, taking advantage of an internalising therapeutic antibody against HER3 developed by Mediapharma. This naked antibody is endowed with a moderate anticancer activity related to its ability to suppress HER3 signalling [7–12]. The antibody was later improved by linking different antineoplastic agents, generating ADCs with potent anticancer activity in a variety of HER3+cancers, including melanoma and breast tumours [13–17]. EV20 was therefore prioritised for conjugation experiments with Omomyc. In previous studies, it was reported that expression of HER receptor family members may represent a novel prognostic factor for paediatric cancer outcome [18,19], and in immunohistochemical analysis screenings we found that 20% of human neuroblastomas express HER3 (Natali, Iacobelli and Sala, unpublished data). Furthermore, EGFR family members, including HER3, have been shown to be expressed and involved in the proliferation of neuroblastomas [20]. Neuroblastomas, as well as other paediatric malignancies of the nervous system, are still very difficult to treat. Molecular therapies, some of which are in Phase I/II clinical trials, are based on the development of drugs targeting overexpressed or mutated signalling molecules important for neuroblastoma cell proliferation, survival or DNA repair. The ALK kinase, which is mutated or activated in about 10% of neuroblastomas, has been used as a target with different generations of ALK inhibitors with some success [21]. However, in a recent clinical trial with the third generation ALK inhibitor Lornatinib, there were fewer responses in younger patients harbouring MYCN amplified tumours, suggesting that anti-MYC strategies should be included for a better outcome of biomarker-directed precision therapies [22]. Indeed, neuroblastoma is one of the cancer types most addicted to MYC or MYCN expression [23]. MYCN is amplified in more than half of high-risk neuroblastomas, where it drives a gene expression program required for the proliferation, metabolic activity and survival of tumour cells [24]. Given the importance of targeting MYC in high-risk neuroblastoma, we elected to use this system for a proof of principle validation study of EV20/Omomyc.

2. Results

2.1. Assessment of the anticancer activity of free Omomyc against neuroblastoma cells

It has been reported that the anti-MYC mini-protein Omomyc inhibits proliferation of a wide range of cell lines expressing different levels of MYC or MYCN [4]. To confirm the anticancer activity of Omomyc in neuroblastoma cells, we quantified the anti-proliferative effect of free Omomyc in MYCN amplified (Kelly, IMR32) or non MYCN amplified (SKNAS) neuroblastoma cell lines, using 72 h as endpoint and a concentration of the peptide of 20 μM. Cells were cultured in the presence or absence of the peptide, after which cell proliferation was quantified by MTT assay. While at longer time points (i.e. two weeks) all cell lines are sensitive to MYC inhibition by Omomyc (data not shown), this short time point identifies differences in sensitivity between the MYCN amplified cancer cell lines and those with lower levels of MYC/MYCN expression. Only the IMR32 and Kelly cell lines were significantly inhibited by Omomyc, whereas the SKNAS cell line was unperturbed (Fig. 1A, left panel). Notably, sensitivity to Omomyc correlated with the expression of MYCN, but not with that of its partner protein MAX (Fig. 1A, right panel).

2.2. Expression of HER3 in human neuroblastomas tissues and generation of a neuroblastoma cell line overexpressing HER3 on the cell surface

To confirm HER3 expression in human neuroblastomas, we analysed a panel of 50 primary tumours from the Gaslini hospital by immune-histochemistry. Positivity to the HER3 antibody was cytoplasmic and detected in 48% of the samples (example staining shown in Fig. 1B), with percentages of positive tumour cells ranging from 3 to 100% (mean 60% ± 6.8). In order to evaluate the relationship between HER3 expression levels in neuroblastomas and patients' clinicopathological features, we utilized a semi-quantitative scoring system for HER3 immunohistochemical staining, based on the method reported by Izycka-Swieszewska et al. [25] HER3 levels in tumour cells were categorized as "Negative" (n =25),"Low-expression" (n =13), or "High-expression" (n =12) and then further divided into either"Negative/Low" (n =38) or "High" (n=12) HER3-expressing tumours for statistical analysis. At the chi-square test, we found no significant association between HER3 expression levels and patients' clinicopathological characteristics (Table 1). Next, we inspected a panel of patient derived and previously established neuroblastoma cell lines by western blotting with an HER3 antibody. Surprisingly, none of the cell lines showed positivity for HER3 expression (Fig. 1C). This could be a consequence of the lower expression of HER3 in neuroblastoma stages 3–4, from which neuroblastoma cell lines have been isolated, than stages 1–2. We also noted that drug resistance caused reactivation of HER3 expression in a neuroblastoma cell line, suggesting that positive HER3 immunostaining in primary neuroblastoma samples could reflect treatments. We therefore decided to select the MYCN amplified Kelly cell line, which easily forms subcutaneous or metastatic tumours in immunodeficient mice, for genetic manipulation. Kelly cells were infected with a lentivirus containing the HER3 cDNA. After selection, the infected cell line showed strong HER3 protein expression detected by western blot analysis; expression on the cell surface was confirmed by flow cytometry (Fig. 1D). To assess whether the EV20 antibody could engage the overexpressed HER3 molecule on neuroblastoma cells, we cultured Kelly-HER3 cells in the presence of increasing concentrations of EV20/MMAF ADC (DAR between 4 and 5), previously shown to specifically act against HER3 positive cells [16]. Low nanomolar concentrations of the ADC killed Kelly-HER3 cells with high efficiency, whereas Kelly-Mock cells were not affected (Fig. 1E), confirming that the anticancer activity of the antibody depends on HER3 expression.

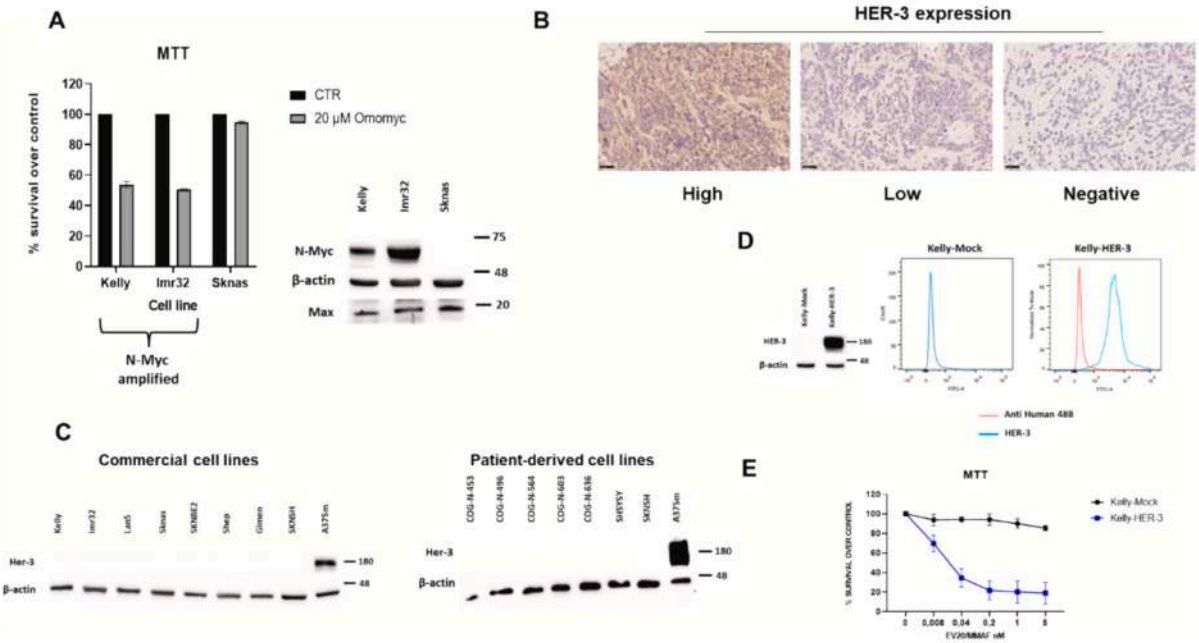


Fig. 1: Generation of HER3 overexpressing neuroblastoma cells. (A) A panel of neuroblastoma cell lines were treated for 72 h with 20 µM of Omomyc and cell viability measured by MTT staining (left panel). Expression of MYCN/MAX was assessed by western blotting; a beta actin antibody was used to verify equal protein loading (right panel); (B) Examples of high, low, and negative HER3 IHC expression levels in human neuroblastoma tissues; (C) Commercially available and patient-derived cell lines were analysed for HER3 expression by western blotting. Melanoma A375m cells were used as a positive control; (D) Flow cytometry analysis and western blotting showing HER3 overexpression in Kelly-HER3 cells. (E) Cell proliferation assay showing Kelly-HER3 sensitivity to EV20/MMAF ADC. Error bars indicate standard deviations.

Table 1. HER3 status according to clinicopathological features of NB patients

Variable	HER3		P*
	Negative/Low: n (%)	High: n (%)	
Age			
≤ 18 months	13 (72.2)	5 (27.8)	
> 18 months	25 (78.1)	7 (21.9)	0.735
Gender			
Male	15 (71.4)	6 (28.6)	
Female	23 (79.3)	6 (20.7)	0.738
Tumour location			
Adrenal	23 (82.1)	5 (17.9)	
Extra-adrenal	15 (68.2)	7 (31.8)	0.324
Tumour stage			
Localized	17 (70.8)	7 (29.2)	
Metastatic	21 (80.8)	5 (19.2)	0.514
Tumour differentiation			
Undifferentiated	2 (66.7)	1 (33.3)	
Poorly differentiated	31 (75.6)	10 (24.4)	
Differentiating	3 (100)	0 (0.0)	0.576
MYCN			
Nonamplified	16 (69.6)	7 (30.4)	
Amplified/Gain	19 (79.2)	5 (20.8)	0.517
Tumour relapse			
No	27 (75.0)	9 (25.0)	
Yes	11 (78.6)	3 (21.4)	1.000
Prognostic Group			
Very low	7 (53.8)	6 (46.2)	
Low	5 (100)	0 (0.0)	
Intermediate	3 (75.0)	1 (25.0)	
High	23 (82.1)	5 (17.9)	0.129
Patient Survival			
Alive	25 (75.8)	8 (24.2)	
Dead	10 (90.9)	1 (9.1)	0.411

*Pearson's χ^2 test.

2.3. Generation of an EV20/Omomyc targeting HER3

We conjugated the Omomyc molecule to EV20 and named it EV20/Omomyc. It consists of 3 domains: a) Omomyc, b) a bifunctional linker, and c) the EV20 anti-HER3 antibody (Fig. 2 A). In a nutshell, the bifunctional linker small molecule attached to the mAb enables disulfide-mediated conjugation to a C-terminal cysteine residue on the Omomyc moiety. This disulfide link gets spontaneously reduced in the cytoplasm of cells, freeing both molecular moieties. EV20 is an antibody that is internalized very efficiently by HER-3 positive cells following the endosomal–lysosomal degradation pathway. Using different payloads and conjugation/linker chemistry we have demonstrated that EV20 is an excellent moiety for drug delivery into cancer cells [13–16,26]. The detailed procedures are described in the methods section. Successful conjugation of the peptides was confirmed through mass spectrometry (Fig. 2B), SDS-PAGE analysis in reducing and non reducing conditions (Fig. 2C) and anti-Omomyc or anti-human Western Blot analysis (Fig. 2D). EV20/Omomyc resulted to be conjugated with a drug-to-antibody ratio (DAR) of 1 and a percentage of residual unconjugated antibody estimated as around 50%. We then assessed if the immunoconjugate bound to HER3 with an affinity similar to the parental EV20 antibody. Both the ELISA binding assay (Fig. 2E) and flow cytometry carried out with A375m melanoma cells, expressing high levels of endogenous HER3 (Fig. 3A), confirmed that EV20/Omomyc binds HER3 antigen with an affinity comparable to the naked antibody. In order to assess EV20/Omomyc stability, we developed a sandwich anti-Omomyc ELISA using a murine anti-Omomyc as bait antibody and HRP-labelled goat anti-human IgG for the detection. The assays effi- ciently discriminated the EV20/Omomyc immunoconjugate from the naked EV20 antibody (Fig. 2F). Subsequently, stability of the immune conjugate was evaluated incubating EV20/Omomyc at 37◦C in human serum for different time intervals, up to 72 h. Around 50% of the immunoconjugate was detected after 24 h of incubation (Fig. 2G). Since Omomyc was shown to internalize into several cell types [4,5], we assessed if the EV20/Omomyc conjugate retained the same internalization capacity and could allow efficient delivery and release of the Omomyc moiety to the nuclei, where MYC exerts its functions. Confocal microscopy confirmed that EV20/Omomyc was detected inside HER3+ A375 melanoma cells, confirming the ability of the immunoconjugate to penetrate cells (Fig. 3B). Interestingly, after EV20/Omomyc was internalized, the EV20 antibody was detected in the perinuclear/Golgi area of the cell, whereas Omomyc was localized in the nuclear compartment (Fig. 3C), suggesting their separation after penetration.

Notably, while the amount of internalized EV20/Omomyc was significantly different between Mock and HER3 transduced Kelly cells, no difference was observed in cells incubated with free Omomyc, indicating that EV20/Omomyc preferential penetration into HER3 positive cells is driven by HER3 (Fig. 4A). However, the residual amount of EV20/Omomyc observed in HER3 negative cells (Fig. 4A) probably reflects the intrinsic cell penetrating properties of Omomyc [5]. However, binding of the immunoconjugate on HER-3 negative cells is detected only at high concentration (>10 μg/ml) as also observed by flowcytometry (Fig. 4B). Indeed, to assess whether target specificity could be increased by lowering the concentration of EV20/Omomyc, a titration experiment was implemented using mock infected and HER3 expressing Kelly cells. We observed that lowering the concentration of EV20/Omomyc to 0.2 μg/ml highlighted the specificity of the immunoconjugate for HER3 positive NB cells (Fig. 4C).

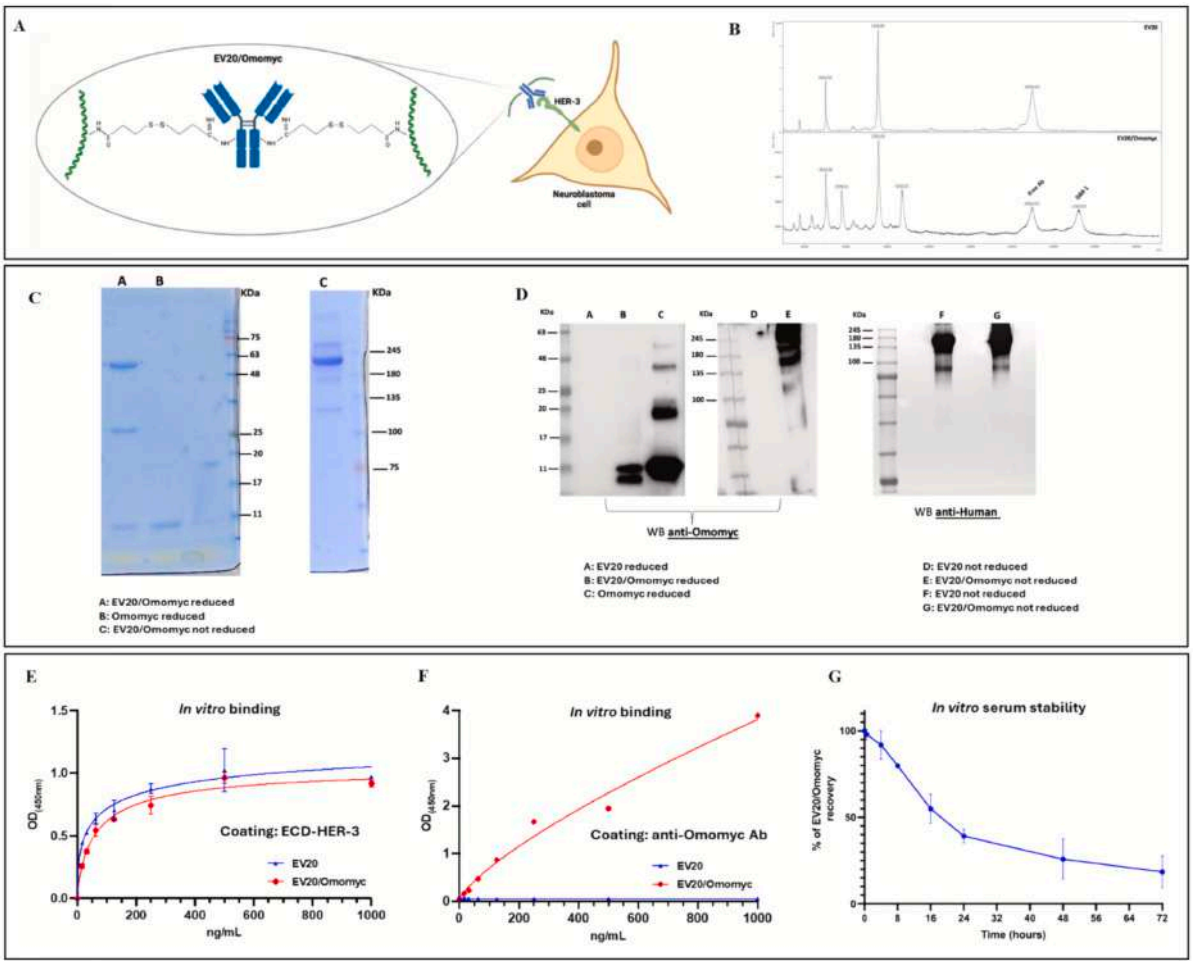


Fig. 2: Schematic structure and characterization of the EV20/Omomyc fusion protein.

Schematic structure of EV20/Omomyc; (B) Mass spectrometry analysis of naked and Omomyc-conjugated EV20; (C) Coomassie blue staining showing EV20/Omomyc in reduced and non-reduced conditions; (D) 5 µg of purified EV20/Omomyc immunoconjugate was analysed by western blotting in non-reducing (right and middle panel) and reducing conditions (left panel). Anti-Omomyc and anti-human antibodies were used as indicated; (E) *In Vitro* binding of naked and Omomyc-conjugated EV20 antibodies. ELISA was performed using as capture antigen the HER-3 extra cellular domain (ECD) and bound EV20 or EV20/Omomyc were detected by HRP labelled goat anti-human IgG; (F) Sandwich ELISA was performed using the murine anti-Omomyc antibody as coating and HRP-labelled goat anti-human IgG for detection; (G) *In Vitro* stability assay performed using anti-Omomyc ELISA on human serum samples containing EV20/Omomyc incubated at 37◦C for the indicated times. Error bars indicate standard deviations.

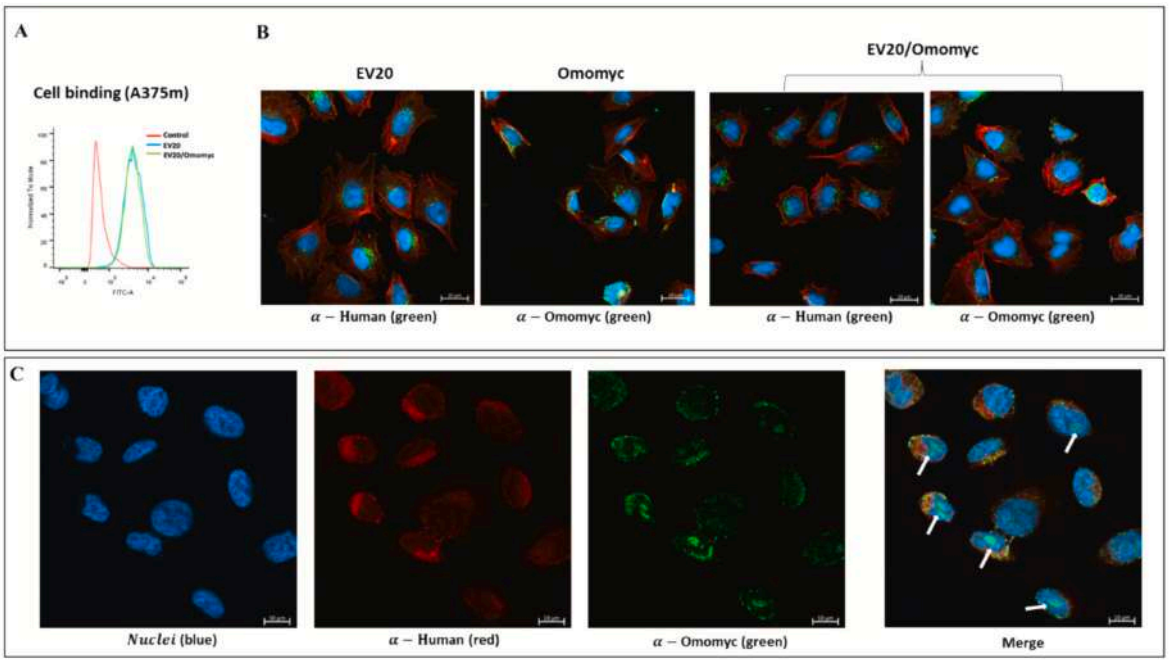


Fig. 3: Cell binding and internalization of EV20/Omomyc in HER3+melanoma cells.

(A) Cell binding analysis of EV20/Omomyc by flow cytometry of A375m melanoma cells; (B) Confocal images showing EV20/Omomyc internalization in A375m melanoma cells. Cells were treated for 4 h at 37◦C with 20 μg/ml for EV20 and EV20/Omomyc or with Omomyc (0.6 μg/ml), then fixed, permeabilized and stained with anti-human 488-conjugated secondary antibody or with murine anti-Omomyc antibody followed by anti-mouse 488-conjugated secondary antibody. Nuclei are visualized in blue with DAPI, actin is stained in red with TRITC-phalloidin; (C) Confocal imaging of EV20/Omomyc -treated A375m cells stained with anti-human 594-conjugated secondary antibody (EV20/red) and with murine anti-Omomyc antibody followed by anti-mouse 488-conjugated secondary antibody (Omomyc/green) showing Omomyc nuclear localization. Nuclei are visualized in blue with DAPI. White arrows indicate Omomyc nuclear localization.

2.4. Anticancer activity of EV20/Omomyc

We recently established a pseudo-metastatic neuroblastoma model based on intravenous injections of Kelly cells [27,28]. Firstly, we used this model to confirm that HER3 modified Kelly cells were sensitive to EV20/MMAF ADC [16], previously shown to inhibit HER3 positive cancers. As expected, the EV20/MMAF ADC showed a strong anti-metastatic activity against Kelly-HER3 cells, but it was unable to antagonise the growth of control vector-infected Kelly cells *In Vivo* (Fig. 5A). Next, we assessed the metastatic growth of Kelly-HER3 cells in mice injected intravenously with Omomyc (0.6 mg/Kg), EV20 (5 mg/Kg), or EV20/Omomyc (5 mg/Kg) compared to sham injected, control mice. It should be noted that the free Omomyc concentration used in these experiments (0.6 mg/Kg) is approximately 50 times less than that previously used in preclinical *In Vivo* experiments with the naked Omomyc [5] and it is about 4 times higher than the amount of Omomyc loaded in the immunoconjugate (EV20/Omomyc). Strikingly, there was a significant reduction of Kelly-HER3 metastases in the livers of mice treated with EV20/Omomyc, but not in mice treated with naked Omomyc or the anti-HER3 antibody (Fig. 5B). No reduction of liver metastases was observed in mice injected with control vector-infected Kelly cells and treated with EV20/Omomyc, naked Omomyc or EV20. In agreement with these observations, there was a target-dependent accumulation

of EV20 only in Kelly-HER3 tumour tissues, demonstrating selective accumulation of EV20/Omomyc in HER3 positive cells *In Vivo* (Fig. 5C,D).

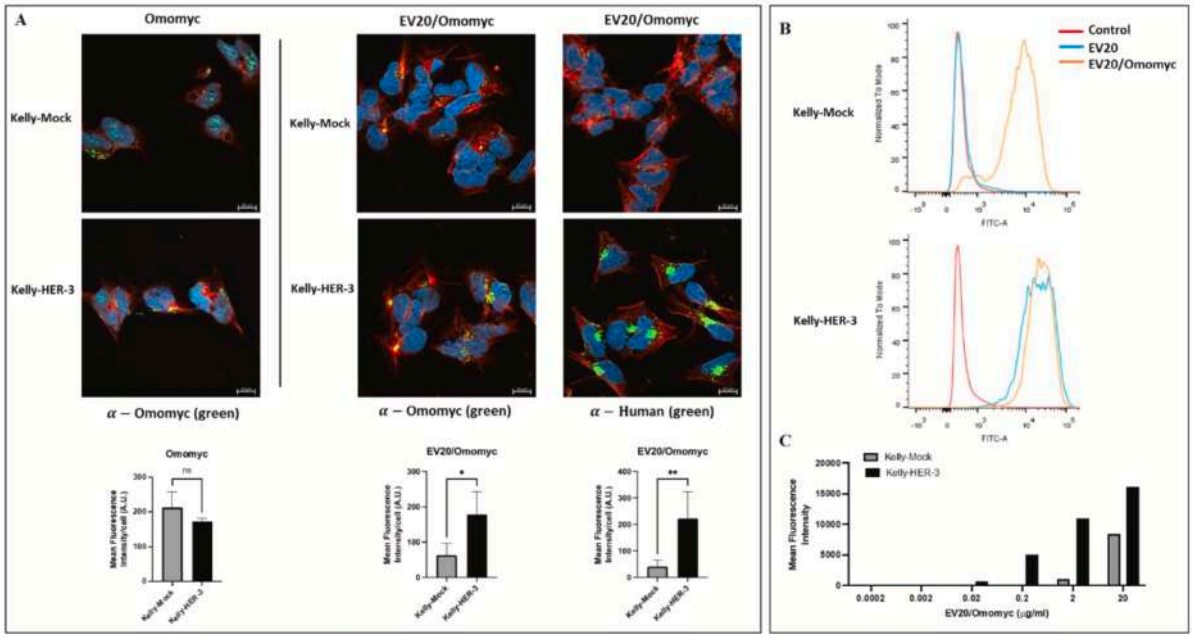


Fig. 4: Conjugation with the EV20 antibody increases Omomyc nuclear delivery in HER3 expressing Kelly neuroblastoma cells. (A) Confocal images showing EV20/Omomyc internalization in Kelly-Mock and Kelly-HER3 neuroblastoma cells. Cells were treated for 4 h at 37◦C with (20 μg/ml) EV20/Omomyc or (2 μg/ml) Omomyc, then they are fixed, permeabilized and stained with anti-human 488-conjugated secondary antibody or with murine anti- Omomyc antibody followed by anti-mouse 488-conjugated secondary antibody. Nuclei are visualized in blue with DAPI, actin is stained in red with TRITC phalloidin. Below histograms representing quantification of the internalization using mean fluorescence intensity of AF-488 in individual cells. Unpaired t-Test *p=0.01; **p=0.002 B) EV20/Omomyc cell binding on Kelly-Mock and Kelly-HER3 neuroblastoma cells by flow cytometry. EV20 antibody is used as control. Cells were stained with anti-human 488-conjugated secondary antibody and analysed by flow cytometry; (C) Titration of EV20/Omomyc on Kelly-Mock and Kelly-HER3 neuroblastoma cells. Cells were detached and treated with increasing doses of EV20/Omomyc at 4◦C for 30 min, washed and incubated with anti-human 488-conjugated secondary antibody, followed by flow cytometric analysis.

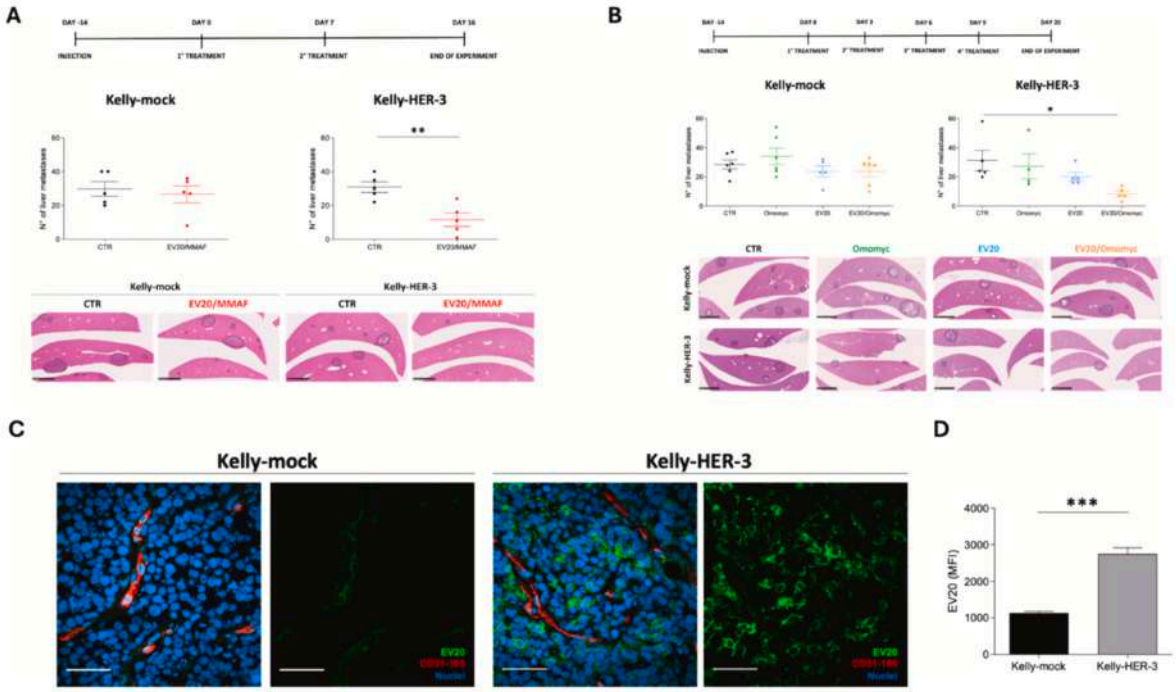


Fig. 5: ADC and EV20/Omomyc activity in Kelly pseudo-metastatic model. Experimental metastasis assays performed with Kelly-Mock and Kelly-HER3 neuroblastoma cell model. (A) PBS and EV20/MMAF (10 mg/kg) intravenous injections were administered weekly for a total of 2 doses. Metastatic lesions in liver were analysed and plotted on graphs as mean number of lesions +/− SD. **p < 0,01 determined by Student t-test. (B) PBS, EV20 (5 mg/kg), EV20/Omomyc (5 mg/kg) and free Omomyc (0.6 mg/kg) intravenous injections were administered weekly for a total of 4 doses. Metastatic lesions in liver were analysed and plotted on graphs as mean number of lesions +/-SD. *p=0,03 determined by one-way ANOVA; (C) Representative immunofluorescence images showing EV20 accumulation in tumour tissues derived by subcutaneous injection of Mock or HER3 transduced Kelly cells. After EV20/Omomyc circulated for 24 h, tumour tissues were excised and subjected to immunofluorescence staining with anti-human IgG (green); blood vessels were stained using anti CD31/CD105 antibodies (red); cell nuclei were stained by DAPI (blue); (D) Quantification of mean fluorescence intensity (MFI) of anti-human IgG performed on digital images of 3 tumours per group (5×400 microscopic field per sample).

3. Discussion

The Omomyc-derived therapeutic (OMO-103) is the first anti-MYC mini-protein tested in the clinic. OMO-103 recently showed safety and positive signs of drug activity in a dose-escalation study in all-comers solid tumour patients [29]. OMO-103 is now being tested in a Phase Ib study in first line metastatic pancreatic ductal adenocarcinoma patients in combination with standard of care chemotherapy (NCT06059001). An interesting feature of Omomyc is that it possesses tissue penetrating characteristics, therefore it can enter cells and exert anticancer activity without other aids [4,5]. It has been shown in animal models that Omomyc's effects on normal tissues are only slightly anti proliferative and reversible, whereas it causes growth arrest and death in cancer tissues [6]. These preclinical results have been validated in the clinical trial, in which no severe toxicity of OMO-103 was detected in patients (manuscript under revision). Despite the great promise of Omomyc for adult types of human cancers, the use of the drug in the paediatric setting has not been explored. In this

context, improving the specific tumour tissue delivery could potentially allow for improved therapeutic index and reduce the dose required to treat a paediatric patient population. To explore this avenue, we sought to combine the anticancer activity of the Omomyc mini-protein with antibody-mediated precision targeting to generate a new, non-toxic and potentially more effective drug against hard-to-reach MYC-dependent cancers. Paediatric solid tumours are particularly susceptible to MYC inhibition, given the complete dependence of some cancer subtypes on MYC/MYCN expression, including for example medulloblastoma and neuroblastoma. In neuroblastoma, expression of HER3 was detected in 20–50% of cases in independent patient cohorts and HER3 is highly expressed in many human solid tumours, especially in the context of drug resistance [30,31]. In this study, we have taken advantage of a preclinical anti-HER3 monoclonal antibody developed in our laboratory and conjugated it to Omomyc using a bifunctional linker. However, when we looked for suitable cancer cell targets to test this therapeutic, we could not detect HER3 in commonly used neuroblastoma cell lines, nor in PDX-derived tumour cells (Fig. 1C). To overcome this difficulty, we have transduced a classic MYCN amplified neuroblastoma cell line (Kelly) with a lentiviral vector encoding HER3. Surface expression of HER3 made these neuroblastoma cells susceptible to killing by a previously characterised HER3 ADC, EV20/MMAF, whereas control cells were unaffected. We then used this cell model system to assess whether a HER3 antibody conjugated to Omomyc could be used to increase uptake of the drug into neuroblastoma cells expressing the receptor. Indeed, conjugation of Omomyc to the HER3 antibody dramatically increased its uptake at lower doses, reflected by its more effective anticancer activity, compared to the free mini-protein, in a pseudo-metastatic model of neuroblastoma. In principle, this strategy could be adapted to other paediatric cancers driven by MYC for which antibodies targeting surface antigens have been developed. In fact, MYC expression is elevated in the high risk group 3 medulloblastoma and its ectopic expression can induce aggressive growth and promote metastasis in low risk groups [32]. In rhabdomyosarcoma, MYCN is a downstream effector of the oncogenic PAX3-FOXO1 fusion protein and its destabilisation by an Aurora A kinase inhibitor has therapeutic effects in PDX models of the disease [33]. Interestingly, using publicly available databases, we found a significant correlation between expression of MYC/MYCN and HER3 in rhabdomyosarcoma and neuroblastoma. In conclusion, we have validated a new immunoconjugate, EV20/Omomyc, which targets HER3 expressing MYCN addicted neuroblastoma cells. MYC members are potentially very important targets for paediatric embryonal tumours but developing direct inhibitors has been very challenging [34]. In this proof of principle study, we observed significant therapeutic activity of the EV20/Omomyc immunoconjugate despite a DAR of 1, suggesting that the unconjugated antibody does not negatively affects the therapeutic activity of Omomyc. However, in view of a potential clinical development of the reagent, optimization of the conjugation efficiency and purification phase will be essential. The advantages of using Omomyc compared to other classical cyotoxic payloads are its low toxicity, high stability and broad anticancer activity based on its anti-MYC function. It will be interesting to investigate whether this new reagent can be effective against other paediatric solid tumours expressing HER3, such as medulloblastoma and rhabdomyosarcoma.

4. Material & Methods

4.1. Cell lines

Melanoma (A375m) and neuroblastoma (SKNAS, SH-SY5Y, SHEP, SKNBE(2), SKSNH, GIMEN, IMR32) cells were purchased from American Type Culture Collection (Rockville, MD, USA). LAN-5 neuroblastoma cell line was purchased from Leibniz Institute DMSZ (German Collection of Microorganism and Cell Culture GmbH). Kelly neuroblastoma cell line was purchased from Sigma-Aldrich (St. Louis, MO, USA). Kelly-Mock and Kelly-HER3 cell lines were generated in our lab by lentiviral infection, as described below. All cell lines were cultured < 3 months after resuscitation. The cells were cultured according to manufacturer's instructions, using a medium supplemented with 10% heat inactivated fetal bovine serum (FBS; Invitrogen, Carlsbad, CA, USA), L-glutamine, 100 units/ml penicillin, and 100 µg/ml streptomycin (Sigma-Aldrich Corporation, St. Louis, MO, USA), and incubated at 37◦C in humidified air with 5% CO2. For patient-derived cell lines (COG-N-603; COG-N-636; COG-N-453; COG-N-496; COG-N-564), they were obtained from the Children's Oncology Group (COG) Cell Culture and Xenograft Repository at Texas Tech University Health Sciences Center (www.COGcell. org). Patient-derived cell lines were cultured *In Vitro* using IMDM medium supplemented with 20% heat-inactivated fetal bovine serum (FBS; Invitrogen), 1% ITS (Insulin-Tranferrin-Selenium; Thermo Fisher Scientific, Waltham, MA, USA) 100 units/ml penicillin, and 100 µg/ml streptomycin (Sigma-Aldrich Corporation, St. Louis, MO, USA), and incubated at 37◦C in humidified air with 5% CO2.

4.2. Generation of HER3 expressing neuroblastoma cell line

The vectors used for HER3 overexpression are the following: ErbB 3 (ERBB3) (NM_001982) Human Tagged Lenti ORF Clone (CAT#: RC209954L3; Origene, Rockville, Maryland, United States) cloned in a pLenti-C-Myc-DDK-P2A-Puro vector and pLenti-C-Myc-DDK-P2A-Puro Lentiviral Gene Expression Vector (CAT#: PS100092; Origene, Rockville, Maryland, United States) for control Mock-Kelly cells. Lentiviruses were produced by transient cotransfection of a 3 plasmid expression system in the packaging 293 T cells, using lipofectamine 2000 (Invitrogen, Life Technologies). 293 T packaging cells were incubated for 8 h with the transfection reagents, then viral supernatant was collected 24 and 48 h after transfection and filtered through 0.45 µm pore vacuum sterile filtration system (Millipore, Life Science, Darmstadt, Germany). Then, Kelly cells were plated in a six-multiwell at a density of 125,000 cells/well, and they were subjected to 2 rounds of infections with 293 T filtered viral supernatant harvested 24 h and 48 h after transfection. To select for infected Kelly-HER3 and Kelly-Mock cells, puromycin was added to the media at the concentration determined in the steps above; one uninfected plate of cells in parallel was maintained in puromycin as a positive control for the puromycin selection.

4.3. Coomassie Staining

For characterization of the reagent, purified EV20 antibody, EV20/Omomyc or free Omomyc were resuspended in reducing or not reducing Laemmli Buffer and boiled for 10 min at 95◦C. Then they were separated by SDS/PAGE on 15% (non-reducing conditions, without 2-mercaptoethanol) or 8% (reducing conditions) polyacrylamide gel and Coomassie staining was performed. Briefly, gels were incubated with 50% (v/v) ethanol, 10% (v/v) acetic acid solution in water for fixing, then they were

stained with 0.1% (w/v) Coomassie blue R350, 20% (v/v) methanol, and 10% (v/v) acetic acid solution in water, and finally destained with 50% (v/v) methanol in water with 10% (v/v) acetic acid.

4.4. Western Blotting

For characterization of the reagent, purified EV20 antibody, EV20/Omomyc or free Omomyc were resuspended in reducing or not reducing Laemmli Buffer and boiled for 10 min at 95◦C. Then they were separated by SDS/PAGE on 15% (non-reducing conditions, without 2-mercaptoethanol) or 8% (reducing conditions) polyacrylamide gel and transferred to nitrocellulose membrane. Membranes were blocked with 5% non-fat dry milk in PBS 0.1% Tween 20 for 1 h at room temperature and incubated with the following antibodies. For Omomyc detection it was used murine anti-Omomyc antibody (Ximbio, Anti-Omomyc [21− 1− 3]; 1:1000 dilution) overnight at 4◦C followed by goat anti-mouse IgG HRP-conjugated secondary antibody (Biorad, Berkeley, CA, USA; 1:10000 dilution) for 1 h at RT; for EV20 antibody detection it was used goat anti-human IgG-HRP-conjugated secondary antibody (#A01070, Sigma-Aldrich Corporation; 1:20000 dilution) for 1 h at RT. For cell lysates analysis, cells were lysed in RIPA Buffer (50 mM Tris-HCl, 1% NP40, 0.1% SDS, 150 mM NaCl) supplemented with protease inhibitor cocktail (Sigma-Aldrich) and phosphatase inhibitor cocktail (Roche) for 30 min in ice. Insoluble material was removed by centrifugation (13,000 rpm for 20 min at 4◦C) and protein concentration was assessed by Bradford assay. Equal amounts of protein were separated by SDS/PAGE on 15% or 8% polyacrylamide gel and transferred to nitrocellulose membrane. Membranes were blocked with 5% non-fat dry milk in PBS 0.1% Tween 20 for 1 h at room temperature and incubated overnight at 4◦C with primary antibodies. The primary antibodies used were: N-Myc (sc-53,993, Santa Cruz Biotechnology, 1:500 dilution), Max (#4739, Cell Signalling Technology, 1:1000 dilution), Actin (Sigma Aldrich Corporation, 1:40000 dilution), HER3/ErbB3 (#12708, Cell Signalling Technology 1:1000 dilution). After washing with PBS containing 0.1% Tween-20, blots were incubated with a goat anti-mouse IgG HRP-conjugated (Biorad, Berkeley, CA, USA; 1:20000 dilution) and an anti-rabbit IgG HRP-conjugated antibody (Biorad, Berkeley, CA, USA; 1:20000 dilution) as secondary antibodies, at room temperature for 1 h. Detection of signal bands was performed with Clarity Western ECL substrate (#1705061; Biorad, Hercules, CA, USA). Images of membranes were acquired with a Uvitec FireReader (Cambridge, UK).

4.5. MTT cell viability assay

Cytotoxicity was assessed by MTT [3-(4,5-dimethyldiazol-2-yl)-2,5-diphenyl tetrazolium bromide] assay. Cells were seeded into 96-well plates at a density ranging from 3.5 ×103 to 5 ×103 cells/well in 200 µl of complete culture medium and cultivated under standard growth conditions for 24 h at 37◦C in 5% CO2. Afterwards, cells were treated in complete medium with Omomyc 20 µM for 72 h, and with increasing doses of EV20/MMAF for 120 h. At the end of the incubation periods, cells were incubated with 100 µl of MTT solution [3-(4,5- dimethyldiazol-2-yl)-2,5-diphenyl tetrazolium bromide] (Sigma-Aldrich) (0.5 mg/ml of MTT in serum free medium) for 2 h at 37◦C. After removal of the MTT solution, cells were incubated with 100 µl of dimethyl sulfoxide (DMSO) for 10 min and the optical density was measured at 570 nm using a multi-plate reader. All experiments were performed in triplicate.

4.6. Patients

The study cohort was formed by 50 neuroblastoma (NB) patients diagnosed between 2012 and 2018 at IRCCS"G. Gaslini" Institute, Genoa, Italy. All patients gave written consent to the study. The study was approved by Chieti-Pescara Local Ethics Committee (E.C. number 06/07.04.2022). All patients gave written consent to the study. The median age of all patients was 23.5 months old (range, 2–88), and 60.3% of the NB patients (35 out of 58) were female. The clinical and pathological characteristics of NB patients are summarized in Table 2 (supplemental materials).

4.7. Immunohistochemistry

The expression study was performed on whole paraffin sections that were deparaffinized and prepared for the immunohistochemical staining with the anti-HER3 rabbit monoclonal antibody (clone SP-71; dilution Journal of Controlled Release 374 (2024) 171–180 1:100) purchased from AbCam. Antigen retrieval was performed by microwave treatment at 750 W (10 min) in Tris-EDTA buffer (pH 8.0). The anti-rabbit EnVision kit (Agilent, K4003) was used for signal amplification. To exclude the unspecific staining, isotype control was included. In neuroblastoma cells, HER3 showed exclusive cytoplasmic immunohistochemical pattern. Briefly, the level of HER3 expression was obtained on a sum of the scored percentage of positive cells (i.e., <5%, score 0; 5–50%, score 1; >50%, score 2) and scored labeling (i.e., Negative, score 0; Faint, score 1; Moderate, score 2; Strong, score 3). The final HER3 expression level was categorized as "Negative" (i.e., Sum of scores: 0, 1),"Low-expression" (i.e., Sum of scores: 2, 3), or "High-expression" (i.e., Sum of scores: 4, 5).

4.8. Generation of EV20/Omomyc

EV20/Omomyc immunoconjugate was developed through the conjugation of Omomyc to EV20 antibody by means of a hetero-bifunctional linker reacting to amine residues on Omomyc (introducing a disulphide linker on the protein surface) and a second hetero bifunctional reagent on EV20 (introducing a free -SH group) thus to favour the formation of intermolecular disulphide bridge between the 2 proteins. To prepare the samples for the reaction, the EV20 antibody and reduced Omomyc were buffer exchanged to 100 mM Borate Buffered Saline pH 9 (BBS) with centrifugal filter units with cutoff 30 kda (for EV20) and 3 kda (for Omomyc). EV20 was chemically modified with 2-Iminothiolane (2-IT, Thermofisher, USA; stock dissolved in water) using 1.5 M excess of this reagent, while Omomyc was chemically modified with succinimidyl 3-(2-pyridyldithio)propionate (SPDP, SIGMA-Aldrich, USA; stock dissolved in DMSO) using 1.7 M excess of the reagent. Excess reagents were removed by gel filtration on a G25 column (GE Healthcare, USA) equilibrated in BBS buffer. Fractions containing the 2 proteins were collected, and EV20-2IT and Omomyc-SPDP were then mixed with 1:5 ratio respectively. The reaction for the formation of disulfide bond between EV20 and Omomyc was carried out over 2 h at room temperature, and monitored following the release of pyridine-2-thione at 343 nm by spectrophotometer. After the reaction, the mixture was concentrated to 5 mg/ml with a centrifugal filter unit of 30 kDa cutoff. Removal of Omomyc-2IT unreacted product was done on G25 (40 ml volume) column with FPLC in Phosphate Buffered Saline pH 7.4 (PBS) with an isocratic flow rate at 1.5 ml/min. Further residual Omomyc-2IT was then removed by ion exchange chromatography on a Q-Sepharose Column in 20 mM Trizma pH 9, eluting with PBS in isocratic flow rate (1 ml/min). Purified samples were analysed by western blotting using anti-Omomyc antibody (Ximbio, Anti-Omomyc [21–1-3]). DAR was assessed by mass spectrometry performed by Toscana Life Sciences (http://www.toscanalifesciences.org/it/). The naked EV20 and

EV20/Omomyc were desalted using Spin Trap G25 (Cytiva). For each sample, 2 μL of the resulting solution was mixed with 2 μL of a saturated solution of s-DHB in 0.1% TFA in acetonitrile:water (50:50, v/v). The mixture was spotted onto the MALDI plate and left to dry in the air. Successively, 1 μL of the saturated matrix solution was added to each dried spot and it was let to dry again. A protein standard II calibration mixture from Bruker Daltonics (GmbH, Bremen, Germany) was used for the calibration procedure. The mass spectra were acquired over the mass range m/z 30–220 kDa, in linear mode, using an UltrafleXtreme (Bruker Daltonics, GmbH) MALDI mass spectrometer.

4.9. ELISA

For EV20/Omomyc *In Vitro* binding assay, 96-well plates NUNC Maxisorp modules were coated with Recombinant HER-3 extracellular domain (ECD) (1 μg/ml) overnight at 4◦C. After blocking with 1% BSA in PBS at room temperature for 1 h, increasing concentrations of EV20/Omomyc or EV20 as control were added and incubated at room temperature for 1 h. After several washes with PBS +0,05% Tween-20, a goat anti-human IgG-HRP solution (Sigma-Aldrich Corporation) was added to each well and incubated at room temperature for 1 h. After washes, stabilized chromogen was added to each well for at least 10 min in the dark, then the reaction was stopped with the addition of 1 N H2SO4 and the resulting color read at 450 nm with an ELISA plate reader. For *In Vitro* serum stability analysis, 37.5 μg of EV20/Omomyc was incubated in human serum at 37◦C for a period of time. Serum samples are drawn at different time points and the amount of conjugated antibody are measured using anti-Omomyc sandwich ELISA to calculate the degree of drug loss. In detail, 96-well plates NUNC Maxisorp modules were coated with murine anti-Omomyc antibody (0,5 μg/ml) overnight at 4◦C. After blocking with 1% BSA in PBS at room temperature for 1 h, increasing concentrations of EV20/Omomyc or EV20 as control were added and incubated at room temperature for 1 h. After several washes with PBS +0,05% Tween-20, a goat anti-human IgG-HRP solution (Sigma-Aldrich Corporation) was added to each well and incubated at room temperature for 1 h. After washes, stabilized chromogen was added to each well for at least 10 min in the dark, then the reaction was stopped with the addition of 1 N H2SO4 and the resulting color read at 450 nm with an ELISA plate reader.

4.10. Confocal imaging

A375m, Kelly-Mock and Kelly-HER3 cells at 70% of confluence were grown on coverslips for 24 h and then incubated with EV20 (20 μg/ml), EV20/Omomyc (20 μg/ml) or Omomyc (2 or 0.6 μg/ml) for 4 h at 37◦C. Cells were then fixed in 4% paraformaldehyde for 15 min at room temperature, permeabilized with 0.25% Triton X-100 for 5 min, and blocked with goat serum 5% in PBS as blocking solution for 60 min at RT. Coverslips were then incubated overnight at 4◦C with murine anti-Omomyc antibody (Ximbio, Anti-Omomyc [21–1-3]; 1:100 dilution) followed by AlexaFluor-488 conjugated anti-mouse IgG 1:100 (A11017, Invitrogen, Life Technologies) 1 h at RT for Omomyc detection; and with AlexaFluor-488 conjugated anti-human IgG 1:100 (A11013, Invitrogen, Life Technologies) or AlexaFluor-594 conjugated anti-human IgG 1:100 (A11014, Invitrogen, Life Technologies) 1 h at RT for EV20 antibody detection. DAPI solution (P62248; Thermo Fisher Inc., Waltham, MA, USA) was used to visualize nuclei, actin is stained in red with TRITC-phalloidin and coverslips were mounted using ProLong Gold Antifade Mountant (P36930; Thermo Fisher Inc., Waltham, MA, USA). Confocal images were acquired using a Zeiss LSM800 inverted confocal microscope system (Carl Zeiss, Gottingen, Germany); detector gain voltages and

pinhole were set at the beginning of the experiment and maintained constant during the acquisition of all samples. No significant fluorescent signal was detectable with the secondary antibodies alone. Fluorescence intensity of the internalized EV20/Omomyc or Omomyc was quantified using ImageJ Software and normalized for DAPI-labelled cell nuclei.

4.11. FACS analysis

For HER3 surface expression analysis, A375m, Kelly-Mock and Kelly-HER3 cells were harvested and labelled with indicated doses of EV20/ Omomyc or EV20 as control for 30 min on ice. After washing, cells were labelled with AlexaFluor-488 conjugated anti-human IgG (A11013, Invitrogen, Life Technologies) at a dilution of 1:300. Analysis was per- formed using a FACS Canto II cytometer (BD Biosciences).

4.12. Experimental Metastasis Assay

Immunodeficient NSG mice were purchased from Jackson Laboratory and bred in the animal facility of CAST, G. D'Annunzio University, Chieti. Animal care and experimental procedures were approved by the Ethics Committee for Animal Experimentation of the Institute according to Italian law (Authorization n◦ 292/2017-PR). 8-week old male NSG mice were injected via the lateral tail vein with 5 ×105 Kelly-Mock or Kelly-HER3 neuroblastoma cells; after 2 weeks, mice were randomly divided into 2 groups that received PBS or EV20/MMAF (10 mg/Kg) weekly for a total of 2 doses or in 4 groups that received PBS, EV20 (5 mg/Kg), EV20/Omomyc (5 mg/Kg) and free Omomyc (0.6 mg/kg) weekly for a total of 4 doses. The animal health status was monitored daily, and body weight was measured once a week during the treatments. 11 days after last treatment mice were sacrificed and livers were harvested, fixed in 10% neutral buffered formalin, paraffin embedded, sectioned and stained with Hematoxylin and Eosin (Bio-Optica) for metastasis analysis. To optimize the detection of microscopic metastases and ensure systematic uniform and random sampling, livers were cut transversally into 2.0 mm thick parallel slabs with a random position of the first cut in first 2 mm of the organ, resulting in 6–8 slabs. The slabs were then embedded cut surface down and sections were stained with Hematoxylin and Eosin. Slides were independently evaluated by 2 pathologists to quantify the number of lesions. Sections were scanned with Nanozoomer scanner from Hamamatsu and images were acquired with NDP.view 2 software.

4.13. Immunofluorescence analysis of tumour xenografts

Xenografts were generated injecting subcutaneously into both flanks of mice a suspension of 5 ×106 Kelly-Mock and Kelly-HER3 cells in a total volume of 200 µl of PBS and Matrigel (ratio 1:1). When xenografts became palpable (approximately 100 mm3), animals received one single intravenous injection of EV20/Omomyc at the dose 10 mg/Kg and were sacrificed 24 h later. Fresh tumour tissues were frozen in a crioembedding medium (OCT, Bio-Optica) and cryostat sections were incubated with the following antibodies: AlexaFluor-488 conjugated anti-human IgG (A11013, Invitrogen, Life Technologies) in order to detect EV20 and rat monoclonal anti-CD31 (550,274, BD Pharmingen), mixed with rat monoclonal anti-CD105 (550,546, BD Pharmingen), followed by AlexaFluor-546 conjugated secondary antibody (A11081, Invitrogen, Life Technologies) in order to detect endothelial cells. Nuclei were stained with DAPI solution (Sigma). Images were acquired using Zeiss LSM 800 confocal microscope. Quantification of mean fluorescence intensity (MFI) of anti-human

IgG was performed on digital images of 3 tumours per group (5 ×400 microscopic field per sample) using ZEN software.

4.14. Statistical analysis

For fluorescence intensity quantification and for metastasis analysis in Fig. 5A, p values were determined by unpaired Student's t-test and considered significant for $p < 0.05$. For metastasis analysis in Fig. 5B, one-way ANOVA statistical analysis with Tukey multiple comparison test was used to determine differences between treatment groups, * $p < 0.05$ indicates significant difference between the groups. All statistical analysis was performed with GraphPad Prism 5.0 software.

Funding

This work was supported partially by Mediapharma and by Fondazione-AIRC(GS: IG GRANT 2016, Id 18,467).

References

[1] R. Dhanasekaran, et al., The MYC oncogene - the grand orchestrator of cancer growth and immune evasion, Nat. Rev. Clin. Oncol. 19 (2022) 23–36, https://doi.org/10.1038/s41571-021-00549-2.

[2] M. Conacci-Sorrell, L. McFerrin, R.N. Eisenman, An overview of MYC and its interactome, Cold Spring Harb. Perspect. Med. 4 (2014) a014357, https://doi.org/10.1101/cshperspect.a014357.

[3] R. Zeid, et al., Enhancer invasion shapes MYCN-dependent transcriptional amplification in neuroblastoma, Nat. Genet. 50 (2018) 515–523, https://doi.org/10.1038/s41588-018-0044-9.

[4] D. Masso-Valles, L. Soucek, Blocking Myc to treat Cancer: reflecting on two decades of Omomyc, Cells 9 (2020), https://doi.org/10.3390/cells9040883.

[5] M.E. Beaulieu, et al., Intrinsic cell-penetrating activity propels Omomyc from proof of concept to viable anti-MYC therapy, Sci. Transl. Med. 11 (2019), https://doi.org/10.1126/scitranslmed.aar5012.

[6] L. Soucek, et al., Modelling Myc inhibition as a cancer therapy, Nature 455 (2008) 679–683, https://doi.org/10.1038/nature07260.

[7] J.M. Vicencio, et al., Osimertinib and anti-HER3 combination therapy engages immune dependent tumor toxicity via STING activation in trans, Cell Death Dis. 13 (2022) 274, https://doi.org/10.1038/s41419-022-04701-3.

[8] M. Momeny, et al., Heregulin-HER3-HER2 signaling promotes matrix metalloproteinase-dependent blood-brain-barrier transendothelial migration of human breast cancer cell lines, Oncotarget 6 (2015) 3932–3946, https://doi.org/10.18632/oncotarget.2846.

[9] R. Ghasemi, et al., Dual targeting of ErbB-2/ErbB-3 results in enhanced antitumor activity in preclinical models of pancreatic cancer, Oncogenesis 3 (2014) e117, https://doi.org/10.1038/oncsis.2014.31. Journal of Controlled Release 374 (2024) 171–180

[10] G. Sala, et al., EV20, a novel anti-ErbB-3 humanized antibody, promotes ErbB-3 Down-regulation and inhibits tumor growth *In Vivo*, Transl. Oncol. 6 (2013) 676–684, https://doi.org/10.1593/tlo.13475.

[11] G. Sala, et al., An ErbB-3 antibody, MP-RM-1, inhibits tumor growth by blocking ligand-dependent and independent activation of ErbB-3/Akt signaling, Oncogene 31 (2012) 1275–1286, https://doi.org/10.1038/onc.2011.322.

[12] P.R. Prasetyanti, et al., ErbB-3 activation by NRG-1beta sustains growth and promotes vemurafenib resistance in BRAF-V600E colon cancer stem cells (CSCs), Oncotarget 6 (2015) 16902–16911, https://doi.org/10.18632/oncotarget.4642.

[13] D. D'Agostino, et al., EV20sssvc/MMAF, an HER3 targeting antibodydrug conjugate displays antitumor activity in liver cancer, Oncol. Rep. 45 (2021) 776–785, https://doi.org/10.3892/or.2020.7893.

[14] E. Capone, et al., EV20/NMS-P945, a novel Thienoindole based antibody-drug conjugate targeting HER-3 for solid tumors, Pharmaceutics 13 (2021), https://doi.org/10.3390/pharmaceutics13040483.

[15] L. Gandullo-Sanchez, et al., HER3 targeting with an antibody-drug conjugate bypasses resistance to anti-HER2 therapies, EMBO Mol. Med. 12 (2020) e11498, https://doi.org/10.15252/emmm.201911498.

[16] E. Capone, et al., EV20-mediated delivery of cytotoxic auristatin MMAF exhibits potent therapeutic efficacy in cutaneous melanoma, J. Control. Release 277 (2018) 48–56, https://doi.org/10.1016/j.jconrel.2018.03.016.

[17] E. Capone, et al., EV20-sap, a novel anti-HER-3 antibody-drug conjugate, displays promising antitumor activity in melanoma, Oncotarget 8 (2017) 95412–95424, https://doi.org/10.18632/oncotarget.20728.

[18] P. Varlet, et al., Comprehensive analysis of the ErbB receptor family in pediatric nervous system tumors and rhabdomyosarcoma, Pediatr. Blood Cancer 69 (2022) e29316, https://doi.org/10.1002/pbc.29316.

[19] E. Izycka-Swieszewska, et al., Expression and significance of HER family receptors in neuroblastic tumors, Clin. Exp. Metastasis 28 (2011) 271–282, https://doi.org/10.1007/s10585-010-9369-1.

[20] R. Ho, et al., Proliferation of human neuroblastomas mediated by the epidermal growth factor receptor, Cancer Res. 65 (2005) 9868–9875, https://doi.org/10.1158/0008-5472.Can-04-2426.

[21] B. Qiu, K.K. Matthay, Advancing therapy for neuroblastoma, Nat. Rev. Clin. Oncol. 19 (2022) 515–533, https://doi.org/10.1038/s41571-022-00643-z.

[22] K.C. Goldsmith, et al., Lorlatinib with or without chemotherapy in ALK-driven refractory/relapsed neuroblastoma: phase 1 trial results, Nat. Med. 29 (2023) 1092–1102, https://doi.org/10.1038/s41591-023-02297-5.

[23] L.L. Wang, et al., Augmented expression of MYC and/or MYCN protein defines highly aggressive MYC-driven neuroblastoma: a Children's oncology group study, Br. J. Cancer 113 (2015) 57–63, https://doi.org/10.1038/bjc.2015.188.

[24] M. Bansal, A. Gupta, H.F. Ding, MYCN and metabolic reprogramming in neuroblastoma, Cancers (Basel) 14 (2022), https://doi.org/10.3390/cancers14174113.

[25] E. Izycka-Swieszewska, et al., Expression and significance of HER family receptors in neuroblastic tumors, Clin. Exp. Metastasis 28 (2011) 271–282, https://doi.org/10.1007/s10585-010-9369-1.

[26] E. Capone, et al., HER-3 surface expression increases in advanced colorectal cancer representing a potential therapeutic target, Cell Death Dis. 9 (2023) 400, https://doi.org/10.1038/s41420-023-01692-8.

[27] E. Capone, et al., Targeting vesicular LGALS3BP by an antibody-drug conjugate as novel therapeutic strategy for neuroblastoma, Cancers (Basel) 12 (2020), https://doi.org/10.3390/cancers12102989.

[28] S. Bibbo, et al., Repurposing a psychoactive drug for children with cancer: p27(Kip1)-dependent inhibition of metastatic neuroblastomas by Prozac, Oncogenesis 9 (2020) 3, https://doi.org/10.1038/s41389-019-0186-3.

[29] M.-E. Beaulieu, et al., Abstract 3435: identification of potential biomarkers of response to OMO-103, a first-in-modality pan-MYC inhibitor, in patients with advanced solid tumors, Cancer Res. 83 (2023) 3435, https://doi.org/10.1158/1538-7445.AM2023-3435.

[30] L. Gandullo-S´ anchez, A. Ocana, A. Pandiella, HER3 in cancer: from the bench to the bedside, J. Exp. Clin. Cancer Res. 41 (2022) 310, https://doi.org/10.1186/s13046-022-02515-x.

[31] H. Lyu, A. Han, E. Polsdofer, S. Liu, B. Liu, Understanding the biology of HER3 receptor as a therapeutic target in human cancer, Acta Pharm. Sin. B 8 (2018) 503–510, doi:https://doi.org/10.1016/j.apsb.2018.05.010.

[32] R. Hartley, T.N. Phoenix, MYC promotes aggressive growth and metastasis of a WNT-medulloblastoma mouse model, Dev. Neurosci. (2023), https://doi.org/10.1159/000533270.

[33] J. Ommer, et al., Aurora a kinase inhibition destabilizes PAX3-FOXO1 and MYCN and synergizes with Navitoclax to induce rhabdomyosarcoma cell death, Cancer Res. 80 (2020) 832–842, https://doi.org/10.1158/0008-5472.Can-19-1479.

[34] T. Shalaby, M.A. Grotzer, MYC as therapeutic target for embryonal tumors: potential and challenges, Curr. Cancer Drug Targets 16 (2016) 2–21, https://doi.org/10.2174/1568009615666150916092745.

CHAPTER 2

1959-Based Non-Internalizing Antibody–Drug Conjugates Targeting Secreted LGALS3BP

The second principal project focused on the design, development, and analysis of an antibody–drug conjugate (ADC) targeting LGALS3BP. This research utilized the laboratory's anti-LGALS3BP antibody platform 1959, which is derived from the murine SP-2 cell line.

2.1 LGALS3BP

LGALS3BP is a multifunctional secreted protein, also known as 90K, Mac-2 binding protein (Mac-2BP/M2BP), or galectin-3 binding protein (Gal-3BP). Other names include gp90 and, in some contexts, CyCAP (cyclophilin C–associated protein) (110). LGALS3BP is found in many human cancers and is often linked to more aggressive disease. It promotes a multitude of pathways involved in cancer progression by altering the tumor microenvironment and affecting immune responses (110,111), schematized in Figure 10. Research on LGALS3BP began in the late 1980s after its identification as a tumor-associated antigen in body fluids and cancer specimens. Early studies developed assays to quantify 90K in blood. These confirmed that 90K is reliably detected in cancer patients and is a secreted glycoprotein rather than an intracellular marker (110). Initially seen mainly as a tumor antigen, later research showed that 90K is actively secreted, accumulates extracellularly, and exerts biological effects beyond passive release from dying cells. In 1993, Koths and colleagues cloned and described human Mac-2BP as a secreted protein with about 567 amino acids that forms large complexes present in many body fluids (111). Ullrich and colleagues showed that 90K strongly stimulates the immune system. This established its role in immune activation (112). Exposure of cells to 90K alters their immune properties, including antigen presentation. This indicates that 90K modulates immune surveillance at the tumor-host interface. (113,114). In the 1990s, researchers determined key mechanisms for antibody recognition of 90K. Tinari and colleagues found that both SP2 and L3 monoclonal antibodies bind the same region (domain D2) of 90K. This demonstrated that SP2 binds a structural protein domain rather than a glycan moiety (115). This mapping showed SP2 targets a conserved region valuable for antibody humanization, and that antibody binding could block protein interactions at this site. Altogether, these findings support a role for functional inhibition beyond detection (115).

In 1998, Sasaki and colleagues showed that Mac-2BP acts as a cell-adhesive protein in the extracellular matrix. The recombinant protein is highly glycosylated, forms large oligomers, and assembles into ring-like structures. These promote cell adhesion via β1 integrins and other matrix interactions (116). When tumor cells secrete LGALS3BP assemblies, they can create adhesive microenvironments that support cancer cell survival, migration, stromal interactions, or immune modulation, depending on the receptors and lectins available. Evidence shows that extracellular LGALS3BP modulates cancer cell behavior as a microenvironment ligand (111). Fornarini and colleagues found that immobilized 90K changes lymphoma cell sensitivity to apoptosis. Blood 90K levels correlate with clinical responses, suggesting that 90K-rich environments may protect against cellular stress (117). Thus, extracellular LGALS3BP may influence responses to stress and therapies. In the early 2000s, Ozaki and colleagues used lung cancer models to show that increased 90K/M2BP

levels change cell-matrix adhesion and raise metastatic potential (118–120). Collectively, these studies support the view that LGALS3BP function is determined by its relative abundance, its molecular form (oligomerization state), glycosylation, and accessibility of functional domains in the extracellular space.

Mechanistically, LGALS3BP is a secreted hub protein that interacts with many partners, including galectins (especially galectin-3), integrins, tetraspanin complexes, and immune lectin receptors such as DC-SIGN and Siglecs. Two main features enable these: oligomer formation, which clusters receptors, and complex glycosylation, which provides lectin-binding sites and affects receptor conformation and stability. Together, these features enable LGALS3BP to act as a matrix hub, supporting ligand assembly, receptor clustering, and modulation of signaling pathways. A key finding was that LGALS3BP is a ligand for C-type lectin receptors involved in antigen presentation and myeloid cell programming. Nonaka and colleagues showed DC-SIGN recognizes Mac-2BP through its glycans. This explains LGALS3BP's modulation of dendritic cell function (121). Later studies demonstrated that LGALS3BP can inhibit monocyte-to-fibrocyte differentiation in a DC-SIGN–dependent way. This suggests it can reprogram immune or stromal cells at the tumor–stroma interface (122). In practical terms, tumor-secreted LGALS3BP is positioned to act upstream of stromal remodeling (fibrocyte generation, collagen deposition) and immune-infiltration patterns, thereby shaping a microenvironment that can restrain or enable tumor progression depending on context.

Another important finding is that LGALS3BP binds inhibitory sialic-acid–binding receptors. Läubli and colleagues showed that LGALS3BP binds CD33-related Siglecs, suppressing neutrophil activation and aiding tumor immune evasion (123). This is relevant because neutrophils and Siglec-expressing cells are common in many cancers. A secreted protein can limit its activity and promote immune escape. The Siglec pathway highlights the importance of LGALS3BP glycosylation, as it directly affects receptor engagement and immune signaling. Importantly, LGALS3BP is not always pro-tumorigenic. In colorectal cancer, it can act as a tumor suppressor in some settings. Lee and colleagues found that 90K expression is reduced in advanced colorectal cancer and can inhibit Wnt/β-catenin signaling via an ISGylation-dependent mechanism with CD9/CD82 complexes. This reveals an antitumor pathway that is lost during progression (124). Later studies confirmed that reduced LGALS3BP is associated with worse outcomes. This suggests that in some epithelial cancers, LGALS3BP promotes differentiation and restrains Wnt signaling (125) In sum, LGALS3BP is a context-dependent extracellular regulator. Its effects are determined by binding partners, glycan composition, and cues like interferons and cytokines. Another important function is the interferoninteraction and involment into inflammation processes. Loimaranta and colleagues showed that LGALS3BP expression increases in response to inflammatory signals. The protein acts in innate immunity through both extracellular and intracellular mechanisms. This indicates that LGALS3BP is part of overall host defense, not just a cancer-associated protein (126). Supporting this view, Hong and colleagues found that Gal-3BP can dampen NF-κB signaling by blocking TAK1 activation. This links LGALS3BP to feedback control of inflammation (127). Further work showed that LGALS3BP acts as an interferon-stimulated antiviral effector. Xu and colleagues reported that inducible LGALS3BP/90K boosts antiviral innate immunity through TRAF complexes. This promotes interferon and pro-inflammatory programs (128). Together, these studies show that LGALS3BP is an immune-regulatory node. It can stimulate antiviral defenses and limit harmful inflammation. In cancer, these traits may be hijacked to support immune exclusion via inhibitory lectin receptors or to modulate inflammatory tone. This can influence angiogenesis and stromal activation.

Angiogenesis is another key axis in LGALS3BP's role in cancer biology. Piccolo and colleagues showed that LGALS3BP secreted by breast cancer cells functions as a pro-angiogenic factor. It promotes endothelial tubulogenesis and influences VEGF-related pathways by both inducing VEGF and directly stimulating cancer-associated endothelial cells (129). This work linked abundant tumor-secreted LGALS3BP to vascular remodeling. It provides a rationale for using LGALS3BP-binding antibodies as therapy. Neutralizing extracellular LGALS3BP's pro-angiogenic effects with antibodies may limit tumor growth without entering tumor cells. This was tested with the murine antibody SP-2. Traini and colleagues found SP-2 acts as a functional antagonist of LGALS3BP. It blocks endothelial tubulogenesis driven by tumor-conditioned media or recombinant LGALS3BP and suppresses phosphorylation of key signaling proteins (FAK, AKT, ERK) central to adhesion-driven angiogenic signaling (130). *In Vivo*, SP-2 reduced tumor growth and angiogenesis. This proved that targeting extracellular matrix–associated proteins with antibodies can inhibit tumors via the microenvironment. These findings highlight LGALS3BP as an active and targetable extracellular factor.

Since the initial development of blood assays for 90K (110), LGALS3BP has been investigated as a tumor-associated molecule detectable in the circulation. More recent studies have identified LGALS3BP in extracellular vesicles and plasma EV fractions. This suggests its potential utility as a liquid biopsy marker in certain contexts. However, the primary focus of this chapter is on the functional roles and therapeutic applications of LGALS3BP, not its diagnostic potential. These biomarker studies are included to emphasize that LGALS3BP is present in blood, extracellular vesicles, and the tumor microenvironment. This distribution supports its promise as an early biomarker for liquid biopsy-based cancer diagnosis. This topic is explored further in Chapter 4.

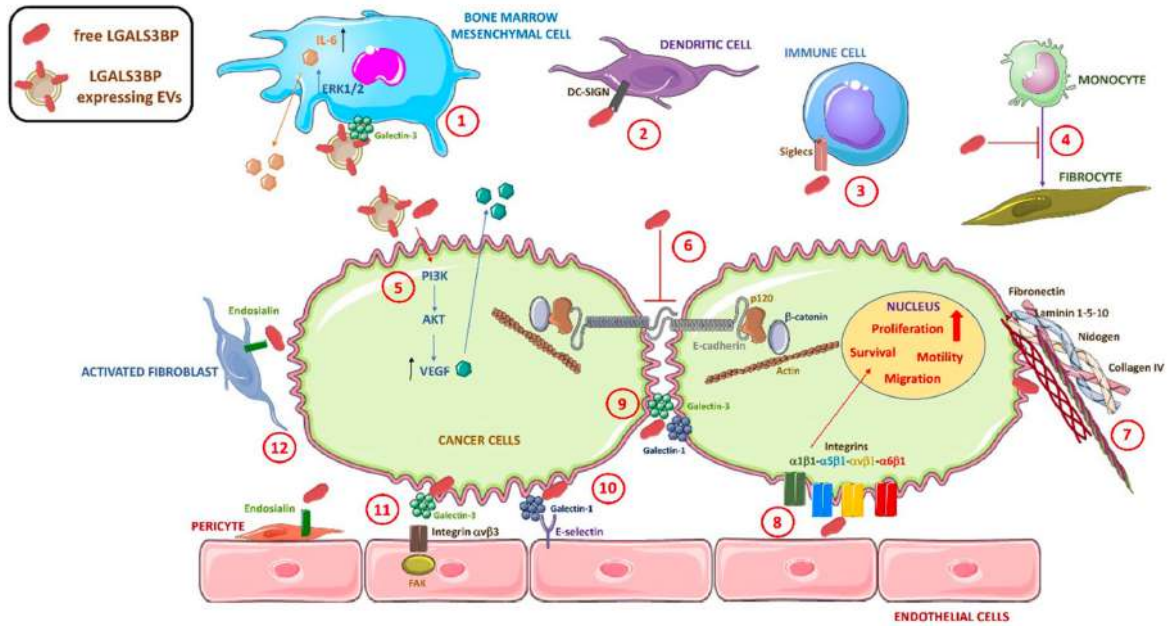


Figure 10. Schematic representation of proposed LGALS3BP functions in cancer. 1. EVs-associated LGALS3BP induces IL-6 production from bone marrow mesenchymal cells contributing to the creation of pro-tumorigenic microenvironment. 2. LGALS3BP interacts with DC-SIGN to suppress Dendritic Cells maturation. 3. LGALS3BP interacts with Siglecs receptor on immune cells stimulating immune evasion. 4. LGALS3BP is involved in inhibition of monocyte-fibrocyte differentiation. 5. Free and EVs-associated LGALS3BP induces VEGF production in cancer cells via PI3K/AKT signaling promoting angiogenesis. 6.

LGALS3BP destabilizes adherens junctions of cancer cells via dissociation of the E-cadherin–p120-catenin complex. 7. LGALS3BP mediates adhesion of cancer cells to several matrix extracellular proteins like fibronectin, nidogen, laminin 1-5-10 and collagen IV. 8. LGALS3BP has a role in the integrins-mediated adhesion of cancer cells to endothelial cells, promoting survival, proliferation, motility and migration pathways. 9. LGALS3BP mediates homotypic aggregation cell induced by galectin-1 and galectin-3. 10. LGALS3BP is involved in E-selectin mediated adhesion to endothelial cells. 11. LGALS3BP promotes angiogenesis through binding to endothelial integrins and FAK activation mediated by galectin-3. 12. LGALS3BP has a role in crosstalk between tumor and stroma mediated by endosialin expressed on pericytes and activated fibroblasts. *Image source: Capone et Al. 2021 (131)*

2.2 1959-sss/DM4 ADC

The 1959 antibody was developed by humanizing the murine SP-2 antibody, preserving its specificity for secreted LGALS3BP for therapeutic applications, in particular ADCs (131) The efficacy of non-internalizing antibody-drug conjugates depends on three main factors: antibody accumulation in the tumor extracellular space, sustained retention at the target site, and release of a membrane-permeable cytotoxin that induces cytotoxicity in neighboring cells. This approach aligns with the biological properties of LGALS3BP, which is secreted by various tumors and accumulates at cell boundaries and in the stroma. These features make LGALS3BP a stable extracellular target and a potential node for disrupting tumor signaling. Literature reviews show that extracellular or non-internalizing ADCs are most effective when the linker supports drug release in the tumor microenvironment. The payload should be highly potent and membrane-permeable, and the antibody must show tumor selectivity with minimal off-target effects (8) These principles guided the design of 1959-sss/DM4, which uses extracellular chemistry to regulate drug release.

A detailed preclinical demonstration of a 1959-based, non-internalizing ADC targeting secreted LGALS3BP was reported by Giansanti and colleagues. In that study, the humanized 1959 antibody selectively localized to tumor cells rather than normal cells, consistent with extracellular accumulation of LGALS3BP in tumor microenvironments (132). To achieve cytotoxic efficacy, the antibody was conjugated using a controlled, site-specific reaction. A 1959 variant with cysteines (“sss” format) enabled precise attachment of thiol-reactive maytansinoid payloads. The resulting ADCs, including those with DM3 and DM4, had a defined drug-to-antibody ratio (DAR) of 2 (Figure 11). They showed significant antitumor activity in xenograft models, with durable regressions and cures in melanoma mouse models (132). These findings support two conclusions. First, LGALS3BP provides enough tumor selectivity at the extracellular level to maintain a therapeutic index. Second, extracellular drug release is effective *In Vivo* when paired with a potent cytotoxic payload (132). DM4, a maytansinoid microtubule inhibitor, can be released as an active species in disulfide-based designs under reducing or thiol-exchange conditions. Such conditions are more common in tumors than in normal tissues. In non-internalizing ADCs, the released payload must cross cell membranes to induce cytotoxicity. Maytansinoids are often used in ADCs for their potency and physicochemical properties, which support this need. In the 1959-sss/DM4 model, the antibody delivers DM4 into the tumor's LGALS3BP-enriched extracellular space, permeate cancer cell membrane, inducing cytotoxic exposure and cell death. Subsequently, it diffuses to neighbouring tumor and stromal cells by the Bystander effect. This approach helps treat tumors with heterogeneous antigen expression or complex stromal structures, as bystander killing can eliminate antigen-negative cell populations that might otherwise escape therapy (133).

The presence of LGALS3BP in extracellular vesicles (EVs) further supports the rationale for using 1959-based ADCs. LGALS3BP is often detected in tumor-derived EVs, which transfer proteins into neighboring tissue and enable long-range communication between cancer cells, and their environment (96) Preclinical studies show that targeting or delivering drugs to EV-associated LGALS3BP produces significant antitumor effects. In a 2023 glioblastoma study, Dufrusine and colleagues found that vesicular LGALS3BP serves as a viable extracellular target. 1959-sss/DM4 accumulates in tumor tissue and triggers strong, dose-dependent antitumor responses *In Vivo* after DM4 release (133). The development of LGALS3BP-targeting radioimmunoconjugates for immunoPET further supports the notion that antibody-based therapies can reach only LGALS3BP-expressing tumors *In Vivo* (134).

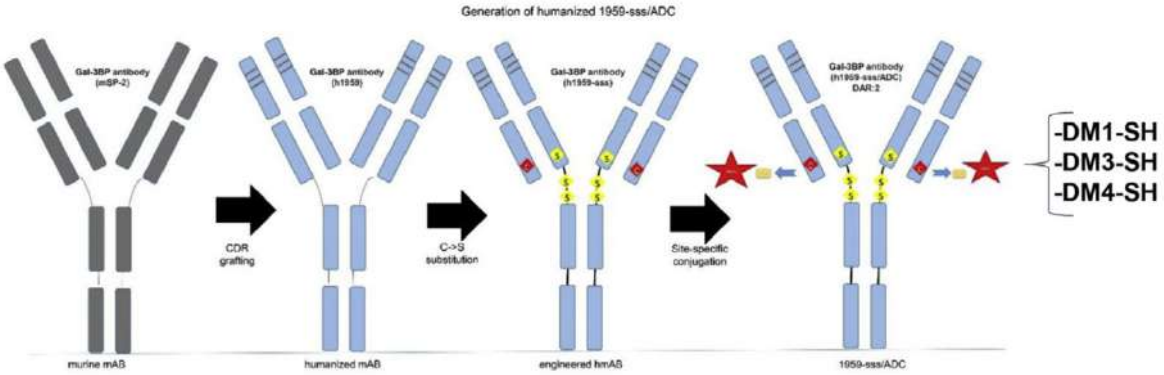


Figure 11. Schematic representation of 1959-sss based-ADCs generation. *Image source: Giansanti et Al. 2019* (135)

2.3 1959-sss/DM4 ADC based combination therapy

LGALS3BP is a highly glycosylated, bioactive protein at the tumor-stroma interface. It helps remodel the extracellular matrix, interacts with lectins and glycan-binding receptors, and modulates immune pathways that affect antitumor responses. By this way, can targeting LGALS3BP by ADC therapy modify the tumor immune microenvironment, rather than just causing tumor regression? This is especially important in neuroblastoma. Neuroblastoma is immunologically “cold” due to a microenvironment that suppresses immune responses and blocks T-cell activation, limiting the effectiveness of immunotherapy (135,136). These challenges point to the need for combination strategies that boost inflammation and immune recognition, rather than simply adding immunotherapies to non-inflamed tumors (136). Previous studies show that LGALS3BP is abundant in extracellular compartments and vesicles. The 1959-sss/DM4 ADC can be targeted effectively, resulting in strong, durable antitumor effects in neuroblastoma models (137).

In parallel, Immunogenic cell death (ICD) is defined by the release of signals like calreticulin, ATP, and HMGB1 from dying cells. These signals alert and activate the immune system. They can also help cytotoxic therapies act as in situ vaccines at the tumor site (138). Maytansinoid ADCs, including those with maytansine, have been shown to induce ICD in preclinical studies. Administration of these agents can kill tumor cells and stimulate immune activity under favorable conditions (139). However, both ICD and therapy-induced inflammation may also foster immune resistance. One recurring

mechanism is IFN-γ–induced elevation of PD-L1 expression on tumor cells. In these cases, blocking the PD-1 or PD-L1 pathway can help preserve T-cell function after initial therapy (140).

Microtubule-targeting drugs, including those related to ravtansine, can activate innate immune sensors. These include the cGAS–STING and type I interferon pathways, triggered by mitotic disruption. These agents also increase the expression of immune checkpoints, such as PD-L1, in many tumor types (141). Microtubule disruption can thus improve antitumor immune responses but may also increase levels of checkpoint proteins that suppress immunity (141,142). In neuroblastoma, both baseline and cytokine-induced PD-L1 expression are present. PD-1–positive immune cells are also found in the bone marrow of these patients. These facts strongly support targeting the PD-1 pathway in combination regimens to overcome immune resistance in neuroblastoma (143,144).

In summary, evidence shows that 1959-sss/DM4 selectively targets and kills cancer cells, induces immune stress, and may work with PD-1 blockers to overcome resistance. This concept is the chapter's focus and is described in the following work:

Cela, I., Capone, E., Pece, A., et al. (2025). LGALS3BP antibody–drug conjugate enhances tumor-infiltrating lymphocytes and synergizes with immunotherapy to restrain neuroblastoma growth. Journal of Translational Medicine, 23(1), 431. https://doi.org/10.1186/s12967-025-06434-1 (145)

LGALS3BP antibody-drug conjugate enhances tumor-infiltrating lymphocytes and synergizes with immunotherapy to restrain neuroblastoma growth

Ilaria Cela[1,2], Emily Capone[2,3], Asia Pece[2], Giulio Lovato[1,2], Pasquale Simeone[2,4], Martina Colasante[5], Alessia Lamolinara[2,6], Anna Piro[7], Manuela Iezzi[2,6], Paola Lanuti[2,4], Vincenzo De Laurenzi[1,2], Rodolfo Ippoliti[5], Stefano Iacobelli[8] and Gianluca Sala[1,2*]

[1] Department of Innovative Technologies in Medicine & Dentistry, "G. d'Annunzio" University of Chieti-Pescara, Chieti, Italy

[2] Center for Advanced Studies and Technology (CAST), "G. d'Annunzio" University of Chieti-Pescara, Chieti, Italy

[3] Department of Science, "G. d'Annunzio" University of Chieti-Pescara, Via Luigi Polacchi, 11, Chieti Scalo, Chieti 66100, Italy

[4] Department of Medicine and Aging Sciences, G. d'Annunzio University of Chieti-Pescara, 66100 Chieti, Italy

[5] Department of Life, Health and Environmental Sciences, University of L'Aquila, 67100 Coppito, Italy

[6] Department of Neurosciences, Imaging and Clinical Sciences, "G. d'Annunzio" University of Chieti-Pescara, Via Luigi Polacchi, 11, Chieti Scalo, Chieti 66100, Italy

[7] Department of Pharmacy, "G. d'Annunzio" University of Chieti-Pescara, 66100 Chieti, Italy

[8] MediaPharma s.r.l, Via Colonnetta 50/A, Chieti, Italy

Abstract

LGALS3BP, also referred as Gal-3BP, Mac2-BP, or 90 K, is a heavily glycosylated, secreted protein prominently localized at the surface of cancer-derived extracellular vesicles (EVs). Its levels are significantly elevated in various types of cancer, including neuroblastoma, and are generally associated with advanced disease and tumor progression. Our previous research has shown that LGALS3BP is an effective target for ravtansine (DM4)-based Antibody-Drug Conjugate (ADC) therapy in multiple preclinical models.

We assessed total and extracellular vesicles (EVs)-associated LGALS3BP through ELISA assay in serum of a pseudometastatic neuroblastoma model to evaluate the correlation of LGALS3BP levels with tumor dissemination. We employed a syngeneic neuroblastoma mouse model using murine neuroblastoma NXS2 cells overexpressing human LGALS3BP in order to evaluate immunogenic cell death (ICD) induced by anti-LGALS3BP ADC therapy and investigated the nature of the tumor immune infiltrate by cytofluorimetry. Furthermore, we designed a six-arm *In Vivo* experiment to evaluate the efficacy of ADC in combination with an immune check-point inhibitor (ICI) anti-PD-1. Finally, a rechallenge assay was conducted on cured mice to assess the presence of immunological memory.

Here, we report that circulating and EVs-associated LGALS3BP levels significantly correlate with neuroblastoma progression and dissemination. Moreover, we show that in the syngeneic NXS2 neuroblastoma model, DM4 treatment induces cell surface expression of ICD markers calreticulin, HSP70, and HSP90, and an increased PD-L1expression *In Vitro*, followed by enhanced tumor-infiltrating lymphocytes *In Vivo*. Notably, the combination therapy of anti-LGALS3BP-targeting ADC with anti-PD-1 results in a higher inhibition of tumor growth and prolonged survival compared with either agent given alone. Rechallenge assay reveals that mice previously treated and cured with

the ADC retain immune memory, suggesting the therapy's ability to induce a durable and protective antitumor immune response.

1. Introduction

Neuroblastoma (NB) is the most common and aggressive extracranial solid tumor of pediatric age [1]. Almost half of NB patients show high metastatic potential and a 5-year survival rate approximately of 50% [2]. Currently, diagnosis of NB relies on biopsy and clinical symptoms, making early intervention difficult besides issues related to histological invasiveness [3] and disease's heterogeneity [4]. Therefore, identification of reliable and early detectable biomarkers is of primary importance. In this context, detection and quantification of circulating EVs released by cancer cells may serve as an innovative and promising tool for liquid biopsy [5, 6], facilitating tracking of neuroblastoma progression and therapeutic response [7]. To date, high risk NB patients undergo a multimodal therapeutic regimen consisting of a combination of surgery, chemo- and radiation therapy, and, as recently enclosed, immunotherapy [8], which has significantly improved patient outcomes through the introduction of dinutuximab, a monoclonal antibody targeting the surface antigen GD2 [8]. However, long-term side-effects and high rates of toxicity indicate the need of finding new therapeutic approaches. As far as immune check-point inhibitors (ICIs), the inconsistent clinical responses to these agents [9] seems to support the notion of neuroblastoma as an "immunologically cold" tumor [10], with general absence of tumor-reactive infiltrating T cells in most cases [11, 12]. Combination immunotherapies based on the association of Antibody Drug-Conjugates (ADCs) with ICIs has gained great interest in recent years, with the demonstration of a synergistic anti-tumor effect due to the stimulating of the host's immune responses and turning on the immunological cold tumor microenvironment (TME) of neuroblastoma into a "hot" and highly T-cells infiltrated one [13, 14]. This therapeutic combination would take advantage by the use of ADCs' cytotoxic payloads able to induce immunogenic cell death (ICD), a type of death of cells that releases typical damage-associated patterns (DAMPs) acting as signals for antigen-presenting cells (APCs), which in turn prime adaptive immune responses, especially involving T cells [15]. LGALS3BP (also known as Gal-3BP, Mac2-BP or 90 K) is a heavily glycosylated protein found to be overexpressed in several types of human cancer and involved in various cellular processes, including immune response modulation, cell adhesion, and signaling [16]. As a matter of fact, LGALS3BP has emerged as a crucial factor in regulating cancer-stroma interactions and is one of the most abundant surface components of cancer-derived EVs. Importantly, recent findings have reported the contribution of LGALS3BP in the cross-talk between neuroblastoma and tumor stroma cells and the LGALS3BP-dependent secretion of pro-tumorigenic cytokines (i.e., IL-6) from mesenchymal stem cells (MSCs) after internalization of neuroblastoma-derived EVs [17–19]. Specifically, LGALS3BP levels are significantly elevated in various cancers, including neuroblastoma, and can be detected in body fluids such as blood or urine, making this molecule a promising candidate for non-invasive diagnostic approaches. Here, we present evidence of the potential role of circulating LGALS3BP as a neuroblastoma biomarker for liquid biopsy. Additionally, we provide evidence for a role of the protein as a potential therapeutic target for ADC therapy in combination with immunotherapy.

2. Materials and methods

2.1 Cell lines and reagents

Human neuroblastoma SKNAS cells were purchased from American Type Culture Collection (ATCC; Rockville, MD, USA). The NXS2 murine neuroblastoma cell line was kindly provided by Holger N. Lode (University Medicine Greifswald, Germany) [20]. SKNAS, parental NXS2 cells, and stable-transduced NXS2 CTRL and hLGALS3BP cells were all cultured in Dulbecco's modified Eagle's medium (DMEM, Gibco; Whaltman, MA, USA) supplemented with 10% heat-inactivated fetal bovine serum (FBS) (Gibco), 100U/mL penicillin and 100 µg/mL streptomycin (Sigma-Aldrich Corporation, St.Louis, MO, USA). All cells were maintained at 37 °C in a humidified air with 5% CO2. All cell lines were tested for mycoplasma contamination through polymerase chain reaction (PCR). SH-DM4 was purchased from MedChemExpress (HY-12454; New Jersey, USA). Oxaliplatin was purchased from Sigma-Aldrich (#O9512). Anti-mouse PD-1 monoclonal antibody (InVivoMAb, CD279; clone RMP1-14,#BE0146) was purchased from BioXCell (NH, USA).

2.2 Stable lentiviral transduction

NXS2 CTRL and NXS2 hLGALS3BP cell lines were obtained by stable lentiviral transduction starting from NXS2 parental cell lines. Lentivirus particles were produced by transient co-transfection of packaging cell line HEK 293T with a three-plasmid expression system using Lipofectamine 2000 (Invitrogen, Thermo-Fisher, Waltham, MA, USA). Lentiviral plasmid pLenti-CMV-PURO-hLGALS3BP for stable overexpression of human LGALS3BP cDNA was obtained as follows: custom cloning was performed by Genscript (USA) by inserting human LGALS3BP cDNA in XbaI/SalI sites of the backbone pLenti-CMV-GFP-PURO (685-5) plasmid and excluding GFP sequence, a gift from Eric Campeau & Paul Kaufman (Addgene plasmid #17488, http://n2t.net/addgene:17448; RRID: Addgene_17448) [21]. Control plasmid (empty vector) pLenti-CMV-PURO was purchased from Origene (S100092; MD, USA). Briefly, HEK 293T cells were incubated for 6 h with transfection reagents. Lentiviral particles were collected after 48 and 72 h and filtered through 0.45 µm pore sterile filters (Corning, NY, USA). The day before the first cycle of transduction, 2×105 NXS2 cells were plated. After 24 h cells were incubated for 6 h with media containing viral particles together with 4 µg/mL of polybrene to increase transduction efficiency. After the first cycle of transduction, cells were washed and cultured with fresh medium overnight before a second cycle of transduction the day after. Cells were then let grow under standard growth conditions for 72 h before being put under selection with 1 µg/mL of puromycin (Sigma-Aldrich). Selection was maintained throughout all experiments performed. LGALS3BP levels were assessed through quantitative real-time PCR (qRT-PCR), western blotting and ELISA analysis.

2.3 Western blotting

Murine neuroblastoma cells (5×105) were seeded in complete medium and after 48 h they were lysed in RIPAbuffer (50mM Tris/HCl pH 7.6, 150mM NaCl, 1% NP-40, 0.5% Na-Deoxycholate, 0.1% SDS, 1mM EDTA pH 8) containing protease inhibitor cocktail (Sigma-Aldrich), phosphatase inhibitor cocktail (Roche, Thermo-Fisher), and Na3VO4 (Sigma-Aldrich). Lysates were clarified by centrifugation at 13,000 rpm for 30 min at 4 °C. Equal amounts of protein lysates (20 µg per sample), previously heated at 95 °C for 5 min, were subjected to SDS-PAGE electrophoresis and then electrotransferred to nitrocellulose membranes for Western blot analysis. Membranes were blocked

for 1 h at RT with 5% non-fat dry milk in PBS with 0.1% Tween20. Membranes were then incubated overnight at 4 °C with the following primary antibodies: anti-human LGALS3BP (goat polyclonal; 1:1000, #AF2226; R&D Systems, MN, USA); anti-β-actin (mouse monoclonal; 1:40000, #A5441; Sigma-Aldrich). After three washes in PBS-0.1% Tween20, the membranes were hybridized with horseradish peroxidase (HRP)-conjugated secondary antibodies (goat or mouse; Biorad, CA, USA). Detection of signal bands was performed with Clarity Western ECL substrate (#1705061; Biorad). Images of membranes were acquired with a UvitecFire reader (Cambridge, UK) and analysed with Alliance Uvitec software (Cambridge, UK).

2.4 Quantitative reverse transcription-PCR (qRT-PCR)

A total of 5×105 murine neuroblastoma cells were cultured in complete medium for 48 h, then total RNA was isolated from collected cells by RNeasy kit (#74136; Qiagen, Germany). One microgram of total RNA was reverse transcribed to cDNA by using High-capacity cDNA reverse transcription kit (#4368814; Applied Biosystems, MA, USA) according to the manufacturer's instructions. Real-time qPCR was performed with a CFX96 Touch Real-Time PCR Detection system (Biorad) using SsoAdvanced Universal SYBR Green supermix (#1725271; Biorad), according to manufacturer's instructions. The primers used at a final concentration of 350nM were: hLGALS3BP FOR 5'-GAA CCC AAG GCG TGA ACGAT-3', hLGALS3BP REV 5'- GTC CCA CAG GTT GTC ACA CA-3'; h-β-actin FOR 5'- CAG CTC ACC ATG GAT GAT GAT ATC-3', h-β-actin REV 5'-AAG CCG GCC TTG CAC AT-3'; mLGALS3BP FOR 5'-TCT CTT GCT CCC AGG GTT GG-3', mLGALS3BP REV 5'-CCG TTA ACC AAG CGC ATG TC-3'; m-β-actin FOR 5'-CTA AGG CCA ACC GTG AAA AG-3', m-β-actin REV 5'-ACC AGA GGC ATA CAG GGA CA-3'. Each sample analysis was performed in triplicate. As a negative control, a no template control was performed. The following PCR program was used: 95 °C for 30s, 40 cycles of denaturation at 95 °C for 15s and annealing/extension at 57 °C for 30s. In order to verify the specificity of the amplification, a melting curve analysis was performed immediately after the amplification protocol. qRT-PCR results were calculated using the ΔΔCt method and normalized using human or mouse β-actin as reference gene.

2.5 Immunofluorescence and confocal imaging

For confocal live cell staining, 2×105 NXS2 CTRL or NXS2 hLGALS3BP were plated on glass coverslips in 12-well plates and cultured under standard growth conditions. After 24 h, cells were incubated for 90 min at 37 °C with 10 µg/mL of anti-LGALS3BP antibody 1959 in PBS Ca2+/Mg2+ with 3% BSA. Cells were then fixed with 4% paraformaldehyde for 10 min at RT and stained with anti-human AlexaFluor-488 conjugated secondary antibody (1:200, #A11013; Invitrogen) and Hoechst3342 (1:500; Sigma-Aldrich) for 30 min at RT in the dark. Confocal images were acquired using a Zeiss LSM800 inverted confocal microscope system (Carl Zeiss, Germany).

2.5 Enzyme-linked immunosorbent assay (ELISA)

A total of 5×105 murine neuroblastoma cells were cultured in complete medium for 48 h were collected. Secreted human LGALS3BP levels were evaluated by sandwich ELISA that was performed as follows: Maxisorp 96-well plates (Nunc, Thermo-Fisher) were coated with murine anti-LGALS3BP antibody SP2 [22] [2 µg/mL] overnight at 4 °C. After blocking with 1% bovine serum albumin (BSA) in PBS for 1 h at RT, 100 µl of cell culture media were added and incubated for 1 h

a RT. After three washes with PBS-0.05% Tween20, humanized anti-LGALS3BP antibody 1959 [1 μg/mL] was incubated for 1 h at RT. For the detection, after three washes with PBS-0.05% Tween20, anti-human IgG-HRP (#A01070; Sigma-Aldrich) was added (1:5000) and incubated for 1 h at RT. After three washes, stabilized chromogen was added for at least 10 min in the dark before stopping the reaction with the addition of 1 N H2SO4. The resulting color was finally read at 450 nm with an ELISA plate reader (Tecan, Switzerland). Secreted mouse LGALS3BP levels were assessed by using mouse Galectin-3-Binding protein (LGALS3BP) ELISA kit according to manufacturer's instructions (#MBS9717790; MyBio Source, CA, USA). For the evaluation of serum and EVs-associated human LGALS3BP levels in human neuroblastoma pseudometastatic experiments, human LGALS3BP ELISA Kit was performed according to manufacturer's instructions (#KE00155; Proteintech, USA). In particular, EVs samples were isolated from mouse serum by using ExoQuick Exosome Precipitation Solution (#EXOQ5A-1; System Biosciences, CA, USA) according to manufacturer's instructions. Once isolated, EVs were quantified with Bradford assay (Biorad) and read in a 96-well plate reader (Tecan).

2.6 Extracellular vesicles (EVs) purification and analysis from cell culture media

Once reached the 80% confluence, NXS2 CTRL or NXS2 hLGALS3BP cells were grown for 48 h in serum-free medium. Around 100 mL of cell culture supernatant was collected, and differential ultracentrifugation was performed for EVs isolation. Briefly, supernatants were centrifuged at 2000 g and 10,000 g for 20 and 30 min, respectively, at 4 °C to remove dead cells and cellular debris. Then, to collect exosomes, supernatants were ultracentrifuged at 100,000 g for 70 min at 4 °C and then washed with PBS and re-collected by centrifugation at 100,000 g for 70 min at 4 °C. Protein content was quantified by Bradford assay (Biorad) prior to western blotting analysis, besides whole-cell lysates previously lysed in RIPA buffer as previously described. Blots were then probed with anti-human LGALS3BP (goat polyclonal; 1:1000, #AF2226; R&D Systems), anti-β-actin (mouse monoclonal; 1:40000, #A5441; Sigma-Aldrich), anti-Alix (mouse monoclonal; 1:500, #MA1-83977; Invitrogen), anti-Tsg101 (mouse monoclonal; 1:1000, #MA1-23296; Invitrogen).

2.7 Nanoparticle tracking analysis (NTA)

Size and concentration of EVs were characterized by nanoparticle tracking analysis (NTA) on a ZetaView system (Particle Metrix, Meerbusch, Germany) equipped with a blue laser (488 nm, 40 mW) and a long-pass emission filter. The autofocus was calibrated to ensure optimal particle visualization. Consistent and optimized post acquisition settings were applied throughout the analyses. Each sample was analyzed by capturing videos across 11 fields, with the resulting measurements compiled into reports detailing all relevant parameters, such as mean and median EV sizes.

2.8 Cytotoxicity assay

Murine neuroblastoma cells were cultivated into 24-well plates at a density of 8×103 cells per well under standard growth conditions. After 24 h, cells were treated for 72 h with increasing doses of SH-DM4 (from 0.00064nM to 250nM) or naked 1959-sss antibody (from 0.0064nM to 100nM). At the end of treatments, cells were incubated with 3-(4,5-dimethylthiazol-2-yl)-2,5-diphenyltetrazolium bromide (MTT) solution (medium serum-free with 0.5 mg/mL of MTT) for 2 h. After the

removal of the MTT solution, dimethylsulfoxide (DMSO) was added to each well and then the absorption value at 570 nm was measured using a multi-plate reader (Tecan). All experiments were performed in triplicate at least in two independent experiments. IC50 (Inhibition of cellular proliferation by 50%) values were calculated by using GraphPad Prism 9.0 software (GraphPad Software, Inc., CA, USA).

2.9 FACS analysis of ICD markers and PD-L1 levels

For the evaluation of surface ICD markers, 5×105 NXS2 cells were plated and treated or not with SH-DM4 (DM4) 5nM or Oxaliplatin (OXA) 60μM for 72 h in complete medium. All cells were harvested after 24, 48 and 72 h from treatment and labelled for 30 min in ice with the following primary antibodies: anti-mouse calreticulin (rabbit monoclonal; 1:800, #12238, clone D3E6; Cell Signaling Technology, USA), anti-mouse HSP70 (rabbit polyclonal; 1:400; #NBP1-77455; Novus Biologicals, USA), or anti-mouse HSP90 (mouse monoclonal; 1:100, #ADI-SPA-830, clone AC88; Enzo Life Sciences, USA). After washing, cells were labelled for 30 min at 4 °C in the dark with AlexaFluor-488 conjugated secondary antibodies (anti-mouse or anti-rabbit; 1:1000, #A28175 or #A27034; Thermo-Fisher). Samples were acquired by FACSCanto II cytometer (BD Biosciences) and analysis was performed using a BD FACSDiva v.8.0.3 (BD Biosciences). For the evaluation of PD-L1 levels, 5×105 NXS2 cells were plated and treated with DM4 3nM for 72 h. Cells were harvested and fixed for 15 min at RT with 4% paraformaldehyde. After washing, cells were permeabilized for 15 min at RT with 0.1% Triton X-100 and labelled for 30 min at 4 °C with primary antibody anti PD-L1 (rabbit polyclonal; 1:100, #PA5-20343; Invitro- gen). Then cells were labelled for 30 min at 4 °C in the dark with AlexaFluor-488 conjugated anti-rabbit secondary antibody (1:300, #A27034; Thermo-Fisher). Samples were acquired by FACSCanto II cytometer (BD Biosciences) and analysis was performed using a BD FACSDiva v.8.0.3 (BD Biosciences).

2.10 In Vivo mouse models and treatments

Human neuroblastoma pseudometastatic NSG mouse model NSG mice were purchased from Jackson Laboratory and bred in the animal facility of CAST, G. d'Annunzio University of Chieti. Animal care and experimental procedures were approved by the Ethics Committee for Animal Experimentation of the Institute according to Italian law (Authorization n° 1118/2020-PR). The animal health status was monitored daily, and body weight was measured once a week during experiments. For the evaluation of LGALS3BP levels in correlation with metastatic lesions, 8-weeks male NSG were tail-vein injected with 1×106 SKNAS cells and blood was collected after 7, 14, 21, or 28 days after injection. Blood was collected by intracardiac puncture immediately after mice sacrifice in a tube containing a glass Pasteur pipette to induce blood clotting. Serum was obtained after centrifugation of clotted blood samples at 3000 g for 15 min at 4 °C and stored at -80 °C. At the same time-points (7, 14, 21, or 28 days after injection), lungs, liver, and kidneys were harvested, fixed in 10% neutral buffered formalin, paraffin embedded, sectioned and properly stained.

2.11 Syngeneic murine neuroblastoma A/J mouse model

A/J female mice (5–6 weeks old) were purchased from Envigo (Bresso, Italy) and maintained at 22–24 °C under pathogen-limiting conditions. Mice were given a standard diet and water ad libitum and acclimatized for 2–3 weeks before the start of experiments. Housing and all procedures involving

the mice were performed according to the protocol approved by the Institutional Animal Care and Use Committee (Authorization n°385/2023-PR). For subcutaneous growth, 2×106 exponentially growing NXS2 CTRL or hLGALS3BP were s.c. inoculated into the right flank of the mice. Once tumors reached approximately 100 mm3 tumor volume, animals were randomly divided into groups and intravenously injected with vehicle (PBS), naked 1959-sss (10 mg/kg), or ADC 1959-sss/DM4 (10 mg/kg), or intra-peritoneally injected with anti-PD-1 (10 mg/kg). Doses and schedules are described in the individual figure legends. Mice were weighed twice weekly to monitor possible signs of toxicity. Tumor volume was monitored twice weekly by a caliper and calculated using the following formula: tumor volume (mm3) = (length x width2)/2. A tumor volume of 1-1.5 cm3 was chosen as humane endpoint for all experiments after which mice were sacrificed. Blood was collected just after mice sacrifice to obtain serum and tumors were collected in formalin and embedded in paraffin. For re-challenge experiments, 2×106 exponentially growing NXS2 CTRL cells were s.c. implanted into the left flank of A/J tumor naïve or cured mice. Tumor growth was monitored twice weekly, and tumor volumes were measured using a caliper. A tumor volume of 1-1.5 cm3 was chosen as humane endpoint for all experiments after which mice were sacrificed. Blood was collected just after mice sacrifice to obtain serum and tumors were collected in formalin and embedded in paraffin. For tumor immunoinfiltrate analysis, A/J female mice were implanted s.c. with 2 ×106 NXS2 hLGALS3BP cells into the right flank. Once tumors reached a volume of approximately 100 mm3, mice were randomly divided into three groups and intravenously treated with vehicle (PBS), naked 1959-sss (10 mg/kg), or ADC 1959-sss/DM4 (10 mg/kg). Two or four mice were treated once or twice, respectively, prior to being sacrificed at 72 h or 7 days from starting treatments and tumors collected for further analysis.

2.12 Tumor-infiltrating immune cells (TIIC) analysis in syngeneicneuroblastoma mouse model

For the evaluation of tumor-infiltrating immune cells (TIIC), mice were sacrificed and tumor collected after 72 h or 7 days after the first treatment administration. Tumors were weighed, cut into small pieces and enzymatically dissociated into gentleMACS C tubes (Miltenyi Biotec, Germany) with enzyme mix of mouse Tumor Dissociation Kit (#130-096-730; Miltenyi Biotec) by using a gentleMACS Octo Dissociator with Heaters (#130-096-427; Miltenyi Biotec) using 37C_m_TDK_1 dissociation program. Dissociated tumors were then passed through a 70 μm cell strainer and cell suspensions were centrifuged at 300 g for 7 min; red blood cells were lysed twice for 10 min at RT in agitation with Red Blood Cell lysis solution (#130-094-183; Miltenyi Biotec), then centrifuged at 1200 rpm for 10 min. Cells were counted and approximately 107 cells for each sample were incubated with mouse FcR blocking reagent (#130-092-575; Miltenyi Biotec) for 10 min in the refrigerator. Cell suspensions were stained for 30 min at 4 °C with LIVE/DEAD Fixable Near-IR fluorescent dye (#L34975; Invitrogen). For surface antigens staining, cells were incubated for 30 min at 4 °C in BD Brilliant Buffer (#563794; BD Biosciences) with the following antibodies from BD Biosciences: BV711 anti-mouse CD45 (#563709), BV605 anti-mouse CD3e (#563004), BV510 anti-mouse CD4 (#563106), RB705 anti-mouse CD8a (#570255), BV786 anti-CD11b (#569504), PE-CF594 anti-mouse CD49b (#562453), BV421 anti-mouse CD69 (#562920), RB780 anti-mouse CD11c (#755338). After washing, cells were fixed and permeabilized with BD Cytofix/Cytoperm Fixation/Permeabilization kit (#554714; BD Biosciences) according to manufacturer's instructions and then intracellularly labelled with APC anti-Granzyme B REAfinity (Miltenyi Biotec) for 30 min at 4 °C. After washing, cells were finally stained with SYTO16 (#S7578; Molecular Probes, Life

Technologies, Thermo-Fisher) for nucleated cells and acquired with a CytoFLEX cytometer (Beckman Coulter, USA). All antibodies and probes were titrated under assay conditions, to obtain optimal dilutions. Flow cytometer performance, stability, and data reproducibility were checked by using Daily QC Fluorospheres (#C65719, Beckman Coulter, USA). Compensations were calculated using Versa Comp Antibody Capture Kit (B22804, Beckman Coulter, USA) [23, 24].Carryover between samples was prevented by appropriate instrument cleaning at the end of each sample acquisition. In order to assess non-specific fluorescence, fluorescence minus one samples (FMO) were used. Samples were analyzed using FlowJo v. 10.10 (BD Biosciences). Boolean gates were used to identify all cell subpopulations.

2.12 1959-sss/DM4 conjugation and characterization

1959-sss antibody (MediaPharma Srl, Italy), previously described (US 2008/0305044 A1) [22, 25], was reduced with a 60-fold molar excess of TCEP (Tris(2-carboxy-ethyl)phosphine; Thermo Fisher Scientific) in phosphate-buffered saline (PBS, pH 7.4; Sigma-Aldrich). The reaction was carried out overnight at RT. To stabilize the reduced antibody and prevent precipitation, 100 mM phosphate buffer (pH 7.4) was added. The reduced antibody was then incubated with a 100-fold molar excess of DTNB (5,5′-Dithiobis(2-nitrobenzoic acid); Sigma-Aldrich) overnight at RT. The reaction was quenched by passing the 1959-sss/DTNB mixture through a G25 Sephadex column pre-equilibrated with PBS containing 5% sucrose and 10% DMA (N, N′-dimethylacetamide; Sigma-Aldrich). The DTNB-modified 1959-sss antibody was subsequently reacted with a 10-fold molar excess of thiol-maytansinoid DM4-SH (MedChemExpress) in the same buffer system overnight at RT. The reaction was terminated by adding a 500-fold molar excess of iodoacetamide (Sigma-Aldrich). Unreacted maytansinoid was removed by passing the mixture through a G25 Sephadex column equilibrated with PBS/5% sucrose/10% DMA at a flow rate of 1 ml/min. The final concentration of the ADCs was determined by UV-VIS spectrophotometry using an extinction coefficient of $\varepsilon 280=1.6\ M^{-1}\ cm^{-1}$. All ADC products were analyzed by SDS-PAGE and Hydrophobic Interaction Chromatography (HIC). Both the naked 1959-sss antibody and the ADCs were analyzed using a MabPac HIC-Butyl column (Thermo Fisher Scientific) equilibrated in 1.5 M ammonium sulfate, 5% isopropanol, and 50 mM sodium phosphate (pH 7.0). Elution was achieved with a linear gradient from 0 to 100% 50 mM sodium phosphate (pH 7.0) with 20% isopropanol at a flow rate of 1 ml/min. The Drug-Antibody Ratio (DAR) was calculated to be 1,6.

2.13 Immunohistochemistry (IHC)

Sections were immunostained with anti-human LGALS3BP antibody (#AF2226, R&D). Microwave pre- treatment (10 min) in citrate buffer (pH 6.0) was performed for antigen retrieval. The biotinylated horse anti-goat IgG secondary antibody (BA-9500, Vector Laboratories) and the HRP Detection IHC kit (ab93677, Abcam) were used to detect the antigen. After incubation with the chromogen 3,3-diaminobenzidine DAB (K3468, Dako), slides were counterstained in Hematoxylin (CATHE-MM, Biocare Medical) and scanned with Nanozoomer scanner from Hamamatsu. Images were acquired with NDP.view 2 software.

2.14 Statistical analysis

IC50 values were calculated by using GraphPad Prism 9.0 software (GraphPad Software, Inc., San Diego, CA, USA). For FACS analysis of ICD markers and PD-L1 levels, p values were determined by unpaired Student's t test and $p < 0.05$ was considered as statistically significant. Statistical differences between experimental groups in the *In Vivo* analysis of TILs were determined by unpaired Student's t test and $p < 0.05$ was considered as statistically significant. For Kaplan-Meier survival analysis, a Log-rank (Mantel-Cox) test was used to compare each of the groups. All statistical analysis was performed with GraphPad Prism 9.0 software.

3. Results

3.1 Circulating LGALS3BP correlates with neuroblastoma dissemination in a pseudometastatic model

We recently demonstrated that LGALS3BP is largely expressed and secreted by neuroblastoma cells mainly through the release of cancer-associated extracellular vesicles [26]. We therefore wondered whether the circulating protein could be used as a biomarker of this tumor. To this aim, we employed a pseudometastatic mouse model in which LGALS3BP highly expressing human neuroblastoma SKNAS cells were tail-vein injected into mice. Following the experimental scheme shown in Fig. 1A, we were able to detect circulating LGALS3BP, both as associated to EVs and as free protein in serum collected from tumor bearing mice (Figs. 1B). Interestingly, we found a strong correlation trend over time between circulating LGALS3BP and the number of SKNAS-induced metastatic lesions in liver, lungs and kidneys (Fig. 1C-F). On the contrary, circulating LGALS3BP was undetectable in tumor-free (TF) mice and in SKNAS-injected mice after 7 days (Fig. 1B), consistently with the absence of metastatic lesions in the examined organs (Fig. 1C-F). Next, we evaluated the potential of circulating LGALS3BP as an early detection biomarker for neuroblastoma. We focused on an early time-point, corresponding to 14 days after inoculation of SKNAS cells, in the same pseudometastatic mouse model used before. As shown, we successfully detected EVs-associated LGALS3BP (Figs. 2A-B) and circulating LGALS3BP (Fig. 2C) in serum with high sensitivity given the detection of LGALS3BP levels even in the presence of a minimal number of metastases. In addition, these levels tightly correlated with the number of neuroblastoma lesions observed in mouse organs, with a greater number of metastases identified in the liver and lungs compared to those found in the kidneys (Figs. 2D–F), a result consistent with the higher tropism of SKNAS cells for these organs. As expected, no levels of LGALS3BP were measurable in TF mice. These findings indicate that circulating LGALS3BP levels could serve as a reliable biomarker for neuroblastoma, given the strong correlation observed with the presence of metastases.

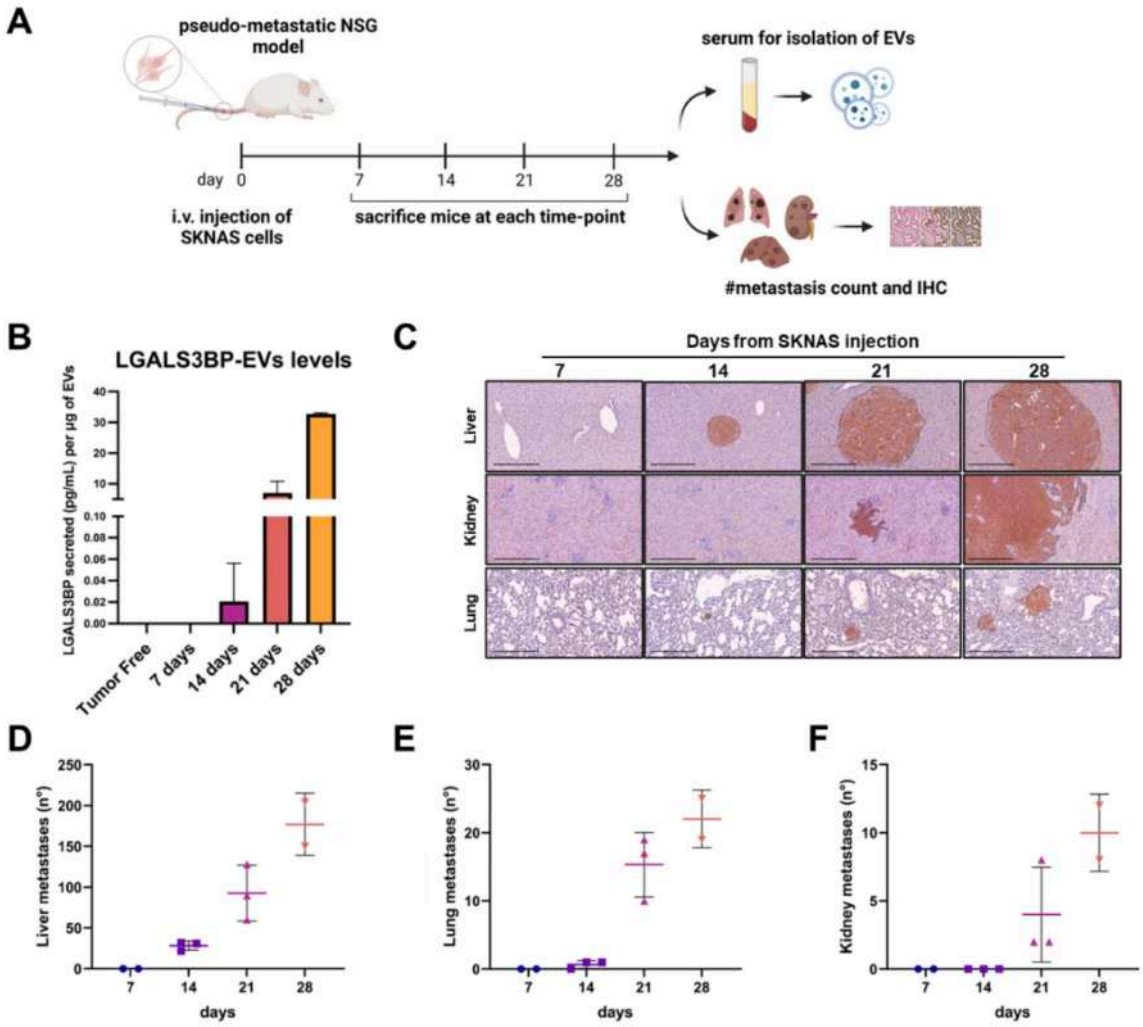


Fig. 1: EVs-associated LGALS3BP levels correlate with metastatatic lesions and increase accordingly over time in a pseudometastatic model of human neuroblastoma. (A) Representative scheme of pseudometastatic model: human neuroblastoma SKNAS cells were tail-vein injected in NSG mice and blood was collected after 7 (n=2), 14 (n=3), 21 (n=3), and 28 (n=2) days. (B) EVs-associated LGALS3BP levels detected in ELISA (pg/mL) per µg of EVs isolated from mouse serum after 7 (n=2), 14 (n=3), 21 (n=3), or 28 (n=2) days. Tumor free mice (n=2) were considered as controls. (C) Immunohistochemistry staining with hematoxylin/eosin for metastatic lesions and LGALS3BP levels in metastatic lesions over time. Scale bar: 250 µm. Number of metastases detected in (D) liver, (E) lung, and (F) kidney of NSG mice after 7 (n=2), 14 (n=3), 21 (n=3), and 28 (n=2) days

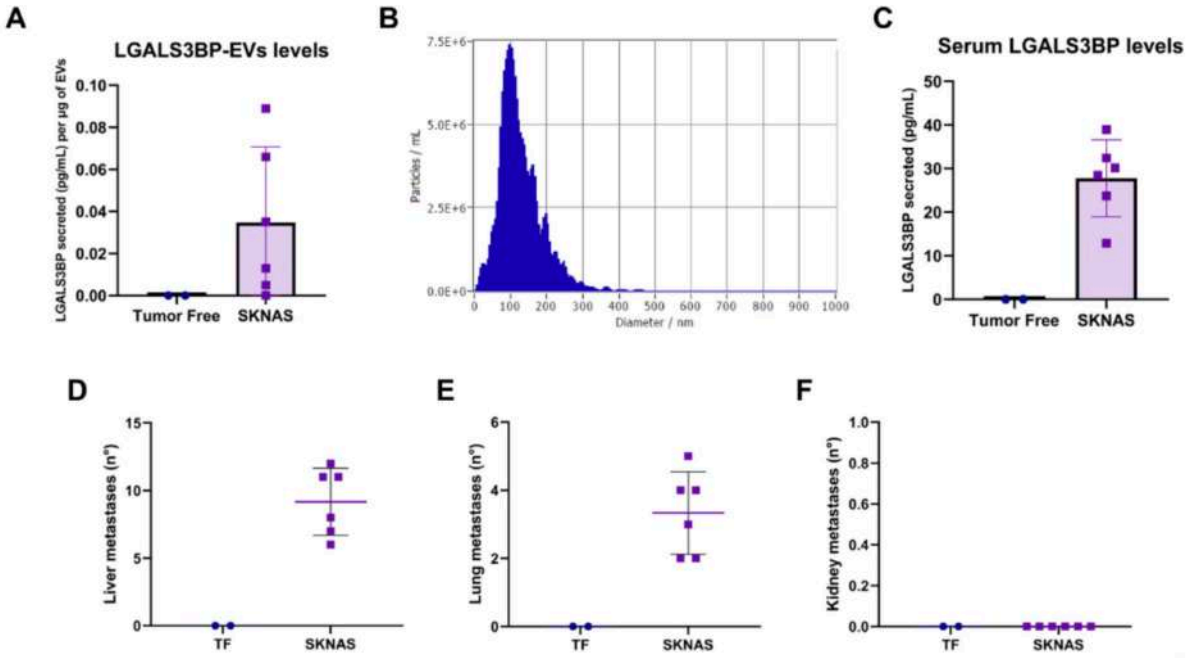


Fig. 2: Circulating and EVs-associated LGALS3BP could function as early detection biomarker of neuroblastoma lesions in a human neuroblastoma pseudometastatic model. (A) EVs-associated LGALS3BP levels detected in ELISA (pg/mL) per µg of EVs isolated from mouse serum collected 14 days after NSG mice (n=6) were tail-vein injected with human neuroblastoma SKNAS cells. Tumor free mice (n=2) were considered as controls. (B) Representative NTA profile of EVs isolated from mouse serum after 14 days from tail-vein injection of SKNAS cells. (C) Circulating LGALS3BP levels detected in ELISA (pg/mL) inmouse serum (diluted 1:4) after 14 days (n=6). Tumor free mice (n=2) were considered as controls. Number of metastases detected in (D) liver, (E) lung, and (F) kidney of NSG at 14 days post-injection

3.2 Establishment of a murine neuroblastoma cell model with overexpression of human LGALS3BP

The potential of LGALS3BP as a therapeutic target was next investigated. We previously showed that 1959-sss/DM4, an ADC targeting LGALS3BP, was able to halt neuroblastoma growth in several preclinical models [26]. Here, we analyzed the therapeutic activity of this ADC when combined with immunotherapy. First, we generated a syngeneic model by engineering neuroblastoma NXS2 cells through lentiviral transduction. The resulting cell lines were characterized as control (empty vector) or hLGALS3BP. While endogenous expression of murine LGALS3BP was barely detectable in both cell lines, NXS2 hLGALS3BP cells showed a marked overexpression of the protein, as evaluated by mRNA and protein analysis (Fig. 3A-C). Of note, expression level of the secreted protein was comparable to those of LGALS3BP-high-expressing human cancer cell lines [25–27] (Fig. 3D). At confocal microscopy, the anti-LGALS3BP antibody 1959 intensively and specifically labeled the cell surface/milieu of hLGALS3BP-expressing cells, with no staining in control cells (Fig. 3E). Consistently, EVs isolated from hLGALS3BP-expressing cells showed prominent expression of human LGALS3BP, which was absent in EVs obtained from the control cell line (Fig. 3F).

3.3 Cytotoxic payload DM4 induce ICD and PD-L1 expression in murine neuroblastoma cells

To verify NXS2 sensitivity to ravtansine DM4, a cell killing assay was performed. As shown in Fig. 4, this maytansine-derivative cytotoxic compound used as payload for building the anti-LGALS3BP ADC exhibits a potent cytotoxic activity with an IC50 in the nanomolar range (0.32 nM), which was the same in both control and hLGALS3BP-expressing cells (Fig. 4A left panel). In contrast, no cytotoxicity was observed in cells treated with the naked 1959 antibody (1959-sss) (Fig. 4A right panel). The ability of DM4 to induce ICD was evaluated using a sub-lethal drug concentration chosen from the previous IC50 curves. For these experiments, NXS2 cells were exposed to 5nM DM4 for 72 h or to 60μM oxaliplatin (OXA) as the ICD-inducer for 48 h, and the expression levels of calreticulin, HSP70, and HSP90 analyzed by flow cytometry. Interestingly, all three ICD markers were significantly upregulated, indicating that DM4 induces ICD in this neuroblastoma cell model (Fig. 4B-D). To gain insight into the potential mechanism of resistance of neuroblastoma cells through the modulation of immune check-point proteins, we analyzed expression of PD-L1 in NXS2 control and hLGALS3BP cells in response to treatment with DM4. A significant upregulation of PD-L1 surface expression in both cell lines was observed, confirming the ability of DM4 to induce a potential resistance mechanism (Fig. 4E).

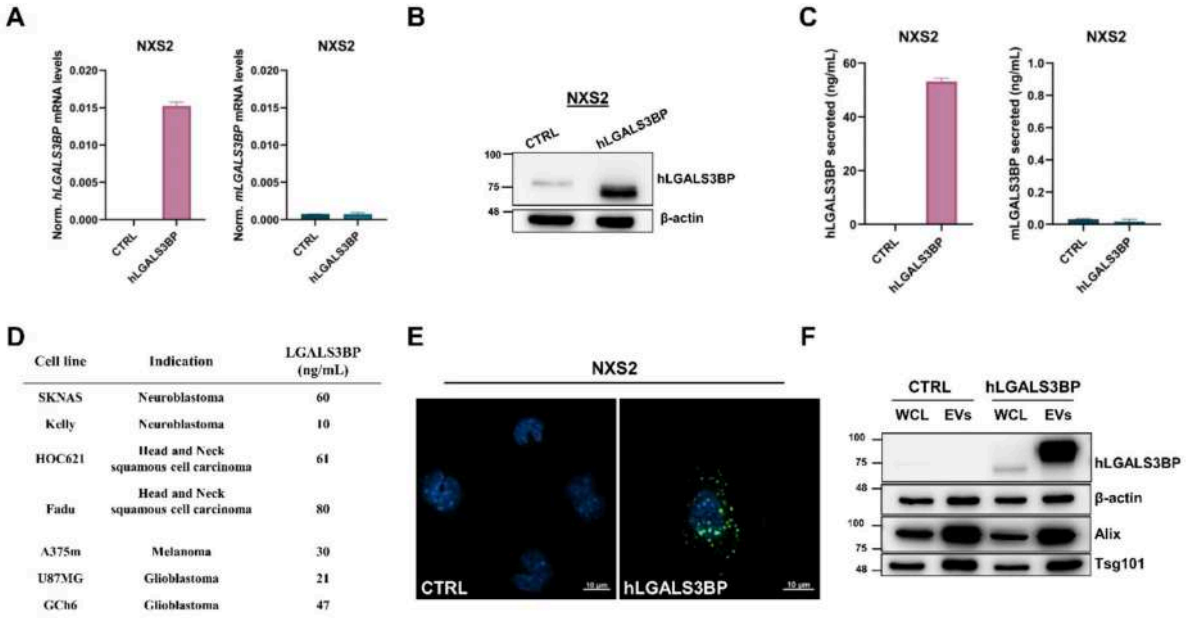


Fig. 3: Human LGALS3BP is overexpressed and secreted by engineered murine neuroblastoma NXS2 hLGALS3BP cells. (A) Histograms showing transcriptional levels of human (hLGALS3BP) and murine (mLGALS3BP) LGALS3BP in NXS2 CTRL and hLGALS3BP cells normalized to housekeeping gene (β-actin). Values refer to two independent biological replicates. (B) Western blotting images showing intracellular protein levels of hLGALS3BP in NXS2 CTRL and hLGALS3BP cells. Equal amounts of protein were loaded for each sample. β-actin was used as loading control. Images are representative of two independent biological replicates. (C) Secreted levels (ng/mL) of hLGALS3BP and mLGALS3BP assessed by ELISA assay in NXS2 CTRL and hLGALS3BP cells. Values refer to two independent biological replicates. (D) Table showing secreted LGALS3BP expression level in a panel of human cancer cell lines. (E) Confocal imaging of NXS2 CTRL and hLGALS3BP cells showing LGALS3BP (green) and nuclei (Hoechst). Scale bar: 10 μm. (F) Immunoblot showing EVs-associated hLGALS3BP and positive/negative exosomal markers expression in

whole cell lysates (WCL) or EVs isolated from NXS2 CTRL or hLGALS3BP. Equal amount of protein were loaded for each sample.

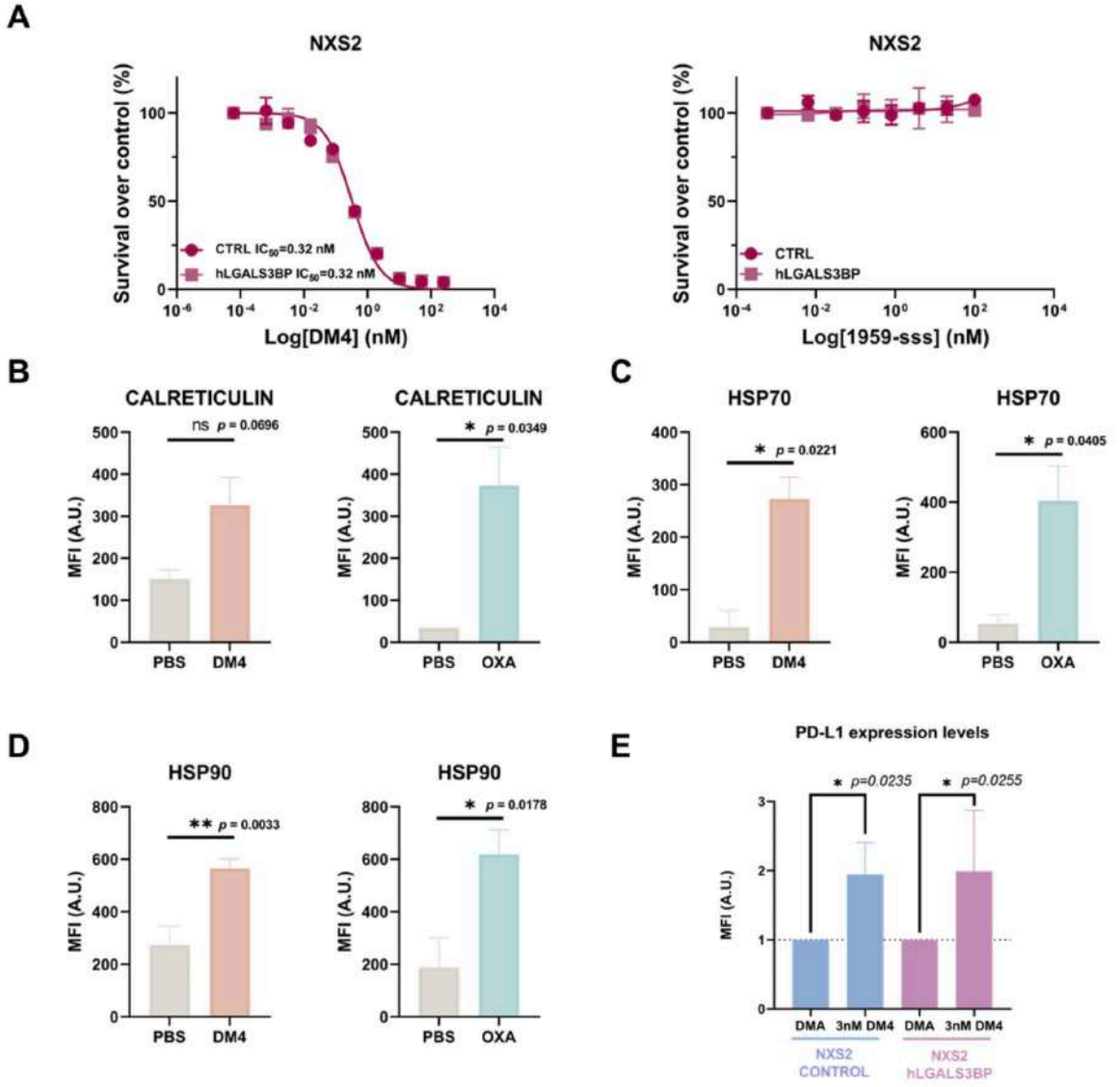


Fig. 4: NXS2 cells are susceptible to the cytotoxic payload DM4 and expose immunogenic cell death (ICD) markers after treatment with DM4, which may also induce tumor resistance in NXS2 cell lines by upregulation of PD-L1. (A) *In Vitro* IC50 curves assessed through cytotoxicity assays by exposing for 72 h NXS2 CTRL and hLGALS3BP cells to increasing doses of payload DM4 (left panel) or naked 1959-sss antibody (right panel). IC50 values are reported for each cell line considered upon the different treatments. Values refer to two independent biological replicates. Surface levels of ICD markers (B) calreticulin, (C) HSP70, and (D) HSP90 expressed as mean fluorescence intensity (M.F.I.) signals evaluated through FACS analysis on NXS2 cells treated or not with DM4 5nM for 72 h or with Oxaliplatin (OXA) 60μM for 48 h. Asterisks indicate statistical significance through unpaired t-test compared to each experimental time control (PBS); *p < 0.05, **p < 0.01. Exact p-values are reported. Values refer to two or three independent biological replicates. (E) Surface levels of PD-L1 evaluated through FACS analysis expressed as fold change of mean fluorescence intensity (M.F.I.) signals of treated samples over controls of NXS2 control and hLGALS3BP cells treated with 3nM DM4 or with DMA (control) for 72 h. Asterisks indicate statistical significance through unpaired t-test compared to

each experimental control (DMA); *p < 0.05. Exact p-values are reported. Values refer to three independent biological replicates

3.4 Anti-LGALS3BP ADC induces shrinkage of neuroblastoma tumors and the recruitment of activated TILs

Next, we wondered whether the antitumor activity of LGALS3BP ADC was maintained in the syngeneic model and, more importantly, whether it was specific for cells expressing the target. We set the ADC dosage at 10 mg/kg twice weekly as the most effective anti-tumor dosage based on our previous works [5, 25, 26, 28]. ADC treatment resulted in a significant shrinkage of hLGALS3BP-expressing tumors, which was accompanied by an increased survival, but not of control-derived tumors (Fig. 5A and B). However, this effect was not sustained over time, as tumor regrowth was observed two weeks following the final treatment. To determine whether the therapeutic response could be improved by combining the ADC with immunotherapy, we first analyzed the composition of the tumor infiltrate in animals treated with two doses of the ADC after 7 days from starting of treatments. The analysis was conducted within the time window corresponding to the maximum response to the drug. As shown in Fig. 5C, NXS2-hLGALS3BP tumors treated with anti-LGALS3BP ADC displayed a significant increase in activated tumor-infiltrating T lymphocytes (TILs), as evidenced by flow cytometry analysis of CD69+/CD45+CD3+ cells. Furthermore, ADC-treated tumors showed a marked enhancement in the CD8+/CD69+ and CD8+/ CD69+ / Granzyme B+ cell subpopulation frequencies, which represents the primary T-cell population involved in the anti-tumor immune response.

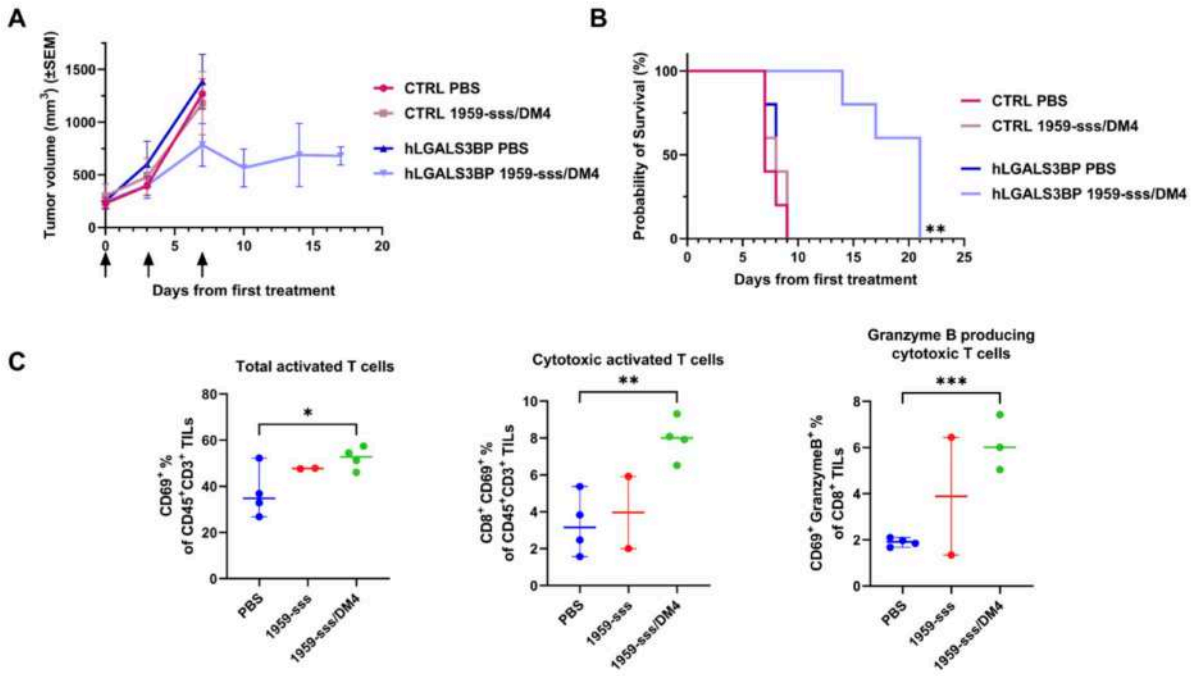


Fig. 5: Targeted and effective anti-tumor activity of anti-LGALS3BP ADC 1959-sss/DM4 in murine syngeneic neuroblastoma model. (A) Tumor growth expressed as tumor volume (mm3) from first treatment of NXS2 CTRL or hLGALS3BP allografts in syngeneic A/J mice treated or not with ADC 1959-sss/DM4 (10 mg/kg;

twice weekly; three total i.v. injections). Arrows indicate treatments administration. 4 or 5 mice per group were considered. (B) Kaplan-Meier curve showing probability of survival in percentage of mice bearing NXS2 CTRL or hLGALS3BP allografts treated or not with ADC 1959-sss/DM4 from first treatment. Log-rank (Mantel-Cox) test: ** $p < 0.01$. (C) TILs flow cytometric analysis of PBS (n=4), 1959-sss (n=2) and 1959-sss/DM4 (n=4) treated tumors at 7 days after starting treatments, showing percentage of activated CD69+ within the total population of CD3+ T cells (left panel); percentage of activated CD8+ CD69+ within the total population of CD3+ T cells (middle panel). In the right panel is shown the percentage of CD69+ Granzyme B+ over cytotoxic CD8+ T cells. Differences were compared using unpaired T test, and considering significant $p < 0.05$, as indicated with an asterisk (* $p < 0.05$, **$p < 0.01$, *** $p < 0.001$)

3.5 Anti-LGALS3BP synergizes with anti-PD-1 immunotherapy promoting durable anti-tumor activity

These findings provided a rationale for evaluating the effect of combination therapy of the ADC with an immune check-point inhibitor. In this respect, we decided to test 1959-sss/DM4 in combination with immune check-point inhibitor anti-PD-1, with a six-arm therapeutic trial comparing the effects of monotherapy with those of the combination of ADC and anti-PD-1 on NXS2-hLGALS3BP-derived tumors. We used the same ADC dosage of the previous therapeutic experiment (10 mg/kg, twice weekly) while we built anti-PD-1 treatments schedule by setting dosage at 10 mg/kg with two injections per week based on other prior combination immunotherapy works [29–31]. A significant enhancement of antitumor activity was observed in mice treated with the combination therapy compared to those treated with the single agents, which resulted in prolonged survival up to 60 days from the start of treatment (Fig. 6A-B). Of note, in the combo group, 4 out of 6 mice were cured after 60 days from the start of the treatment. To verify whether these cured mice still possessed immune memory against the tumor, we used them as rechallenge models (Fig. 7). We injected parental NXS2 cells in the 4 cured mice and as control in two "naïve" animals. Tumors in the cured mice exhibited slower growth and reduced attachment efficiency compared to those in naïve mice, as evidenced by smaller tumor volumes 14 days post-injection and the failure of one tumor in the cured group to attach and grow. All these observations strongly suggest that the cured mice may possess a stronger or more efficient immune response that contributed to controlling tumor growth (Fig. 7B). Moreover, a significant response, marked by initial tumor shrinkage, was observed in mice bearing tumors when treated with anti-PD-1 therapy (administered in three doses) (Fig. 7), indicating that these mice had a heightened or 'primed' immune state due to the earlier treatment, which made them more responsive to the immune check-point blockade therapy compared to naïve mice treated in the previous experiment (Fig. 6A).

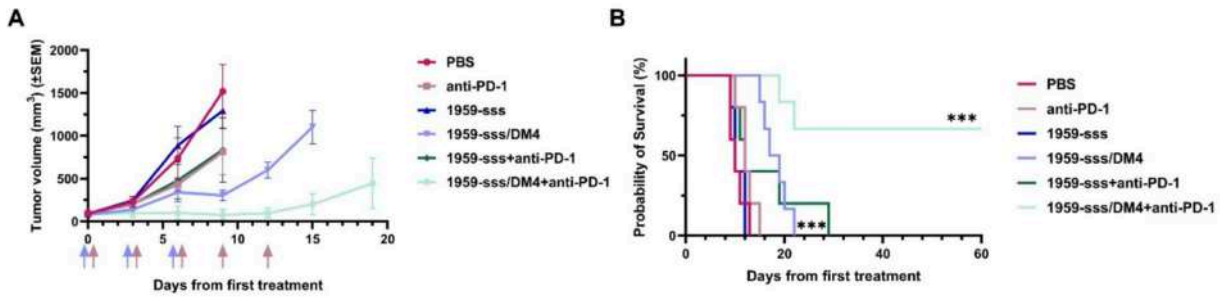


Fig. 6: Synergistic and durable anti-tumor activity of combination therapy based on anti-LGALS3BP ADC 1959-sss/DM4 and immune check-point inhibitor anti-PD-1 in murine syngeneic neuroblastoma model. (A) Tumor growth expressed as tumor volume (mm3) from first treatment of NXS2 hLGALS3BP allografts in syngeneic A/J mice treated or not with anti-PD-1 (10 mg/kg; twice weekly; five total i.p. injections), naked 1959-sss (10 mg/kg; twice weekly; three total i.v. injections), ADC 1959-sss/DM4 (10 mg/kg; twice weekly; three total i.v. injections), or combination of 1959-sss and anti-PD-1, or combination of 1959-sss/DM4 and anti-PD-1. Blue and pink arrows indicate 1959-sss or 1959-sss/DM4 and anti-PD-1 treatments administration, respectively. 5 or 6 mice were considered per experimental group. (B) Kaplan-Meier curve showing probability of survival of mice bearing NXS2 hLGALS3BP allografts treated or not with anti-PD-1, 1959-sss, ADC 1959-sss/DM4, combination of 1959-sss and anti-PD-1, or combination of 1959-sss/DM4 and anti-PD-1 from first treatment. Log-rank (Mantel-Cox) test: *** $p < 0.001$

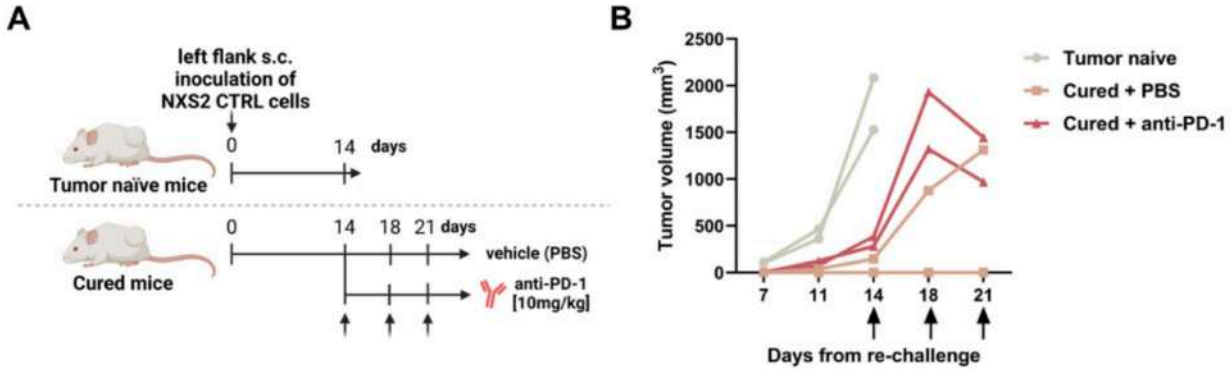


Fig. 7: Cured mice displayed superior tumor growth control compared to naïve animals. (A) Representative scheme of rechallenge experiment. Cured mice are those animals that show complete tumor regression from combination therapy with 1959-sss/DM4 + anti-PD-1. (B) Tumor growth expressed as tumor volume (mm3) from rechallenge of NXS2 CTRL allografts in tumor naïve mice, cured mice treated with PBS, or cured mice treated with anti-PD-1. Arrows indicate administration of vehicle (PBS) or anti-PD-1 (10 mg/kg; twice weekly; three total i.p. injections). Two mice were considered per experimental group and curves reported refer to tumor growth of allografts of each single animal considered per group

4. Discussion

Neuroblastoma is often driven by specific genetic mutations and remains extremely challenging to treat [32]. Children with this aggressive form of the disease typically undergo intensive therapies, which are not always successful [33]. Tragically, nearly half of these patients do not survive beyond the age of five. For survivors, the lifesaving but harsh treatments frequently result in permanent side effects, significantly impacting their quality of life [34]. These challenges underscore the urgent need for more effective therapies and the development of novel targeted approaches, combined with reliable biomarkers for disease monitoring. In this study, we investigated the potential of LGALS3BP protein as a disease biomarker. Our results demonstrate that circulating LGALS3BP can serve as an effective liquid biopsy biomarker for detecting the presence of the disease. Additionally, we show that an ADC-based therapy displays a synergistic effect when combined with an immune check-point inhibitor, holding promising clinical relevance for neuroblastoma treatment. Our group, along with

others, has identified LGALS3BP as a driver of tumor progression in various cancers, including neuroblastoma, due to its role in sustaining cancer proliferation, modulating cell motility and adhesion within the tumor microenvironment, and promoting angiogenesis (reviewed by Capone et al. [16]). Previous studies investigating protein downregulation have demonstrated that these mechanisms are significantlyreduced or impaired, further reinforcing the notion that LGALS3BP plays an active role in tumor progression [35–39]. Importantly, LGALS3BP was found as a critical mediator in the interaction between neuroblastoma cells and the TME [18, 19]. LGALS3BP is a predominant surface component of cancer-derived EVs. These EVs play a significant role in shaping a particular type of TME that promotes cancer progression to which they also contribute by facilitating immune escape, stimulating angiogenesis, and preparing the pre-metastatic niche [40]. This evidence underscores LGALS3BP's involvement in neuroblastoma pathophysiology, making it a compelling target for therapeutic intervention and a valuable biomarker for monitoring disease dynamics. Using a neuroblastoma pseudometastatic preclinical model, we demonstrate that EVs-associated LGALS3BP correlates with disease progression and dissemination. These findings align with a recent study by Morini and colleagues, which reported upregulation of LGALS3BP in extracellular vesicles isolated from high-risk neuroblastoma patients compared to controls [41]. Moreover, we found that 1959-sss/DM4 LGALS3BP ADC possesses immune-modulating properties, by showing that ravtansine DM4 is able to induce ICD. Our findings clearly highlight the potential of ADC/immune check-point combination strategy in neuroblastoma. Recently, Pasto et al. showed that pyrrolobenzodiazepine (PBD)-based GD2 ADC induces ICD mainly by reprogramming tumor milieu. In our setting, a DM4-armed anti-LGALS3BP ADC is directed against a vesicular highly glycosylated protein which is enriched at the tumor surface and in stroma. 1959-sss/DM4 is a linker-less ADC with a fixed DAR around 2, which has demonstrated potent antitumor activity against different malignancies, including melanoma, neuroblastoma, glioblastoma and adenoid cystic carcinoma [5, 25, 26, 28]. Importantly, this ADC has demonstrated potent, target-dependent antitumoractivity and high tolerability in multiple mouse preclinical models [5, 25, 26, 28]. Furthermore, previous exploratory toxicology studies in rabbits, where the 1959 antibody cross-reacted with endogenous LGALS3BP protein, reported no mortality or treatment-related toxicity [25]. To highlight the ADC's ability to modify the immune landscape of treated tumors, we employed the A/J syngeneic model. As a cellular model, we engineered murine neuroblastoma NXS2 cells to overexpress the human LGALS3BP protein. This step was essential to establish a reliable preclinical model because: (i) murine neuroblastoma cells inherently express very low levels of the ADC target, and (ii) the 1959 monoclonal antibody does not cross-react with murine LGALS3BP. One of the aims of the present study was to evaluate whether DM4 payload possesses the capacity to induce ICD in the context of neuroblastoma. To date, there is only one study addressing this specific matter [42]. ICD is a widely investigated mechanism in ADC therapy, as strong immune modulation induced by the payload provides a compelling rationale for combining ADCs with ICIs. In our syngeneic model, ADC treatment resulted in a substantial increase in tumor-infiltrating lymphocytes (TILs) within the tumor tissue. Notably, treatment with the anti-LGALS3BP ADC resulted in a significant enrichment of activated cytotoxic T-lymphocytes (CD69+/GranzymeB+subpopulation) in tumor tissue, strongly supporting the potential for enhancing ADC activity through immunotherapy. Indeed, the combination of the ADC with anti-PD-1 resulted in a significant boost of antitumor activity with prolonged survival of treated mice. Four out of six mice treated with the combination therapy remained tumor-free 60 days after the start of treatment, whereas animals in the control group reached the tumor growth cut-off value by day 15. Using a rechallenge model, we tested whether cured mice had developed immune memory against the tumor. Importantly, we observed two key phenomena: (i) tumor growth was significantly delayed in 'cured' mice compared to naïve animals, indicating the

presence of immune memory; and (ii) tumors in these mice exhibited increased sensitivity to anti-PD-1 monotherapy, suggesting an enhanced antitumor immune response. This suggests that these mice had a heightened or 'primed' immune state due to the earlier treatment, which made them more responsive to the immune check-point blockade therapy compared to naïve mice (as shown in Fig. 6A). This implies that immune memory induced by the ADC facilitated a more effective immune response upon reactivation with anti-PD-1 therapy. This reinforces the idea that initial treatment with the ADC, which is followed by ICD induction, can prime the immune system and enhances the efficacy of subsequent immunotherapy. However, the intrinsic limitations of these experimental settings must be considered, as we are forcing a system in which a human protein interacts with a murine TME, which may not fully reflect the dynam- ics of a patient's TME. Nevertheless, this is a common limitation of all preclinical models used to evaluate the impact of immunotherapies on TME immune cells. Although these preclinical findings are encouraging, many challenging issues need to be addressed for ADC clinical translation. One potential issue is the emergence of ADC resistance, which can arise through various mechanisms, including antigen-related resistance, disruptions in ADC trafficking pathways, overexpression of drug transporter proteins, and other adaptive processes. To date, there are two FDA-approved antibody maytansinoid conjugates (AMCs) and several others on preclinical development [43]. However, such in the case of trastuzumab emtansine (T-DM1), dysfunctional intracellular processing of T-DM1 or altered DM1-induced cell death due to higher drug efflux or mutations in DM1 molecular targets were all reported as maytansinoid-related resistance mechanisms [44]. Similarly, DM4-armed ADC resistance could arise for the same reasons. In this context, combination therapies might improve the design of therapeutic strategies to limit resistance issues. As a supporting tool, the discovery of biomarkers able to monitor the therapeutic response and the possible onset of resistance mechanisms could be useful. In relation to this, an intriguing aspect of anti-LGALS3BP therapy with ADCs is the potential use of circulating protein levels as a biomarker to monitor therapeutic response. Furthermore, we recently demonstrated that this ADC, labelled with Zirconium-89, effectively visualized LGALS3BP-secreting tumors in preclinical models using PET imaging. Therefore, it has the potential to serve as a companion theranostic for identifying patients most likely to respond to LGALS3BP-targeted therapeutics, such as 1959-sss/DM4 [45]. In sum, this study highlights two aspects of LGALS3BP which have an important role in neuroblastoma: (i) the ability to act as a circulating biomarker and (ii) the potential to serve as a therapeutic target in strategies combining ADC therapy with immunotherapy. Both these aspects warrant further exploration.

Funding

This work was supported by Fondazione-AIRC: GS [IG 2021 id 25696].

References

[1]. Pieniążek B, et al. Neuroblastoma, A review of combination immunotherapy. Int J Mol Sci. 2024;25(14):7730.

[2]. DuBois SG, Macy ME, Henderson TO. High-Risk and relapsed neuroblastoma: toward more cures and better outcomes. Am Soc Clin Oncol Educ Book. 2022;42:1–13.

[3]. Weiser DA, et al. Progress toward liquid biopsies in pediatric solid tumors. Cancer Metastasis Rev. 2019;38(4):553–71.

[4]. Trigg RM, Shaw JA, Turner SD. Opportunities and challenges of Circulating biomarkers in neuroblastoma. Open Biol. 2019;9(5):190056.

[5]. Dufrusine B et al. Extracellular LGALS3BP: a potential disease marker and actionable target for antibody-drug conjugate therapy in glioblastoma. Mol Oncol, 2023.

[6]. Zhuo Z, et al. Advances in liquid biopsy in neuroblastoma. Fundam Res. 2022;2(6):903–17.

[7]. Kalluri R, LeBleu VS. The biology, function, and biomedical applications of exosomes. Science, 2020. 367(6478).

[8]. Krystal J, Foster JH. Treatment of High-Risk neuroblastoma. Children. 2023;10(8):1302.

[9]. Davis KL, et al. Nivolumab in children and young adults with relapsed or refractory solid tumours or lymphoma (ADVL1412): a multicentre, open-label, single-arm, phase 1–2 trial. Lancet Oncol. 2020;21(4):541–50.

[10]. Grobner SN, et al. The landscape of genomic alterations across childhood cancers. Nature. 2018;555(7696):321–7.

[11]. Apps JR, et al. The immune environment of paediatric solid malignancies: evidence from an immunohistochemical study of clinical cases. Fetal Pediatr Pathol. 2013;32(4):298–307.

[12]. Wienke J, et al. The immune landscape of neuroblastoma: challenges and opportunities for novel therapeutic strategies in pediatric oncology. Eur J Cancer. 2021;144:123–50.

[13]. Pascual-Pasto G, et al. GPC2 antibody–drug conjugate reprograms the neuroblastoma immune milieu to enhance macrophage-driven therapies. J Immunother Cancer. 2022;10(12):e004704.

[14]. Zhang L, et al. Antibody–drug conjugates and immune checkpoint inhibitors in cancer treatment: a systematic review and meta-analysis. Sci Rep.2024;14(1):22357.

[15]. Galluzzi L, et al. Immunogenic cell death in cancer: concept and therapeutic implications. J Translational Med. 2023;21(1):162.

[16]. Capone E, Iacobelli S, Sala G. Role of galectin 3 binding protein in cancer progression: a potential novel therapeutic target. J Transl Med. 2021;19(1):405.

[17]. Nakata R, et al. Contribution of neuroblastoma-derived exosomes to the production of pro-tumorigenic signals by bone marrow mesenchymal stromal cells. J Extracell Vesicles. 2017;6(1):1332941.

[18]. Silverman AM, et al. A galectin-3-dependent pathway upregulates inter- leukin-6 in the microenvironment of human neuroblastoma. Cancer Res. 2012;72(9):2228–38.

[19]. Fukaya Y, et al. Identification of galectin-3-binding protein as a factor secreted by tumor cells that stimulates interleukin-6 expression in the bone marrow stroma. J Biol Chem. 2008;283(27):18573–81.

[20]. Greene LA, et al. Neuronal properties of hybrid neuroblastoma X sympathetic ganglion cells. Proc Natl Acad Sci U S A. 1975;72(12):4923–7.

[21]. Campeau E, et al. A versatile viral system for expression and depletion of proteins in mammalian cells. PLoS ONE. 2009;4(8):e6529.

[22]. Traini S, et al. Inhibition of tumor growth and angiogenesis by SP-2, an anti-lectin, galactoside-binding soluble 3 binding protein (LGALS3BP) antibody. Mol Cancer Ther. 2014;13(4):916–25.

[23]. Lanuti P et al. Picture of the favourable immune profile induced by Anti-SARS-CoV-2 vaccination. Biomedicines, 2021. 9(8).

[24]. Lanuti P, et al. A standardized flow cytometry network study for the assessment of Circulating endothelial cell physiological ranges. Sci Rep.2018;8(1):5823.

[25]. Giansanti F, et al. Secreted Gal-3BP is a novel promising target for non-internalizing Antibody-Drug conjugates. J Control Release. 2019;294:176–84.

[26]. Capone E et al. Targeting vesicular LGALS3BP by an Antibody-Drug conjugate as novel therapeutic strategy for neuroblastoma. Cancers (Basel), 2020.12(10).

[27]. Cela I, et al. LGALS3BP is a potential target of antibody-drug conjugates in oral squamous cell carcinoma. Oral Dis. 2024;30(4):2039–50.

[28]. Capone E, et al. Anti-LGALS3BP antibody-drug conjugate treatment induces durable and potent antitumor response in a preclinical model of adenoid cystic carcinoma. Oral Oncol. 2024;148:106635.

[29]. Rigo V, et al. Combined immunotherapy with anti-PDL-1/PD-1 and anti-CD4 antibodies cures syngeneic disseminated neuroblastoma. Sci Rep.2017;7(1):14049.

[30]. Ivasko SM et al. Combination of GD2-directed bispecific trifunctional antibody therapy with Pd-1 immune checkpoint Blockade induces anti-neuroblastoma immunity in a syngeneic mouse model. Front Immunol, 2023. 13.

[31]. Haratani K, et al. U3-1402 sensitizes HER3-expressing tumors to PD-1 Blockade by immune activation. J Clin Investig. 2020;130(1):374–88.

[32]. Krystal J, Foster JH. Treatment of High-Risk neuroblastoma. Child (Basel), 2023.10(8).

[33]. Qiu B, Matthay KK. Advancing therapy for neuroblastoma. Nat Rev Clin Oncol.2022;19(8):51533.

[34]. Wahba A, Wolters R, Foster JH. Neuroblastoma in the era of precision medicine: A clinical review. Cancers (Basel), 2023. 15(19).

[35]. Liu Y, et al. Aberrant expression of LGALS3BP drives an unfavorable prognosis and more aggressive in HCC via regulating PI3K/AKT signaling. Tissue Cell. 2024;89:102471.

[36]. Li L, et al. LGALS3BP is a novel and potential biomarker in clear cell renal cell carcinoma. Aging. 2024;16(4):4033–51.

[37]. Choi Y-S et al. Antibody-mediated blockade for galectin-3 binding protein in tumor secretome abrogates PDAC metastasis. Proceedings of the National Academy of Sciences. 2022;119(30):e2119048119.

[38]. Kim S-S, et al. Secreted LGALS3BP facilitates distant metastasis of breast cancer. Breast Cancer Res. 2025;27(1):4.

[39]. Piccolo E, et al. LGALS3BP, lectin galactoside-binding soluble 3 binding protein, induces vascular endothelial growth factor in human breast cancer cells and promotes angiogenesis. J Mol Med (Berl). 2013;91(1):83–94.

[40]. Kalluri R, McAndrews KM. The role of extracellular vesicles in cancer. Cell. 2023;186(8):161026.

[41]. Morini M, et al. Plasma-Derived exosome proteins as novel diagnostic and prognostic biomarkers in neuroblastoma patients. Cells. 2023;12(21):2516.

[42]. Nicolazzi C, et al. Abstract 3740: Tusamitamab Ravtansine induces Immunogenic cell death and synergizes with anti-PD-1 or anti-PD-L1 antibody combination in solid tumor. Cancer Res. 2024;84(6Supplement):3740–3740.

[43]. Perra M, et al. Maytansinoids in cancer therapy: advancements in antibody-drug conjugates and nanotechnology-enhanced drug delivery systems. Discov Oncol. 2025;16(1):73.

[44]. García-Alonso S, Ocaña A, Pandiella A. Trastuzumab Emtansine: mechanisms of action and resistance, clinical progress, and beyond. Trends Cancer. 2020;6(2):130–46.

[45]. Keinanen O, et al. Visualizing Galectin-3 binding protein expression with ImmunoPET. Mol Pharm. 2023;20(6):3241–8.

CHAPTER 3

Analytical Characterization of Antibody–Drug Conjugates: DAR, Linker Stability, and Payload Quantification in Biological Matrices

The development of antibody–drug conjugates (ADCs) require analytical methods capable of accurately measuring Drug-to-Antibody Ratio (DAR), stability, payload distribution and Pharmacokinetics and Pharmacodynamics of a new ADC, as these parameters are closely associated with pharmacological activity (9). Hydrophobic interaction chromatography (HIC) and reversed-phase chromatography, frequently coupled with mass spectrometry (LC–MS), are established techniques for evaluating DAR and drug-load distributions. These analytical approaches facilitate process development and enable comparative assessments across different ADCs (24). Analytical measurements are essential not only for quality control but also for defining critical ADC characteristics and elucidating the relationship between manufacturing processes and *In Vivo* behavior during both preclinical and clinical studies (9,24). The present research primarily focused on the development of the 1959-sss/DM4 ADC, including optimization of the conjugation process, characterization of its properties, and establishment of a method to quantify DM4 payload distribution in tumor-bearing mice.

3.1 How to analyse an ADC

Antibody–drug conjugates (ADCs) are complex therapeutics that combine monoclonal antibodies and cytotoxic payloads, necessitating comprehensive analytical evaluation. Their structural complexity and heterogeneity make quantifying critical attributes—such as drug-to-antibody ratio (DAR), drug attachment sites, and aggregation levels—challenging (146,147). To address this, a combination of techniques is used. Hydrophobic interaction chromatography (HIC) and capillary electrophoresis separate intact ADCs by drug loading, while size-exclusion chromatography (SEC) distinguishes aggregates and higher-molecular-weight species (9,148). Additional liquid chromatography (LC) modalities, including reversed-phase, ion-exchange, and mixed-mode, separate ADC variants and small molecules (149). Mass spectrometry (MS) delivers detailed information on drug attachment and DAR values (25,150), and its integration with LC–MS enhances sensitivity and precision in payload analysis and conjugation site localization (25,151).

Detecting free payloads such as maytansinoids in biological matrices, including plasma, serum, or tumor tissue, poses significant analytical challenges, as these compounds are often near the quantification limit and are extremely hydrophobic, leading to aggregation and fast clearance with plasma protein. For example, Cahuzac and Devel found that unconjugated maytansinoids were often undetectable in clinical samples: free DM1 was below a 0.20 ng/mL limit, and free DM4 was detectable only within 24 hours post-dosing, at a 0.50 ng/mL threshold (152). These results highlight the need for highly sensitive assays. Additional complications include matrix effects and the hydrophobicity of the payloads, which can lead to adsorption or interactions with endogenous components, thereby impeding recovery and quantification (152,153). To overcome these issues, LC–MS/MS is frequently used after rigorous sample preparation, such as protein precipitation or solid-phase extraction, to enrich analytes and remove interference (152). However, assay sensitivity still depends on payload chemistry and instrumentation (152). Imaging mass spectrometry

techniques, such as MALDI imaging, localize released drugs in tissues by unique mass signatures, reducing interference from conjugated forms (154). Label-free LC–MS methods, such as LESA–LC–MS, quantify payload–linker metabolites in tissue samples (155). Despite advances, quantifying trace amounts of drugs remains challenging, underscoring the need for robust, high-throughput analytical platforms. Traditional ligand-binding assays (LBAs), like ELISA or electrochemiluminescence (ECL), quantify total or conjugated antibody but cannot distinguish molecular forms or directly measure free payload. LBAs also require specific reagents and may lack sensitivity for small fragments (153). Consequently, LC–MS-based methods that quantify small-molecule payloads or conjugated fragments are vital for ADC bioanalysis. Still, the hydrophobicity of payloads and biological matrix complexity demand rigorous validation of detection limits and selectivity for reliable data (152,153).

3.2 Chromatographic and Mass Spectrometric Techniques for ADCs characterization

Analytical workflows for ADCs employ orthogonal chromatographic techniques and mass spectrometry to characterize molecular attributes. Hydrophobic interaction chromatography (HIC) is widely used for DAR analysis, separating ADC species by hydrophobicity under non-denaturing salt-gradient conditions; higher drug loading correlates with greater hydrophobicity (149,156). HIC resolves DAR species and facilitates average DAR calculation via peak integration, generally preserving antibody structure, though resolving power may decrease in highly heterogeneous samples or with very hydrophobic payloads (149,156). Reversed phase (RP) HPLC is used with partly denatured or reduced subunits, separating light and heavy chains or fragments to reveal conjugation and linker stability. RP-HPLC, operating under denaturing conditions, can lead to strong interactions with hydrophobic payloads, resulting in peak broadening or carryover (151); it is often paired with MS for subunit- or peptide-level analysis. Size-exclusion chromatography (SEC) monitors aggregation and high-molecular-weight species, as conjugation minimally affects protein size; thus, SEC does not resolve DAR variants but does detect aggregates effectively.

Mass spectrometry (MS) enables detailed characterization of ADCs. With intact proteins, high-resolution MS measures ADC mass and estimates DAR distributions (150,151), as shown in Figure 12. At the subunit level, reduction or partial digestion generates fragments that ionize well and maintain DAR and glycosylation data as needed (25,150). At the peptide level, enzymatic digestion pinpoints drug attachment sites and quantifies payload-linked peptides, providing detailed structural insight despite requiring extensive sample preparation and lacking a comprehensive DAR overview (25). Therefore, integrating multiple analytical techniques is necessary for complete ADC structural and functional analysis.

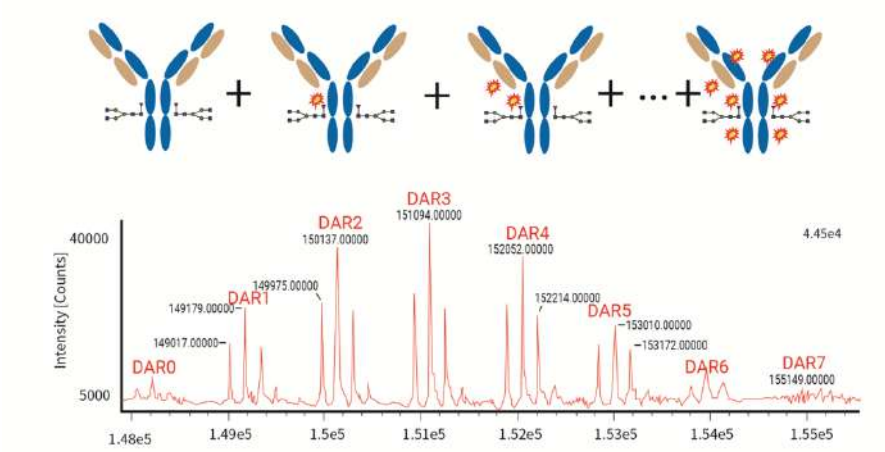


Figure 12. Antibody-Drug conjugate DAR characterization results. Classical conjugation leads to a mixture of ADC with different DARs. With the LC-MS platform, the characterization of ADCs with different DARs can be realized and the average DAR can be calculated.

Image taken from WuXi AppTec website. *Image source: https://dmpkservice.wuxiapptec.com/articles/13-antibody-drug-conjugate-adc-bioanalysis-strategies-based-on-lc-ms/*

3.3 Analytical methods applied to ADC Preclinical Evaluation

Preclinical studies require assays to quantify total ADC, free antibody, and free payload in plasma to assess pharmacokinetics and safety. ADCs with high DAR values are cleared from circulation more rapidly, affecting both efficacy and toxicity (157). Regulatory authorities mandate validated assays for ADC and payload quantification during development (146,158). LC–MS and LC–MS/MS are standard for structural ADC analysis and sensitive detection of released payloads but have practical and technical limitations (159). They require costly instrumentation and expertise, limiting some labs' access. Matrix effects, such as ion suppression or enhancement caused by co-eluting substances, require extensive sample preparation for reliable, compliant data. Highly hydrophobic payloads complicate analysis by promoting adsorption, carryover, and instrument contamination, impacting consistency (152,153). As alternatives, traditional HPLC with optical detection, such as HPLC–DAD, offers robustness and lower susceptibility to matrix effects but usually provides lower resolution. When validated, they provide reliable data on payload release in biological matrices, supporting preclinical work. The initial section of Chapter 3 details the development and validation of an HPLC–DAD method for simultaneous detection and quantification of free DM4 and its metabolite S-Me-DM4 in plasma. The subsequent study, to which the present author contributed, outlines the validation of this method in accordance with standard analytical guidelines and its application to plasma samples containing the 1959-sss/DM4 ADC. This approach enables quantification of payload release and systemic exposure, thereby supporting subsequent preclinical pharmacokinetic investigations:

Lovato, G., Ciriolo, L., Perrucci, M., Federici, L., Ippoliti, R., Iacobelli, S., Capone, E., Locatelli, M., & Sala, G. (2023). HPLC–DAD validated method for DM4 and S-methyl-DM4 quantification in biological matrices. Journal of Pharmaceutical and Biomedical Analysis, 235, 115642. https://doi.org/10.1016/j.jpba.2023.115642 (160)

HPLC-DAD validated method for DM4 and its metabolite S-Me-DM4 quantification in biological matrix for clinical and pharmaceutical applications

Giulio Lovato [a,c,1], Luigi Ciriolo [b,1], Miryam Perrucci [b,1], Luca Federici [a,c], Rodolfo Ippoliti [d], Stefano Iacobelli [e], Emily Capone [a, c], Marcello Locatelli [b], Gianluca Sala [a, c]

[a] Department of Innovative Technologies in Medicine and Dentistry, Center for Advanced Studies and Technology (CAST), University of Chieti-Pescara "G. d'Annunzio", Via dei Vestini 31, Chieti 66100, Italy

[b] Department of Pharmacy, University of Chieti-Pescara "G. d'Annunzio", Via dei Vestini 31, Chieti 66100, Italy

[c] Center for Advanced Studies and Technology (CAST), University of Chieti-Pescara "G. d'Annunzio", Via dei Vestini 31, Chieti 66100, Italy

[d] Department of Life, Health and Environmental Sciences, University of L'Aquila, 67100 Coppito, Italy

[e] MediaPharma s.r.l., Via Colle dell'Ara, Chieti 66100, Italy

Abstract

The present study focuses on the development and validation of an HPLC-DAD methodology for the detection of a potent chemotherapeutic agent, Maytansinoid Ravtansine (DM4), and its metabolite, S-methyl-DM4 (S-Me-DM4), in plasma samples. Methodologically, after a simple protein precipitation with acetonitrile and after drying 1 mL of supernatant, the sample (suspended with N,N-Dimethylacetamide, DMA) was directly analyzed by HPLC under isocratic elution using a mobile phase comprising milliQ water and methanol (25:75, v:v), both acidified with 0.1 % v:v formic acid. Employing a flow rate of 1.0 mL/min and a reversed-phase GraceSmart RP18 column thermostated at 40 °C, we achieved complete resolution and separation of DM4 and S-Me-DM4 within 13 min. The optimized injection volume of 20 μL and the wavelength set at 254 nm were utilized for quantitative analyses. Rigorous validation has not only ensured its reliability and reproducibility but has also addressed potential limitations associated with methodological inconsistency. The limit of detection and quantification of the method were 0.025 and 0.06 μg/mL for both the analytes, respectively. The calibration curve showed a good linearity in the range 0.06–20 μg/mL. For both analytes, the intraday precision and trueness were 2.3–8.2 % and −1.1 to 3.1 %, respectively, while the interday values were 0.7–10.1 % and −10.4 to 7.5 %, respectively. The developed methodology enables the concurrent determination and quantification of free DM4 and its metabolite, free S-Me-DM4, making it a valuable tool for assessing the pharmacokinetics and pharmacodynamics of DM4-based therapies. In addition, the procedure was successfully applied to analyse the presence of free DM4 or its metabolite, free S-Me-DM4, in human plasma samples spiked with the 1959-sss/DM4 antibody-drug conjugate (ADC). The utilization of the herein validated methodology allowed to confirm the presence of these analytes, thereby providing insights into their potential release from the ADC structure.

1. Introduction

Maytansinoids, a class of compounds derived from the natural product maytansine, have garnered significant attention in the field of drug development owing to their potent antimitotic activity and promising applications as payloads in antibody-drug conjugates (ADCs) [1]. Among these maytansinoids, N2′-Deacetyl-N2′-(4-mercapto-4-methyl-1-oxopentyl)-maytansine or Ravtansine or

simply DM4 (DM4) has emerged as a particularly compelling candidate, exhibiting improved biological activity and enhanced stability when conjugated to antibodies [1]. Structurally, maytansinoid derivatives, DM1, DM3, and DM4, differ from each other based on the number of methyl groups present on the carbon adjacent to sulfur, zero, one, or two, respectively. The introduction of methyl groups contributes to the heightened potency of the free drug, likely due to increased hydrophobicity and improved membrane permeability [2]. DM4, is thiol-containing compound which undergoes methylation within cells through the activity of methyltransferases, resulting in the formation of S-Me-DM4 [2]. This metabolite demonstrates notable cytotoxicity. Importantly, both DM4 and S-Me-DM4 possess the ability to traverse cell membranes, leading to an enhanced phenomenon known as the "bystander effect" where the drug can diffuse out of a targeted cell into adjacent cells [3]. S-Me-DM4, exert its cytotoxic effect by inhibiting microtubule formation and disrupting the assembly of the mitotic spindle. The presence of a further methyl groups results in increasing potency of free drug as a higher hydrophobicity induces major membrane permeability [2,4]. However, due their extremely high cell killing potency (with IC50 in the picomolar range), such compounds cannot be used as free drugs.

Indeed, to mitigate cytotoxic effects and enhance selectivity, Antibody-Drug Conjugates (ADCs) were developed, providing a targeted approach to specifically deliver the drug to the tumor site [5]. The first ADC incorporating a maytansinoid payload was approved and introduced to the market in 2013, marking a significant milestone in the advancement of targeted cancer therapies [6]. ADCs consist of three components: a monoclonal antibody (mAb), a cytotoxic drug, and a linker that connects both components. The antibodies recognize and bind to specific target antigens present on the surface of tumor cells, enabling the selective delivery of the potent drug [6-11]. Simultaneously, it is crucial for the ADC to remain stable during circulation but release its payload upon reaching the intended target site. The combination of antibody's selectivity and drug's potency contributes to the therapeutic efficacy of ADCs in cancer treatment [5-8]. The evaluation of ADC efficacy requires the assessment of various parameters, including *In Vivo* activity on cell and animal lines, Drug-Antibody Ratio (DAR), and bond stability. These analyses are crucial to prevent drug losses before reaching the tumor site and to minimize adverse toxicity reactions [7, 10, 11].

In Fig. 1, a schematic representation of linkers used in internalizing and non-internalizing ADCs was reported, as also highlighted by Ashman et al. [12]. Thanks to these characteristics there are some ADC available on the market: Gemtuzumab ozogamicin (Mylotarg®), the first ADC available from 2000, Brentuximab Vedotin (Adcetris®), trastuzumab emtansine (Kadcyla™), and InotuzuWhile liquid chromatography coupled mass spectrometry (LC-MS) is commonly employed for such assessments, it often requires sophisticated instrumentation, substantial maintenance costs, and specialized expertise. Considering these factors, the primary objective of this study is to develop and validate a high-performance liquid chromatography (HPLC)-based method for the simultaneous quantification of free DM4 and its primary metabolite, S-Me-DM4, in human plasma samples. The method was further applied to a DM4 containing ADC, 1959-sss/DM4, which is a linkerless non-internalizing ADC previously described [5, 9, 12-15]. This method should be employed in future non-clinical and clinical studies to evaluate the stability of both the free drug and its metabolite, as well as the ADC, in biological matrices. By establishing a robust HPLC methodology, we aim to provide an accessible and cost-effective analytical approach that can support comprehensive evaluations of free DM4 and S-Me-DM4 in several contexts. This research may will contribute to the advancement of DM4-based therapies and ADC development, ultimately improving the efficacy and safety of targeted cancer treatments.

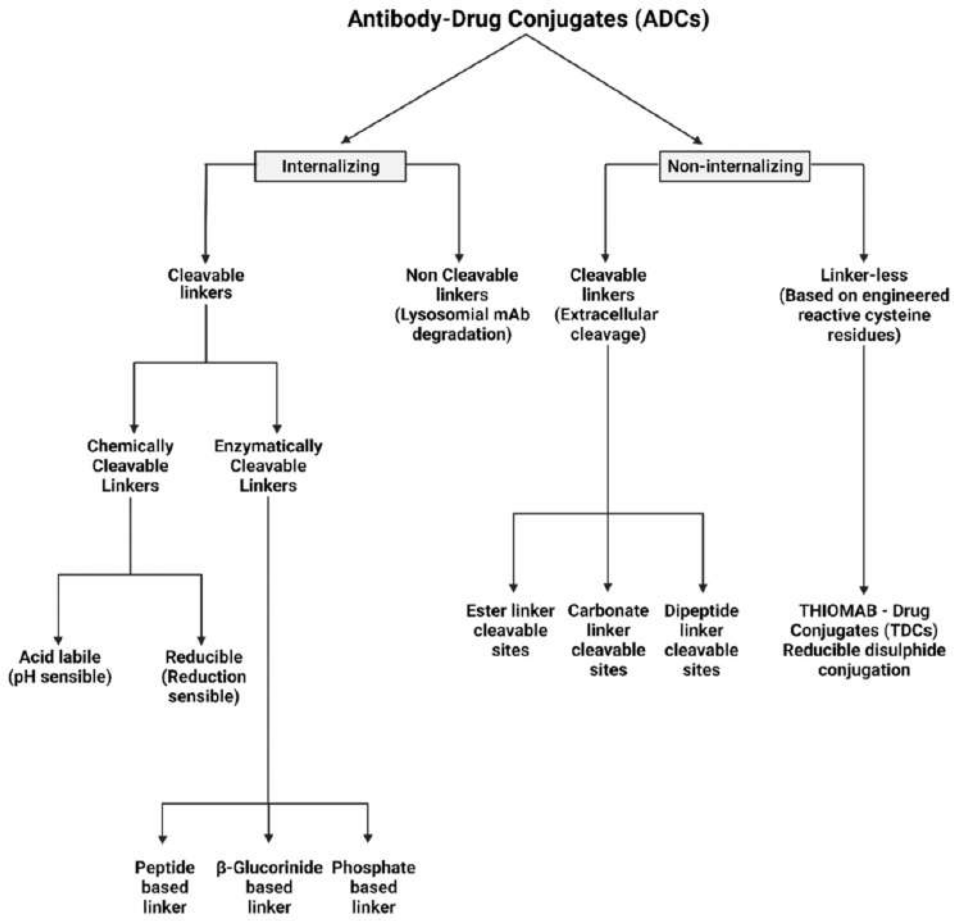


Fig. 1: Schematic representation of linkers.

2. Materials and methods

2.1 Chemicals and Reagents

For the HPLC analysis, Ravtansine (DM4) and its main metabolite S-methyl-DM4 (S-Me-DM4) were obtained from MedChemExpress (New Jersey, USA). N,N-Dimethylacetamide (DMA) was purchased from Sigma-Aldrich (St. Louis, MO, USA). Methanol (MeOH) and Acetonitrile (AcN) (HPLC grade) were bought from VWR Chemicals (Pennsylvania, USA) and Formic Acid (HPLC grade) was obtained from Carlo Erba Reagents (Milan, Italy). The water was purified using Milli-Q Lab Water by Merck (Darmstadt, Germany).

2.2 Preparation of standard solutions

The stock solution of DM4 and S-Me-DM4, each at a concentration of 1 mg/mL, was prepared by accurately weighing 1 mg of each compound and dissolving it in 1 mL of DMA. To aid in solubilization, the stock solution was subjected to sonication in an ultrasonic bath for two minutes at 20° C, following the guidelines provided by MedChemExpress. Working standard solutions covering a concentration range of 0.025 to 20 µg/mL were prepared by diluting the stock solutions with DMA.

Both the stock and working solutions were stored at -20° C and showed stability for a period of one month.

2.3 Plasma samples preparation

Plasma samples holding the analytes (obtained from whole blood with citrate as an additive) were prepared at concentrations of 0.025, 0.06, 0.08, 0.10, 0.20, 0.50, 1.00, 4.00, 5.00, and 20.00 µg/mL. Quality control (QC) samples were also prepared at concentrations of 0.25, 2, and 10 µg/mL. Working standard solutions of the analytes were prepared at concentrations ranging from 0.25 to 200 µg/mL, considering the dilution factor (10-fold) and were spiked into human plasma containing citrate.

To prepare each sample, an aliquot of 270 µL of blank human plasma was taken, and 30 µL of the corresponding concentration of the working solution holding a mixture of DM4 and S-Me-DM4 in DMA was added. The chosen volumes ensured that the matrix modification remained below 15%, as required for bioanalytical method validation. After spiking, the samples were gently shaken using a vortex mixer (VELP Scientifica, Monza, Italy). Subsequently, three volumes (900 µL) of AcN were added to achieve protein precipitation. All samples were vortexed and centrifuged at 12,000 x g for 15 minutes. From each sample, a standardized volume of supernatant (1 mL) was collected and dried under vacuum using the SC110A SPEEDVAC® concentrator. The dried samples were reconstituted with 300 µL of DMA, followed by vortexing and centrifugation at 12,000 x g for 3 minutes to remove non-soluble particulates. The resulting supernatant was directly injected into the HPLC instrumentation.

2.4 HPLC-DAD method validation

The analysis of DM4 and S-Me-DM4, both in DMA and human plasma citrate, as well as the subsequent monitoring of analyte stability in human plasma citrate, were conducted using an Agilent 1100 liquid chromatography system (Agilent Technologies, Waldbronn, Germany). The system consisted of a solvent pump, on-line degasser, thermostated autosampler and column compartment, and diode array detector (DAD). Data acquisition and processing were performed using Chemstation Software (Agilent). During method development, various chromatographic parameters and mobile phases were evaluated. A C18 reversed-phase packing column (GraceSmart RP18, 4.6 × 150 mm, 5 µm; Grace, Deerfield, IL, USA) was employed for the separation. Different temperatures (40° C and 50° C) and flow rates (0.8 mL/min, 1.0 mL/min and 1.2 mL/min) were tested. The quantitative analyses were conducted at 254 nm, which was determined to be the optimal wavelength for maximum sensitivity of DM4 and S-Me-DM4.

For the analysis in both DMA and human plasma, the best results were achieved using the GraceSmart RP18 column (4.6 mm × 150 mm × 5 µm) thermostated at 40° C (±1° C). The mobile phase consisted of a mixture of milliQ water and methanol (25:75, v:v), both acidified with 0.10% v:v formic acid. Isocratic elution at a flow rate of 1.00 mL/min was employed, and the injection volume was set at 20 µL. Figure 2 illustrates the chromatograms obtained at 254 nm for a single analyte in the solvent (DMA) and for the analyte mixture. The method was validated according to International Guidelines, including assessments of linearity, selectivity, precision, trueness (both intraday and interday), ruggedness, limit of detection (LOD), and limit of quantification (LOQ) [16, 18]. By optimizing the instrumental setup and developing a comprehensive method validation,

reliable quantification of DM4 and S-Me-DM4 was achieved, ensuring the accuracy and precision necessary for further analyses and stability studies.

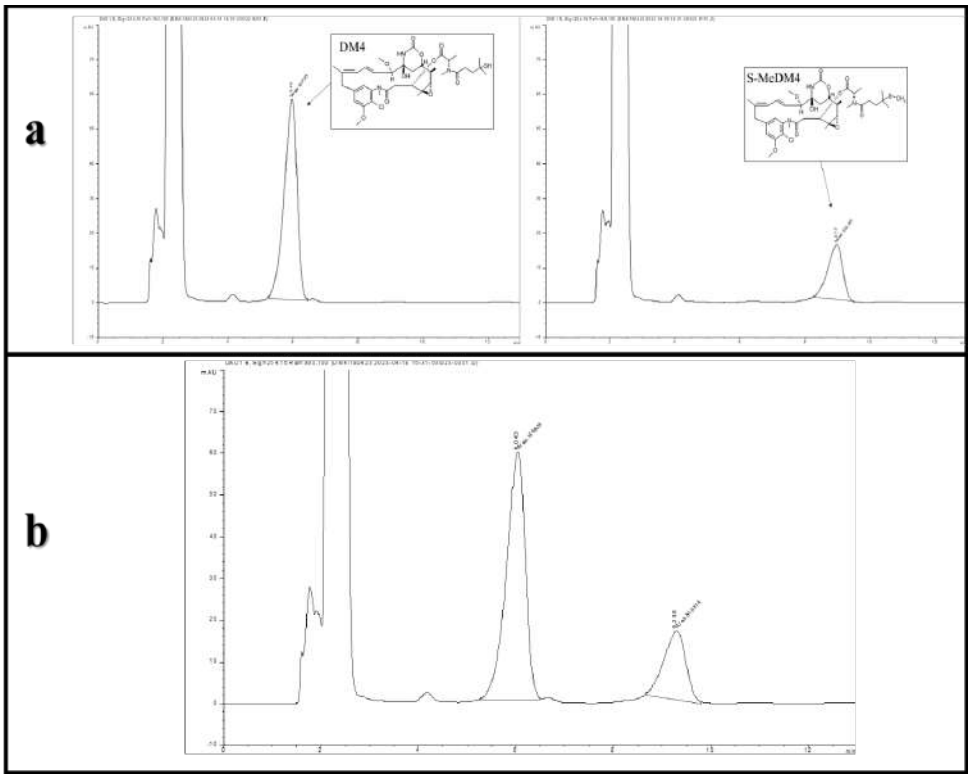


Fig. 2: Reference chromatograms obtained at 254 nm of the analytes in solvent DMA (a, left DM4 and right S-Me-DM4), the mix of the two analytes (b).

2.5 Real samples analysis

Following the successful completion of the method validation process, such protocol was applied to investigate the behavior of DM4 and S-Me-DM4 in human plasma. Samples were subjected to the previously described preparation procedure and then analyzed. In this study, various time points were considered, namely t0, 30 min, 1 h, 2 h, 4 h, 8 h, and 24 h. For each time point, 270 µL of plasma was spiked with 30 µL of a DM4/S-Me-DM4 mixture (100 µg/mL) to achieve a final analyte concentration of 10 µg/mL. The samples were then subjected to incubation under stirring conditions at 37° C, or keeping in an ice water bath temperature of 2-4° C.

In addition, to assess the applicability of the method, we examined the presence of free payload following the incubation, along the time points, of an aliquot of 1959-sss/DM4 antibody-drug conjugate (ADC) in plasma; 270 µL of human plasma and 30 µL of the ADC solution in phosphate buffer (1.25 mg/mL) were combined. This concentration reflects the dosage used in *In Vivo* mouse experiments, where a dose of 10 mg/kg was reported [5]. The incubation of the ADC samples was carried out at 37° C to simulate physiological conditions.

3. Results and discussion

3.1 Sample preparation

DM4, a lipophilic drug with a LogP value of 5.39, exhibits significant hydrophobic characteristics. Its main metabolite, S-Me-DM4, undergoes intracellular enzymatic S-methylation, potentially increasing its lipophilicity [19, 20]. To establish the linearity of the method, working solutions were prepared by diluting a stock solution of DM4 and S-Me-DM4 (1 mg/mL in DMA) with various solvents, including water, PBS at pH 7.4, H2O:MeOH (25:75, v:v), and DMA.

Analysis of samples prepared in water and phosphate buffer yielded disparate results, showing inadequate linearity across different concentrations. This can be attributed to incomplete solubilization of the analytes or their tendency to form aggregates, as discussed in a study by Mohamed H.E. et al., which characterized emtansine (DM1), a precursor of DM4, with similar physicochemical properties [21]. A mixture with a prevalent organic phase (H2O:MeOH, 25:75, v:v) increased solubility, but the optimal chromatographic profile was obtained when samples were prepared in DMA. This solvent choice improved peak symmetry and significantly enhanced the response signal strength, leading to an increased signal-to-noise ratio (S/N). Notably, it was observed that the addition of a small amount of DMA did not induce plasma protein precipitation or cause other modifications in the matrix during the fortification step. Consequently, DMA was selected as the ideal solvent for effective solubilization of the analytes in human plasma citrate.

Subsequent sample preparation involved protein precipitation (PP) using a 1:3 ratio of AcN to sample (v:v). The samples were vortexed and centrifuged at 20000 x g for 15 minutes. The resulting supernatant (1 mL) was carefully transferred to a new Eppendorf tube and dried under vacuum using a SpeedVac system. Each dried sample was reconstituted with 300 µL of DMA, subjected to ultrasound bath treatment (2 minutes), followed by centrifugation (3 minutes). After supernatant recovery, and a simple vortex step, samples were transferred to HPLC vials for subsequent HPLC-DAD analysis.

3.2 Method optimization

During method optimization, various HPLC variables were investigated, including the composition of the mobile phase and the column temperature. Initially, different ratios of H2O:MeOH (30:70, 25:75, and 20:80, v:v) were tested, followed by H2O:AcN (25:75, 35:65, 40:60, v:v) and ammonium acetate (10 mM and 20 mM, pH 7):MeOH (25:75, v:v). The best performance in terms of resolution and peak intensity was achieved with H2O:MeOH (25:75, v:v). The other tested conditions resulted in asymmetrical peaks that were either too close to the void time or had excessively long elution times, leading to peak broadening.

To further enhance peak shape, the addition of varying percentages of formic acid (0.05, 0.10, 0.15, and 0.20% v:v) was evaluated in both the aqueous and organic phases. Although only minor differences were observed, the final composition selected was H2O:MeOH (25:75, v:v) acidified with 0.10% v:v of formic acid. Alterations in column temperature (ranging from 40° C to 50° C) did not yield significant improvements, thus the lower temperature of 40° C was chosen for method validation.

Under these optimized conditions, the chromatographic profiles of blank human plasma and fortified human plasma samples are depicted in Figure 3. As illustrated, at 254 nm, no interfering peaks were

observed, and the two analytes, DM4 and S-Me-DM4, were fully resolved without noticeable peak asymmetry or fronting/tailing issues. The retention times for DM4 and S-Me-DM4 under the optimized conditions were determined to be 5.6±0.5 and 9.2±1.2, respectively.

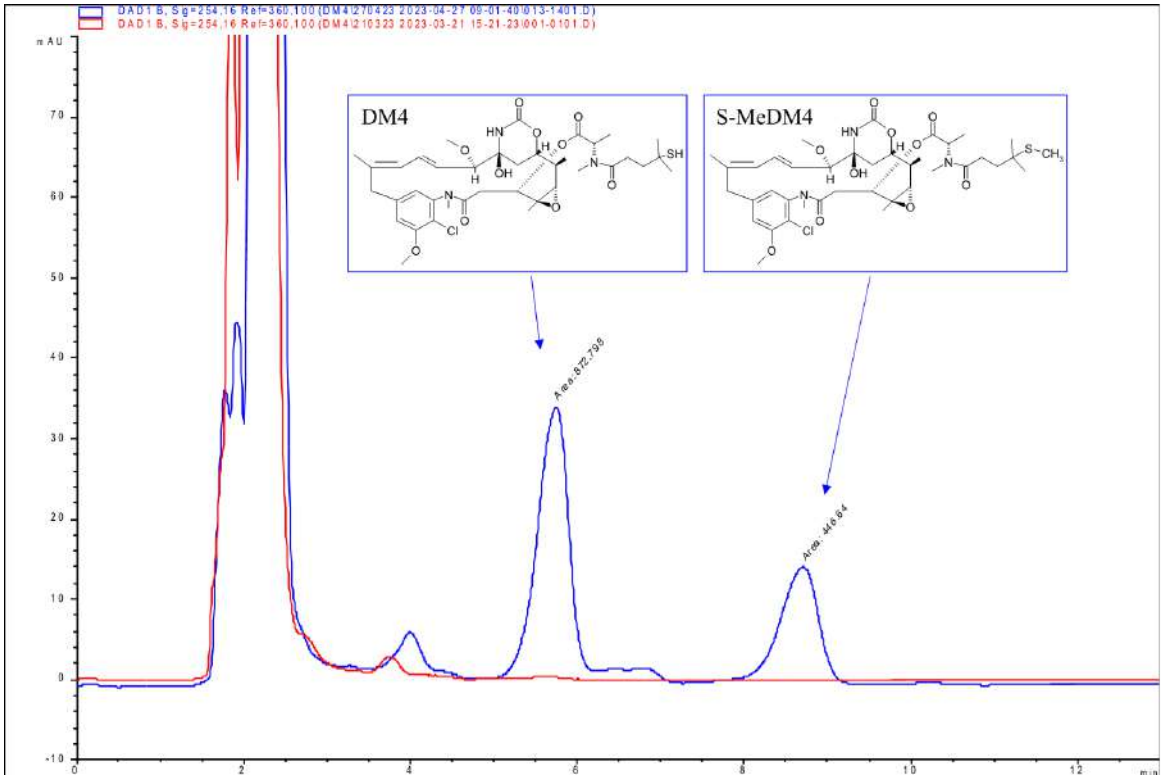


Fig. 3: Chromatograms obtained at 254 nm for the blank human plasma (red trace), and the blank human plasma fortified with the mix (DM4/S-Me-DM4) (blue trace).

3.3 Method validation

The method was validated under the optimized conditions according to the ICH Q2(R1) International Guidelines. The validation parameters assessed included linearity, selectivity, precision, trueness (both intraday and interday), ruggedness, LOD, and LOQ [16-18]. Additionally, a stability study of the processed samples was conducted at 4° C. The results obtained indicated that the method exhibited linearity within the concentration range of 0.06-20 µg/mL, with an R2 value equal to or greater than 0.9881. The calibration curves were plotted using a weighting factor of 1/x2, as recommended by the International Guidelines. The LOD was determined to be 0.025 µg/mL, corresponding to a signal-to-noise (S/N) ratio of 3. The LOQ was established at 0.06 µg/mL for both analytes, based on a signal-to-noise ratio of 10 and the BIAS% value for the back-calculated concentration. The precision and trueness, evaluated both intraday and interday, were found to be below ±15%, as presented in Table 1. The selectivity of the method was assessed by analyzing blank human plasma samples to confirm the absence of interfering substances. In Table 2 were reported the main figure of merits related to the calibrations during intra- and interday data elaboration.

Table 1. Figure of merits of the validated HPLC-DAD method for DM4 and its metabolite S-Me-DM4 quantification in human plasma citrate matrix

					Intraday		Interday	
Analyte	**Linearity (μg/mL)**	**LOD (μg/mL)**	**LOQ (μg/mL)**		**Precision (Std. Dev.)**	**Trueness (BIAS%)**	**Precision (Std. Dev.)**	**Trueness (BIAS%)**
DM4	0.06-20	0.025	0.06	QC low (0.25 μg/mL)	8.2	-11.0	10.1	-10.4
				QC med (2 μg/mL)	6.4	-7.7	1.7	-6.2
				QC high (10 μg//mL)	2.3	3.1	0.7	-4.4
S-Me-DM4	0.06-20	0.025	0.06	QC low (0.25 μg//mL)	5.2	-9.4	4.7	-1.0
				QC med (2 μg/mL)	2.4	-4.8	5.8	-4.3
				QC high (10 μg/mL)	3.4	-6.0	8.6	7.5

Table 2. Main figure of merits related to the calibrations during intra- and interday data elaboration.

Analyte	**Parameter**	**Intraday values**	**Interday values**
DM4	Intercept	-0.8153±0.1605	-0.5572±0.1617
	Slope	70.35±1.248	43.69±1.163
	R^2 (unweighted)	0.9881	0.9975
S-Me-DM4	Intercept	0.7770±0.08226	0.8417±0.1061
	Slope	24.03±0.4980	25.62±0.4422
	R^2 (unweighted)	0.9956	0.9960

In Figure 4 was reported an example of calibration curves obtained during the intraday validation.

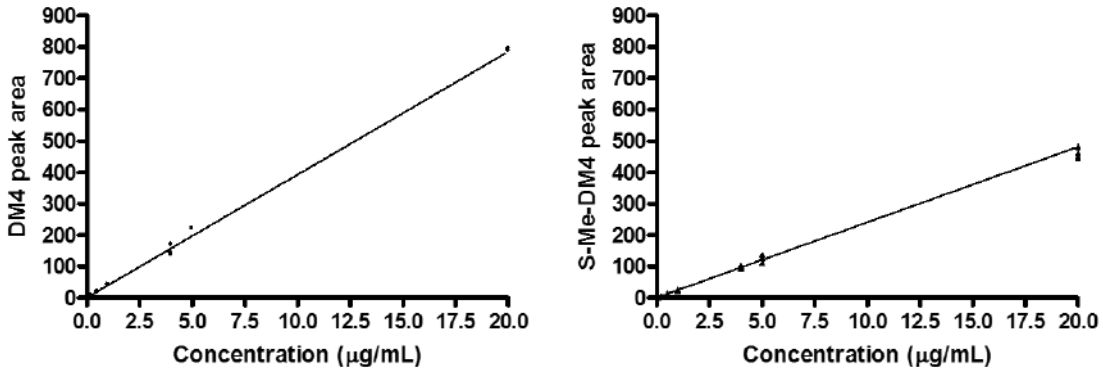


Fig. 4: Example of calibration curves for DM4 and its metabolite S-Me-DM4 in human plasma citrate

3.4 Ruggedness and System Suitability Test

To assess the ruggedness of the validated method, a standard sample containing DM4 and S-Me-DM4 was utilized to evaluate the performance of the method under intentionally varied instrumental parameters. Small but deliberate changes were made to parameters such as flow rate, temperature, mobile phase percentage, and composition. The results obtained from these experiments, as summarized in Table 3, indicate that the procedure is robust and reliable, making it suitable for clinical laboratory applications. The method demonstrates simplicity, speed, and the ability to withstand minor deviations in instrumental parameters without compromising its performance.

Table 3. Ruggedness of the validated method in human plasma citrate

		Optimized *	Flow (mL/min)		T (°C)		Mobile phase (%)		Composition	
			0.8	1.2	37°	43°	30%-70%	20%-80%	0.05% formic acid	0.15% Formic acid
	Pressure (bar)	**83**	78	95	84	80	86	74	72	79
	Void Ret. Time (min)	**1.59**	1.91	1.31						
DM4	**Ret. Time (min)**	**5.63**	6.68	4.60	5.89	5.42	9.57	3.90	4.49	6.18
	Peak area	**740.46**	916.03	612.44	745.25	738.46	741.55	763.44	744.47	767.843
	Peak height	**28.6**	28.6	28.0	28.0	28.6	21.3	34.2	28.3	27.4
	Peak simmetry	**1.61**	1.77	1.5	1.62	1.71	1.49	1.72	1.536	1.46
	Peak width (min)	**0.43**	0.53	0.36	0.44	0.43	0.58	0.37	0.439	0.46
	k'_1	**2.54**	2.49	2.53	2.71	2.41	5.02	1.45	1.82	2.89
	N_1	**2741**	2538	2613	2869	2542	4355	1777	1672	2888
	H_1 (cm)	**0.055**	0.059	0.057	0.052	0.059	0.034	0.084	0.090	0.052
S-Me-DM4	**Ret. Time (min)**	**8.47**	9.97	6.97	8.98	8.07	16.64	5.14	6.60	9.59
	Peak area	**291.16**	340.8	240.25	295.37	282.483	292.28	287.49	312.9	305.417
	Peak height	**8.9**	8.9	8.5	8.7	9.0	5.9	11.5	8.5	8.3
	Peak simmetry	**1.6**	1.66	1.5	1.66	1.59	1.42	1.74	1.816	1.53
	Peak width (min)	**0.54**	0.64	0.47	0.56	0.52	0.82	0.41	0.613	0.61
	k'_2	**4.33**	4.22	4.34	4.65	4.07	9.47	2.23	3.15	5.03
	N_2	**3935**	3884	3516	4111	3852	6589	2515	1854	3955
	H_2 (cm)	**0.038**	0.039	0.043	0.036	0.039	0.023	0.060	0.081	0.038
	$a_{(2,1)}$ **	**1.70**	1.69	1.72	1.72	1.69	1.89	1.54	1.73	1.74
	$R_{2,1}$	**5.86**	5.63	5.70	6.17	5.57	10.10	3.18	4.01	6.37

* Flow 1 mL/min. T= 40°C. 25% (H2O + 0.1% formic acid): 75% Methanol + 0.1% formic acid); ** a was evaluated considering DM4 (peak 1) and S-Me-DM4 (peak 2)

3.5 Real sample results

This experiment was taken to investigate the temperature dependent behavior of DM4 and S-Me-DM4 in human plasma, aiming to provide indications into their *In Vitro* characteristics such as plasma protein binding, aggregate formation, and metabolite formation. The concentration changes of the analytes were monitored over various incubation times. Samples corresponding to each time point,

both for 37° C and 4° C incubations, were prepared as described (Section 2.5) and analyzed using the validated method (Table 4, Figure 5). Concurrently, a similar experiment was conducted on 1959-sss/DM4 ADC to assess the presence of free DM4 at each time point. After the designated incubation time, all samples were treated and analyzed as outlined (Table 5).

The results depicted in Table 4 provide information into the recovery of DM4, approximately 93% at t0 (0 hours) 37° C. The concentration of DM4 decreases rapidly up to 2 hours of incubation, followed by a relatively constant fraction of approximately 3% from 4 to 24 hours. These findings suggest a time-dependent binding of DM4 to plasma proteins until a dynamic equilibrium is achieved. In contrast, the stability observed for S-Me-DM4 (approximately 99% at t0 and 37°C, decreasing to approximately 15% at 24 hours) follows a more linear trend over time. The presence of an S-methyl group instead of an -SH group significantly reduces interactions related to time-dependent binding to plasma proteins, resulting in improved stability in human plasma. These values align closely with the free DM4 detected on average over 24 hours, previously described, designed to assess the release of free payload from the ADC.

The same experiment conducted in an ice water bath (4° C) showed higher recovery for both DM4 and S-Me-DM4, indicating a temperature-dependent effect. Specifically, for DM4, the average recovery between 1 and 8 hours was approximately 60%, which further decreased to 30% at 24 hours. In the case of S-Me-DM4, considering the same time points, the average recovery was approximately 85%, significantly higher than that of DM4 due to the exclusion of disulfide binding with proteins. Notably, the recovery values for t0 and 30 minutes for both analytes were lower compared to those obtained at 37° C. These values are likely influenced by the lower solubility of DM4 and its metabolite in human plasma at low temperatures, resulting in incomplete homogeneity of the solution at these time points. Therefore, the observed trend for both analytes suggest an initial increase in recovery within the first 30 minutes due to improved solubility, reaching its maximum at 1 hour, followed by a decrease over 24 hours due to protein interactions.

Table 4: DM4 and S-Me-DM4 at 5 µg/mL in human plasma at 37° C and in ice bath (2-4° C)

		Incubation at 37°C			**Incubation in ice bath (2-4°C)**		
	Time (h)	**Concentration (µg/mL)**	**%**	**Loss**	**Concentration (µg/mL)**	**%**	**Loss**
DM4	**0**	4.64±0.52	92.72±9.30	7.28±0.89	2.24±0.26	44.85±4.45	55.15±5.15
	0.5	2.29±0.28	45.89±5.60	54.11±6.84	2.27±0.28	45.57±4.56	54.43±5.60
	1	0.86±0.32	17.18±2.40	82.82±8.85	3.36±0.36	67.37±6.65	32.63±3.60
	2	0.21±0.06	4.21±0.63	95.79±10.3	3.43±0.32	68.70±7.10	31.30±2.90
	4	0.19±0.08	3.84±0.28	96.16±9.91	2.50±0.23	50.05±5.23	49.96±5.01
	8	0.14±0.05	2.74±0.22	97.26±9.80	2.43±0.26	48.68±5.10	51.32±5.20
	24	0.10±0.06	2.02±0.18	97.98±10.2	1.54±0.14	30.90±2.90	69.10±7.05
S-Me-DM4	**0**	4.994±0.56	99.87±8.54	0.13±0.05	3.88±0.35	77.63±7.80	22.37±2.34
	0.5	4.878±0.68	97.56±5.24	2.44±0.26	4.06±0.41	81.30±7.98	18.70±1.94
	1	4.471±0.54	93.41±7.98	6.59±0.74	4.28±0.42	85.77±8.45	14.23±1.43
	2	4.126±053	82.53±8.20	17.47±1.82	4.60±0.48	92.16±9.34	7.84±0.78
	4	3.244±0.35	64.89±4.65	35.11±4.51	4.40±0.45	88.02±8.96	11.98±1.25

8	2.621±0.31	52.42±5.82	47.58±4.20	4.35±0.41	87.06±8.65	12.94±1.34
24	0.730±0.09	14.60±1.87	85.40±7.96	3.93±0.38	78.72±7.89	21.28±2.15

Values were reported as mean ± standard deviation (n=3)

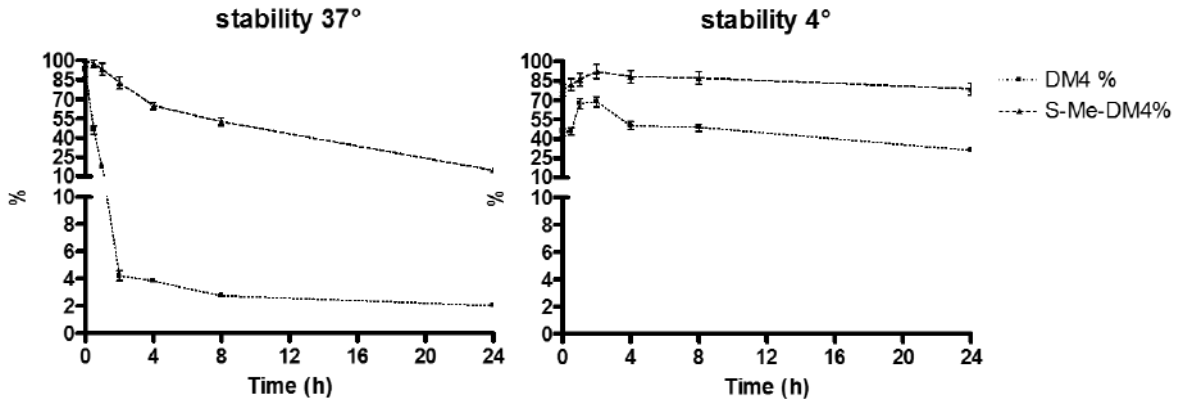


Fig. 5: Time course profiles for DM4, and S-Me-DM4 in human plasma incubated at 37° C (left) and +4°C (ice bath, right). Values are referred to Tables 4.

As highlighted in Table 5, the percentage of free DM4 derived from the ADC in human plasma at 37° C remained relatively stable, at approximately 3% both after 30 minutes and within 24 hours (free fraction).

These results collectively prove the applicability of the developed method to detect free DM4 and its metabolite S-Me-DM4.

Table 5: ADC 125 µg/mL in human plasma at 37° C

Time (h)	**Incubation at 37°C**	
	Concentration (µg/mL)	**% DM4**
0	-	-
0.5	-	-
1	0.05±0.02	1.83±0.2
2	0.06±0.02	2.10±0.2
4	0.05±0.02	1.96±0.2
8	0.10±0.03	3.72±0.4
24	0.08±0.02	2.98±0.3

Values were reported as mean ± standard deviation (n=3)

3.6 Comparison with literature

The validated method presented in this study offers significant advantages compared to other methods reported in the literature. A comprehensive analysis of previously published procedures reveals various drawbacks and limitations (Table 6).

For instance, Heudi et al. focused only on DM1 as the target analyte, employing a complex sample preparation and instrumentation. The use of gradient elution and incomplete validation procedures, omitting crucial aspects such as optimization of injection volume to enhance ionization efficiency and sensitivity, may restrict its practical applicability [22]. Similarly, Wei et al. exclusively considered DM4 as the target analyte, using gradient elution in LC-MS/MS analysis [23]. Fu et al. investigated both DM4 and its S-Me-DM4 metabolite but employed complex sample preparation, intricate instrumentation, and gradient elution, posing potential challenges for method transferability [24]. Lazar et al. presented an unvalidated procedure with a complex instrument configuration and focused on standard solution analysis, employing gradient elution. While their method was applied to determine optimal conditions for the analysis of Antibody-maytansinoid conjugates, its suitability for broader applications remains uncertain [25]. Widdison et al. employed a complex instrument configuration (LC-MS/MS) with gradient elution and an unvalidated procedure, resulting in a lengthy LC runtime of 60 minutes [26]. Similarly, Erickson et al. described an unvalidated procedure utilizing a complex instrument configuration and gradient elution, with the additional use of scintillation reagents for analyte detection [27].

In contrast, the current study represents a significant advancement as the first to simultaneously determine DM4 and S-Me-DM4 in human plasma using a well-established HPLC-DAD instrument. The method employs a rapid, easy, and robust sample preparation procedure. Furthermore, it has been fully validated in the biological matrix of human plasma, demonstrating performance characteristics suitable for clinical and pre-clinical studies. While the sensitivity of this method may not match that of LC-MS/MS setups, it is sufficient for clinical and pre-clinical applications. Moreover, the use of fully compatible mobile phases with MS instrumentation, isocratic elution, fast HPLC analysis (achieving resolution within 13 minutes), and the absence of the need for highly specialized personnel facilitate seamless method transfer to other configurations. This opens possibilities for enhanced sensitivity without sacrificing transferability, which is of utmost importance in the clinical and pharmaceutical fields.

Moreover, in comparison to the work presented by Wei et al. the current study offers notable advantages, albeit with a slightly longer and less sensitive analysis due to the employed instrumental configuration [23]. Notably, the present study encompasses both DM4 and its metabolite, addresses the issue of thiol reactivity specific to DM4, and includes experiments conducted at physiological temperatures, rather than solely stability tests at low temperatures as conducted by Wei et al. [23].

Table 6. Comparison with other published methods.

Analyte	Matrix	Extraction	System	Elution	Column	Runtime (min)	LOD (ng/mL)	LOQ (ng/mL)	Ref.
DM1	Human serum	*On line* SPE	LC-MS/MS	Gradient	C18	10	-	0.2	[22]
DM4	Monkey plasma	LLE	LC-MS/MS	Isocratic	PFP	2	-	0.5	[23]
	Rat plasma								
DM4	Human plasma	PP followed by SPE	LC-MS/MS	Gradient	C18	3.1	-	0.1	[24]
S-Me-DM4									
Antibody-maytansinoid conjugates	Standard solution	Deglycosylation followed by desalting	HPLC-MS	Gradient	C18 and SEC	-	-	-	[25]
Primary antibody−maytansinoid conjugates metabolites	Human liver microsomes	-	LC-MS/MS	Gradient	C8	60	-	-	[26]
Three antibody-maytansinoid conjugates	Mouse tumour tissue	Tissue homogenate followed by LLE	HPLC-DAD-β-counter	Gradient	C18	-	-	-	[27]
DM4	Human plasma	PP	HPLC-DAD	Isocratic	C18	13	25	60	Current
S-Me-DM4									work

PP: protein precipitation; LLE: liquid-liquid extraction; PFP: pentafluorophenyl; LC-MS/MS: liquid chromatography tandem mass spectrometry; HPLC-DAD: high performance liquid chromatography diode array detector; SPE: solid-phase extraction; SEC: size exclusion chromatography.

4. Conclusion and future perspective

Our validated HPLC-DAD methodology enables accurate detection and quantification of Maytansinoid DM4 and its metabolite S-Me-DM4in human plasma samples. The concurrent determination of DM4 and S-Me-DM4 provides valuable information regarding their behaviour's profiles. The successful application of our methodology in assessing the presence of the free amount of this analyte in plasma samples treated with the 1959-sss/DM4 ADC demonstrates its utility in future ADC pharmacokinetics studies. This method represents a significant advancement in the field and holds great potential for facilitating clinical trials characterized by large sample sizes. The developed and validated method employed in this study offers significant advancements compared to existing literature. Previous procedures encountered limitations such as complex sample preparation, gradient elution, and incomplete validation. In contrast, our streamlined and robust HPLC-DAD method allows for the simultaneous determination of DM4 and S-Me-DM4 in human plasma, providing accurate and reliable results. The simplified and efficient sample preparation procedure enables rapid analysis, making it highly suitable for clinical and pre-clinical applications. Comparative analysis with existing literature highlights the notable advantages of our method. While LC-MS/MS approaches offer enhanced sensitivity, our HPLC-DAD method maintains compatibility with MS instrumentation, utilizes isocratic elution, and ensures straightforward method transferability without compromising analytical performance.

Notably, with our findings it can be supposed a time-dependent bond between DM4 and plasma proteins, reaching a dynamic equilibrium. In contrast, the presence of an S-methyl group in S-Me-DM4 enhances its stability, as demonstrated by a linear concentration decrease over time. This observation underscores the significance of payload structure in antibody-drug conjugates.

Furthermore, temperature-dependent behaviour was elucidated, with higher recovery observed at lower temperatures. The impact of temperature on solubility and protein interactions is evident, emphasizing the importance of precise temperature control during experimental procedures.

In conclusion, this study provides comprehensive insights into the behaviour of DM4 and S-Me-DM4 in human plasma, facilitated by a robust and validated HPLC-DAD method. The obtained results contribute to a partial and initial understanding of antibody-drug conjugate stability and pave the way for further investigations in clinical and pre-clinical studies. The applicability of our method, along with its potential for sensitivity enhancements and optimization, positions it as a valuable tool for studying the behaviour of antibody-drug conjugates and their payloads in biological matrices.

References

[1] M. Lopus, E. Oroudjev, L. Wilson, S. Wilhelm, W. Widdison, R. Chari, Jordan, "Maytansine and cellular metabolites of antibody-maytansinoid conjugates strongly suppress microtubule dynamics by binding to microtubules". Mol Cancer Ther. (2010) 9, 2689–99. https://doi.org/10.1158/1535-7163.MCT-10-0644.

[2] B.A. Kellog, L. Garret, Y. Kovtun, K.C. Lai, B. Leece, M. Miller, G. Payne, R. Steeves, K.R. Whiteman, W. Widdison, H. Xie, R. Singh, R.V.J. Chari, J.M. Lambert, R.J. Lutz, Disulfide-Linked Antibody−Maytansinoid Conjugates: Optimization of *In Vivo* Activity by Varying the Steric Hindrance at Carbon Atoms Adjacent to the Disulfide Linkage. Bioconjug. Chem. (2011) 22, 717–727. https://doi.org/10.1021/bc100480a

[3] A. Gazzah, P.L. Bedard, C. Hierro, Y.-K. Kang, A. Abdul Razak, M.-H. Ryu, B. Demers, N. Fagniez, C. Henry, M. Hospitel, J.-C. Soria, J. Tabernero, Safety, pharmacokinetics, and antitumor activity of the anti-CEACAM5-DM4 antibodyâ€“drug conjugate tusamitamab ravtansine (SAR408701) in patients with advanced solid tumors: first-in-human dose-escalation study. Annals of Oncology, (2022) 33, 4, 416-425, ISSN 0923-7534, https://doi.org/10.1016/j.annonc.2021.12.012.

[4] H.K. Erickson, P.U. Park, W.C. Widdison, Y.V. Kovtun, L.M. Garrett, K. Hoffman, R.J. Lutz, V.S. Goldmacher, W.A. Blattler. Antibody-maytansinoid conjugates are activated in targeted cancer cells by lysosomal degradation and linker-dependent intracellular processing. Cancer Res. (2006) 66, 4427-4433. https://doi.org/10.1158/0008-5472.CAN-05-4489

[5] F. Giansanti, E. Capone, S. Ponziani, E. Piccolo, R. Gentile, A. Lamolinara, A. Di Campli, M. Sallese, V. Iacobelli, A. Cimini, V. De Laurenzi, R. Lattanzio, M. Piantelli, R. Ippoliti, G. Sala, S. Iacobelli, Secreted Gal-3BP is a novel promising target for non-internalizing Antibody-Drug conjugates. J. Control. Release (2019) 294, 176-184. https://doi.org/10.1016/j.jconrel.2018.12.018

[6] M.W. Walko, H.J. West, Antibody drug conjugates for cancer treatment. Jama Oncol. (2019) 5, 1648. https://doi.org/10.1001/jamaoncol.2019.3552

[7] J.S. Drago, S. Modi, S. Chandarlapaty, Unlocking the potential of antibody– drug conjugates for cancer therapy. Nat. Rev. Clin. Oncol. 18 (2021) 327-344. https://doi.org/10.1038/s41571-021-00470-8

[8] P. Zhao, Y. Zhang, W. Li, C. Jeanty, G. Xiang, Y. Dong, Recent advances of antibody drug conjugates for clinical applications. Acta Pharm. Sin. B 10 (2020) 1589-1600. https://doi.org/10.1016/j.apsb.2020.04.012

[9] S. Ponziani, G. Di Vittorio, G. Pitari, A.M. Cimini, M. Ardini, R. Gentile, S. Iacobelli, G. Sala, E. Capone, D.J. Flavell, R. Ippoliti, F. Giansanti, Antibody-Drug Conjugates: The New Frontier of Chemotherapy. Int. J. Mol. Sci. 21 (2020) 5510. https://doi.org/10.3390/ijms21155510

[10] C. Corti, F. Giugliano, E. Nicolò, L. Ascione, G. Curigliano, Antibody–Drug Conjugates for the Treatment of Breast Cancer. Cancers 13 (2021) 2898. https://doi.org/10.3390/cancers13122898

[11] Z. Fu, S. Li, S. Han, C. Shi, Y. Zhang, Antibody drug conjugate: the "biological missile" for targeted cancer therapy. Signal Transduct. Target. Ther. 7 (2022) 93-118. https://doi.org/10.1038/s41392-022-00947-7

[12] E. Capone, A. Lamolinara, F. Pastorino, R. Gentile, S. Ponziani, G. Di Vitorio, D. D'Agostino, S. Bibbò, C. Rossi, E. Piccolo, V. Iacobelli, R. Lattanzio, V. Panella, M. Sallese, V. De Laurenzi, F. Giansanti, A. Sala, M. Iezzi, M. Ponzoni, R. Ippoliti, S. Iacobelli, G. Sala, Targeting Vesicular LGALS3BP by an Antibody-Drug Conjugate as Novel Therapeutic Strategy for Neuroblastoma. Cancers 12 (2020) 2989 1-18. https://doi.org/10.3390/cancers12102989

[13] B. Dufrusine, E. Capone, S. Ponziani, R. Lattanzio, P. Lanuti, F. Giansanti, V. De Laurenzi, S. Iacobelli, R. Ippoliti, A. Mangiola, G. Trevisi, G. Sala, Extracellular LGALS3BP: a potential disease marker and actionable target for antibody-drug conjugate therapy in glioblastoma. Molecular oncology, (2023) 10.1002/1878-0261.13453. Advance online publication. https://doi.org/10.1002/1878-0261.13453

[14] O. Keinänen, S. M. Sarrett, S. Delaney, C. Rodriguez, E. J. Dayts, E. Capone, F. Sauniere, R. Ippoliti, G. Sala, S. Iacobelli, B. M. Zeglis, Visualizing Galectin-3 Binding Protein Expression with ImmunoPET. Mol. Pharm., (2023) 20(6), 3241–3248. https://doi.org/10.1021/acs.molpharmaceut.3c00241

[15] E. Capone, S. Iacobelli, G. Sala, Role of galectin 3 binding protein in cancer progression: a potential novel therapeutic target. J. Transl. Med. (2021) 19, 405 https://doi.org/10.1186/s12967-021-03085-w

[16] CDER e CVM. Bioanalytical Method Validation-Guidance for Industry, Food and Drug Administration, May 2018. Available online: https://www.fda.gov/downloads/drugs/guidances/ucm070107.Pdf (accessed on 15 June 2023)

[17] International Conference on Harmonization of Technical Requirements for registration of Pharmaceuticals for Human Use, ICH Harmonised Tripartite Guideline (2005) Validation of Analytical Procedures: Text and Methodology Q2(R1), Geneva, 2005. Available online: https://www.ich.org/fileadmin/Public_Web_Site/ICH_Products/Guidelines/Quality/Q2_R1/Step4/Q2_R1_Guideline.pdf (accessed on 15 June 2023)

[18] International Conference on Harmonization of Technical Requirements for registration of Pharmaceuticals for Human Use, ICH Harmonized Tripartite Guideline, ICH guideline M10 on bioanalytical method validation and study sample analysis (2022). Available online: https://www.ema.europa.eu/en/documents/scientific-guideline/ich-guideline-m10-bioanalytical-method-validation-step-5_en.pdf (accessed on 15 June 2023)

[19] R. Tang, S. Cohen, J.Y. Perrot, A.M. Faussat, C. Zuany-Amorim, Z. Marjanovic, H. Morjani, F. Fava, E. Corre, O. Legrand, J.P. Marie. P-gp activity is a critical resistance factor against AVE9633 and DM4 cytotoxicity in leukaemia cell lines, but not a major mechanism of chemoresistance in cells

from acute myeloid leukaemia patients. BMC cancer 9 (2009) 1-10. https://doi.org/10.1186/1471-2407-9-199

[20] W. Widdison, S. Wilhelm, K. Veale, J. Costoplus, G. Jones, C. Audette, B. Leece, L. Bartle, Y. Kovtun, R. Chari. Metabolites of antibody–maytansinoid conjugates: characteristics and *In Vitro* potencies. Mol. Pharm. 12 (2015) 1762-1773. DOI: https://doi.org/10.1021/mp5007757

[21] H.E. Mohamed, A.A. Mohamed, M.A. Al-Ghobashy, F.A. Fathalla, S.S. Abbas. Stability assessment of antibody-drug conjugate Trastuzumab emtansine in comparison to parent monoclonal antibody using orthogonal testing protocol. J. Pharm. Biomed. Anal. 150 (2018) 268-277. https://doi.org/10.1016/j.jpba.2017.12.022

[22] O. Heudi, S. Barteau, F. Picard, O. Kretz, Quantitative analysis of maytansinoid (DM1) in human serum byon-line solid phase extraction coupled with liquid chromatographytandem mass spectrometry - Method validation and its application toclinical samples, J. Pharm. Biomed. Anal. 120 (2016) 322–332. https://doi.org/10.1016/j.jpba.2015.12.026

[23] D. Wei, M. Sullivanb, O. Espinosab, L. Yanga, A sensitive LC–MS/MS method for the determination of free maytansinoid DM4 concentrations, Method development, validation, and application to the nonclinical studies of antitumor agent DM4 conjugated hu-anti-Cripto Mab B3F6 (B3F6-DM4) in rats and monkeys. Int. J. Mass Spectrom. 312 (2012) 53– 60. https://doi.org/10.1016/j.ijms.2011.05.010

[24] Y. Fu, S. Gorityala, W. Li, D. Humphries, A. Ledvina, S. Cape, F. Picard. Sensitive LC-MS/MS quantification of unconjugated maytansinoid DM4 and its metabolite S-methyl-DM4 in human plasma. Bioanalysis. 14 (2022) 357-368. https://doi.org/10.4155/bio-2021-0275

[25] A.C. Lazar, L. Wang, W. A. Blättler, G. Amphlett, J.M. Lambert, W. Zhang, Analysis of the composition of immunoconjugates using size-exclusion chromatography coupled to mass spectrometry, Rapid Commun. Mass Spectrom. 19 (2005) 1806–1814. https://doi.org/10.1002/rcm.1987

[26] W. Widdison, S. Wilhelm, K. Veale, J. Costoplus, G. Jones, C. Audette, B. Leece, L. Bartle, Y. Kovtun, R. Chari, Metabolites of Antibody−Maytansinoid Conjugates: Characteristics and *In Vitro* Potencies, Mol. Pharm. 12 (2015) 1762−1773. https://doi.org/10.1021/mp5007757

[27] H.K. Erickson, W.C. Widdison, M.F. Mayo, K. Whiteman, C. Audette, S.D. Wilhelm, R. Singh, Tumor Delivery and *In Vivo* Processing of Disulfide-Linked and Thioether-Linked Antibody-Maytansinoid Conjugates, Bioconjug. Chem. 21 (2010) 84–92. https://doi.org/10.1021/bc900315y

The second manuscript in this chapter builds upon previous data by extending the established analytical method described below to tumor tissues in preclinical neuroblastoma models, enabling the analysis of DM4 and S-Met-DM4 distribution and accumulation in tumors (158).

Lovato, G., Perrucci, M., Cela, I., Lamolinara, A., Mercatelli, A., De Laurenzi, V., Capone, E., Locatelli, M., & Sala, G. (2025). Evaluation of antibody–drug conjugate performances using a novel HPLC–DAD method for tumor-specific detection of DM4 and S-methyl-DM4. ACS Omega. https://doi.org/10.1021/acsomega.5c07693 (161)

Collectively, these studies demonstrate that rigorous development of analytical methods facilitates the transition from plasma-based analysis of antibody-drug conjugate (ADC) stability to quantifying the extent and localization of ADC accumulation in tissues. This strategy enables comprehensive *In Vivo* evaluation of ADC performance.

Evaluation of Antibody-Drug Conjugate Performance Using a Novel HPLC-DAD Method for Tumor-Specific Detection of DM4 and S-Methyl-DM4

Giulio Lovato [1, 2, #]; Miryam Perrucci [1, 3, #]; Ilaria Cela [1, 2]; Alessia Lamolinara[4]; Vincenzo De Laurenzi[1,2], Emily Capone [2,5]; Marcello Locatelli [5*] and Gianluca Sala [1, 2*]

[1] Department of Innovative Technologies in Medicine and Dentistry, Center for Advanced Studies and Technology (CAST), University of Chieti-Pescara "G. d'Annunzio", Via dei Vestini 31, Chieti, 66100, Italy.

[2] Center for Advanced Studies and Technology (CAST), University of Chieti-Pescara "G. d'Annunzio", Via dei Vestini 31, Chieti, 66100, Italy.

[3] Department of Biosciences and Agro-Food and Environmental Technologies, University of Teramo 64100 Teramo, Italy

[4] Department of Medicine and Aging Sciences, G. d'Annunzio University of Chieti-Pescara, 66100 Chieti, Italy

[5] Department of Science, University of Chieti-Pescara "G. d'Annunzio" 66100 Chieti, Italy

Abstract

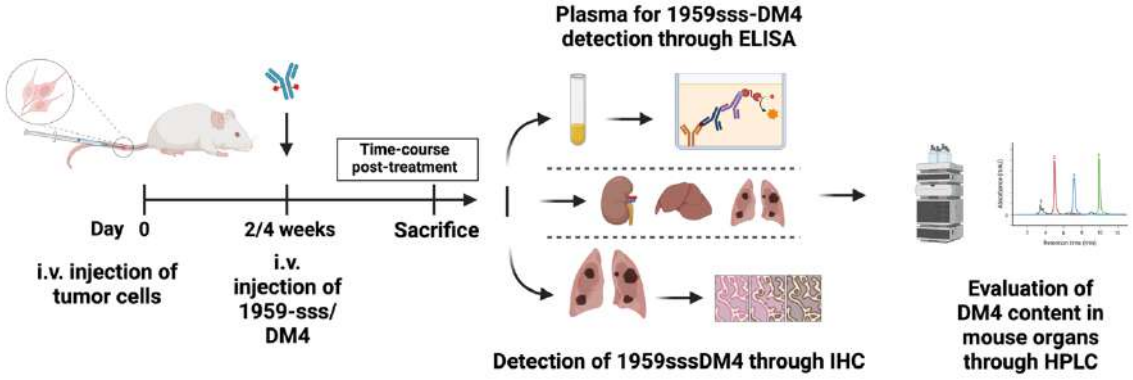
Antibody-drug conjugates (ADCs) are an emerging class of therapeutics that have gained significant interest in the context of precision medicine for cancer treatment. This approach combines the targeted delivery capabilities of monoclonal antibodies, directed against tumor-associated antigens, with the potent cytotoxicity of small-molecule drugs. The goal is to enhance the therapeutic window by maximizing tumor cell killing while minimizing off-target toxicity. One of the most important aspects in the development of compounds of this type is the ability to effectively target the cytotoxic agent to the tumor site. Consequently, having a robust analytical methodology to quantify the actual accumulation of the payload in tumor tissue becomes a critical priority.

In our lab we have developed 1959-sss/DM4, a novel ADC targeting the highly glycosylated LGALS3BP, which is a protein implicated in tumor progression and metastasis. This ADC has shown potent and durable antitumor activity in several preclinical models, including melanoma, glioblastoma, oral cancer and neuroblastoma. Here, we developed and validated a novel high-performance liquid chromatography (HPLC) method capable of simultaneously detecting DM4 and its primary metabolite, S-methyl-DM4, in biological matrices. The method was validated according to ICH guidelines, achieving high sensitivity, precision, and reproducibility, with applications across neuroblastoma preclinical models. We employed a patient-derived neuroblastoma cell line (hNB CTRL), which naturally lacks LGALS3BP expression, alongside a counterpart cell line (hNB LGALS3BP) in which LGALS3BP expression was ectopically induced via lentiviral-mediated gene transduction. Furthermore, a second metastatic experimental model using SKNAS neuroblastoma cells, which endogenously express LGALS3BP, was utilized to study the kinetics of payload accumulation.

Notably, selective accumulation of the ADC payload was observed in LGALS3BP+ metastases, with no off-target delivery to healthy tissues or LGALS3BP- lesions. Moreover, time-course analysis revealed a rapid accumulation of DM4 in metastatic tissues, followed by a decline as the compound was metabolized, and a subsequent increase in levels of the active metabolite, S-methyl-DM4.

In conclusion, this study establishes a validated HPLC method for the quantification of ADC-delivered cytotoxic payloads within tumor tissues. The approach allows for the simultaneous

detection of DM4 and its metabolite S-methyl-DM4, offering a valuable tool for comparative assessment of ADC performance in preclinical models.



Graphical Abstract. Schematic representation of tumor-induced pseudo-metastatic experiment for the detection of DM4 and S-Met-DM4 after 1959-sss/DM4 acute treatment: cells were tail-vein injected in NSG mice and after 14/28 days mice were i.v. treated with 1959-sss/DM4 (10mg/kg). Tissue collection of mouse serum, livers, lungs and kidneys was performed for ELISA, IHC and HPLC analysis. n=2 mice per condition were considered.

1. Introduction

Antibody–drug conjugates (ADCs) have emerged as an innovative oncology therapy by combining the selectivity of monoclonal antibodies with the potent cytotoxicity of small-molecule drugs[1-4]. This strategy enables the targeted delivery of highly toxic agents directly to tumour cells, thereby minimizing damage to normal tissues, a concept validated by several approved ADCs and numerous candidates currently under clinical evaluation [5-7]. An attractive target for ADC therapy is LGALS3BP, a heavy glycosylated protein that resulted to be overexpressed in a wide range of malignancies and implicated in tumour progression, metastasis, and immune modulation [8]. Its abundant secretion into the tumour microenvironment supports the use of a non-internalizing ADC strategy, where the therapeutic antibody accumulates in the tumour milieu and locally releases its cytotoxic payload[4, 9].

This agent utilizes a humanized therapeutic anti-LGALS3BP antibody (1959) that has been engineered by substituting key cysteine with serine residues to allow precise, site-specific conjugation of the maytansinoid DM4 via a disulphide linker[9-11]. This strategy achieves a well-defined drug–antibody ratio while preserving high affinity for LGALS3BP. Upon systemic administration, 1959-sss/DM4 selectively localizes to LGALS3BP-positive tumours. In the reducing tumour environment, the disulphide bond is cleaved to release DM4. Owing to its hydrophobicity, DM4 readily crosses cell membranes, where it binds to tubulin, disrupts microtubule dynamics, induces cell cycle arrest, and triggers apoptosis.

This ADC is endowed with a potent and durable antitumor activity as evaluated in several preclinical model using different cancer models[12-15]. Furthermore, this ADC when labelled with Zirconium-89, effectively visualized LGALS3BP-secreting tumours in mouse models using PET imaging [16].

Notably, DM4 undergoes metabolic transformation (S-methylation) to yield S-methyl-DM4, a metabolite that demonstrates notable cytotoxicity as its parental drug [17, 18]. In addition to its direct cytotoxic effect, the ADC's efficacy is further amplified by the "bystander effect" [19]. This phenomenon allows the released DM4 and S-methyl-DM4 to diffuse into adjacent tumour cells and cancer-associated cells (such as cancer-associated fibroblasts, immune cells, and adipocytes) that may lack or express low levels of LGALS3BP, thereby broadening the antitumor response. However, this beneficial bystander killing may also lead to off-target toxicity if free DM4 or its metabolites accumulate in normal tissues. Hence, comprehensive pharmacokinetic and biodistribution studies of both DM4 and S-methyl-DM4 are essential for optimizing the therapeutic window of DM4-based ADCs. Traditional mass spectrometry-based methods offer high sensitivity and accuracy; however, their high cost and requirement for specialized expertise often restrict widespread adoption [20]. To address these limitations, our study presents a novel high-performance liquid chromatography (HPLC) method coupled with diode array detection (DAD) that enables the simultaneous quantification of DM4 and its primary metabolite, S-methyl-DM4, in biological matrices. We applied this method to tissue samples from pseudo-metastatic neuroblastoma models, previously validated in preclinical studies, to comprehensively characterize the pharmacokinetics and biodistribution of DM4 released from the ADC. This approach further enables us to evaluate the stability and tumour-targeting efficiency of 1959-sss/DM4, while elucidating the relationship between payload release, metabolic conversion, and antitumor efficacy.

2. Materials and Methods

2.1 Cell lines and Biochemicals

Human neuroblastoma SKNAS cells were purchased from American Type Culture Collection (ATCC; Rockville, MD, USA). The primary human neuroblastoma hNB cell line was isolated from a non-MYCN amplified tumour metastasized in the neck of a 3-year-old male patient. The 11q and ALK status is not known [12]. SKNAS were grown in Dulbecco's modified Eagle's medium (DMEM, Gibco; Whaltman, MA, USA), while stable transduced hNB CTRL and LGALS3BP in Roswell Park Memorial Institute (RPMI) 1640 (Gibco). All media were supplemented with 10% heat-inactivated fetal bovine serum (FBS) (Gibco), 100 U/mL penicillin and 100 µg/mL streptomycin (Sigma-Aldrich Corporation, St. Louis, MO, USA). All cells were maintained at 37°C in a humified air with 5% CO2. All cell lines were tested for mycoplasma contamination through polymerase chain reaction (PCR).

2.2 Chemicals

For high-performance liquid chromatography (HPLC) analysis, Ravtansine (DM4) and its primary metabolite, S-methyl-DM4 (S-Met-DM4), were sourced from MedChemExpress (New Jersey, USA). N,N-Dimethylacetamide (DMA) was obtained from Sigma-Aldrich (St. Louis, MO, USA). Acetonitrile (AcN) and formic acid, both of HPLC grade, were supplied by Carlo Erba Reagents (Milan, Italy). Milli-Q purified water (Merck, Darmstadt, Germany) was used for all procedures requiring high-purity water.

The lysis buffer was prepared with 6M urea, 100 mM Tris-base, 2% CHAPS, 1% Triton X-100, and 50 mM DTT (pH 7.5), with all reagents obtained from Merck. The extraction solvent consisted of ethyl acetate and methanol in a 7.5:1 (v: v) ratio, both purchased from VWR Chemicals

(Pennsylvania, USA). N-Ethylmaleimide (NEM) and ethyl butyl ether were also obtained from Merck. Phosphate-buffered saline (PBS; Oxoid) was prepared by dissolving one tablet per 100 mL of purified water. Ammonium sulphate and ammonium acetate were acquired by PanReac (Barcellona, Spain).

2.3 1959-sss/DM4 Purification and Characterization

The 1959-sss/DM4 antibody-drug conjugate (ADC) was prepared as previously described [4]. In brief, the 1959-sss antibody was reduced using a 60-fold molar excess of tris(2-carboxyethyl) phosphine (TCEP; Thermo Fisher Scientific) in phosphate-buffered saline (PBS; Sigma-Aldrich) at pH 7.4. The reaction was allowed to proceed overnight at room temperature (RT). Following reduction, the antibody was incubated in 100 mM phosphate buffer (pH 7.4) with a 100-folds molar excess of 5,5′-dithiobis-(2-nitrobenzoic acid) (DTNB; Sigma-Aldrich) under the same conditions. The reaction was halted by passing the resulting 1959-sss/DTNB complex through a G25 Sephadex column pre-equilibrated with PBS containing 5% sucrose and 10% N,N-dimethylacetamide (DMA; Sigma-Aldrich). To conjugate DM4, the DTNB-modified 1959-sss antibody was incubated overnight at RT with a 10-fold molar excess of thiol-maytansinoid DM4 in PBS supplemented with 5% sucrose and 10% DMA. The reaction was then quenched by adding a 500-folds molar excess of iodoacetamide (Sigma-Aldrich). Unconjugated DM4 was removed by size-exclusion chromatography using a G25 Sephadex column equilibrated with PBS/5% sucrose/10% DMA, under isocratic conditions at a flow rate of 1 mL/min. The final ADC concentration was determined by UV/Vis spectrophotometry, using an extinction coefficient (ε280) of 1.6 M^{-1} cm^{-1}.

The resulting ADC were characterized by SDS-PAGE and hydrophobic interaction chromatography (HIC) to determine the drug-to-antibody ratio (DAR). Analyses were conducted using an Agilent 1100 liquid chromatography system equipped with a diode array detector (DAD). The stationary phase was a MAbPac HIC-Butyl column (4.6 × 100 mm, 5 µm), maintained at 25°C (±1°C). The chromatographic run lasted 20 min. and utilized gradient elution to resolve three key components: the free antibody, the antibody conjugated to one molecule of DM4, and the antibody conjugated to two molecules of DM4. Mobile phase A consisted of 2 M ammonium sulphate in 0.1 M phosphate buffer (pH 7), while mobile phase B was 0.1 M phosphate buffer (pH 7), following the approach described by Tumey [21].

2.4 Stable lentiviral transduction

hNB CTRL and hNB LGALS3BP cell lines were obtained by stable lentiviral transduction starting from hNB parental cell line, as previously described[14]. Briefly, lentivirus particles were produced by transient co-transfection of packaging cell line HEK 293T with a three-plasmid expression system using Lipofectamine 2000 (Invitrogen, Thermo-Fisher, Waltham, MA, USA). Lentiviral plasmid pLenti-CMV-PURO-hLGALS3BP for stable overexpression of human LGALS3BP cDNA was obtained as previously described [14]. Briefly, HEK 293T cells were incubated for 6 h with transfection reagents. Lentiviral particles were collected after 48 h and 72 h and filtered through 0.45 µm pore sterile filters (Corning, NY, USA). The day before first cycle of transduction, 1.5 x 105 hNB cells were plated. After 24 h cells were incubated for 6 hours with media containing viral particles together with 4 µg/mL of polybrene to increase transduction efficiency. After the first cycle of transduction, cells were washed and cultured with fresh medium overnight before a second cycle of transduction the day after. Cells were then let grow under standard growth conditions for 72 h before

being put under selection with 1 μg/mL of puromycin (Sigma-Aldrich). Selection was maintained throughout all experiments performed. LGALS3BP levels were assessed through quantitative real-time PCR (qRT-PCR), western blotting and ELISA analysis.

2.5 Western blotting analysis

Human neuroblastoma cells (5 x 105) were seeded in complete medium and after 48 h they were lysed in RIPA buffer (50 mM Tris/HCl pH 7.6, 150 mM NaCl, 1% NP-40, 0.5% Na-Deoxycholate, 0.1% SDS, 1 mM EDTA pH 8) containing protease inhibitor cocktail (Sigma-Aldrich), phosphatase inhibitor cocktail (Roche, Thermo-Fisher), and Na3VO4 (Sigma-Aldrich). Lysates were clarified by centrifugation at 13000 rpm for 30 min at 4°C. Equal amounts of protein lysates (20 μg per sample), previously heated at 95°C for 5 min, were subjected to SDS-PAGE electrophoresis and then electro-transferred to nitrocellulose membranes for Western blot analysis. Membranes were blocked for 1 h at RT with 5% non-fat dry milk in PBS with 0.1% Tween20. Membranes were then incubated overnight at 4°C with the following primary antibodies: anti-human LGALS3BP (goat polyclonal; 1:1000, #AF2226; R&D Systems, MN, USA); anti-β-actin (mouse monoclonal; 1:40000, #A5441; Sigma-Aldrich). After three washes in PBS-0.1% Tween20, the membranes were hybridized with horseradish peroxidase (HRP)-conjugated secondary antibodies (goat or mouse; Biorad, CA, USA). Detection of signal bands was performed with Clarity Western ECL substrate (#1705061; Biorad). Images of membranes were acquired with an UvitecFire reader (Cambridge, UK) and analysed with Alliance Uvitec software (Cambridge, UK).

2.6 Quantitative reverse transcription-PCR (qRT-PCR)

A total of 5 x 105 human neuroblastoma cells were cultured in complete medium for 48 h, then total RNA was isolated from collected cells by RNeasy kit (#74136; Qiagen, Germany). One microgram of total RNA was reverse transcribed to cDNA by using High-capacity cDNA reverse transcription kit (#4368814; Applied Biosystems, MA, USA) according to the manufacturer's instructions. Realtime qPCR was performed with a CFX96 Touch Real-Time PCR Detection system (Biorad) using SsoAdvanced Universal SYBR Green supermix (#1725271; Biorad), according to manufacturer's instructions. The primers used at a final concentration of 350nM were: hLGALS3BP FOR 5'-GAA CCC AAG GCG TGA ACG AT-3', hLGALS3BP REV 5'-GTC CCA CAG GTT GTC ACA CA-3'; h-β-actin FOR 5'-CAG CTC ACC ATG GAT GAT GAT ATC-3', h-β-actin REV 5'-AAG CCG GCCTTG CAC AT-3'. Each sample analysis was performed in triplicate. As a negative control, a no template control was performed. The following PCR program was used: 95°C for 30s, 40 cycles of denaturation at 95°C for 15s and annealing/extension at 57°C for 30s. To verify the specificity of the amplification, a melting curve analysis was performed immediately after the amplification protocol. qRT-PCR results were calculated using the ΔΔCt method and normalized using human β-actin as reference gene.

2.7 Immunofluorescence and confocal imaging

For confocal live cell staining, 2 x 105 hNB CTRL or LGALS3BP were plated on glass coverslips in 12-well plates and cultured under standard growth conditions. After 24 h, cells were incubated for 90 min at 37°C with 10 μg/mL of anti-LGALS3BP antibody 1959 in PBS Ca2+/Mg2+ with 3% BSA. Cells were then fixed with 4% paraformaldehyde for 10 min at RT and stained with anti-human

AlexaFluor-488 conjugated secondary antibody (1:200, #A11013; Invitrogen) and Hoechst3342 (1:500; Sigma-Aldrich) for 30 min at RT in the dark. Confocal images were acquired using a Zeiss LSM800 inverted confocal microscope system (Carl Zeiss, Germany).

2.8 In Vivo mouse models and treatments

NOD.Cg-Prkdcscid Il2rgtm1Wjl/SzJ (NSG) mice were purchased from Jackson Laboratory and bred in the animal facility of CAST, University "G. D'Annunzio" of Chieti-Pescara. Mice were maintained at a temperature of 24–26°C under pathogen-limiting conditions as required. Cages, bedding and food were autoclaved before use, and food and water were provided ad libitum. Animal care and experimental procedures were approved by the Ethics Committee for Animal Experimentation of the Institute in accordance with Italian law (Authorization No. 1118/2020-PR). The animal health status was monitored daily, and body weight was measured once a week during experiments. For HPLC method optimization and preliminary analyses, healthy female NSG mice (8 weeks old) were sacrificed, and lungs, liver, kidneys, and serum were collected.

- hNB CTRL and hNB LGALS3BP NSG pseudo-metastatic model:

For the therapeutic pseudo-metastatic experiment, 8-week-old female NSG were injected intravenously (lateral tail vein) with 1 x 104 hNB CTRL or LGALS3BP cells. After 7 days, mice were randomly divided into groups (n=6) that received vehicle (PBS) or ADC 1959-sss/DM4 (10 mg/kg; twice weekly i.v administration; three total administrations). After 18 days post-injection (4 days after the last treatment), blood was collected through intra-cardiac puncture to obtain serum, and lungs were harvested, fixed in 10% neutral buffered formalin, paraffin-embedded and sectioned at a 5-µm thickness for histological analysis. To optimize the detection of microscopic metastases and ensure systematic, uniform and random sampling, samples were transversally cut into 2.0 mm thick parallel slabs, with the first cut randomly positioned within the first 2mm of the organ, resulting in 5–8 slabs per lung and kidney and 6–8 slabs per liver. The slabs were then embedded cut-surface down, and sections were stained with Haematoxylum and Eosin (H&E) for metastasis analysis. Two pathologists independently evaluated slides, and images were acquired using Nanozoomer scanner (Hamamatsu). To quantify the extent of metastatic lesions at each time point, the percentage of metastatic area relative to the total liver area was assessed using the area annotation tool in NDP.view2 software.

For acute treatments, after 14 days post-injection of 1 x 104 hNB CTRL or LGALS3BP cells, mice were randomly divided into groups (n=3) that received single i.v. administration of PBS or 1959-sss/DM4 (10mg/kg). Tumour free (TF) mice (n=1) were treated with PBS or 1959-sss/DM4 as controls. After 72 h from treatment, mice were sacrificed and mouse sera, lungs and livers were collected, instantly frozen in liquid nitrogen and stored at -80°C for further analysis.

- SKNAS NSG pseudo-metastatic model:

To investigate the pharmacokinetics of DM4 and S-Met-DM4 following 1959-sss/DM4 administration, 8-week-old female NSG mice were injected via the lateral tail vein with 1×10^6 SKNAS cells. After three weeks, mice received a single 10 mg/kg dose of 1959-sss/DM4 and were sacrificed at predefined time points: 0, 8, 16, 24, 36, 48, 56-, 72-, 96-, and 168-hours post-

administration (n=2 mice for time point). Sera, lungs, livers, and kidneys were collected, with half of each organ fixed, embedded, sectioned, and H&E-stained for metastasis analysis as before, while the remaining portion was snap-frozen for homogenization and analyte extraction. For efficient tissue homogenization, organs were finely minced immediately upon collection as an initial sample-processing step before snap freezing in liquid nitrogen.

2.9 Immunohistochemistry (IHC)

Sections were immunostained with anti-human LGALS3BP (#AF2226, R&D). Microwave pretreatment (10 min) in citrate buffer (pH 6.0) was performed for antigen retrieval. The biotinylated horse anti-goat IgG secondary antibody (BA-9500, Vector Laboratories) and the HRP Detection IHC kit (ab93677, Abcam) were used to detect the antigen. After incubation with the chromogen 3,3-diaminobenzidine DAB (K3468, Dako), slides were counterstained in Haematoxylin (CATHE-MM, Biocare Medical) and scanned with Nanozoomer scanner from Hamamatsu. Images were acquired with NDP.view 2 software.

2.10 ELISA

To evaluate LGALS3BP cell media concentration, 5 x 105 human neuroblastoma cells were cultured in complete medium for 48 h before supernatants were collected. Secreted human LGALS3BP levels were evaluated by sandwich ELISA that was performed as follows: Maxisorp 96-well plates (Nunc, Thermo-Fisher) were coated with murine anti-LGALS3BP antibody SP2 (at 2 µg/mL) overnight at 4°C [11]. After blocking with 1% bovine serum albumin (BSA) in PBS for 1 h at RT, 100 µl of cell culture media or recombinant LGALS3BP (15-1000 ng/mL) were added and incubated for 1 h a RT. After three washes with PBS-0.05% Tween20, humanized anti-LGALS3BP antibody 1959 (at 1µg/mL) was incubated for 1 h at RT. For the detection, after three washes with PBS-0.05% Tween20, anti-human IgG-HRP (#A01070; Sigma-Aldrich) was added (1:5000) and incubated for 1 h at RT. After three washes, stabilized chromogen was added for at least 10 min in the dark before stopping the reaction with the addition of 1N H2SO4. The resulting colour was finally read at 450nm with an ELISA plate reader (Tecan, Switzerland).

To assess the pharmacokinetics of 1959-sss/DM4 *In Vivo*, a custom ELISA-based quantification was performed on serum samples from SKNAS pseudo-metastatic mice collected at specific time points (8, 16, 24, 32, 48, 56, 72, 100h) from mice treated with a dose of 10 mg/kg of body weight. Based on the weights recorded at the time of injection, the total ADC administered ranged from approximately 269 to 354 µg per mouse. Serum concentrations of intact ADC were then interpolated and converted to total circulating levels by assuming a blood volume of 1.5 mL per animal.

NUNC Maxisorp 96-well plates (Thermo Fisher Scientific) were coated overnight at 4°C with 1 µg/mL of a mouse anti-DM4 monoclonal antibody in PBS. The following day, wells were blocked with 1% (w/v) BSA in PBS for 1 hour at room temperature (RT). Mice serum samples, diluted 1:1000 in PBS, or 1959-sss/DM4 standards (1–60 ng/mL) were added (100 µL per well) and incubated for 1 h at1 RT. After three washes with PBS containing 0.05% (v/v) Tween-20, detection was performed using an anti-human IgG-HRP conjugate (#A01070, Sigma-Aldrich) diluted 1:5000 in PBS, followed by a 1-hour incubation at RT. Following another wash step, stabilized chromogen was added and incubated for 10 min in the dark. The reaction was then stopped with 1 N H_2SO_4, and absorbance was measured at 450 nm using a Tecan microplate reader (Männedorf, Switzerland).

2.11 Analysis of DM4 and S-Me-DM4 in Tissue Extracts

Stock solutions of DM4 and S-Met-DM4 were prepared at a concentration of 1 mg/mL by dissolving 1 mg of each compound in 1 mL of DMA. To ensure complete solubilization, these solutions were sonicated in an ultrasonic bath for 2 min at 20°C.

Blank tissue samples (lung, liver, and kidney) from mice were utilized to establish calibration curves. After homogenizing the tissues in lysis buffer, known amounts of DM4 and S-Met-DM4 were spiked into the homogenates at concentrations ranging from 0.04 to 20 µg/mL. For both standard and ex vivo samples, entire organs were weighed and homogenized with lysis buffer at a 1:5 (w: v) ratio for 1 min at low speed in an ice bath with a tissue raptor and incubated for 30 min to allow complete lysis. Extraction is performed using ethyl acetate: methanol (7.5: 1, v: v) at a 1:1 (v: v) ratio with the sample, followed by centrifugation at 10000 rpm for 10 min to recover the organic phase. This step is repeated three times, with all organic phases pooled and subjected to an additional centrifugation at 10000 rpm for 15 min at 4°C. The resulting supernatant is dried in a SpeedVac for 2 h, reconstituted in DMA, sonicated for 10 min, and centrifuged at 14000 rpm for 15 min at 4°C before chromatographic analysis.

Tissue extracts containing DM4 and S-Met-DM4 were analysed using an HPLC method previously described [22]. Briefly, was used an Agilent 1100 liquid chromatography system (Agilent Technologies, Waldbronn, Germany), featuring a solvent pump, an online degasser, a thermostated autosampler with a column compartment, and a diode array detector (DAD), with data acquisition and processing handled by Chemstation Software (Agilent).

The column used is a C18 reversed-phase column (GraceSmart RP18, 4.6 × 150 mm, 5 µm; Grace, Deerfield, IL, USA) thermostated at 40°C (±1°C). Quantitative measurements were performed at 254 nm. The mobile phase consisted of Milli-Q water and methanol in a 25:75 (v: v) ratio, with both solvents acidified using 0.10% (v: v) formic acid. Isocratic elution was conducted at a flow rate of 1 mL/ min, with an injection volume of 20 µL. The method was rigorously validated in accordance with international guidelines, with assessments covering linearity, selectivity, precision, trueness (both intraday and interday), ruggedness, as well as limits of detection (LOD) and quantification (LOQ).

2.12 Software analysis and statistical evaluation

Data acquisition and processing was performed using Chemstation Software (Agilent). For statistical analysis and method validation parameters GraphPad Prism 9.0 Software (GraphPad Software, Inc., San Diego, CA, USA). For quantitative and pharmacokinetic data, was used Excel and the add on “PK Solver”. For the evaluation of statistical significance of metastatic areas, unpaired t-test was used and $p<0.05$ was considered as statistically significant.

3. Results

3.1 ADC generation, characterization, and payload analysis

The linker-less non-internalizing ADCs targeting LGALS3BP was obtained through the site-specific conjugation of the Ravtansine (DM4) maytansinoid to the engineered mAb 1959-sss, as previously described [9].

To evaluate the Drug Antibody Ratio (DAR), we optimized a Hydrophobic Liquid Chromatography (HIC) method using a mobile phase A composed of 1.5 M ammonium sulfate with 0.1 M sodium phosphate (pH 7) and mobile phase B of 0.1 M sodium phosphate (pH 7). Various gradient profiles were tested to fine-tune the resolution between peaks, and through the final gradient conditions, the corresponding chromatogram clearly distinguishes the free antibody, and the ADC conjugated with two DM4 molecules.

The drug-antibody ratio (DAR) was determined by calculating the area percentage of each chromatographic peak using the following equation:

$$DAR=[(AUC0\%\times 0)+(AUC1\%\times 1)+(AUC2\%\times 2)]100$$

Where 〖AUC〗_0% is related to the free antibody, 〖AUC〗_1% and 〖AUC〗_2% represents antibody conjugated to one or two molecules, respectively. As reference control for retention time free antibody was injected before conjugation. The ADC batch produced and used in this work displayed an average DAR equal to 2 and their purity was confirmed by SDS-PAGE.

With the aim to analyse ADC payload in tumour samples we developed a chromatographic method able to detect and quantify both DM4 and its metabolite S-Met-DM4. First, tissue extraction protocol was optimized to obtain the highest chromatographic sensitivity. Analytes were spiked in blank tissues and different weight-to-volume (w: v) ratios (1: 2, 1: 5, and 1: 10) were tested for homogenization, using a Tissue Rupture device at low speed for 1 minute to minimize drug loss. The 1: 5 ratios offered the best balance between analyte recovery and matrix effects, making it the preferred choice. This is due to matrix interference in 1: 2 w: v ratio, differently than 1: 5 and 1: 10, which were almost equal. To follow GC principles the lower lysis buffer volume was chosen. Although sonication was initially considered to enhance cell lysis, it resulted in sample oxidation and was therefore excluded from the final protocol.

Regarding analyte extraction, early attempts with protein precipitation (PP) through acetonitrile (AcN) or dimethylacetamide (DMA) in a 1:3 (v:v) ratio yielded poor analyte recovery. As a result, a liquid-liquid extraction (LLE) strategy was adopted. Various homogenization solvents were evaluated, including 10 mM Tris-HCl, PBS (pH 7.5), acidified water (pH 4), alkaline water (pH 10), a 50:50 (v:v) water-methanol mixture, and lysis buffer with and without N-ethylmaleimide (NEM). Alkaline water (pH 10) caused complete tissue saponification and was excluded. Ultimately, lysis buffer without NEM provided the highest recovery and was selected as the optimal solvent. For LLE, two extraction solvent systems were compared: ethyl acetate: methanol (7.5: 1, v: v) and ethyl acetate: methyl butyl ether (1:1, v: v). The latter caused a significant increase in HPLC system pressure, making ethyl acetate: methanol (7.5:1, v: v) the preferred option. In keeping with Green Chemistry principles, we minimized the extraction solvent volume from a 3.4:1 to a 1:1 ratio with

the homogenate without compromising efficiency. Drying time was also optimized, revealing that a 2-hour SpeedVac process effectively removed solvent while preventing heat-induced degradation of the analytes. Moreover, instead of using only a representative portion of the tissue, the entire sample was homogenized to maintain reproducibility in drug quantification.

Finally, to determine the optimal experimental conditions for validating our novel HPLC method, extraction efficiency for each tissue type was evaluated by comparing the integrated chromatographic peak areas of samples spiked with DM4 or S-Met-DM4 either before (i.e., spiked directly into the lysis buffer) or after the homogenization process, as required by ICH guidelines [23-25]. In accordance with these guidelines, a recovery test was performed. The results demonstrate that the extraction method is reproducible and minimizes analyte loss during the optimized procedure. Given the use of different biological matrices, the test was repeated across all matrices employed for method validation, revealing consistent recovery values.

3.2 Method validation

The analytical method was validated in accordance with international guidelines for linearity, selectivity, precision, trueness, and sensitivity. The chromatographic conditions used were the same of our previous work [22]. Both DM4 and its primary metabolite S-Met-DM4 were obtained after been spiked in blank homogenized tissues. Calibration curves for both DM4 and its primary metabolite S-Met-DM4 were linear over the range of 0.06 to 20 µg/mL, with correlation coefficients (R^2) of 0.9928, ensuring that the method reliably quantified the analytes even at low concentrations.

For DM4, the mean retention time was established at 3.87 minutes. Intra-day and inter-day precision were confirmed by examining quality control (QC) samples at low, medium, and high concentration levels. For instance, the intra-day precision (n = 33) showed a standard deviation (ST DEV) of 0.03 with retention times consistently near 3.87 minutes, while inter-day precision (n = 55) demonstrated similar reliability with minor variations (RSD values of 0.74% to 1.71%). The method's trueness was validated with QC samples showing slight negative biases (around –7.6% to –11.2% for DM4), yet these values were within acceptable limits. Sensitivity metrics further confirmed the robustness of the method, with limits of detection (LOD) of 0.04 µg/mL and limits of quantification (LOQ) of 0.06 µg/mL. The calibration slopes (48.30 for intra-day and 47.70 for inter-day) and intercepts (approximately 1.345 to 1.487) reinforced the method's linear response.

S-Met-DM4, with a mean retention time of 5.37 minutes, exhibited comparable performance. The intra-day and inter-day precision were confirmed by ST DEVs of 0.07 and 0.12, respectively, with relative standard deviations (RSDs) ranging from 1.25% to 2.32%. Slight variations in retention time (minimum values near 5.25 minutes and maximum values up to 5.80 minutes) were observed. The slopes for S-Met-DM4 were around 14.44 to 14.57, with intercepts close to 6.395 and 6.318, and R^2 values of 0.995 and 0.992. Together, these parameters underline the method's high sensitivity, precision, and reliability for both analytes. To ensure robustness and reproducibility, the method was validated across different tissue types: for not only lung but also Liver, Kidney and solid tumour. Blank Matrices were compared to matrices spiked with DM4 and S-Met-DM4 of either liver, kidney or solid tumour to avoid interferences due to change of matrix and to ensure the correct response of the previously optimized protocol.

Once linearities were achieved, t-test was investigated to check out intercept and slope trend matching all tissues. Pairwise comparisons between the four matrices were performed using

independent two-sample t-tests. Six pairwise tests were conducted to evaluate potential differences between all possible combinations (lung vs kidney, lung vs liver, lung vs tumour, kidney vs liver, kidney vs tumour, liver vs tumour) of matrices for drug and its main metabolite. Confidence level between various matrices is allowable, being above 99%. At the end, the method was successful validated in lung, liver, kidney and solid tumour tissues.

3.3 Specific anti-tumour activity and accumulation of anti-LGALS3BP ADC in neuroblastoma pseudo-metastatic mouse models

To assess the specificity and robustness of the method, the previously described ADC 1959-sss/DM4 was employed for *In Vivo* detection and monitoring of its released payloads, DM4 and S-Met-DM4. The primary human neuroblastoma cell line hNB, which lacks endogenous LGALS3BP expression, was used to generate an engineered variant ectopically overexpressing high level of human LGALS3BP. This model enabled a direct comparison of ADC targeting in LGALS3BP-positive versus LGALS3BP-negative tumors. As shown in Figure 1A, ELISA assay of hNB LGALS3BP cell medium exhibited significantly elevated ectopic expression of the protein compared to parental cells (hNB CTRL), whose expression was confirmed by intracellular protein analyses and mRNA levels (Figure 1B–C). Furthermore, the engineered cells displayed both intracellular and secreted LGALS3BP levels comparable to those of SKNAS neuroblastoma cells, which endogenously express the protein. Importantly, we confirmed 1959 antibody specificity trough confocal microscopy analysis in which cell surface and cell milieu were specifically labelled in hNB LGALS3BP but not in control cells (Figure 1D).

The selective targeting of the 1959-sss/DM4 ADC and payload accumulation were evaluated in the pseudo-metastatic NSG mice model where hNB derived lesions (LGALS3BP positive or negative) were analysed after ADC or PBS administrations. Specifically, after 72 h from treatment animals were sacrificed, and lung and liver tissues were harvested for anti-human immunostaining on tissue sections and HPLC analysis to quantify DM4 and its metabolite, S-Met-DM4 (Figure 1E). We firstly confirmed the specific accumulation of anti-LGALS3BP ADC in hNB LGALS3BP-induced lesions, as observed by the anti-human immunostaining performed on lung sections (Figure 1F).

Chromatographic analysis of lung tissues from PBS-treated, non-tumour-bearing mice yielded clean baselines with no detectable interference at the analyte retention times, thereby affirming the specificity and reliability of our analytical method. In ADC-treated groups, clear and distinct peaks for both DM4 and S-Met-DM4 were observed (Figure 1G and Table 1). Notably, lung tissues, recognized as the primary site for hNB cell attachment, from mice bearing LGALS3BP-positive tumours exhibited significantly elevated levels of both analytes compared to those from LGALS3BP-negative tumours, where DM4 and S-Met-DM4 were below the limit of detection, suggesting that ADC facilitates efficient payload release and accumulation at the intended target site (Figure 1G, left panel). Conversely, in liver tissues, which serve as central hub for drug metabolism and clearance, both DM4 and S-Met-DM4 were consistently detected across all ADC-treated groups (Figure 1G, right panel). Interestingly, at 72 hours post-treatment, nearly all DM4 that reached the metastatic lung tissue resulted to be metabolized into S-Met-DM4, meanwhile, the liver exhibited relatively higher levels of DM4 compared to the targeted lung tissues in both LGALS3BP-positive and -negative tumour-bearing mice. In these cases, the presence of DM4 and the absence of S-Met-DM4, suggests that DM4 may rapidly reach the target tissue and subsequently be delivered to the liver for metabolic elimination.

Additionally, the therapeutic activity of 1959-sss/DM4 was validated in a treatment setting where NSG mice were treated starting 7 days after hNB cell injection (Figure 1H), a time point at which metastases were already detectable. Treatment was administered twice weekly, with a total of three doses at 10 mg/kg, while control animals received vehicle (PBS). A potent, target-dependent ADC effect was observed, as evidenced by a significant reduction in metastatic lesion area, especially in mice injected with LGALS3BP-expressing hNB cells, but not in those bearing parental hNB tumors (Figure 1I-J). Overall, these findings confirm the specificity of HPLC analytical method in detecting DM4 and S-Met-DM4 in complex biological matrices also providing compelling evidence for the ADC's selective tumour targeting in metastatic neuroblastoma preclinical model.

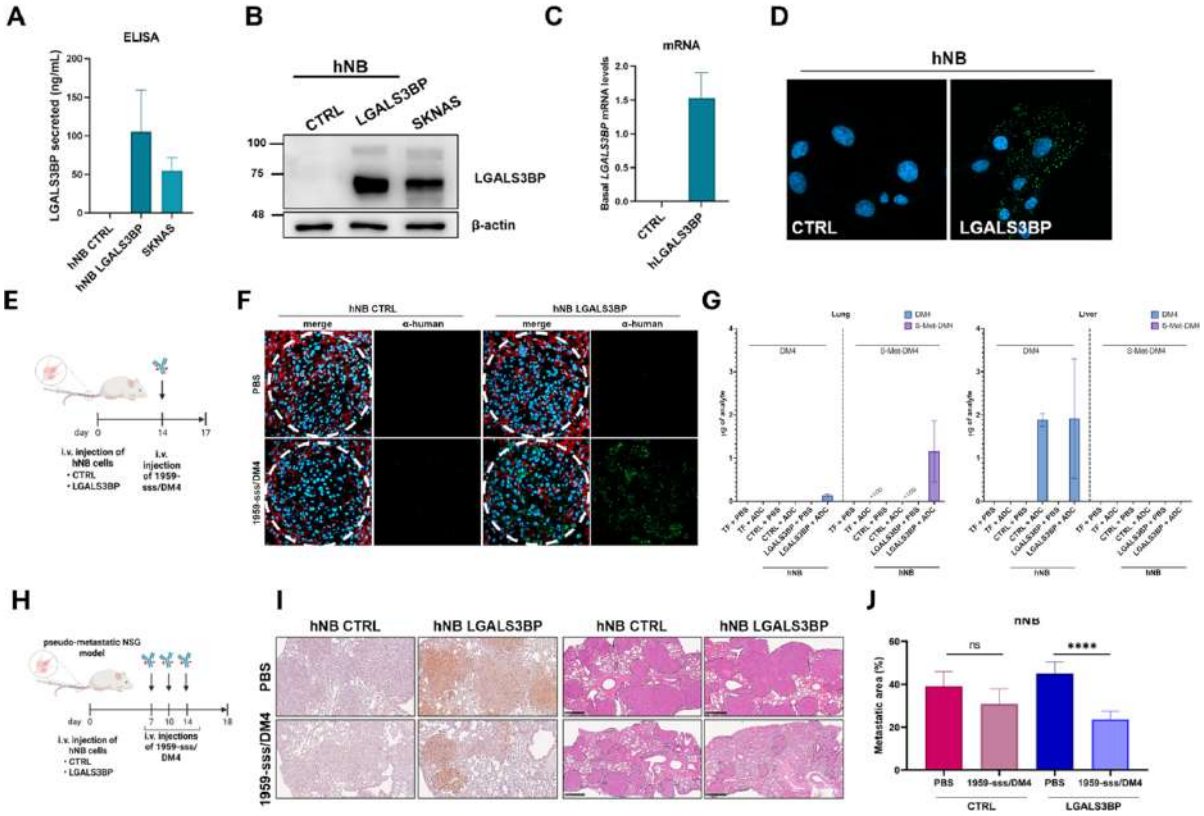


Fig. 1: (A) Secreted levels (ng/mL) of LGALS3BP evaluated by ELISA assay in hNB CTRL, hNB LGALS3BP, or SKNAS neuroblastoma cells. (n=2) (B) Western blotting images showing intracellular protein levels of LGALS3BP in hNB CTRL, hNB LGALS3BP, or SKNAS neuroblastoma cells. Equal amounts of protein were loaded for each sample. β-actin was used as loading control. (n=2) (C) Histogram showing transcriptional levels of LGALS3BP in hNB CTRL and hNB LGALS3BP cells normalized to housekeeping gene (β-actin). (n=3) (D) Confocal imaging of hNB CTRL and LGALS3BP cells showing LGALS3BP (green) and nuclei (Hoechst). Scale bar: 20µm. (E) Schematic representation of acute treatment (72 h) of hNB-induced pseudo-metastatic experiment: hNB CTRL or LGALS3BP cells were tail-vein injected in NSG mice, and at 14 days post-injection, a single i.v. administration of vehicle (PBS) or 1959-sss/DM4 (10mg/kg) was performed. Mice were sacrificed after 72 h post-treatment to evaluate biodistribution of 1959-sss/DM4 and abundance s-Met-DM4 in lung metastases. 3 mice were used per group. Tumor free (TF) mice were treated with vehicle (PBS) or 1959-sss/DM4 (10mg/kg) as controls (n=1). (F) Representative sections of lung metastases induced by hNB CTRL or hNB LGALS3BP cells in NSG mice i.v. treated in acute for 72 h with PBS or 1959-sss/DM4 immunostained with anti-human (green) for the detection of 1959-sss/DM4, with anti-CD31-105 (red) as endothelial marker, and Hoechst (blue) for nuclei. Merge of immunostaining or anti-human staining are reported for each condition. Scale bar: 100 µm. (G) Histogram of the abundance (µg/mL) of DM4 (Left panel)

and S-Met-DM4 (Right panel) metabolite obtained through HPLC detection after 72 h post-treatment in lung metastases and livers. TF stays for Tumor Free, CTRL for hNB LGALS3BP-negative and LGALS3BP for hNB LGALS3BP-positive. (H) Schematic representation of therapeutic hNB-induced pseudo-metastatic experiment: hNB CTRL or LGALS3BP cells were tail-vein injected into NSG mice, and at 7 days post-injection mice were treated with vehicle (PBS) or with 1959-sss/DM4 (10 mg/kg; twice weekly; three total injections). 6 mice were used per group. (I) Immunohistochemistry staining of human LGALS3BP (left) or haematoxylin/eosin (right) at the end of experiment (day 18) on lung metastases induced by hNB CTRL or LGALS3BP cells in NSG mice treated with vehicle (PBS) or with 1959-sss/DM4. Scale bars: 100 μm for LGALS3BP staining IHC; 500μm for haematoxylin/eosin staining. (J) Percentages of metastatic areas detected in lungs of mice at the end of experiment (day 18). Statistical significance (t-test) is reported: ns, not significant; ****p<0.0001.

Table 1. Total extracted amount (μg) of DM4 and its metabolite S-Met-DM4 through HPLC detection after 72 h post-treatment in lung and liver metastases. LOD, limit of detection.

Treatment Group	**LUNG**		**LIVER**	
1959-sss/DM4	**DM4 (μg)**	**S-Met-DM4 (μg)**	**DM4 (μg)**	**S-Met-DM4 (μg)**
LGALS3BP-Positive hNB	0.14 ± 0.03	1.16 ± 0.71	1,91 ± 1,39	–
LGALS3BP-Negative hNB	<LOD	<LOD	1,88 ± 0,15	–
Non-Tumour-Bearing (PBS Control)	<LOD	<LOD	–	–

3.4 Comparative Pharmacokinetic Behavior of Intact 1959-sss/DM4 and its Released Payload in Tumor Tissues and Systemic Circulation

To better evaluate the potential of the novel HPLC method developed, we employed a second pseudo-metastatic model of neuroblastoma using SKNAS cell line, which endogenously express considerable amount of LGALS3BP (Figure 1A-B). In this setting, we evaluated the biodistribution and pharmacokinetics of DM4 and its metabolite S-Met-DM4, over a nine-time-point period (8, 16, 24, 36, 48, 56, 72, 100, and 168 hours) post single administration of 1959-sss/DM4 ADC. As the primary site of metastasis of SKNAS cells is the liver, hepatic tissues were collected, and analytes were extracted and analysed by HPLC. While DM4 was detectable only during early time points (from 8 to 24 hours), suggesting a swift uptake followed by rapid metabolic conversion or clearance (Figure 2A, left) and reaching peak concentration at 8 h, by contrast the S-Met-DM4 metabolite demonstrated a delayed kinetic profile, reaching peak levels at 32 hours and remaining detectable from 16 to 56 h post treatment (Figure 2A, right). Lung and kidney tissues, which are secondary metastatic organs, also exhibited ADC-derived analytes, albeit at substantially lower levels, in line with the reduced number of metastatic lesions observed (data not shown).

Serum pharmacokinetics of the intact 1959-sss/DM4 ADC was evaluated by ELISA, in tumor bearing mice. The data revealed a rapid decline in circulating ADC levels after injection. At 8 hours, intact ADC was still detectable in the bloodstream, with circulating quantities corresponding to roughly 25–30% of the total administered dose. This suggests that during the initial distribution phase, a substantial fraction of the ADC payload is released at the tumor lesions, consistent with DM4 accumulation observed by HPLC at 8 h. Over the following 24 to 48 h, serum levels of intact ADC continued to decrease, with only a minor fraction of the original dose remained in circulation,

approximately below 10%. These findings support the hypothesis that DM4 is predominantly released from the ADC moiety within the first 24 hours post-administration, suggesting a relatively rapid release kinetic.

The pharmacokinetic data provide a compelling picture of the ADC's behavior and its payload (Figure 2B) release dynamics *In Vivo*. In the metastatic tissues, the released DM4 payload displays a rapid elimination profile, with a half-life of approximately 5.6 hours and a Tmax of 8 hours, indicating that its release from the ADC occurs quickly upon reaching the tumor microenvironment. In contrast, the metabolite S-Met-DM4 shows a distinctly delayed Tmax of 32 hours and a prolonged mean residence time of around 28.5 hours, suggesting how, following the initial release of DM4, metabolic conversion to S-Met-DM4 occurs gradually, resulting in a sustained presence of the active cytotoxic species within the tumor tissue. Although the overall exposure (AUC ~63.7 µg·h) for S-Met-DM4 is comparable to that of free DM4 (AUC ~56.6 µg·h) (Table 2).

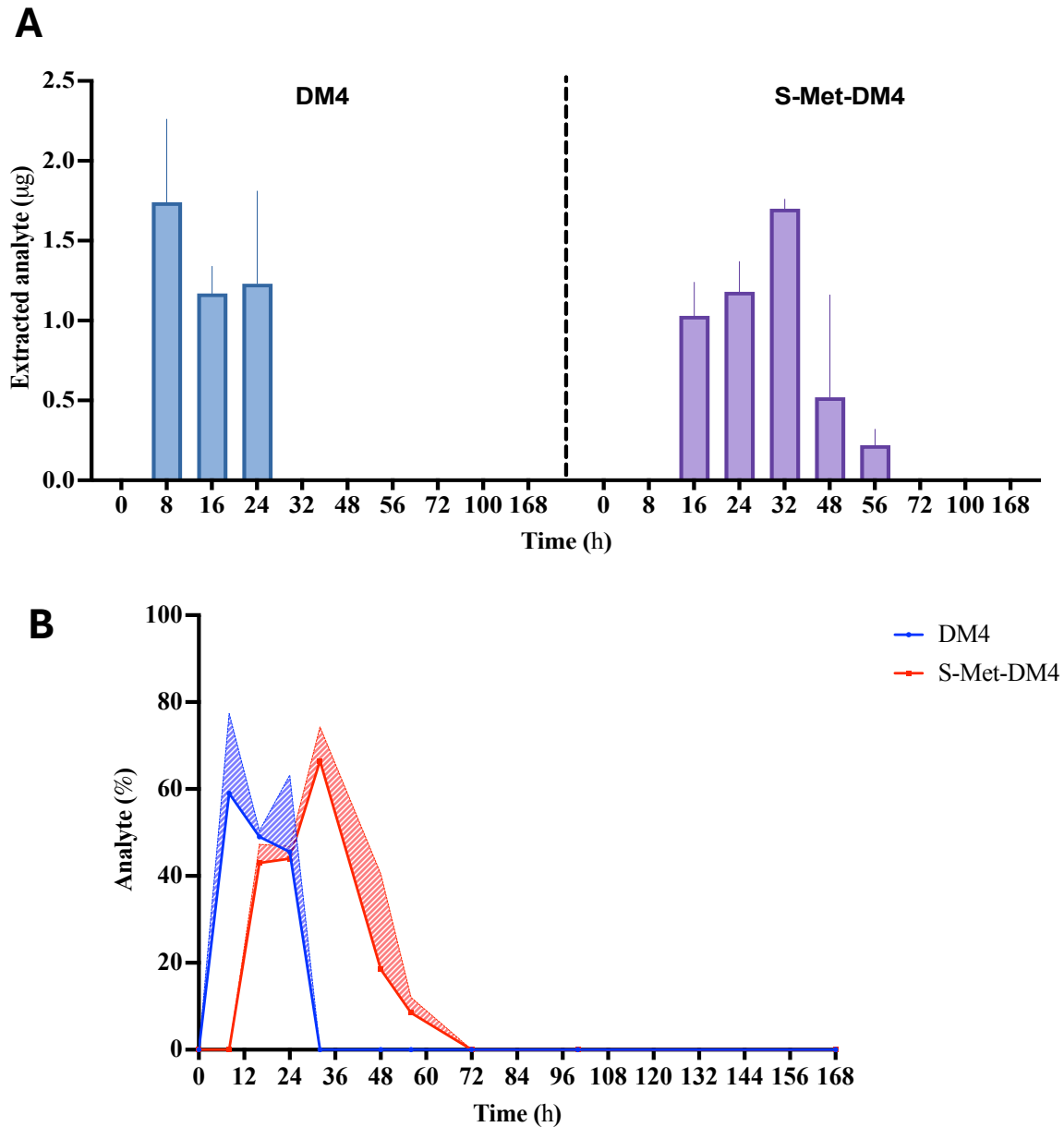


Fig. 2: (A) Histogram showing accumulation (µg) of DM4 (**Left panel**) and S-Met-DM4 **(Right panel)** through HPLC detection at the indicated time-points in mouse metastatic livers. **(B)** Dispersion graph showing recovered analyte (%) of DM4 (Blue) and S-Met-DM4 (Red) through HPLC detection at the indicated time-points in mouse livers.

Table 2. Pharmacokinetic parameters of *In Vivo*, cancer metastasis, ADC-delivered DM4 and S-Met-DM4.

Parameter	**Unit**	**DM4**	**S-Met-DM4**
Lambda_z	1/h	0,12	0,07
t1/2	h	5,60	9,72
Tmax	h	8,00	32,00
Cmax	ug	1,87	1,70
C0	ug	2,99	1,03
Clast_obs/Cmax		0,02	0,17
AUC 0-t	ug*h	56,32	59,68
AUC 0-inf_obs	ug*h	56,56	63,74
AUC 0-t/0-inf_obs		1,00	0,94
AUMC 0-inf_obs	ug*h^2	772,63	1816,45
MRT 0-inf_obs	h	13,66	28,50
Vz_obs	(µg)/(ug)	36,43	56,07
Cl_obs	(µg)/(ug)/h	4,51	4,00
Vss_obs	(µg)/(ug)	61,59	113,99

3.5 Greenness of the method

The analytical method's environmental sustainability was assessed using tools such as AGREE, AGREEprep, BAGI, and MoGAPI, which confirmed its alignment with green chemistry principles. A notable limitation identified was the offline collection of animal samples, necessitated by ethical guidelines for obtaining pharmacokinetic parameters [28-30]. The method's use of ethyl acetate and minimal methanol enhances its environmental profile, as these solvents are considered fewer toxic alternatives in chromatographic applications. The isocratic elution and 15-minute run time contribute to energy efficiency and facilitate scalability to more sensitive configurations, such as liquid chromatography coupled with mass spectrometry. The method's simplicity allows for the quantification of the drug and its main metabolite across various tissues without interference from different biological matrices, using standard instrumentation that requires less energy and does not necessitate highly specialized personnel. The straightforward sample preparation and analysis procedures suggest potential applicability in clinical settings. The almost overlap of most of the used tools means a good applicability, following various aspects of GC, as shown in Figure 3.

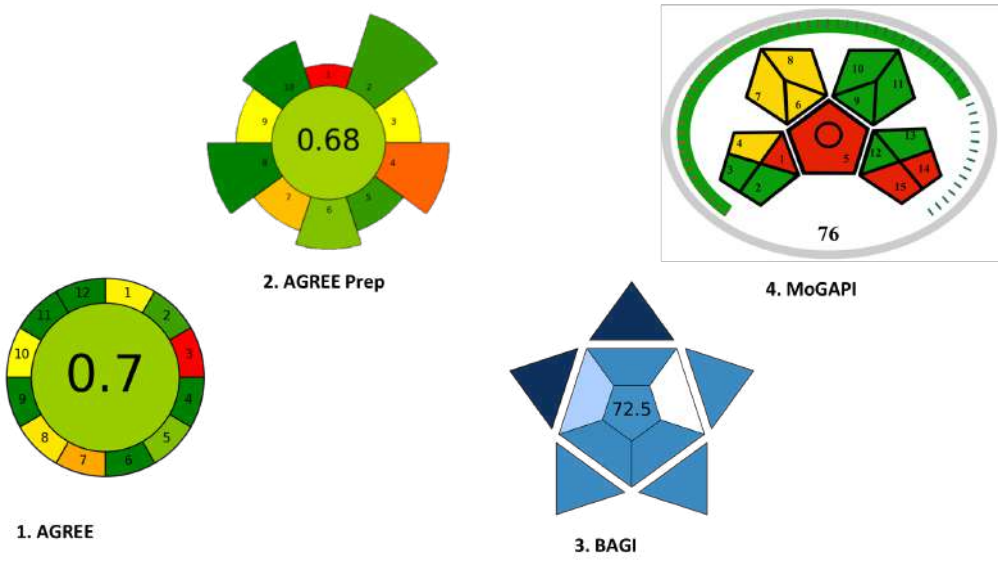


Fig. 3: Pictograms related to the herein reported procedure.

4. Discussion

In this study, we present a validated HPLC-DAD method that enables the simultaneous quantification of DM4 payload and its active metabolite, S-methyl-DM4, in biological matrices. To our knowledge, this is the first validated method capable of simultaneously quantifying both DM4 and its primary metabolite, S-methyl-DM4, in multiple biological matrices using HPLC-DAD. A comprehensive review of the literature revealed that existing quantification methods for these compounds rely almost exclusively on LC–MS/MS platforms, particularly in preclinical and pharmacokinetic studies. No peer-reviewed reports describing the use of HPLC-DAD for DM4 or S-methyl-DM4 detection in tissues such as liver, lung, or kidney were found [22-33]. Furthermore, many LC–MS/MS methods show variable extraction recoveries and typically require complex and costly instrumentation. In contrast, our method achieves high and consistent recovery across all tested matrices using a more accessible detection system, while maintaining strong linearity, precision, and reproducibility. These features position this HPLC-DAD approach as a novel, technically accessible and reproducible alternative capable of resolving both analytes directly in solid tissues, without the need for derivatization, radiolabelling, or protein tagging.

Following analytical validation, the HPLC-DAD assay was employed to profile the payload accumulation on tumor sites of the non-internalizing 1959-sss/DM4 ADC, which is currently under preclinical development [9, 12, 14-16]. To demonstrate the validity and specificity of this method, we utilized an LGALS3BP-negative neuroblastoma cell line (hNB), engineered to ectopically express LGALS3BP, to establish a robust system for specifically detecting the target-dependent ADC-delivered DM4 and S-Met-DM4 accumulation within tumor lesions. HPLC analysis revealed highly selective payload accumulation only in LGALS3BP-positive lesions. In hNB LGALS3BP-bearing mice, DM4 and S-Met-DM4 peaks were detected in lung tissues 72 h post-treatment, whereas both analytes remained below the limit of detection in parental hNB controls and vehicle-treated animals. Conversely, liver samples, reflecting systemic clearance, consistently contained both analytes in ADC-treated groups regardless of LGALS3BP status. In addition, HPLC data were

consistent with the *In Vivo* therapeutic effect of 1959-sss/DM4. Our data show a significant reduction in lung metastatic burden in hNB LGALS3BP-injected mice treated with 1959-sss/DM4, confirming both the functional specificity and therapeutic efficacy of this ADC.

Subsequently, we decided to better profile the behaviour of the released payload over time. In the pseudo-metastatic SKNAS model, where metastatic lesions localize preferentially to the liver, we observed a selective accumulation of DM4 in tumour-bearing mice, peaking between 8 and 24 hours after ADC administration. Importantly, S-methyl-DM4 levels rose more gradually and persisted over time, consistent with intracellular metabolism of the released payload and diffusion throughout the tumour lesions due to the "bystander" effect. The relative pharmacokinetic evaluation revealed a clear sequential release and turnover of the maytansinoid payload. The parent compound is released rapidly once the ADC localizes in tumour tissue. Over time, metabolic conversion gives rise to the S-methylated metabolite, which accumulates more slowly but remains detectable for an extended period, sustaining anti-tumour activity beyond the initial DM4 release. At the same time, the kinetics of the intact ADC in serum collected from tumor-bearing mice shows a rapid decline, aligning with the observed payload accumulation in tumor tissue. This indicate that payload release rapidly occurs within the tumor microenvironment, strongly suggesting that payload delivery is targeted rather than systemically persistent.

To our knowledge, this is the first report of a fully HPLC-DAD-based approach applied to the analysis of a maytansinoid-conjugated ADC, with potential applications in preclinical pharmacokinetics and biodistribution studies. These findings not only confirm the specificity of 1959-sss/DM4 but also provide a framework for future comparisons with other maytansinoid-based ADCs. Assessing payload accumulation *In Vivo* across different conjugation strategies may also clarify the impact of linker/linkerless chemistry on delivery efficiency. Furthermore, it lays the groundwork for head-to-head comparisons of different conjugation strategies and linker chemistries, and, given its isocratic format, can be readily adapted to LC–MS/MS detection for enhanced sensitivity and multiplexed metabolite profiling.

References

[1] C. Dumontet, J.M. Reichert, P.D. Senter, J.M. Lambert. Antibody–drug conjugates come of age in oncology. Nat Rev Drug Discov. 22 (2023) 641–661. 10.1038/s41573-023-00709-2.

[2] S. Kumari, S. Raj, M.A. Babu, G.K. Bhatti, J.S. Bhatti. Antibody-drug conjugates in cancer therapy: Innovations, challenges, and future directions. Archives of Pharmacal Research. 47(2024) 40-65. 10.1007/s12272-023-01479-6

[3] J.M. Lambert, A. Berkenblit. Antibody–drug conjugates for cancer treatment. Annu Rev Med. 69 (2018) 191–207. 10.1146/annurev-med-061516-121357

[4] S. Ponziani, G. Di Vittorio, G. Pitari, A.M. Cimini, M. Ardini, R. Gentile, S. Iacobelli, G. Sala, E. Capone, D.J. Flavell, R. Ippoliti, F. Giansanti. Antibody-Drug Conjugates: The New Frontier of Chemotherapy. Int. J. Mol. Sci, 21 (2020) 1- 26. 10.3390/ijms21155510

[5] A.V. Kamath, S. Iyer. Challenges and advances in the assessment of the disposition of antibody-drug conjugates. Biopharm Drug Dispos. 37 (2016) 66–74. 10.1002/bdd.1957

[6] L. Sevilla-Carrillo, E. García-Tercero, C. Alonso-Moreno, C. Moya-Lopez. Antibody Drug Conjugates (ADCs): Shaping the Future of Precision Oncology. Anti-Cancer Agents in Medicinal Chemistry. 2025. 10.2174/0118715206348204241128063329

[7] G. Villacampa, P.C. Morgado, L. Carità, V. Navarro, T. Pascual, R. Dienstmann. Safety and efficacy of antibody-drug conjugates plus immunotherapy in solid tumours: A systematic review and meta-analysis. Cancer Treatment Reviews, 131 (2024) 1-11. 10.1016/j.ctrv.2024.102847

[8] E. Capone, S. Iacobelli, G. Sala. Role of galectin 3 binding protein in cancer progression: a potential novel therapeutic target. Journal of translational medicine, 19(2021) 1- 18. 10.1186/s12967-021-03085-w

[9] F. Giansanti, E. Capone, S. Ponziani, E. Piccolo, R. Gentile, A. Lamolinara, A. Di Campli, M. Sallese, V. Iacobelli, A. Cimini, V. De Laurenzi, R. Lattanzio, M. Piantelli, R. Ippoliti, G. Sala, S. Iacobelli. Secreted galectin-3 binding protein as a therapeutic target for non-internalizing antibody–drug conjugates. Cancer Res. 294 (2019) 176- 184. 10.1016/j.jconrel.2018.12.018

[10] E. Piccolo, N. Tinari, D. Semeraro, S. Traini, I. Fichera, A. Cumashi, R. La Sorda, F. Spinella, A. Bagnato, R. Lattanzio, M. D'Egidio, A. Di Risio, P. Stampolidis, M. Piantelli, C. Natoli, S. Iacobelli. LGALS3BP, lectin galactoside-binding soluble 3 binding protein, induces vascular endothelial growth factor in human breast cancer cells and promotes angiogenesis, J of Mol Med. 91 (2013) 83- 94. 10.1007/s00109-012-0936-6

[11] S. Traini, E. Piccolo, N. Tinari, C. Rossi, R. La Sorda, F. Spinella, A. Bagnato, R. Lattanzio, M. D'Egidio, A. Di Risio, F. Tomao, A. Grassadonia, M. Piantelli, C. Natoli, S. Iacobelli. Inhibition of Tumor Growth and Angiogenesis by SP-2, an Anti–Lectin, Galactoside-Binding Soluble 3 Binding Protein (LGALS3BP) Antibody. Mol. Cancer Ther. 13 (2014) 916- 925. 10.1158/1535-7163.MCT-12-1117

[12] E. Capone, A. Lamolinara, F. Pastorino, R. Gentile, S. Ponziani, G. Di Vittorio, D. D'Agostino, S. Bibbò, C. Rossi, E. Piccolo, V. Iacobelli, R. Lattanzio, V. Panella, M. Sallese, V. De Laurenzi, F. Giansanti, A. Sala, M. Iezzi, M. Ponzoni, R. Ippoliti, S. Iacobelli, G. Sala. Targeting Vesicular LGALS3BP by an Antibody-Drug Conjugate as Novel Therapeutic Strategy for Neuroblastoma. Cancers. 12 (2020) 1-18. 10.3390/cancers12102989

[13] E. Capone, V. Perrotti, I. Cela, R. Lattanzio, L. Togni, C. Rubini, V.C.A. Caponio, L. Lo Muzio, M. Colasante, F. Giansanti, R. Ippoliti, S. Iacobelli, M.J. Wick, N.S. Burr, G. Sala. Anti-LGALS3BP antibody-drug conjugate treatment induces durable and potent antitumor response in a preclinical model of adenoid cystic carcinoma. Oral Oncology, 148 (2024) 1- 7. 10.1016/j.oraloncology.2023.106635

[14] I. Cela, E. Capone, A.Pece, G. Lovato, P. Simeone, M. Colasante, A. Lamolinara, A: Piro, M. Iezzi, P. Lanuti, V. De Laurenzi, R. Ippoliti, G. Sala. LGALS3BP antibody-drug conjugate enhances tumor-infiltrating lymphocytes and synergizes with immunotherapy to restrain neuroblastoma growth. J. Transl. Med. 23 (2025) 1- 15. 10.1186/s12967-025-06434-1

[15] B. Dufrusine, E. Capone, S. Ponziani, R. Lattanzio, P. Lanuti, F. Giansanti, V. De Laurenzi, S. Iacobelli, R. Ippoliti, A. Mangiola, G. Trevisi, G. Sala. Extracellular LGALS3BP: a potential disease marker and actionable target for antibody-drug conjugate therapy in glioblastoma. Mol Oncol. 17 (2023) 1460- 1473. 10.1002/1878-0261.13453

[16] O. Keinänen, S.M. Sarrett, S. Delaney, C. Rodriguez, E.J. Dayts, E. Capone, F. Sauniere, R. Ippoliti, G. Sala, S. Iacobelli, B.M. Zeglis. Visualizing galectin-3 binding protein expression with immunoPET. Molecular Pharmaceutics, 20 (2023) 3241-3248. 10.1016/j.oraloncology.2023.106635

[17] H.K. Erickson, P.U. Park, W.C. Widdison, Y.V. Kovtun, L.M. Garrett, K. Hoffman, R.J. Lutz, V.S. Goldmacher, W.A. Blatter. Antibody–maytansinoid conjugates are activated in targeted cancer cells by lysosomal degradation and linker-dependent intracellular processing. Cancer Res. 66 (2006) 4426–4433. 10.1158/0008-5472.CAN-05-4489.

[18] T.D. Nguyen, B.M. Bordeau BM, J.P. Balthasar. Use of Payload Binding Selectivity Enhancers to Improve Therapeutic Index of Maytansinoid-Antibody-Drug Conjugates. Mol Cancer Ther. 22 (2023) 1332–1342. 10.1158/1535-7163.MCT-22-0804.

[19] A.H. Staudacher, M.P. Brown. Antibody drug conjugates and bystander killing: is antigen-dependent internalisation required? Br J Cancer. 117 (2017) 1736–1742. 10.1038/bjc.2017.367

[20] X. Zhu. Novel LC-MS Strategies for Enhancing Understanding of Drug Effects and Exploring Disease Mechanisms (Doctoral dissertation, State University of New York at Buffalo).

[21] L.N. Tumey. Antibody-drug conjugates. Springer US. 2020. 10.1007/978-1-4939-9929-3

[22] G. Lovato, L. Ciriolo, M. Perrucci, L. Federici, R. Ippoliti, S. Iacobelli, E. Capone, M. Locatelli, G. Sala. HPLC-DAD validated method for the simultaneous quantification of DM4 and S-methyl-DM4 in biological matrices. J Pharm Biomed Anal. 235 (2023) 1- 10. 10.1016/j.jpba.2023.115642

[23] CDER e CVM. Bioanalytical Method Validation-Guidance for Industry, Food and Drug Administration, May 2018.

[24] International Conference on Harmonization of Technical Requirements for registration of Pharmaceuticals for Human Use, ICH Harmonised Tripartite Guideline (2005) Validation of Analytical Procedures: Text and Methodology Q2(R1), Geneva, 2005.

[25] International Conference on Harmonization of Technical Requirements for registration of Pharmaceuticals for Human Use, ICH Harmonized Tripartite Guideline, ICH guideline M10 on bioanalytical method validation and study sample analysis (2022).

[26] M. Locatelli, A. Kabir, M. Perrucci, S. Ulusoy, H.I. Ulusoy, I. Ali. Green profile tools: current status and future perspectives. Advances in Sample Preparation. 6 (2023) 1-15. 10.1016/j.sampre.2023.100068

[27] F. Pena-Pereira, W. Wojnowski, M. Tobiszewski. AGREE, Analytical GREEnness metric approach and software. Analytical chemistry. 92 (2020) 10076-10082. 10.1021/acs.analchem.0c01887

[28] W. Wojnowski, M. Tobiszewski, F. Pena-Pereira, E. Psillakis. AGREEprep–analytical greenness metric for sample preparation. TrAC Trends in Analytical Chemistry, 149 (2022) 1- 9. 10.1016/j.trac.2022.116553

[29] F.R. Mansour, J. Płotka-Wasylka, M. Locatelli. Modified GAPI (MoGAPI) tool and software for the assessment of method greenness: case studies and applications. Analytica, 5 (2024) 451-457. 10.3390/analytica5030030

[30] N. Manousi, W. Wojnowski, J. Płotka-Wasylka, V. Samanidou. Blue applicability grade index (BAGI) and software: a new tool for the evaluation of method practicality. Green chemistry. 25 (2023) 7598-7604. 10.1039/D3GC02347H

[31] Y. Fu, S. Gorityala, W. Li, D. Humphries, A. Ledvina, S. Cape, F. Picard. Sensitive LC-MS/MS quantification of unconjugated maytansinoid DM4 and its metabolite S-methyl-DM4 in human plasma. Bioanalysis, 14 (2022) 357-368. 10.4155/bio-2021-0275

[32] Y. Liu, F. Zhou, H. Sang, H. Ye, Q. Chen, L. Yao, P. Ni, G. Wang, J. Zhang. LC–MS/MS method for the simultaneous determination of Lys-MCC-DM1, MCC-DM1 and DM1 as potential intracellular catabolites of the antibody-drug conjugate trastuzumab emtansine (T-DM1). Journal of Pharmaceutical and Biomedical Analysis, 137 (2017) 170-177. 10.1016/j.jpba.2017.01.011

[33] C. Wei, D. Su, J. Wang, W. Jian, D. Zhang. LC–MS challenges in characterizing and quantifying monoclonal antibodies (mAb) and antibody-drug conjugates (ADC) in biological samples. Current Pharmacology Reports, 4 (2018) 45-63. 1

CHAPTER 4

LGALS3BP as a Cancer Biomarker in Liquid Biopsy

LGALS3BP is a tumor-associated protein with two key features relevant to liquid biopsy: it's abundantly secreted in the extracellular space and highly expressed in cancer-derived extracellular vesicles (EVs). These characteristics underscore the involvment of LGALS3BP in tumor–stroma interactions, its potential as an antibody target, and its utility as a measurable marker in body fluids for cancer diagnosis and monitoring (110). Early investigations of 90K/LGALS3BP identified elevated levels in cancer patients, leading to the development of reliable antibody-based assays (110). Current research emphasizes characterizing the various forms of LGALS3BP in blood, including soluble variants, large complexes, and EV-associated forms. The compartmentalization within EVs is particularly important, as it can protect LGALS3BP, facilitate its concentration, and enhance detectability when sample processing is standardized (110).

LGALS3BP has been detected in cerebrospinal fluid (CSF) within small, particle-like structures. This observation supports the use of LGALS3BP as a biomarker in central nervous system (CNS) fluids, which is particularly valuable for brain diseases, where CSF and blood EVs enable less-invasive detection of tumor activity (162). Over the past decade, LGALS3BP has been repeatedly identified as enriched in EVs. In glioma, for example, elevated LGALS3BP levels in plasma-derived EVs have been confirmed by ELISA in both whole plasma and EV fractions, highlighting its potential as a marker for disease burden or tumor characteristics (163).

4.1 Potential Diagnostic Biomarker Across Tumor Types

LGALS3BP has been proposed as an early diagnostic biomarker for various cancer types, either as a standalone marker or as part of multi-marker panels (Figure 13). Elevated circulating LGALS3BP levels in cancer patients compared to healthy controls support its potential as a broadly applicable tumor-associated analyte measurable by immunoassays. EV-associated LGALS3BP provides operational benefits, as EV isolation can enrich and stabilize the signal relative to freely circulating protein, thereby facilitating longitudinal monitoring when workflows are standardized (164). Nevertheless, the field remains heterogeneous in terms of analytical platforms, sampling strategies, and cut-off values. Reproducibility across cohorts is influenced by pre-analytical variables, including collection tubes, processing times, storage conditions, normalization methods, and quality control of EV fractionation. Furthermore, quantifying autoantibodies rather than antigen offers a complementary approach, since LGALS3BP is immunogenic and can induce circulating IgG autoantibodies (165). This orthogonal measurement may reveal immune recognition even when antigen quantification is constrained by clearance dynamics or variable compartmentalization. In addition to its diagnostic applications, LGALS3BP is associated with poorer outcomes and increased disease aggressiveness in several cancer types, except colorectal cancer, where elevated LGALS3BP levels correlate with reduced relapse rates and prolonged survival compared to lower levels (124). For central nervous system (CNS) tumors, LGALS3BP has been proposed as a prognostic marker and for disease monitoring, particularly when repeated tissue sampling is challenging, and imaging modalities are limited (130).

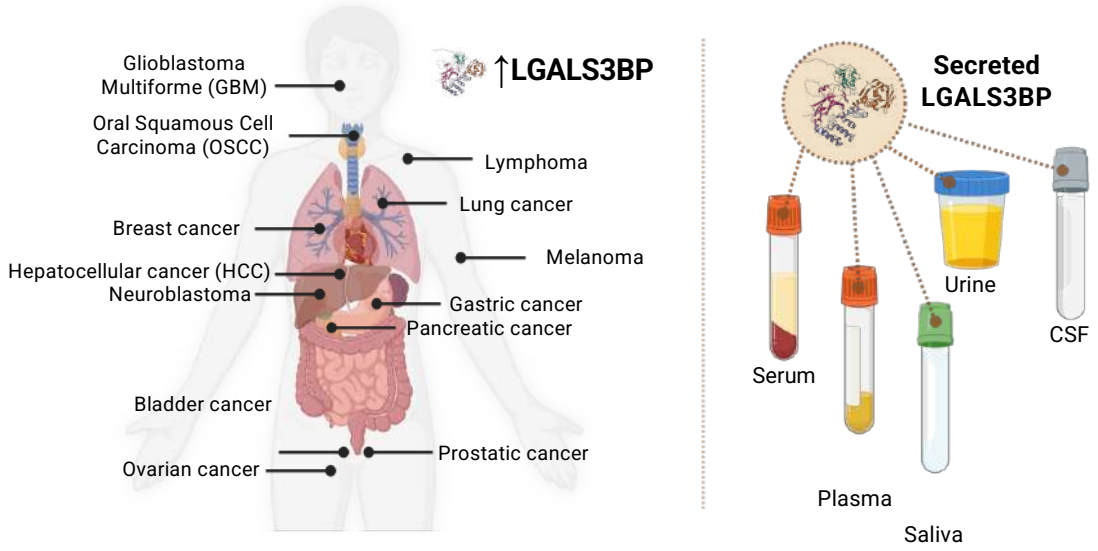


Figure 13. Illustration of cancer types characterized by high LGALS3BP expression and of body fluids showing elevated LGALS3BP secretion in multiple tumor indications associated with unfavorable clinical outcomes. *Image realized with Biorender online tool.*

4.2 LGALS3BP as early Biomarker in Bladder Cancer

In bladder cancer, LGALS3BP is a valuable biomarker due to the ease of serial urine collection and the proximity of urine to the tumor. Bladder cancer (BC) represents a significant global health concern, with GLOBOCAN 2022 reporting approximately 614,298 new cases and 220,596 deaths worldwide, reflecting both high incidence and substantial mortality (167). Many patients initially present with non–muscle-invasive disease; however, BC frequently recurs or progresses, necessitating long-term surveillance. This requirement contributes to some of the highest lifetime care costs among solid tumors, primarily due to repeated procedures and follow-up assessments (167). Early diagnosis is challenging because early-stage BC is often asymptomatic, and hematuria-based tests lack specificity. The primary diagnostic tool, cystoscopy with histological confirmation, is invasive, costly, and impractical for frequent, large-scale screening. Consequently, clinical guidelines continue to recommend cystoscopy for diagnosis and follow-up, placing a burden on both patients and healthcare systems (168). Urine cytology is commonly used in conjunction with cystoscopy due to its high specificity for high-grade disease and carcinoma in situ, but its overall sensitivity is low, particularly for low-grade tumors, limiting its reliability as a standalone early-detection method (169). Several FDA-approved urine assays (including NMP22, BTA Stat/TRAK, ImmunoCyt/uCyt+, and UroVysion FISH) provide additional diagnostic options, yet their variable performance has prevented them from supplanting cystoscopy in routine practice (170). This limitation is attributable to trade-offs between sensitivity and specificity, as well as confounding factors such as inflammation or benign conditions. Concurrently, research in liquid biopsy has expanded, leveraging the advantages of urine as a sample source for bladder tumors. Urine tumor DNA (utDNA) mutation and methylation assays frequently yield accurate diagnostic and monitoring results, while blood-based circulating tumor DNA (ctDNA) is under investigation for prognostication and detection of residual disease (171,172). Collectively, these developments indicate a transition

toward molecular testing for detection and monitoring, which may reduce the reliance on invasive procedures for certain patients.

Given that bladder cancer cells secrete substantial quantities of LGALS3BP, resulting in elevated concentrations in both urine and blood, this study aims to evaluate the potential of LGALS3BP as a urinary biomarker for early diagnosis and improved, less invasive monitoring of bladder cancer. In this context, the following study, to which the present author contributed, aims to demonstrate that LGALS3BP may serve as both a urinary cancer marker and a therapeutic target for the 1959-sss/DM4 ADC treatment or analogous therapeutic strategies, thereby integrating diagnostic and therapeutic approaches:

Pece, A., Lovato, G., Cela, I., Mercatelli, A., Ferro, B., Nikkola, J., Pagotto, S., Grottola, T., De Laurenzi, V., Cicchetti, R., Marchetti, A., Schips, L., Lattanzio, R., Iacobelli, S., Capone, E., Black, P., Daugaard, M., Marchioni, M. and Sala, G. (2026), Glycosylated LGALS3BP is highly secreted by bladder cancer cells and represents a novel urinary disease biomarker. Mol Oncol. https://doi.org/10.1002/1878-0261.70140 (173)

Glycosylated LGALS3BP is highly secreted by bladder cancer cells and represents a novel urinary disease biomarker

Asia Pece[1,2*], Giulio Lovato[1,2*], Ilaria Cela[1,2], Arianna Mercatelli[1,2], Benedetta Ferro[3], Jussi Nikkola[4,5], Sara Pagotto[2,6], Tommaso Grottola[1-7], Vincenzo De Laurenzi[1-2], Rossella Cicchetti [8], Antonio Marchetti[1,2,3], Luigi Schips[6,8], Rossano Lattanzio[1,2], Stefano Iacobelli[9], Emily Capone[2,10], Peter C. Black[4,5], Mads Daugaard[4,5#], Michele Marchioni[6,8#] and Gianluca Sala[1,2#]

[1] *Department of Innovative Technologies in Medicine & Dentistry, "G. d'Annunzio" University of Chieti-Pescara, Chieti, Italy;*

[2] *Center for Advanced Studies and Technology (CAST), "G. d'Annunzio" University of Chieti-Pescara, Chieti, Italy;*

[3] *Diagnostic Molecular Pathology, Unit of Anatomic Pathology, SS Annunziata Hospital, Chieti, Italy,*

[4] *University of British Columbia, Vancouver, BC, Canada;*

[5] *Vancouver Prostate Centre, Vancouver, BC, Canada*

[6] *Department of Medical Oral Science and Biotechnology, G. d'Annunzio University, Chieti, Italy;*

[7] *Unit of Surgical Oncology, Casa di Cura Pierangeli, 65124 Pescara, PE, Italy;*

[8] *Urology Unit, Department of Medical, Oral and Biotechnological Sciences, 'G. d'Annunzio University', Chieti, Italy.;*

[9] *MediaPharma s.r.l., Via Colonnetta 50/A , Chieti, Italy;*

[10] *Department of Science, 'G. d'Annunzio University', Chieti, Italy*

Abstract

Managing bladder cancer remains a major challenge, highlighting the urgent need for novel and effective diagnostic and therapeutic strategies to improve patient outcomes. In this study, we have identified LGALS3BP (Galectin-3-binding protein), a secreted glycoprotein involved in various biological processes such as immune modulation, cell adhesion, and tumor progression, as a potential biomarker and therapeutic target for bladder cancer. We found that LGALS3BP expression was significantly elevated in bladder cancer tissues and correlated with disease progression. Moreover, urinary and serum levels of LGALS3BP were significantly higher in patients compared to healthy individuals, with a strong correlation observed between elevated urinary protein levels and tumor grade. Of note, LGALS3BP produced by tumor cells treated with Kifunensine, a mannosidase I inhibitor, exhibits increased reactivity to the 1959 therapeutic antibody, suggesting that glycosylation of LGALS3BP may influence antibody recognition and protein function. Therapeutically, administration of 1959-sss/DM4 antibody-drug conjugate resulted in complete inhibition of tumor growth in two mouse models of human bladder cancer xenograft. In sum, the findings presented here strongly position LGALS3BP as a promising candidate for bladder cancer research, warranting further investigation in preclinical and clinical settings to uncover its potential both as a urinary biomarker and a therapeutic target for ADC.

Introduction

Bladder cancer (BCa) is a significant global health concern, as it is the most common malignancies of the urinary system, with an estimated 80 000 new cases and 17 980 deaths worldwide in 2020 [1]. Its incidence has steadily risen in recent years, making it the ninth most diagnosed cancer, with a

corresponding increase in mortality rates [1]. BCa is classified into non-muscle-invasive (NMIBC) and muscle-invasive (MIBC) based on tumor invasion depth. NMIBC accounts for approximately 70% of initial diagnoses and is typically treated with transurethral resection of the bladder tumor (TURBT). However, it carries a high risk of recurrence and progression, with about 30% of cases advancing to MIBC. Due to these risks, NMIBC patients require long-term monitoring based on their risk group. In contrast, MIBC is associated with a greater incidence of metastasis and is treated with radical cystectomy, often combined with neoadjuvant chemotherapy to prevent tumor spread [2]. Bladder cancer can be further classified as high-grade (HG), which is fast-growing, invasive, and resistant to therapy; and low-grade (LG), which is characterized by frequent recurrence but has a low likelihood of progressing to HG disease or becoming invasive [3]. Early detection of BCa is crucial for improving patient outcomes. Therefore, there is an urgent need for highly sensitive and specific non-invasive approaches to enhance cancer detection as well as cancer recurrence and spreading [4].

In this study, we explored the potential of LGALS3BP (Galectin-3-binding protein, also known as Mac-2 BP or 90K) as a novel circulating biomarker for liquid biopsy in BCa. LGALS3BP is a secreted, highly glycosylated protein implicated in various biological processes, including immune response modulation, angiogenesis, cell adhesion, migration, and tumor microenvironment interactions, making it closely associated with tumor growth and progression [5]. While LGALS3BP expression remains low in normal tissues, it is significantly elevated in various cancers as circulating protein in body fluids such as blood and saliva, making this protein a valuable candidate for non-invasive diagnostic approaches [6-8]. We developed a custom in-house ELISA to detect LGALS3BP in the serum and urine. This assay is based on LGALS3BP targeting 1959 antibody, which serves as the backbone of the antibody-drug conjugate (ADC) 1959-sss/DM4, formed by conjugation to the maytansine derivative DM4. Our results show that LGALS3BP expression is significantly elevated in BCa patients compared to healthy controls. Moreover, 1959sss/DM4 ADC has demonstrated potent and sustained antitumor activity in preclinical models of bladder cancer. This study is the first report of the contemporary measurement of LGALS3BP in urine and serum. It highlights the potential of the protein as a promising biomarker for liquid biopsy and a therapeutic target for ADC-based treatment in BCa.

Materials and methods

2.1 Cell lines

A panel of eight bladder cancer cell lines (HT-1376, UM-UC-3, HT-1197, SW780, T24, 5637, TCCSUP, RT4), SKNAS neuroblastoma cells and HOC621 cells (head and neck cancer) were purchased from American Type Culture Collection (#TCP-1020, Rockville, MD, USAAll the tumor cells were grown in complete cell culture media purchased from Gibco (Life Technologies, Toulouse, France) supplemented with 10% heat-inactivated FBS, 100U/mL penicillin and 100µg/mL streptomycin, and incubated at 37 °C in humidified air with 5% CO2 . HT-1376, UM-UC-3, HT-1197, TCCSUP were grown in complete MEM supplemented with 1% Essential Amino Acids; T-24 and RT4 in complete McCoy's 5A; SW780, SKNAS and HOC621 in complete DMEM; 5637 in complete RPMI 1640. All cell lines were tested routinely for mycoplasma contamination through polymerase chain reaction (PCR).

2.2 Immunohistochemistry

Formalin-fixed, paraffin-embedded tissue sections were immunostained using a goat polyclonal antibody against human LGALS3BP (1:400 dilution; 60-minute incubation; catalog no. AF2226, R&D Systems). Antigen retrieval was carried out by microwave treatment at 750 W for 10 minutes in 10 mmol/L sodium citrate buffer (pH 6.0). Signal amplification was performed using the secondary biotinylated anti-goat LSAB kit, and 3,3′-diaminobenzidine (DAB) was used as chromogen. Immunostained sections were digitized using the NanoZoomer Digital Pathology (NDP) System (Hamamatsu, Welwyn Garden City, UK). An immunohistochemical score (IHS) was calculated by multiplying the percentage of tumor cells positive for LGALS3BP (0%-100%) by the staining intensity, assessed on a four-level scale: 0 (absent), 1 (mild), 2 (moderate), 3 (strong). The minimum score is "0" and the maximum is "300". Based on the distribution of LGALS3BP immunohistochemical expression, we selected a cut-off value of 200 IHS. This value was chosen arbitrarily and corresponds to the median (50th percentile) expression of LGALS3BP in our cohort of tumor cases, allowing us to dichotomize LGALS3BP expression. This dichotomization enabled us to categorize the cases as "High" and "Low" in terms of LGALS3BP expression.

2.3 Western blotting analysis

To evaluate LGALS3BP protein levels, bladder cancer cells were seeded at a density of 5 × 105 cells in complete medium, harvested and lysed after 48 h with RIPA buffer containing protease inhibitors cocktail and Na3VO4 (Sigma Aldrich Corporation, St. Louis; MO; USA) as phosphatase inhibitor. Lysates were clarified by centrifugation at 13,000 rpm for 10 min at 4 °C. Lysates and cell culture supernatants were subjected to 10% SDS-PAGE electrophoresis and electro transferred to nitrocellulose membrane (Merck Millipore, Germany) for western blotting analysis. The membranes were blocked with 5% non-fat dry milk in PBS with 0.1% Tween20 for 1 h at room temperature. Membranes were incubated overnight at 4°C with anti-human LGALS3BP (goat polyclonal; 1:1000, #AF2226; R&D Systems, Minneapolis, MN, USA) and anti-human GAPDH (rabbit monoclonal, D16H11 clone; 1:1000, #5174, Cell signaling technology). After three washes in PBS-0.1% Tween20, membranes were incubated with horseradish peroxidase (HRP)-conjugated secondary antibodies (anti-rabbit, Biorad, Berkeley, CA, USA; anti-goat, Invitrogen, Life Technologies) at room temperature for 1 h. Signal detection was performed using Clarity Western ECL substrate (1705061; Biorad). Images of membranes were acquired with a UvitecFire reader (Cambridge, UK) and analysed with Alliance Uvitec software (Cambridge, UK).

2.4 Treatment with glycosylation inhibitors

As previously described [9], T24, HOC621 (head and neck cancer) and SKNAS (neuroblastoma) cells were seeded at a density of 1 × 106 in 60-mm dishes under standard growth conditions for 24 h. Cells were then treated with 5 μM of Kifunensine (KIF) (#K1140; Sigma-Aldrich Corporation), 10 μg/mL of Tunicamycin (TUN) (#T7765; Sigma-Aldrich Corporation) or 50μM of OSMI-1 (#SML1621; Sigma-Aldrich Corporation) in serum-free conditions. After 48h, cell culture supernatants were collected, centrifuged at 3000g for 10 min at 4 °C and stored at −80 °C until further usage. Cells were harvested to obtain protein lysates analyzed by western blotting anti-human LGALS3BP (goat polyclonal; 1:1000, #AF2226; R&D Systems, Minneapolis, MN, USA) and anti-human β-actin antibody (mouse monoclonal, 1:40000, #A5441, Sigma-Aldrich Corporation).

2.5 Immunofluorescence and confocal microscopy

T24 cells were plated at 30% of confluence on glass coverslips and grown under standard growth conditions. After 24 h, cells were incubated with KIF (5 μM) or PBS as control for 48 h in serum-free conditions. Then, cells were washed with PBS and fixed with 4% paraformaldehyde. After washing with PBS, cells were incubated with PBS 5% goat serum as blocking solution for 30 min at RT. Cells were then stained with 10 μg/mL of anti-LGALS3BP 1959 antibody at 4°C for 90 min in 5% goat serum. Finally, cells were stained with anti-human AlexaFluor-488 conjugated secondary antibody (1:100, #A11013; Invitrogen, Life Technologies) at 4°C for 1h and mounted using ProLong Gold Antifade Mounting with DAPI (P36935; ThermoFisher Inc., Waltham, MA, USA). Confocal images were acquired as z- stacks using a Zeiss LSM800 inverted confocal microscope system (Carl Zeiss, Gottingen, Germany); detector gain voltages and pinhole were set at the beginning of the experiment and maintained constant during the acquisition of all samples. The z-stacks were then processed and merged using ImageJ software. A maximum intensity projection of the green signal channel was generated, and the resulting images were used for quantification of fluorescence intensity within the software.

2.6 Cytotoxicity assays

Cell proliferation was assessed by MTT [3-(4,5-dimethyldiazol-2-yl)-2,5-diphenyl tetrazolium bromide] assay (Sigma-Aldrich Corporation). T24 and SW780 cells were seeded in 24-well plates at a density of 1 × 104 cells per well, whereas MSC and hGF cells were seeded at a density of 1.5 and 2 x 104 cells per well, respectively; all cells were then cultured under standard growth conditions for 24 h. Cells were then treated with SH-DM4 (DM4) (Sellek Chemicals LLC) or Cisplatin at indicated concentrations for 72 h. At the end of the treatment, cells were incubated with 250 μL of MTT solution (serum-free medium with 0.5 mg/mL of MTT) for further 2 h. After the removal of MTT solution, 200 μL of dimethyl sulfoxide (DMSO) was added to the wells for 10 min and the absorbance at 570 nm was measured using a multi-plate reader (Tecan). IC50 (Inhibition of cellular proliferation by 50%) values were calculated by using GraphPad Prism 9.0 software (GraphPad Software, Inc., CA, USA). All experiments were performed in triplicate.

2.7 In vivo studies

Athymic CD-1 nu/nu female mice were purchased from Envigo RMS (Udine, Italy) at the age of 5–7 weeks. Mice were kept under specific pathogen-free conditions. The room temperature was at 22 ± 2 °C and relative humidity 50 ±15%. Cages, bedding and food were autoclaved before use. Mice were provided with a standard diet and water ad libitum and acclimatized for 2 weeks before the start of the experiments. Housing and all procedures involving the mice were performed according to the protocol approved by the Institutional Animal Care and Use Committee of the Italian Ministry of Health (Authorization no. 1118/2020). 5 × 106 exponentially growing T24 or SW780 cells were subcutaneously inoculated into the right flank of the mice in a total volume of 200 μL of PBS and Matrigel (ratio 1:3). For therapeutic studies, when tumors became palpable (approximately 100 mm3 of volume), animals were randomized into 2 groups to provide a similar range of tumor sizes for each group. The treated group received intravenous injections of 1959-sss/DM4 twice weekly for a total of three injections (10 mg/kg), whereas the control group received PBS only. The mice weight and

the tumor volume were monitored weekly by a caliper and calculated using the following formula: tumor volume (mm3) = (length × width2)/2. A tumor volume of 1 cm3 was chosen as a humane endpoint for all experiments after which mice were sacrificed. Blood was collected by intracardiac puncture immediately after mice sacrifice in a tube containing a glass Pasteur pipette to induce blood clotting. Serum was obtained after centrifugation of clotted blood samples at 3000g for 15 minutes at 4°C and stored at -80°C. Tumors were collected in formalin and embedded in paraffin.

2.8 Enzyme-Linked Immunosorbent Assay (ELISA)

To quantify LGALS3BP in cell-derived supernatants, serum, and urine samples, a custom sandwich ELISA was developed. NUNC Maxisorp 96-well plates (Thermo Fisher Scientific) were coated overnight at 4°C with 2 µg/mL of humanized anti-LGALS3BP antibody 1959 in PBS. Following a blocking step with PBS 1% (w/v) BSA for 1 hour at room temperature (RT), 100 µL of either recombinant LGALS3BP standards (1–250 ng/mL), cell supernatants, diluted urine samples (1:10 in PBS), or controls (PBS and LGALS3BP-depleted urine as blanks) were added to the wells and incubated for 1 hour at RT. Plates were washed three times with PBS containing 0.05% (v/v) Tween-20, followed by the addition of biotinylated anti-LGALS3BP antibody 1959 (1.8 µg/mL) for 1 hour at RT. For the detection, after three washes with PBS-0.05% Tween-20, Streptavidin-HRP was added (Invitrogen, #SA10001, 1:10000) and incubated for 1 h at RT. After washing, stabilized chromogens were added for 6 minutes in the dark, and the reaction was stopped with 1 N H2SO4. Absorbance was measured at 450 nm using a Tecan microplate reader (Männedorf, Switzerland). In the supernatants of glycosylation inhibitors treated cells, LGALS3BP was measured using Proteintech™ Human LGALS3BP ELISA Kit (Cod. KE00155) following the manufacturer's protocol.

2.9 Recombinant human LGALS3BP production

Recombinant human LGALS3BP was purified from serum-free conditioned medium of human embryonic kidney EBNA-293 cells (Invitrogen) transfected with LGALS3BP cDNA, as described previously [10]. Purification was performed using an AKTA Start FPLC system (Cytiva) and an HiTrap NHS-Activated HP affinity column (Cytiva) pre-conjugated with 10 mg of anti-LGALS3BP antibody 1959. The conditioned medium was recirculated overnight at 0.5 mL/min at 4°C. After washing the column with 25 column volumes (CV) of 50 mM Tris - 75 mM NaCl, LGALS3BP was eluted with 2 CV of IgG Elution Buffer (Thermo Fisher Scientific) at 1 mL/min. Elution fractions were neutralized with 1 M Tris-HCl (pH 8.5), pooled, concentrated using 30 kDa MWCO centrifugal filters (Merck), and dialyzed into PBS. The purified protein was aliquoted and stored at −80°C.

2.10 Subjects' enrollment and urine samples processing

All procedures involving human participants were conducted in accordance with the ethical standards of the institutional research committee (Comitato di Etica per la Ricerca Biomedica della Provincia di Pescara e Chieti e dell'Università degli Studi "G. D'Annunzio" di Chieti-Pescara; protocol no. 1767), and the GU Biobank human ethics protocol from the University of British Columbia (H21-03722). All participants were male or female adults who provided informed consent prior to enrollment. 26 and 38 (total = 64) hospitalized patients diagnosed with bladder cancer were enrolled respectively at the "SS. Annunziata" Hospital (Chieti, Italy) and at the Vancouver Prostate Center (VPC, Vancouver, Canada). Urine samples were collected on the day of inclusion, prior to

transurethral resection of bladder tumor (TURBT) surgery. Additionally, urine samples were collected from healthy volunteers (n = 53), resulting in a total of 117 samples included in this retrospective study. Urine samples were centrifuged at 1500g for 20 min at 4°C. Urine supernatants were aliquoted and stored at −80°C until analysis.

2.11 Immunoprecipitation of LGALS3BP from Urine Samples

To isolate LGALS3BP from human urine, samples (300 µL each) were first diluted 1:10 in phosphate-buffered saline (PBS, pH 7.4) to minimize matrix interferences such as high salt and urea concentrations. Pre-clearing was performed by incubating the diluted samples with 50 µg of Protein A-conjugated agarose beads (Thermo Scientific) for 30 minutes at 4°C on a rotator. Samples were then centrifuged at 12000 rpm for 30 seconds at 4°C, and the supernatants (pre-cleared urine) were collected. Immunoprecipitation was carried out by incubating ~5µg of anti-LGALS3BP monoclonal antibody 1959 with the pre-cleared urine overnight at 4°C under continuous rotation. The immune complexes were then captured by adding 100 µg of Protein A agarose beads and incubating for an additional 3 hours at 4°C. Following centrifugation at 12000 rpm for 2 minutes at 4°C, the supernatants were removed and stored as LGALS3BP-depleted urine. The bead-bound immunocomplexes were washed once with 1 mL of ice-cold PBS, centrifuged again, and the pellets resuspended in 100 µL of 5× reducing Laemmli sample buffer to dissociate LGALS3BP from the antibody and incubated at RT for 5–10 minutes with gentle rotation. After another centrifugation, supernatants were collected and then denatured at 90°C for 5 minutes. Eluted proteins were subsequently analyzed by SDS-PAGE and Western blotting.

2.12 Statistical analysis

For ELISA data, P values were determined by Mann–Whitney and Kruskal-Wallis test, for in vivo xenograft growth curves, P values were determined by Mantel–Cox test and considered significant for *$P < 0.05$, **$P < 0.005$ and ***$P < 0.0005$. Experimental sample numbers (n) are indicated in the figure legends. Youden's J index derived from the receiver operating characteristic (ROC) curve was used to determine the optimal cut-off value for LGALS3BP expression in pathological samples, enabling discrimination between patients and healthy controls.

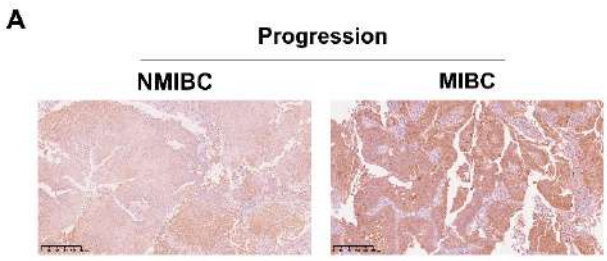
3. Results

3.1 LGALS3BP is highly expressed in bladder cancer tissue

Our previous studies have identified LGALS3BP as a secreted, highly glycosylated protein that is abundantly expressed in various tumors, including melanoma, head and neck (H&N) cancer, neuroblastoma, and glioblastoma [9, 11-13]. In this study, we aimed to assess the expression of the protein in bladder carcinoma. To assess LGALS3BP expression in bladder cancer tissues, we retrospectively analyzed 29 paraffin-embedded tissue samples collected at the time of initial diagnosis from patients with urothelial carcinoma who underwent transurethral resection of bladder tumor (TURBT). Among these samples, 11 resulted MIBC while 18 scored as NMIBC. Among MIBC, 5 of them were diagnosed at the first biopsy while 6 progressed to advanced stage in a 3-years period. Overall, LGALS3BP was highly expressed across all samples (Figure 1). However, when patients were stratified by disease aggressiveness and categorized into high and low

LGALS3BP expression groups using the median value as a cutoff, we observed that 100% of MIBC patients exhibited high LGALS3BP expression at initial TURBT, compared to only 33% of NMIBC patients (Figure 1; $P < 0.0004$). These findings indicate that LGALS3BP is not only highly expressed in bladder cancer but correlates with more advanced disease. While LGALS3BP expression is low in most normal tissues [13], urothelial cells have been found to be positive for LGALS3BP staining, as confirmed by the Human Protein Atlas repository.

(https://www.proteinatlas.org/search/LGALS3BP)



B

		Progression		
		No	Yes	Total
LGALS3BP	High	6	11	17
	Low	12	0	12
	Total	18	11	29

P<0.0004

Fig. 1: LGALS3BP is highly expressed in bladder cancer tissues. (A) Immunohistochemical analysis of LGALS3BP expression in bladder cancer tissues at first TURBT. Representative images of NMIBC and MIBC tissue samples are shown. (B) Contingence table reporting analysis of LGALS3BP expression in patients who progressed (MIBC n=11) or not (NMIBC n=18). Patients were stratified based on expression of LGALS3BP (high or low) and progression (NMIBC vs MIBC).

3.2 LGALS3BP is highly expressed in bladder cancer cell lines and represents a therapeutic target for ADC therapy

To better define LGALS3BP role in bladder cancer, we moved on cellular models. To this aim, we evaluated LGALS3BP both intracellularly and as secreted protein in a panel of human bladder cancer cell lines. Western blotting analysis indicated that LGALS3BP is expressed in all the cell lines tested, although the levels and the molecular size pattern varied in a cell line-depending manner. As shown in figure 2B, we detected the non-glycosylated form of LGALS3BP protein (around 70 kDa) and the mature highly glycosylated form (around 100 kDa) in the intracellular compartment. Interestingly, only the high molecular weight form of the protein was detected in the cell culture supernatant, with slight shifts in band size, suggesting that the glycosylation pattern varies depending on the cellular model used (Figure 2A). To quantify the expression level of the secreted protein, we developed an in-house, sandwich type ELISA, utilizing the therapeutic 1959 anti-LGALS3BP antibody (Figure 2C). Among the different cell lines, high-grade MIBC T-24 and low-grade NMIBC SW780 exhibited the highest levels of both intracellular and secreted LGALS3BP (Figure 2A-C). Therefore, we chose these two cellular models for further studies.

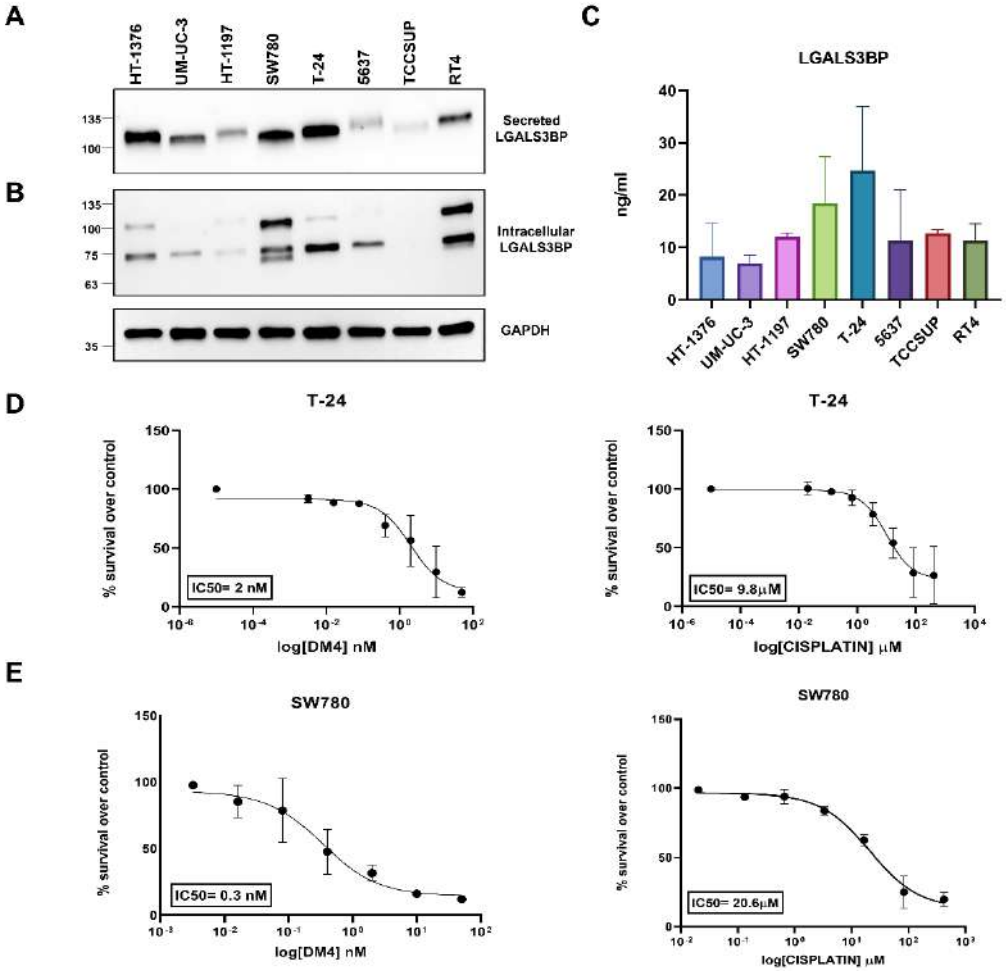


Fig. 2: LGALS3BP expression in bladder cancer cell lines. (A) Secreted and (B) intracellular LGALS3BP protein levels in a panel of human bladder cancer cell lines analyzed through Western Blotting in cell culture supernatants and cell lysates, respectively. Equal amounts of samples were loaded per lane. GAPDH was used as loading control. (C) Histogram showing secreted LGALS3BP levels (ng/mL) evaluated by 1959-based sandwich ELISA. *In Vitro* IC50 curves evaluated by MTT assays by exposing (D) T-24 and (E) SW780 cells for 72 h to increasing doses of Cisplatin and DM4. IC50 values are reported for each cell line considered upon different treatments.

3.3 Therapeutic activity of 1959-sss/DM4 ADC

Next, we evaluated the potential of LGALS3BP as a therapeutic target for ADC using the 1959-sss/DM4 ADC developed by our group. This ADC is designed using site-specific conjugation of DM4-SH to a modified variant of the 1959 antibody, in which the three cysteine residues of the heavy chain have been replaced with serines. This modification enables the generation of an ADC with a fixed drug-to-antibody ratio (DAR) of approximately 2. For therapeutic studies, MIBC T-24 and NMIBC SW780 xenograft models were employed. These two cell lines, that showed high

LGALS3BP levels (Figure 2A-C), exhibited a very marked sensitivity to ADC payload DM4 (IC50 in the nanomolar range) compared to standard chemotherapeutic agents, such as cisplatin (IC50 in the micromolar range) (Figure 2D-E).

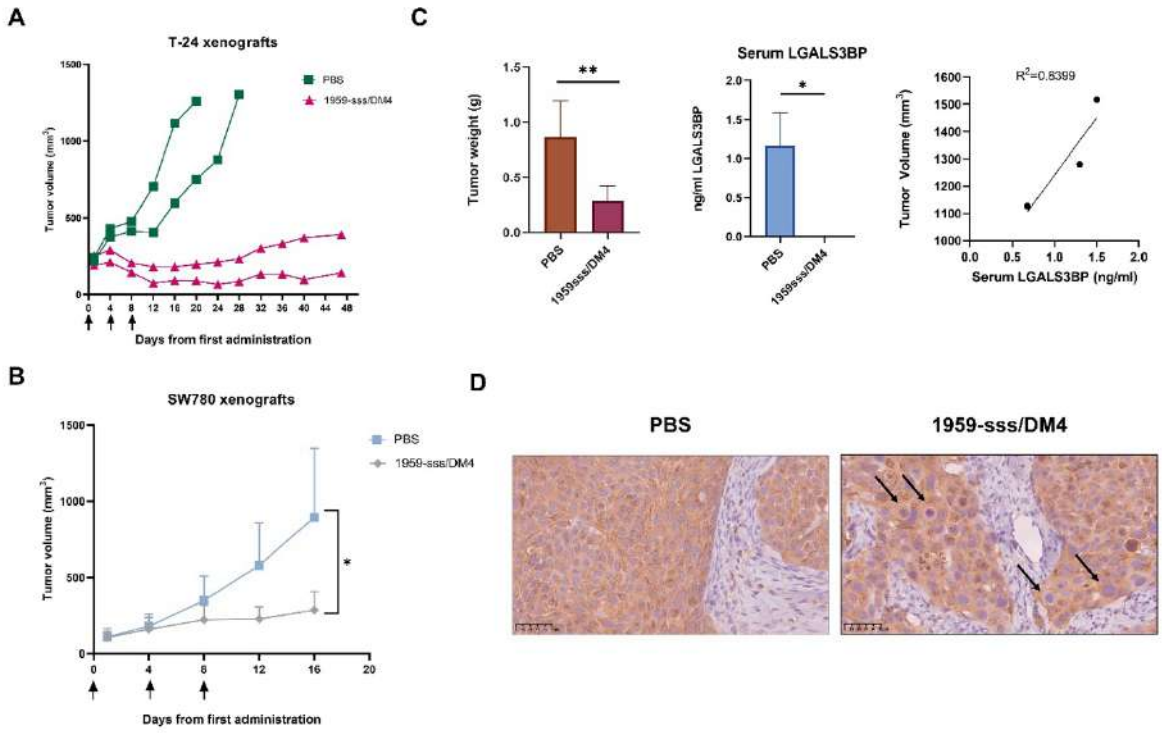


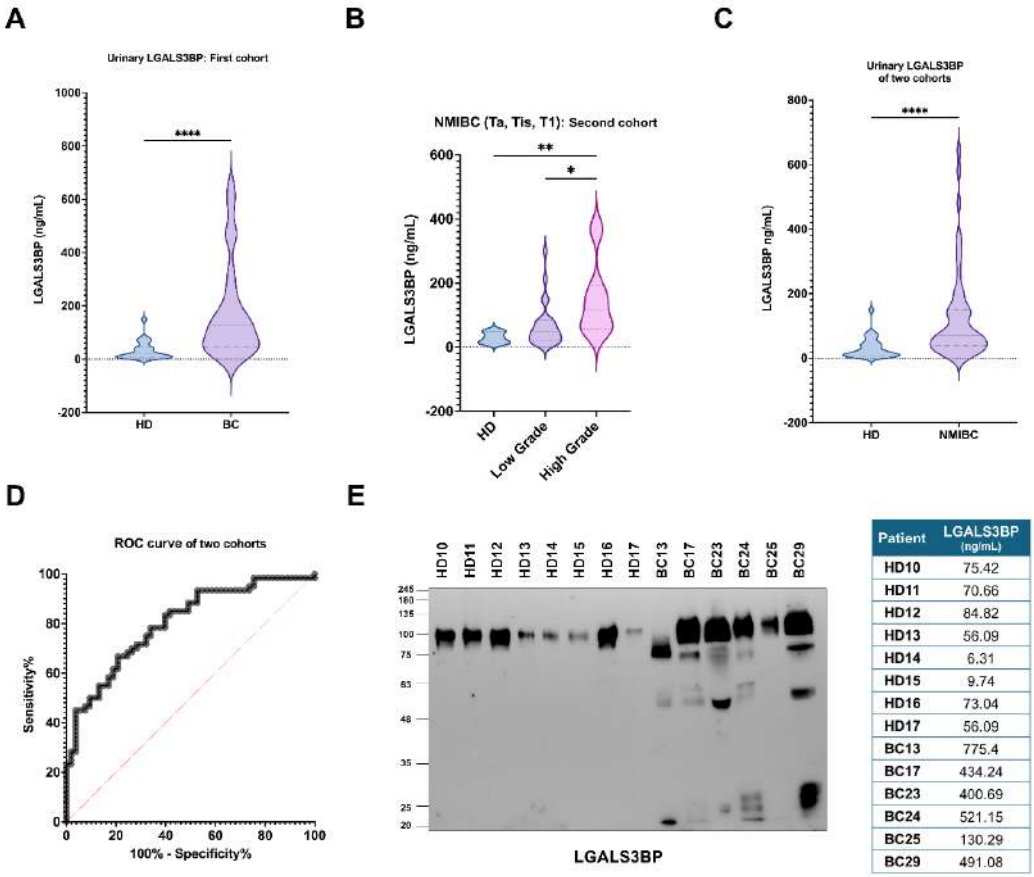
Fig. 3 : 1959-sss/DM4 anti-tumor activity in subcutaneous xenograft models of bladder cancer cells. (A) Single animal tumor growth expressed as tumor volume (mm3) of T-24 subcutaneous xenografts in nude mice treated with vehicle (PBS) or 1959-sss/DM4 (10 mg/kg; twice weekly; three total i.v. injections). Arrows indicate treatments administration. Two mice were considered per group. Data are presented as mean ± standard error of the mean (SEM). (B) Tumor growth expressed as mean tumor volume (mm3) from first treatment of SW780 subcutaneous xenografts in nude mice treated with vehicle (n= 6) or 1959-sss/DM4 (n= 6). Arrows indicate treatments administration (10mg/kg; twice weekly; three total i.v. injections). Data are presented as mean ± SEM. (C) Tumor weight (g) at the end point of SW780-xenograft *In Vivo* therapeutic experiment (left panel). Statistical significance was determined by t test (* $p<0.05$; **$p<0.01$). Commercial anti-LGALS3BP ELISA kit showing circulating LGALS3BP levels (ng/mL) in serum derived from SW780-xenografted mice treated with PBS or 1959-sss/DM4 (middle panel). Correlation between circulating LGALS3BP levels (ng/mL) in PBS-treated SW780-xenografted mice serum and corresponding tumor volumes (mm3) (right panel). Correlation value is reported ($R^2 = 0.8399$). (D) Representative IHC sections of SW780 tumors in mice treated with PBS or 1959-sss/DM4 stained for LGALS3BP. Arrows indicate giant cells, which are the hallmarks of mitotic catastrophe. Magnification 40X.

Due to low growing efficiency, we experienced with MIBC T-24 cells, only 4 xenografts were obtained. They were randomly assigned to receive vehicle (PBS) or ADC 1959-sss/DM4 (10mg/kg). Strikingly, while vehicle-treated mice were sacrificed on day 20 and 28 because their tumor volume

reached the cut-off value, we observed a potent and durable anti-tumor response in ADC-treated mice with initial tumor shrinkage followed by control of the disease over 48 days from starting of treatment (Figure 3A). Despite the lower aggressiveness of the NMIBC SW780 cell model compared to T-24 cells, we were able to obtain better tumor engraftment efficiency with SW780 cell line. Both PBS (n= 6) and ADC (n= 6) groups were treated using the same schedule previously applied to T-24 cells. Once again, a potent and significant anti-tumor response was observed (Figure 3B) in ADC-treated mice bearing SW780 tumors. Tumor weight at the end of the experiment (17 days from starting treatment, defined by a tumor volume cut-off of ≈1 cm^3 for PBS-treated mice) was significantly lower in ADC-treated mice (Figure 3C, left panel). We next evaluated the ability of LGALSBP to serve as a BCa biomarker. First, we measured circulating LGALS3BP levels in mouse serum collected from PBS and ADC-treated animals at the end of the experiment. While LGALS3BP expression levels were around 1 ng/mL in vehicle-treated mice, they were undetectable in ADC-treated animals (Figure 3C, middle panel). Moreover, a correlation trend between LGALS3BP expression levels and tumor volume in PBS-treated xenografts was detected (Figure 3C, right panel). Moreover, immunohistochemical analysis of SW780 tumor tissues collected at the end of the experiment confirmed a high expression of LGALS3BP both in vehicle and ADC treated tumors. Finally, aberrant mitotic figures were observed in ADC-treated but not control tumor tissues, suggesting a payload-induced G2/M cell cycle block (Figure 3D).

3.4 LGALS3BP as a potential biomarker in BCa patients

We recently demonstrated that circulating LGALS3BP is a potential disease biomarker in neuroblastoma and glioblastoma [9, 15]. Given that this protein is highly expressed in bladder cancer tissues, we speculate that its circulating form could serve as a potential urinary biomarker for bladder cancer, offering a non-invasive approach for liquid biopsy. To increase the assay accuracy, we generated a biotinylated version of the therapeutic 1959 antibody and developed a novel in-house ELISA for urinary LGALS3BP detection. Furthermore, to ensure high reproducibility and standardization of the assay, we purified LGALS3BP from EBNA cells stably expressing the protein, using the 1959 antibody for immunoprecipitation as described [16]. The purified protein enabled the generation of an optimal calibration curve, which was applied in all subsequent assays. We first analyzed a cohort of 26 urine samples collected from bladder patients before TURBT and compared them with 47 urine samples collected from healthy donors as controls. The urinary LGALS3BP levels resulted significantly higher in bladder patients compared to healthy donors (Figure 4A). Indeed, while the healthy donors exhibited median LGALS3BP value of 19.29 ng/ml (IQR 6.63-46.88 ng/mL), patient samples showed a significant increase, with a median value of 126.8 ng/ml (IQR 44.06-234.1 ng/mL). Serum LGALS3BP levels were subsequently analyzed in a set of available control (n=19) and bladder cancer patient (n=57) blood samples, revealing a statistically significant elevation in patients relative to healthy individuals.



Patient	LGALS3BP (ng/mL)
HD10	75.42
HD11	70.66
HD12	84.82
HD13	56.09
HD14	6.31
HD15	9.74
HD16	73.04
HD17	56.09
BC13	775.4
BC17	434.24
BC23	400.69
BC24	521.15
BC25	130.29
BC29	491.08

Fig. 4: Increased Urinary LGALS3BP Expression in Bladder Cancer Patients. (A) Biotinylated 1959-based sandwich ELISA showing LGALS3BP expression levels in urine from healthy donors (HD) (n=47) or bladder cancer patient (BC) (n=26) samples of a first cohort of patients. Statistical significance was obtained by using Mann-Whitney test (****p<0.0001). (B) Biotinylated 1959-based sandwich ELISA showing LGALS3BP urinary expression levels (ng/mL) in HD (n=6), BC low-grade (n=26), or BC high-grade (n=12) of a second cohort of patients. Statistical significance was obtained by using Kruskal-Wallis test (**p<0.01; *p<0.05). (C) Biotinylated 1959-based sandwich ELISA showing LGALS3BP urinary expression levels (ng/mL) in HD (n= 53) or NMIBC (n= 60) patients by pooling data from the two previously analyzed patient cohorts. (D) ROC curve generated by pooling data from the two previously analyzed patient cohorts. (E) Western blotting image of LGALS3BP protein pattern in urine samples from HD or BC patients. Equal amounts of samples were loaded per lane. Urinary LGALS3BP levels (ng/mL) detected through biotinylated 1959-based sandwich ELISA assay are reported in the corresponding healthy donors and BC patient samples.

We next evaluated the potential of urinary LGALS3BP as a diagnostic biomarker and repeated the analysis in a second cohort of NMIBC patients, including low (n=26) and high-grade (n=12) bladder cancer samples, and 6 samples from healthy individuals. Notably, when stratified by tumor grade, the increase in urinary LGALS3BP levels was considerably higher in high-grade expression levels (Figure 4B), with median value of 119 ng/ml (IQR 59.2-190.4 ng/mL) compared to low grade patients with median value of 48.13 ng/ml (IQR 19.87-83.56 ng/mL) and healthy donor, median

value of 27.56 ng/mL (IQR 12.59-48.11 ng/mL). Given that all urinary samples were analyzed using the same assay and reference standard, we pooled samples from the two cohorts previously analyzed , 53 healthy individuals and 60 NMIBC patients, to generate a combined ROC curve. We obtained a threshold value of 49.35 ng/ml in healthy individuals while the average value for patients was around 120,36 ng/ml ± 132,26 (Figure 4C). The assay demonstrated an accuracy with 66,67 % sensitivity and 79,25 % specificity (Figure 4D) with an AUC of 0.80. Furthermore, data suggested a potentially greater discriminatory power in males than in females. To evaluate whether urinary LGALS3BP exhibited distinct size patterns, we analyzed urine samples from healthy donors and bladder cancer (BC) patients using Western blotting analysis. Interestingly, the analysis revealed a markedly different profile of LGALS3BP protein in patient urinary samples, characterized by several low molecular weight bands that were absent in healthy controls. These findings suggest that LGALS3BP may undergo aberrant glycosylation and/or proteolytic cleavage in the tumor setting (Figure 4E).

3.5 LGALS3BP glycosylated status in bladder cancer

To better understand the glycosylation pattern of LGALS3BP in bladder cancer, we employed high-expressing T-24 cells as an *In Vitro* model to investigate the effects of various N- and O-linked glycosylation inhibitors on both the glycosylation profile and secretion of the protein. Western blot analysis confirmed that LGALS3BP undergoes glycosylation modifications in bladder cancer cells treated with glycosylation inhibitors (Figure 5A), consistent with our previous observations in glioblastoma cells [2]. ELISA assay further demonstrated that protein secretion was abolished only in cells treated with Tunicamycin, an inhibitor that blocks the early steps of the N-linked glycosylation pathway. Notably, we found that treatment with Kifunensine (KIF), a mannosidase I inhibitor that promotes the accumulation of high mannose enriched species, significantly enhanced the reactivity of the 1959 therapeutic antibody (Figure 5B). Interestingly, this phenomenon is common to other cell lines from different tumors such as glioblastoma [9], neuroblastoma and H&N cancer. In contrast, using a commercially available anti-LGALS3BP ELISA assay, we observed that KIF treatment reduced the signal of the secreted protein (Figure 5C), suggesting that the binding of high-mannose LGALS3BP is antibody-specific. In addition, the increase in 1959 therapeutic antibody binding to high-mannose species was further confirmed by confocal imaging (Figure 5D-E).

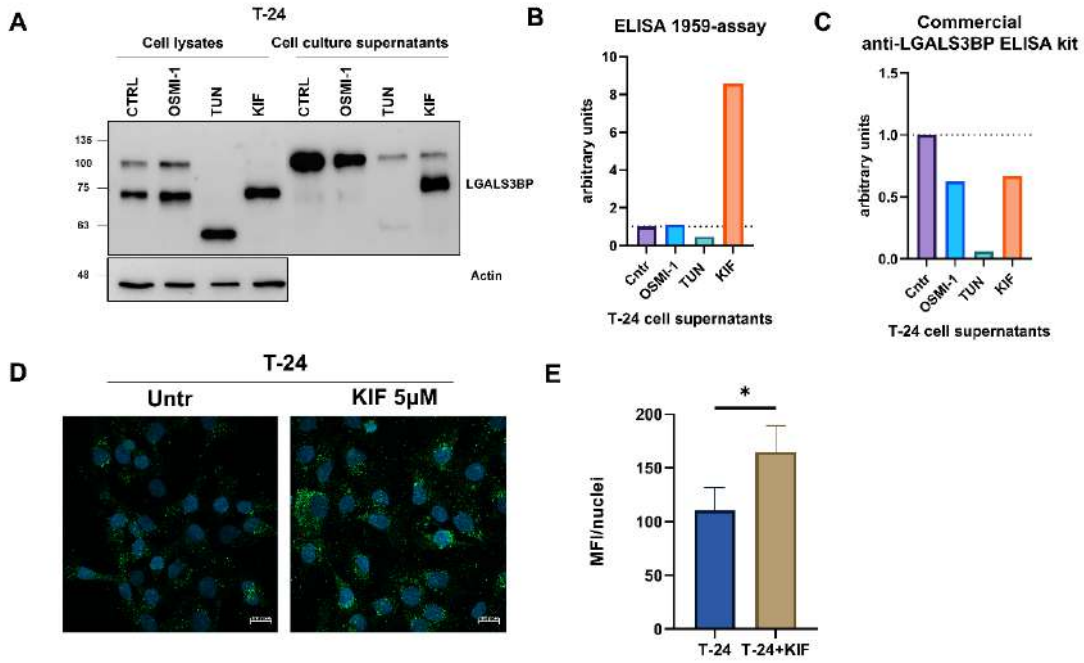


Fig. 5: LGALS3BP glycosylation. (A) Western blot images of LGALS3BP protein pattern in cell lysates and cell culture supernatants of T-24 cells treated or not with OSMI-1 (50µM), TUN (10 µg/mL) or KIF (5 µM). Molecular weight markers are indicated on the left (kDa). (B) 1959-based sandwich ELISA and (C) commercial anti-LGALS3BP ELISA kit for the detection of secreted LGALS3BP levels in cell culture supernatants of T-24 cells under different treatment conditions (control, OSMI-1, TUN, KIF). The bar graph shows normalized values expressed in arbitrary units, with all conditions normalized to the control, which is set to 1. (D) Representative confocal microscopy images of T-24 cells under two conditions: vehicle (left) and treated with 5 µM KIF (right). Nuclei are stained in blue (DAPI), and the green signal represents LGALS3BP. Scale bar:100 pixel. (E) Histogram representing the mean fluorescence intensity (MFI) of LGALS3BP signal per nucleus measured by confocal microscopy in T-24 cells treated or not with KIF 5µM (*$p < 0.05$).

4. Discussion

Urothelial cancer is a malignant disease whose incidence and mortality are increasing alarmingly, requiring an urgent effort to improve the ability to make early diagnosis and therapy. Urine-base liquid biopsy represents an emerging tool for early detection and follow-up [17]. In fact, urine represents, for BCa, the best choice, since it is constantly in contact with the bladder mucosa and the bladder tumor, it contains fewer contaminants than blood, and it is easily obtained, not requiring particular compliance by the patient [18, 19]. Several urinary biomarkers have been investigated for their diagnostic and prognostic potential, including DNA mutations (e.g., FGFR3, TP53) [20], RNA-based markers [21], protein markers (e.g., NMP22, BTA, UroVysion, Bladder EpiCheck) [22], and extracellular vesicles [23]. However, while the FDA has approved the urinary biomarkers BTA TRAK and NMP22, their clinical utility in detecting the disease at its onset remains limited due to

the low sensitivity and specificity of these assays [24]. Therefore, despite these advancements, no single test has yet achieved a level of performance sufficient to fully resolve the challenges of early diagnosis and effective monitoring.

In the present study, we identified LGALS3BP as a potential urinary biomarker and a therapeutic target for ADC therapy. LGALS3BP is a highly glycosylated secreted protein whose levels significantly increase in cancer cells. As a circulating protein, it can be detected in body fluids, including blood, urine and saliva, making it a promising candidate for non-invasive biomarker development. Since 1994, when two studies first identified LGALS3BP as a circulating protein overexpressed in tumors, specifically breast carcinoma and melanoma [25, 26], the interest in this molecule has steadily increased due to its documented role in regulating tumor–stroma crosstalk. The importance of LGALS3BP as a key player in tumor progression and its potential as a circulating biomarker is underscored by a growing body of research, with numerous studies published over the past decade [5, 6, 9, 11-13, 27-33]. Here, we demonstrate that LGALS3BP is overexpressed in bladder cancer, whose higher levels correlates with more advanced disease. Moreover, urinary LGALS3BP levels are significantly elevated in patients compared to healthy donors. Notably, LGALS3BP higher urinary levels are associated with high-grade tumors in NMIBC patients, underscoring the protein's potential as urinary biomarker. An interesting finding is that urinary levels of LGALS3BP appear to be more predictive in males than in females. The relationship between sex and LGALS3BP levels, as well as the underlying biological mechanisms, remains largely unexplored. A recent study from our group found no significant differences in LGALS3BP serum levels based on age or sex in a healthy population {Pellegrino, 2025 #355}. In contrast, an earlier study by Melin et al. in patients with type I diabetes reported that elevated LGALS3BP levels were associated with female sex{Melin, 2019 #354}. These observations support the hypothesis that protein levels in biological fluids may vary by sex, particularly in specific physiological contexts or pathological conditions.

In addition, using cellular models of bladder cancer, we focused on LGALS3BP glycosylation pattern in cancer cells. We confirmed that the intracellular form of the protein has a size of approximately 70 kDa. However, after undergoing glycosylation, it matures into a form of around 100 kDa. In this fully processed state, the protein is secreted from the cell, as demonstrated by Western blot analysis, where only the 100 kDa band is detected in the supernatant. However, it becomes clear from band sizing that the glycosylation state is cell specific, as different size of mature form can be appreciated from western blotting (Figure 2A-B). Moreover, by using different O- and N-glycosylation inhibitors, we determined that only Tunicamycin, which inhibits the initial step of N-linked glycan biosynthesis, was capable of completely blocking protein secretion. In contrast, treatment with the O-glycosylation inhibitor (Osmi) and the mannosidase I inhibitor (KIF) still resulted in the presence of LGALS3BP in the supernatant. However, in KIF-treated cells, the protein exhibited a reduced size of approximately 70–80 kDa. This is consistent with the known effect of KIF, which interrupts glycosylation process by inducing the accumulation of high-mannose forms.

While we observed a slight decrease in the secreted form of LGALS3BP in the supernatants of cells treated with both Osmi and KIF, confirmed both by Western blotting and a commercial ELISA, our results changed strikingly when we repeated the analysis using the ELISA based on the therapeutic antibody 1959. In this case, we observed a dramatic increase in reactivity in the samples treated with KIF, suggesting that the high-mannose form induced by KIF treatment enhances recognition by the 1959 antibody. These results underscore that the distinct glycosylation status of LGALS3BP in tumor

cells can generate specific forms that exhibit enhanced reactivity to the 1959 antibody, potentially functioning as cancer-specific glycoform. To further investigate this, we analyzed urine samples from both patients and healthy controls using Western blotting and confirmed the presence of a distinct banding pattern in patients, likely reflecting altered glycosylation. Notably, in the patient with the highest ELISA values (BC13), we detected a band of similar size to that observed in KIF-treated cells, further supporting the idea that high-mannose glycoforms may be associated with tumor-derived LGALS3BP. A recent study by Kong et al. identified novel protein biomarkers in urine and blood samples from a cohort of 92 bladder cancer (BC) patients [34]. Notably, LGALS3BP was not among the detected proteins as it was not included in the proximity extension analysis (PEA).

Although the present study gives promising results, it has certain limitations as well. The most significant is the small sample size. Additionally, the control population may pose a potential limitation due to imperfect age-matching. Finally, the presence of high urinary protein levels in the control population made the cut-off value not sufficiently sensitive and specific for clinic translation.

This circulating protein may represent a highly valuable and promising tool for improving the management of bladder cancer. It could serve both as a biomarker for the early detection of the disease and as an indicator of therapeutic response. Designing a future study to longitudinally monitor urinary LGALS3BP levels in patients undergoing treatment or follow-up would certainly be worthwhile. In addition, further efforts will be crucial in identifying specific cancer-associated glycosylated forms of LGALS3BP, which could significantly enhance the specificity of urinary assays. Finally, LGALS3BP or its glycosylated variants could be integrated into a multi-panel biomarker system, improving diagnostic accuracy and follow-up efficacy by increasing both sensitivity and specificity.

Regarding advances in precision medicine for bladder cancer, a significant milestone has been achieved with the development of an antibody-drug conjugate (ADC) targeting Nectin-4 of bladder cancer [35]. Indeed, Enfortumab vedotin (EV) has demonstrated potent antitumor activity in preclinical models and became the first ADC of its kind approved for clinical use for bladder cancer therapy. It has shown particularly promising results, especially in combination with immunotherapy [36]. This suggests that ADC therapy, when combined with immune checkpoint inhibitors, may represent a highly effective strategy, particularly in advanced disease settings. In this regard, 1959-sss/DM4, the ADC developed by our group, represents a promising candidate for LGALS3BP targeted therapy in bladder cancer. In fact, this compound that has shown potent and long-lasting antitumor activity in several preclinical models of different tumors, is also particularly effective in bladder cancer as a single agent (Figure 3A-B). We have recently identified a potential synergistic effect of this ADC in combination with the anti-PD-1 immune checkpoint inhibitor (ICI) in neuroblastoma [15]. This synergy appears to be driven by immunogenic cell death (ICD) induced by the DM4 payload, suggesting that 1959-sss/DM4, in combination with ICI-based therapies, could represent a promising therapeutic strategy for bladder cancer. As for potential DM4 toxicity, it's important to note that the safety and toxicity profile of this class of payloads has been extensively characterized in humans. For example, the DM4-based anti–folate receptor alpha ADC mirvetuximab soravtansine-gynx (MIRV) received FDA approval in late 2022{Dilawari, 2023 #363}. A very recent report describes significant MIRV antitumor activity associated with tolerable safety profile on a cohort of platinum-resistant ovarian cancer patients {Matulonis, 2025 #361}.

In conclusion, this study provides the first compelling evidence that the circulating protein LGALS3BP is a potential urinary biomarker for bladder cancer and, simultaneously, a promising therapeutic target for ADC-based therapy. The findings strongly support further investigations to validate clinical utility of LGALS3BP in bladder cancer management.

References

[1] Siegel, R.L., A.N. Giaquinto, and A. Jemal, Cancer statistics, 2024. CA Cancer J Clin, 2024. 74(1): p. 12-49.

[2] Warrick, J., Molecular Subtypes of Bladder Cancer: Component Signatures and Potential Value in Clinical Decision-making. Adv Anat Pathol, 2024. 31(3): p. 178-187.

[3] Contieri, R., et al., Deintensification of Treatment for Low-grade Bladder Tumors: A Collaborative Review by the International Bladder Cancer Group (IBCG). European Urology Oncology, 2025. 8(1): p. 179-189.

[4] Oyaert, M., et al., Novel Urinary Biomarkers for the Detection of Bladder Cancer. Cancers, 2025. 17(8): p. 1283.

[5] Capone, E., S. Iacobelli, and G. Sala, Role of galectin 3 binding protein in cancer progression: a potential novel therapeutic target. J Transl Med, 2021. 19(1): p. 405.

[6] Rana, R., et al., Plasma-Derived Extracellular Vesicles Reveal Galectin-3 Binding Protein as Potential Biomarker for Early Detection of Glioma. Front Oncol, 2021. 11: p. 778754.

[7] Anqi, H., et al., LGALS3BP: A Potential Prognostic Biomarker Influencing Antitumor Immunity in Triple-negative Breast Cancer. Current Medicinal Chemistry, 2025. 32: p. 1-25.

[8] Song, Y., et al., Plasma exosomes from endometrial cancer patients contain LGALS3BP to promote endometrial cancer progression. Oncogene, 2021. 40(3): p. 633-646.

[9] Dufrusine, B., et al., Extracellular LGALS3BP: a potential disease marker and actionable target for antibody-drug conjugate therapy in glioblastoma. Mol Oncol, 2023.

[10] Silvestri, B., et al., Differential effect on TCR:CD3 stimulation of a 90-kD glycoprotein (gp90/Mac-2BP), a member of the scavenger receptor cysteine-rich domain protein family. Clin Exp Immunol, 1998. 113(3): p. 394-400.

[11] Cela, I., et al., LGALS3BP is a potential target of antibody-drug conjugates in oral squamous cell carcinoma. Oral Dis, 2024. 30(4): p. 2039-2050.

[12] Capone, E., et al., Targeting Vesicular LGALS3BP by an Antibody-Drug Conjugate as Novel Therapeutic Strategy for Neuroblastoma. Cancers (Basel), 2020. 12(10).

[13] Giansanti, F., et al., Secreted Gal-3BP is a novel promising target for non-internalizing Antibody-Drug Conjugates. J Control Release, 2019. 294: p. 176-184.

[14] Yang, E., et al., Mesenchymal stem cells in tumor microenvironment: drivers of bladder cancer progression through mitochondrial dynamics and energy production. Cell Death & Disease, 2024. 15(9): p. 688.

[15] Sala, G., et al., Abstract 2609: Vesicular LGALS3BP is a neuroblastoma biomarker and a therapeutic target for combination therapy with antibody-drug conjugate and checkpoint inhibitors. Cancer Research, 2024. 84(6_Supplement): p. 2609-2609.

[16] Piccolo, E., et al., LGALS3BP, lectin galactoside-binding soluble 3 binding protein, induces vascular endothelial growth factor in human breast cancer cells and promotes angiogenesis. Journal of Molecular Medicine, 2013. 91(1): p. 83-94.

[17] Ma, L., et al., Liquid biopsy in cancer: current status, challenges and future prospects. Signal Transduction and Targeted Therapy, 2024. 9(1): p. 336.

[18] Crocetto, F., et al., Liquid biopsy in bladder cancer: State of the art and future perspectives. Crit Rev Oncol Hematol, 2022. 170: p. 103577.

[19] Alberca-Del Arco, F., et al., New Perspectives on the Role of Liquid Biopsy in Bladder Cancer: Applicability to Precision Medicine. Cancers (Basel), 2024. 16(4).

[20] Bakkar, A.A., et al., FGFR3 and TP53 gene mutations define two distinct pathways in urothelial cell carcinoma of the bladder. Cancer Res, 2003. 63(23): p. 8108-12.

[21] Dubois, J., et al., Transcriptome analyses of urine RNA reveal tumor markers for human bladder cancer: validated amplicons for RT-qPCR-based detection. Oncotarget, 2021. 12(10): p. 1011-1023.

[22] Wolfs, J.R.E., et al., Novel urinary biomarkers ADXBLADDER and bladder EpiCheck for diagnostics of bladder cancer: A review. Urol Oncol, 2021. 39(3): p. 161-170.

[23] Teixeira-Marques, A., et al., Extracellular Vesicles as Potential Bladder Cancer Biomarkers: Take It or Leave It? Int J Mol Sci, 2023. 24(7).

[24] Ahangar, M., F. Mahjoubi, and S.J. Mowla, Bladder cancer biomarkers: current approaches and future directions. Front Oncol, 2024. 14: p. 1453278.

[25] Inohara, H. and A. Raz, Identification of human melanoma cellular and secreted ligands for galectin-3. Biochem Biophys Res Commun, 1994. 201(3): p. 1366-75.

[26] Iacobelli, S., et al., Detection of Antigens Recognized by a Novel Monoclonal Antibody in Tissue and Serum from Patients with Breast Cancer1. Cancer Research, 1986. 46(6): p. 3005-3010.

[27] Cela, I., et al., LGALS3BP antibody-drug conjugate enhances tumor-infiltrating lymphocytes and synergizes with immunotherapy to restrain neuroblastoma growth. Journal of Translational Medicine, 2025. 23(1): p. 431.

[28] Capone, E., et al., Anti-LGALS3BP antibody-drug conjugate treatment induces durable and potent antitumor response in a preclinical model of adenoid cystic carcinoma. Oral Oncology, 2024. 148: p. 106635.

[29] Keinanen, O., et al., Visualizing Galectin-3 Binding Protein Expression with ImmunoPET. Mol Pharm, 2023. 20(6): p. 3241-3248.

[30] Choi, Y.S., et al., Antibody-mediated blockade for galectin-3 binding protein in tumor secretome abrogates PDAC metastasis. Proc Natl Acad Sci U S A, 2022. 119(30): p. e2119048119.

[31] Li, L., et al., LGALS3BP is a novel and potential biomarker in clear cell renal cell carcinoma. Aging (Albany NY), 2024. 16(4): p. 4033-4051.

[32] Zhang, X., et al., Increased LGALS3BP promotes proliferation and migration of oral squamous cell carcinoma via PI3K/AKT pathway. Cellular Signalling, 2019. 63: p. 109359.

[33] Kim, S.-S., et al., Secreted LGALS3BP facilitates distant metastasis of breast cancer. Breast Cancer Research, 2025. 27(1): p. 4.

[34] Kong, T., et al., Identification of novel protein biomarkers from the blood and urine for the early diagnosis of bladder cancer via proximity extension analysis. Journal of Translational Medicine, 2024. 22(1): p. 314.

[35] Wong, J.L. and J.E. Rosenberg, Targeting nectin-4 by antibody-drug conjugates for the treatment of urothelial carcinoma. Expert Opin Biol Ther, 2021. 21(7): p. 863-873.

[36] Powles, T., et al., Enfortumab Vedotin and Pembrolizumab in Untreated Advanced Urothelial Cancer. N Engl J Med, 2024. 390(10): p. 875-888.

CHAPTER 5

Methods development

The findings presented in this thesis are based on a sustained research and development effort to establish the methodological foundation of the experimental pipelines. This chapter provides a detailed account of the principal techniques developed by the author in the laboratory: (i) the rational optimization and finalization of conjugation strategies for generating EV20/Omomyc and 1959-sss/DM4 immunoconjugates; (ii) development of reliable tumor tissue homogenization, lysis, and analyte extraction procedures for HPLC quantification; (iii) creation and refinement of an ELISA assay to measure LGALS3BP in various biological liquids.

5.1 EV20/Omomyc conjugation method development

The EV20/Omomyc immunoconjugate was generated through thiol–disulfide exchange, employing heterobifunctional derivatization of both the antibody and the Omomyc protein. EV20 (150 kDa) was thiolated with 2-iminothiolane (Traut's reagent; 1.5 molar excess relative to antibody), while Omomyc (~10 kDa) was independently activated with SPDP (1.7 molar excess relative to Omomyc). Several practical challenges were encountered during the development of the EV20/Omomyc conjugation workflow, primarily due to the coupling of two proteins with markedly different physicochemical properties and the use of reactive chemistries sensitive to buffer composition, pH, and organic cosolvents. The final procedure was designed to maximize coupling efficiency while minimizing precipitation, aggregation, and residual unconjugated Omomyc.

Initial optimization efforts focused on ensuring reaction compatibility. Both protein partners were buffer-exchanged into 100 mM borate-buffered saline (BBS) at pH 9.0 prior to derivatization. NHS-esters such as SPDP react efficiently with primary amines under mildly basic conditions, and Traut's reagent (2-iminothiolane) enables controlled thiolation of lysine residues on the antibody within a pH range that maintains IgG stability during short incubations. However, operating at pH 9 increases the risk of protein instability and non-specific aggregation, particularly when hydrophobic linkers and DMSO are present. To address this, derivatization reactions were limited to 1 hour under covered, gentle stirring, and with carefully controlled molar excesses (EV20:2-IT = 1:1.5; Omomyc:SPDP = 1:1.7), balancing activation yield with the risk of over-derivatization and structural destabilization. A recurring issue was Omomyc precipitation during SPDP activation. Because SPDP is typically prepared as a concentrated stock in DMSO, the combination of basic pH, a reactive hydrophobic linker, and a local increase in organic solvent can cause partial denaturation or insolubility of small proteins. Pre-diluting Omomyc 1:5 in BBS at pH 9.0 before adding SPDP minimized precipitation by reducing local DMSO exposure and moderating acylation kinetics. This step was critical for obtaining a reproducible, soluble Omomyc–SPDP intermediate suitable for downstream coupling. After removing unreacted 2-IT from the antibody and SPDP from Omomyc by G25 size-exclusion chromatography (SEC) in BBS pH 9.0, the main protein fractions were collected based on absorbance at 280 nm. The Omomyc–SPDP preparation often showed an early SEC peak corresponding to aggregates, which, if retained, promoted downstream aggregation and reduced effective coupling. Therefore, only the second, monomer-enriched peak was pooled.

For the conjugation step, EV20-2IT and Omomyc–SPDP were combined at a 1:5 molar ratio and incubated at 4 °C under covered stirring. The protocol included an in-process control to verify

conjugation progress by monitoring pyridine-2-thione release at 343 nm for approximately 2 hours, starting from an aliquot taken at reaction initiation. For downstream purification, the reaction mixture was concentrated using a 30 kDa MWCO filter to facilitate handling, followed by a second G25 SEC step in PBS (pH 7.4) via FPLC to remove unreacted Omomyc and exchange the conjugate into a physiologically compatible buffer. SEC alone was sometimes insufficient, as free Omomyc could partially co-elute with higher-molecular-weight species, depending on column loading and peak broadening. Even small residual amounts of free Omomyc complicated functional interpretation and analytical readouts. To address this, the conjugate was further dialyzed against 20 mM Trizma, pH 9.0, using a 50 kDa membrane.

5.2 1959-sss/DM4 conjugation method optimization

For several years, the 1959-sss/DM4 antibody-drug conjugate (ADC) was synthesized in the host laboratory using a standard protocol as described by *Giansanti, F. et al., 2019* [123]. However, with the introduction of new equipment and personnel, this method yielded a highly heterogeneous ADC, with a drug-to-antibody ratio (DAR) ranging from 1.3 to 1.6, rather than the expected 2. To address this, the protocol was optimized to achieve a more homogeneous product. Specifically, the 1959-sss/DM4 conjugate was prepared using a controlled thiol-chemistry workflow designed to maximize conjugation efficiency while minimizing antibody over-reduction, aggregation, and payload precipitation. 1959sss was quantified by UV absorbance at 280 nm and reduced with tris(2-carboxyethyl)phosphine (TCEP; 60 molar equivalents from a 900 mM stock) at 4 °C overnight. The reduced antibody was then activated with 5,5′-dithiobis(2-nitrobenzoic acid) (DTNB; 20 molar equivalents from a 26.7 mM stock), prepared in ethanol and added after supplementation with phosphate buffer (final 100 mM, from 1 M stock) for 2 hours at room temperature, protected from light. This approach stabilized pH and ionic strength during the organic co-solvent pulse, thereby minimizing turbidity and precipitation. DTNB activation was monitored spectrophotometrically at 412 nm as an in-process control for thiol availability and reaction progression. Excess low-molecular-weight reagents were removed using a Zeba™ Spin 7K MWCO Desalting Column (Thermo Fisher), equilibrated with 10% dimethylacetamide (DMA) and 5% sucrose. This desalting step was optimized to be rapid and efficient, avoiding the more time-consuming G25 size-exclusion chromatography (SEC), which, despite its higher desalting capacity, led to greater product loss. The buffer composition was selected to maintain antibody stability during chromatography and to improve solubility for subsequent hydrophobic payload addition. The activated antibody was reacted with DM4 (10 molar equivalents; stock in DMA, 10 mM) at 4 °C overnight. In contrast to the previous protocol, the final DMA concentration was kept low (typically less than 10%) to prevent partial antibody denaturation, while using a DM4 stock that was 10 times more concentrated. Residual free thiols were quenched by adding iodoacetamide (500 molar equivalents, from a 90 mg/mL stock) to halt further thiol exchange and minimize post-reaction reshuffling. Unconjugated DM4 was removed by a second Zeba™ Spin 7K MWCO Desalting Column, followed by optional concentration (30 kDa MWCO) and extensive dialysis into PBS to remove DMA and sucrose, yielding a formulation compatible with downstream assays and analytical characterization. DAR determination was performed using HIC chromatography as described in Chapter 3.

5.3 DM4 and S-Met-DM4 extraction and quantification method development

For ADC biodistribution studies, we developed an optimized HPLC workflow to extract and quantify DM4 and S-methyl-DM4 from tissues. We began by optimizing tissue processing, since extraction yield and matrix effects limited sensitivity. DM4 and S-methyl-DM4 were spiked into blank tissues and homogenized at w:v ratios of 1:2, 1:5, and 1:10 using a Tissue Ruptor on low for 1-minute, balancing disruption with minimal heat or foam. The 1:5 ratio provided the best recovery and was used for all subsequent work. Sonication was tested for better lysis, but it increased analyte degradation, so it was not included.

Extraction conditions were refined to maximize recovery while preserving analyte integrity. Initial trials using protein precipitation with acetonitrile or dimethylacetamide (1:3, v/v; solvent:homogenate) resulted in poor recovery for both analytes and were discontinued. As a result, a liquid–liquid extraction (LLE) strategy was adopted, and various homogenization/lysis solvents were screened to balance tissue disruption and analyte stability. The solvents evaluated included 10 mM Tris-HCl, PBS (pH 7.5), acidified water (pH 4), alkaline water (pH 10), a 50:50 (v/v) water:methanol mixture, and a proprietary lysis buffer with or without N-ethylmaleimide (NEM). Alkaline water (pH 10) caused extensive tissue saponification and was excluded. The lysis buffer formulation without NEM provided the highest and most reproducible recoveries and was selected for the final procedure. For the LLE step, two extraction solvent systems were compared: ethyl acetate:methanol (7.5:1, v/v) and ethyl acetate:methyl tert-butyl ether (1:1, v/v). The ethyl acetate:methyl tert-butyl ether system significantly increased HPLC backpressure, indicating co-extraction of matrix components that impaired chromatographic performance. Therefore, ethyl acetate:methanol (7.5:1, v/v) was chosen as the preferred extraction mixture. In accordance with Green Chemistry principles, the extraction solvent volume was reduced from an initial 3.4:1 to a 1:1 solvent:homogenate ratio without measurable loss of extraction efficiency. Evaporation parameters were optimized to prevent heat-induced degradation: a 2-hour SpeedVac drying step was sufficient to remove residual organic solvent while maintaining analyte stability. To further improve quantitative reproducibility, whole tissue samples were homogenized rather than using small aliquots, minimizing variability due to tissue heterogeneity. Finally, to establish the most appropriate validation framework for the HPLC method, tissue-specific extraction efficiency was determined by comparing integrated peak areas from samples spiked with DM4 or S-methyl-DM4 either before homogenization (i.e., analytes added directly to the lysis buffer prior to processing) or after homogenization/extraction. For method validation and the most conservative estimate of recovery, the pre-homogenization spiking condition was used as the reference, as it accounts for losses throughout the entire sample-preparation workflow.

The finalized protocol was established as follows:

Tumor and healthy mouse tissues were processed for DM4 and S-methyl-DM4 quantification using a standardized homogenization and liquid–liquid extraction (LLE) workflow designed to preserve analyte stability while maximizing recovery from complex matrices. Immediately after euthanasia, organs (including lung, liver, kidney, heart, and brain) were excised and snap-frozen in liquid nitrogen to arrest enzymatic activity and minimize post-mortem degradation. Frozen specimens were thawed on ice and subdivided into ~40 mg aliquots per sample. Each aliquot was homogenized at a

fixed weight-to-volume ratio of 1:5 by addition of 200 µL of ice-cold denaturing lysis buffer (6 M urea, 100 mM Tris-base, 2% CHAPS, 1% Triton X-100, and 50 mM DTT, pH 7.5), a formulation selected to ensure rapid protein denaturation and efficient tissue disruption while limiting oxidative and thiol-exchange artefacts that can compromise thiolated maytansinoids. Homogenization was performed using a Tissue Ruptor device for 1 min at the minimum speed, with tubes maintained in an ice bath (≈4 °C) to prevent sample warming. To eliminate foam generated by detergent-rich lysis conditions, homogenates were briefly centrifuged (10,000 rpm, 10 s), then gently resuspended by pipetting followed by vortexing (30 s). Complete lysis was achieved by incubation on ice for 30 min.

Extraction of DM4-related analytes was carried out by LLE using an ethyl acetate:methanol mixture (7.5:1, v/v) added at a 1:1 volume ratio relative to the homogenate (200 µL). Samples were inverted 10 times to initiate phase mixing and then vortexed vigorously for 1 min to promote analyte partitioning into the organic phase. Phase separation was obtained by centrifugation (10,000 rpm, 15 min, 4 °C), and the clearest organic layer was carefully collected, avoiding disturbance of the yellow aqueous phase and the pellet. To improve overall yield, the extraction cycle (lysis addition, mixing, centrifugation, and organic phase recovery) was repeated three times per tissue aliquot, with the recovered organic phases pooled. The combined organic extract was clarified by an additional centrifugation step (10,000 rpm, 15 min, 4 °C) to remove residual particulate material. Pooled organic extracts were dried under vacuum using a SpeedVac concentrator for 2 h at the lowest temperature setting (no active warming) to prevent heat-induced degradation. Dried residues were reconstituted in 200 µL dimethylacetamide (DMA) and vortexed for 2 min; re-solubilization was further enhanced by a 5 min ultrasound bath. Insoluble material was removed by centrifugation (13,000 rpm, 15 min, 4 °C), and the supernatant was transferred to a new tube. The clarification step was repeated to ensure particulate-free samples suitable for HPLC injection. Final supernatants were transferred into total-recovery HPLC vials and analyzed for DM4 and S-methyl-DM4 using the validated chromatographic method previously described in Chapter 3.

5.4 Recombinant LGALS3BP expression and purification

Recombinant human LGALS3BP was produced in human embryonic kidney EBNA-293 cells and purified from serum-free conditioned medium using antibody-affinity chromatography. Serum-free culture was chosen to simplify downstream purification by reducing the presence of exogenous serum proteins and other undefined components that could co-purify or interfere with binding and capture steps, thereby improving selectivity and reproducibility. The conditioned medium was harvested and supplemented with 0.1 mg/mL Pefablock serine protease inhibitor, 5 mM EDTA, 1 mM PMSF, and 0.05% sodium azide and then filtered with 0.22 µm sirynge filters (Millex™, Sigma Merck). The medium was loaded onto a HiTrap NHS-Activated HP column on an ÄKTA Start system. NHS-activated resin was selected for its ability to rapidly and covalently immobilize ligands with primary amines, such as antibodies, resulting in a stable affinity matrix with low ligand leakage and robust performance over multiple runs. The anti-LGALS3BP antibody 1959 (10 mg) was coupled to the NHS-activated support to create a highly specific capture matrix. To maximize binding yield from dilute culture supernatants, the conditioned medium was passed once through the column and then recirculated overnight at 0.5 mL/min and 4 °C to enhance protein binding. After loading, the column was washed extensively (10 column volumes) with 50 mM Tris and 75 mM NaCl to remove non-specifically bound material. The Tris/NaCl wash was maintained because moderate ionic strength reduces weak electrostatic interactions and improves removal of background proteins

while preserving the high-affinity antibody–antigen interaction required for selective retention. LGALS3BP was eluted using a low-pH IgG elution buffer (2 column volumes, 1 mL/min). Low-pH elution is a widely used and efficient method for disrupting antibody–antigen interactions without harsh chaotropes, but it can risk acid-mediated unfolding or loss of activity for sensitive proteins. To mitigate this, eluted fractions were immediately neutralized with 1 M Tris-HCl (pH 8.5) to minimize the time LGALS3BP remained at acidic pH, thereby preserving structural integrity and downstream assay performance. Neutralized fractions were pooled and concentrated using 30 kDa MWCO centrifugal filters, then dialyzed into PBS. Finally, purified LGALS3BP was aliquoted and stored at −80 °C to prevent repeated freeze–thaw cycles, which can promote denaturation and aggregation.

5.5 ELISA assay development

To quantify LGALS3BP in cell-derived supernatants and complex biofluids (serum and urine), a custom sandwich ELISA was developed. High-binding Nunc MaxiSorp 96-well plates were selected for their surface chemistry, which supports robust passive adsorption of immunoglobulins and is recommended for sandwich immunoassays where coating homogeneity and signal-to-noise are critical. Plates were coated overnight at 4 °C with 2 µg/mL humanized anti-LGALS3BP antibody 1959 in PBS. After coating, wells were blocked for 1 hour at room temperature with PBS containing 1% (w/v) BSA to reduce non-specific adsorption of sample proteins. For quantification, 100 µL per well of recombinant LGALS3BP standards (1–250 ng/mL), cell supernatants, diluted urine (1:10), or diluted serum (1:500) in PBS were incubated for 1 hour at room temperature. Dilution was specifically introduced to mitigate matrix effects, such as variable ionic strength, urea/salts, and abundant urinary proteins, which can increase background and compress dynamic range. PBS and LGALS3BP-depleted urine were included as blanks to distinguish true antigen-dependent signal from non-specific matrix binding and any residual cross-reactivity inherent to urine. Between steps, plates were washed three times with PBS containing 0.05% (v/v) Tween-20 (PBST). Detection was performed by adding biotinylated anti-LGALS3BP antibody 1959 (1.8 µg/mL, 1 hour at room temperature), followed by streptavidin–HRP (1:10,000, 1 hour). The biotin–streptavidin system was chosen to enhance sensitivity and robustness, eliminating the need for a secondary antibody. Although classical sandwich ELISAs typically use two antibodies recognizing different epitopes, the same clone can be used for both capture and detection when the analyte is multimeric or oligomeric and presents multiple identical binding sites. LGALS3BP (Gal-3BP/90K/Mac-2BP) is known to exist as a monomer as well as dimeric and higher-order oligomeric forms (commonly decamers or dodecamers), enabling effective “single-antibody sandwich” binding in this context. Signal development was performed using a stabilized TMB chromogen (10 minutes, protected from light) and stopped with 1 N H_2SO_4; absorbance was measured at 450 nm using a microplate reader. In supernatants from cells treated with glycosylation inhibitors, LGALS3BP was quantified using a commercial Proteintech Human LGALS3BP ELISA kit (KE00155) according to the manufacturer’s protocol.

DISCUSSION

Over the past two decades, antibody-based conjugates have evolved from sperimental therapies to established cancer treatments. These agents offer potent, highly specific targeting of cancer cells. Their therapeutic success depends not only on target selection and payload potency, but also on efficient drug release at the tumor site, sustained local presence, and the tumor's adaptive responses. These challenges are amplified when novel payloads, diverse targets, or complex tumor microenvironments involving immune components are considered. In my PhD research, we focused on the design, development, and characterization of two innovative immunoconjugates derived from antibody platforms developed in my laboratory: EV20/Omomyc and 1959-sss/DM4.

MYC is a well-established oncogenic driver that has historically been considered "undruggable" due to its intracellular localization and due to difficulties in developing effective compounds. Even when potent inhibitors are available, their clinical utility is often limited by poor tumor penetration or off-target toxicity, rather than insufficient intrinsic activity. The development of OMO-103, the first direct anti-MYC agent, demonstrated the feasibility of targeting MYC safely and effectively in both adult and pediatric cancers, including neuroblastoma. Despite its demonstrated activity, the dosing required in both preclinical studies and clinical settings remains relatively high, likely reflecting the limited tumor selectivity of the drug, which reduces effective accumulation at the target site and necessitates increased systemic exposure to achieve therapeutic efficacy. Building on this advancement, we developed EV20/Omomyc immunoconjugate to evaluate whether HER3-mediated delivery could enhance tumor targeting and Omomyc accumulation. HER3 is expressed in certain neuroblastoma cases and is associated with resistance mechanisms in various solid tumors, making it a compelling delivery target. However, we observed that HER3 was absent in widely used neuroblastoma cell lines and patient-derived tumor cells, despite literature reports of its presence in patient samples. To address this, we engineered HER3 expression in a MYCN-amplified neuroblastoma cell line to assess whether receptor-mediated uptake would improve Omomyc delivery. In this engineered model, HER3 expression increased tumor cell sensitivity to EV20/Omomyc, indicating that the delivery system facilitated enhanced uptake at lower doses compared to free Omomyc. In animal studies, the conjugate was effective even at a low drug-to-antibody ratio, demonstrating that partial conjugation remains functional and underscoring the importance of product definition during development. Collectively, these findings suggest that HER3-targeted delivery of MYC inhibitors, such as Omomyc, may be effective in HER3-positive neuroblastoma, although clinical application will depend on the prevalence and functional status of HER3 in patient tumors. This study provides a preliminary foundation for exploring the potential of an Omomyc-based immunoconjugation platform. In this context, the relatively low expression of HER3 in neuroblastoma suggests that alternative tumor-associated targets may be more suitable for antibody-guided delivery. Among these, the ganglioside GD2 represents a promising candidate. Dinutuximab, a monoclonal antibody directed against GD2, is already approved for the clinical treatment of high-risk neuroblastoma, supporting the feasibility of exploiting this antigen for targeted therapeutic strategies.

Dinutuximab is clinically used in high-risk neuroblastoma following intensive multimodal therapy, typically as post-consolidation immunotherapy in combination with isotretinoin and immune stimulators such as GM-CSF and IL-2 in certain regimens (174). Its antitumor activity is primarily mediated through immune effector mechanisms, including antibody-dependent cellular cytotoxicity (ADCC) and complement-dependent cytotoxicity (CDC) (175). These features make dinutuximab

an appropriate candidate for an antibody-based Omomyc conjugate in neuroblastoma. To improve conjugation efficiency and product efficacy, our engineering efforts will focus on pairing dinutuximab–Omomyc using copper-free click chemistry, thereby preserving protein integrity and avoiding metal-induced damage (176). In this approach, solvent-exposed lysine residues on dinutuximab are derivatized with NHS–PEG4–azide to introduce azide functional groups, while Omomyc is modified with a DBCO-bearing linker (DBCO–S–S–amido–PEG4–maleimide), enabling selective coupling to an engineered reduced cysteine residue on Omomyc. The resulting strain-promoted azide–alkyne cycloaddition (SPAAC) between antibody-bound azides and Omomyc-linked DBCO produces a modular, PEG-spaced bioconjugate. The incorporated disulfide (S–S) motif serves as a chemically programmable element that can be cleaved under intracellular reducing conditions, potentially facilitating payload release. This design is intended to balance systemic stability with effective intracellular delivery of Omomyc to neuroblastoma cells and will be evaluated *In Vitro* and *In Vivo* in relevant neuroblastoma preclinical models.

Another major focus of my PhD research was LGALS3BP, a highly secreted, glycosylated, multimeric protein associated with extracellular vesicles. LGALS3BP contributes to cancer progression, immune modulation, and angiogenesis, making it an attractive target on the cell surface rather than intracellularly. We optimized and characterized a new antibody–drug conjugate (ADC) using the anti-LGALS3BP antibody 1959, conjugated to the potent cytotoxin DM4 via a disulfide linker. Due to the extracellular localization of LGALS3BP, the ADC retains outside cells or on tumor-associated vesicles, enabling drug release through the reductive potential of the tumor microenvironment. Across a broad range of preclinical studies involving multiple tumor types, the 1959/DM4 conjugate has consistently demonstrated marked antitumor activity, supporting its wide therapeutic potential. This efficacy has been observed in models characterized by heterogeneous antigen expression, suggesting that its mechanism of action, likely involving extracellular payload release and a consequent bystander effect, enables effective targeting beyond strictly antigen-positive cells. Moreover, the reproducibility of these findings across diverse experimental systems indicates that the activity of 1959/DM4 is not confined to a single tumor setting but may extend to different malignancies in which the target antigen is present within the tumor microenvironment. Collectively, these observations establish 1959/DM4 as a promising candidate for ADC-based therapy, particularly in tumor contexts that are less amenable to conventional internalizing ADC approaches. In this framework, an additional objective of the study was to determine whether the cytotoxic stress induced by the payload may contribute to remodelling the tumor immune microenvironment, thereby providing a mechanistic rationale for its potential combination with immunotherapeutic strategies. *In Vitro*, DM4 exposure induced surface markers characteristic of immunogenic cell death, including calreticulin exposure, increased heat-shock protein levels, and upregulation of PD-L1 expression. These changes constitute a stress–adaptation signature that supports the rationale for PD-1 axis blockade. *In Vivo*, combining 1959-sss/DM4 with anti-PD-1 therapy produced superior antitumor activity compared to monotherapies, resulting in durable responses and complete cures in some animals. Rechallenge experiments suggested the development of immune memory or at least persistent alterations in tumor–host interactions. Immune infiltrate analysis revealed increased numbers of activated lymphocytes and enrichment of CD8 subsets expressing effector markers. These results demonstrate that targeted maytansinoid delivery is immunologically active and can promote immune engagement when checkpoint inhibition occours.

Demonstrating that a non-internalizing extracellular-targeting ADC achieves localized drug release at the tumor site, rather than systemic distribution, requires precise measurement. Ravtansine-based

ADCs generate multiple intracellular metabolites, and their efficacy cannot be inferred solely from tumor size reduction. To address this, we developed and validated an HPLC–DAD method for simultaneous quantification of DM4 and S-methyl-DM4 in plasma. Stability assessments revealed that DM4 released from the ADC declined rapidly at physiological temperature before stabilizing at a low concentration, likely due to plasma protein binding. S-methyl-DM4 exhibited a more gradual decline and greater stability, attributed to its reduced reactivity with thiols. The sustained low levels of free DM4 over time suggest that systemic exposure is limited by chemical interactions, although active metabolites may display distinct behaviors. We have applied this method to measure DM4 and S-methyl-DM4 in organs such as the liver, lung, and kidney. This enabled *In Vivo* specificity assessment: in a neuroblastoma model engineered to express LGALS3BP, both DM4 and S-methyl-DM4 were detected in the lungs of LGALS3BP-positive animals post-treatment, but not in controls. In the liver, both metabolites were present regardless of LGALS3BP status, consistent with its role in clearance. Time-course studies further demonstrated that DM4 appeared early and peaked within one day, while S-methyl-DM4 accumulated later and persisted longer, supporting the conversion of DM4 to S-methyl-DM4 and sustained cytotoxic activity.

In parallel with the observed immune stress response, these findings inform on the optimal timing of combination therapies. If peak local cytotoxic stress and checkpoint ligand expression coincide with the presence of the drug and its metabolites, administering checkpoint inhibitors during this period may maximize therapeutic efficacy. Building on these preliminary results, we intend to apply the validated HPLC method to compare the pharmacokinetics and tumor-site distribution of various ravtansine-based ADCs, including comparing 1959-sss/DM4 with mirvetuximab soravtansine, by monitoring DM4 levels *In Vivo* following treatment.

In the final phase of my PhD, we investigated LGALS3BP as both a therapeutic target and a tumor biomarker detectable in-patient sample. LGALS3BP is present in multiple cancer types and can be measured in biological fluids such as blood, saliva, urine, and cerebrospinal fluid. Given that the bladder epithelium constitutively express LGALS3BP, we investigated whether its urinary levels are altered in the context of bladder cancer and whether specific protein isoforms could provide additional diagnostic value. Using a biotinylated 1959-based ELISA, bladder cancer patients were found to exhibit significantly increased urinary concentrations of LGALS3BP compared to healthy controls. Notably, elevated levels were associated with more aggressive disease, particularly high-grade non–muscle-invasive bladder cancer, supporting the potential utility of LGALS3BP as a non-invasive biomarker for both diagnosis and risk stratification. The assay demonstrated robust performance with an effective cutoff, supporting its feasibility as a practical, non-invasive biomarker. Western blot analysis revealed disease-specific urinary patterns absent in healthy individuals, including several low–molecular–weight bands, likely reflecting tumor-associated proteolysis or glycosylation changes. Thus, the urinary LGALS3BP signature may provide diagnostic information beyond total protein quantification. Animal model studies further demonstrated that the 1959-sss/DM4 conjugate was effective against bladder cancer, reinforcing LGALS3BP's dual roles as a measurable biomarker and therapeutic target.

To elucidate the observed differences and identify specific glycoforms, we investigated also LGALS3BP glycosylation in cellular models. Across various tumor cell lines, LGALS3BP exhibited a broad range of molecular weights, reflecting cell–type–dependent glycosylation patterns that may correlate with cancer subtype. Inhibition of specific glycosylation pathways revealed that N-glycosylation is essential for LGALS3BP secretion, as tunicamycin treatment completely abrogated its secretion. In contrast, blocking O-glycosylation or α-mannosidase I did not prevent secretion, although α-mannosidase I inhibition produced a lower-mass form (approximately 70–80 kDa)

enriched in high-mannose glycoforms. Based on these findings, we developed a custom sandwich ELISA using the 1959 antibody, which detected high-mannose LGALS3BP with greater sensitivity than a commercial assay, particularly in samples enriched for this glycoform. In patient samples, a unique ~75 kDa LGALS3BP species, absent in healthy urine, was identified in bladder cancer, most prominently in the BC13 sample. These data demonstrate the existence of disease-specific, glycoform-resolved LGALS3BP signatures in urine. We also employed lectin-based profiling: a lectin microarray of secreted LGALS3BP from several cancer models identified a tumor-specific glycoform recognized by UEA-I, which binds α1,2-fucosylation. A UEA-I–based ELISA revealed substantially higher levels of this fucosylated LGALS3BP in head and neck cancer cell lines compared to bladder cancer, which exhibited minimal reactivity (Figure 14). These results suggest that α1,2-fucosylated LGALS3BP is more prevalent in oral tumors and may serve as a salivary biomarker when comparing patient and control samples.

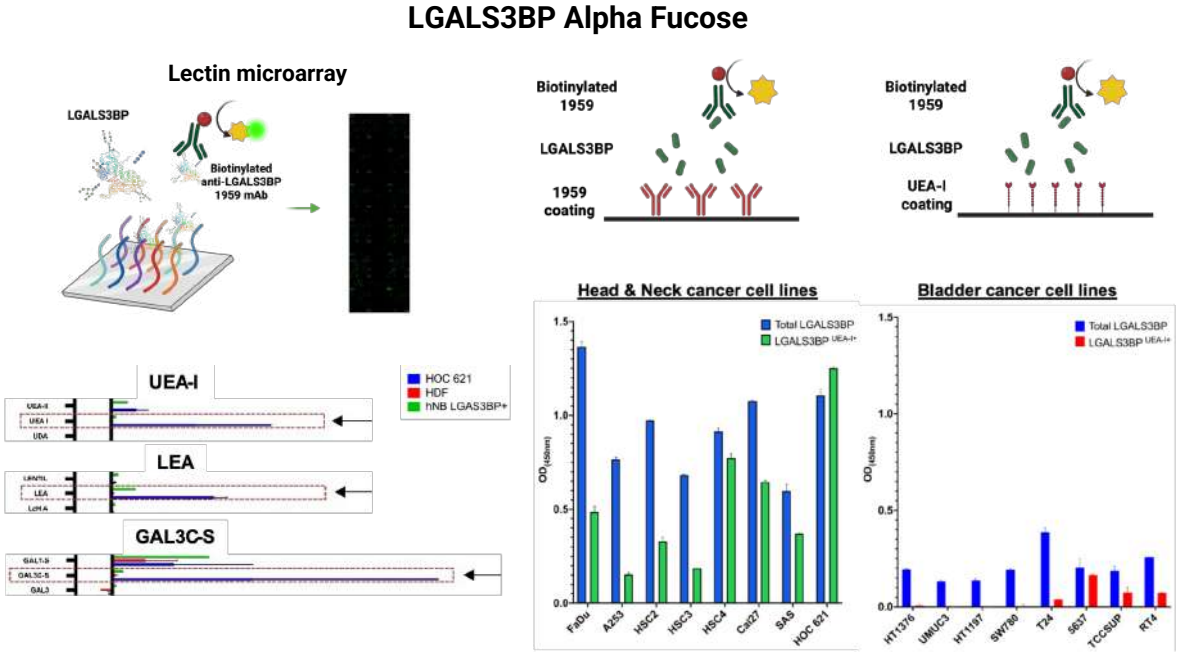


Figure 14: To investigate potential cancer-specific glycoforms, we profiled LGALS3BP surface glycans using a 95-lectin microarray with our 1959 mAB performed on conditioned media from LGALS3BP-positive cancer cell lines (HOC621, hNB-90K) and normal fibroblasts (hDF). Lectins highlighted in the red box (arrows) were selected for further validation. Data identified UEA-I as a significant, cancer-specific lectin compared with normal cells. UEA-I recognizes α-fucose-terminated glycans. Accordingly, we developed a UEA-I/1959 sandwich ELISA to specifically detect α-fucosylated LGALS3BP glycoforms. Among the tested cell lines, head and neck cancer lines showed the greatest expression and secretion of α-fucosylated LGALS3BP, whereas bladder cancer lines showed relatively low levels.

These findings represent ongoing preliminary work, and the next objective is to comprehensively characterize cancer-specific LGALS3BP glycoforms. The primary strategy involves purifying LGALS3BP from patient fluids, including urine and serum, as well as from extracellular vesicle

fractions and healthy donor samples. LGALS3BP is well-suited for this analysis due to its secretion into multiple body fluids and frequent association with tumor-derived vesicles, where glycosylation alterations are common in cancer. The purified protein will be analyzed by mass spectrometry using glycoproteomics techniques to map glycan features—such as high-mannose, fucosylation, or sialylation—that distinguish cancer from controls and to determine their site-specificity. This methodology is sufficiently advanced for large-scale studies of urine and serum and has been successfully applied to other glycoproteins and cancer-associated glycosylation changes, underscoring its practicality and relevance. Concurrently, we will evaluate IR–Raman spectroscopy as a label-free approach to assess glycosylation, as this technique can detect unique sugar features and has been used to differentiate glycosylated forms and, in some cases, assist in sample classification. As a complement to mass spectrometry, IR–Raman could serve as a rapid screening tool for sample stratification. LGALS3BP thus emerges as both a potential therapeutic target and a diagnostic marker, with tumor-specific glycosylation patterns that may serve as molecular signatures. Employing the 1959 antibody in conjunction with lectin-based detection enables selective assessment of mannosylated and fucosylated LGALS3BP forms, offering a promising non-invasive diagnostic strategy for solid tumors. Nonetheless, limitations remain, particularly the small and heterogeneous urine sample cohort, which complicates estimation of clinical accuracy and utility. Future research should encompass larger, multicenter studies, broader fluid sampling (notably urine and saliva), and elucidation of the roles of distinct LGALS3BP glycoforms in cancer progression, vesicle biology, and immune modulation. Ultimately, assays that simultaneously measure high-mannose and fucosylated LGALS3BP may enhance diagnostic accuracy identifying a possible LGALS3BP glycoform cancer specific.

REFERENCES

The references listed below correspond to the citations used across the Background section and within the five thesis chapters. References for published works included as the core content of individual chapters are excluded, as each study reports its own reference list at the end of the corresponding work.

1. Strebhardt K, Ullrich A. Paul Ehrlich's magic bullet concept: 100 years of progress. Nat Rev Cancer. 2008;8(6):473–80. doi:10.1038/nrc2394

2. Chari RVJ. Antibody-drug conjugates: An emerging concept in cancer therapy. Angew Chem Int Ed. 2014;53(15):3796–827. doi:10.1002/anie.201307628

3. Dumontet C, Reichert JM, Senter PD, Lambert JM, Beck A. Antibody-drug conjugates come of age in oncology. Nat Rev Drug Discov. 2023;22(8):641–61. doi:10.1038/s41573-023-00709-2

4. Senter PD. Potent antibody drug conjugates for cancer therapy. Curr Opin Chem Biol. 2009;13(3):235–44. doi:10.1016/j.cbpa.2009.03.023

5. Tsuchikama K, Anami Y, Ha SYY, Yamazaki CM. Exploring the next generation of antibody-drug conjugates. Nat Rev Clin Oncol. 2024;21(3):203–23. doi:10.1038/s41571-023-00850-2

6. Shui L, Wu J, Yang S, He H, Yin T. Antibody-drug conjugates in cancer therapy: Current advances and prospects for breakthroughs. Front Cell Dev Biol. 2025;13:1669592. doi:10.3389/fcell.2025.1669592

7. Cheng Y, Lu J, Zhang C. Overview of antibody-drug conjugates nonclinical and clinical toxicities and related contributing factors. Antib Ther. 2025;8(2):124–44. doi:10.1093/abt/tbaf004

8. Ashman N. Non-internalising antibody-drug conjugates: emerging targets, linker chemistries, and extracellular payload release strategies. J Details PubMed. 2022. 10.1039/d2cs00446a

9. Beck A, Goetsch L, Dumontet C, Corvaïa N. Strategies and challenges for the next generation of antibody-drug conjugates. Nat Rev Drug Discov. 2017;16(5):315–37. doi:10.1038/nrd.2016.268

10. Schumacher D, Hackenberger CPR, Leonhardt H, Helma J. Current Status: Site-Specific Antibody Drug Conjugates. J Clin Immunol. 2016;36(Suppl 1):100–7. doi:10.1007/s10875-016-0265-6

11. Doronina SO, Toki BE, Torgov MY, Mendelsohn BA, Cerveny CG, Chace DF, et al. Development of potent monoclonal antibody auristatin conjugates for cancer therapy. Nat Biotechnol. 2003;21(7):778–84. doi:10.1038/nbt832

12. Francisco JA, Cerveny CG, Meyer DL, Mixan BJ, Klussman K, Chace DF, et al. cAC10-vcMMAE, an anti-CD30-monomethyl auristatin E conjugate with potent and selective antitumor activity. Blood. 2003;102(4):1458–65. doi:10.1182/blood-2003-01-0039

13. Jain N, Smith SW, Ghone S, Tomczuk B. Current ADC Linker Chemistry. Pharm Res. 2015;32(11):3526–40. doi:10.1007/s11095-015-1657-7

14. Caculitan NG, Dela Cruz Chuh J, Ma Y, Zhang D, Kozak KR, Liu Y, et al. Cathepsin B Is Dispensable for Cellular Processing of Cathepsin B-Cleavable Antibody-Drug Conjugates. Cancer Res. 2017;77(24):7027–37. doi:10.1158/0008-5472.CAN-17-2391

15. Dorywalska M, Dushin R, Moine L, Farias SE, Zhou D, Navaratnam T, et al. Molecular Basis of Valine-Citrulline-PABC Linker Instability in Site-Specific ADCs and Its Mitigation by Linker Design. Mol Cancer Ther. 2016;15(5):958–70. doi:10.1158/1535-7163.MCT-15-1004

16. Lewis Phillips GD, Li G, Dugger DL, Crocker LM, Parsons KL, Mai E, et al. Targeting HER2-positive breast cancer with trastuzumab-DM1, an antibody-cytotoxic drug conjugate. Cancer Res. 2008;68(22):9280–90. doi:10.1158/0008-5472.CAN-08-1776

17. Lyon RP, Setter JR, Bovee TD, Doronina SO, Hunter JH, Anderson ME, et al. Self-hydrolyzing maleimides improve the stability and pharmacological properties of antibody-drug conjugates. Nat Biotechnol. 2014;32(10):1059–62. doi:10.1038/nbt.2968

18. Hamblett KJ, Senter PD, Chace DF, Sun MMC, Lenox J, Cerveny CG, et al. Effects of drug loading on the antitumor activity of a monoclonal antibody drug conjugate. Clin Cancer Res. 2004;10(20):7063–70. doi:10.1158/1078-0432.CCR-04-0789

19. Junutula JR, Raab H, Clark S, Bhakta S, Leipold DD, Weir S, et al. Site-specific conjugation of a cytotoxic drug to an antibody improves the therapeutic index. Nat Biotechnol. 2008;26(8):925–32. doi:10.1038/nbt.1480

20. Axup JY, Bajjuri KM, Ritland M, Hutchins BM, Kim CH, Kazane SA, et al. Synthesis of site-specific antibody-drug conjugates using unnatural amino acids. Proc Natl Acad Sci U S A. 2012;109(40):16101–6. doi:10.1073/pnas.1211023109

21. Beerli RR, Hell T, Merkel AS, Grawunder U. Sortase Enzyme-Mediated Generation of Site-Specifically Conjugated Antibody Drug Conjugates with High In Vitro and In Vivo Potency. PLOS ONE. 2015;10(7):0131177. doi:10.1371/journal.pone.0131177

22. Anami Y, Xiong W, Gui X, Deng M, Zhang CC, Zhang N, et al. Enzymatic conjugation using branched linkers for constructing homogeneous antibody-drug conjugates with high potency. Org Biomol Chem. 2017;15(26):5635–42. doi:10.1039/C7OB01027C

23. Thornlow DN, Cox EC, Walker JA, Sorkin M, Plesset JB, DeLisa MP, et al. Dual Site-Specific Antibody Conjugates for Sequential and Orthogonal Cargo Release. Bioconjug Chem. 2019;30(6):1702–10. doi:10.1021/acs.bioconjchem.9b00244

24. Ouyang J. Drug-to-antibody ratio (DAR) and drug load distribution by hydrophobic interaction chromatography and reversed phase high-performance liquid chromatography. Methods in Molecular Biology. 2013. p. 275–83. doi:10.1007/978-1-62703-541-5_17

25. Panowski S, Bhakta S, Raab H, Polakis P, Junutula JR. Site-specific antibody drug conjugates for cancer therapy. mAbs. 2014;6(1):34–45. doi:10.4161/mabs.27022

26. Tolaney SM. Trastuzumab deruxtecan plus pertuzumab in HER2-positive metastatic breast cancer. N Engl J Med. 2025. doi:10.1056/NEJMoa2416394

27. Zhou Q, Stefano JE, Manning C, Kyazike J, Chen B, Gianolio DA, et al. Site-specific antibody-drug conjugation through glycoengineering. Bioconjug Chem. 2014;25(3):510–20. doi:10.1021/bc400505q

28. Dong W, Wang W, Cao C. The Evolution of Antibody-Drug Conjugates: Toward Accurate DAR and Multi-specificity. ChemMedChem. 2024;19(17):e202400109. doi:10.1002/cmdc.202400109

29. Tedeschini T, Campara B, Grigoletto A, Bellini M, Salvalaio M, Matsuno Y, et al. Polyethylene glycol-based linkers as hydrophilicity reservoir for antibody-drug conjugates. J Controlled Release. 2021;337:431–47. doi:10.1016/j.jconrel.2021.07.041

30. Yurkovetskiy AV, Bodyak ND, Yin M, Thomas JD, Clardy SM, Conlon PR, et al. Dolaflexin: A novel antibody-drug conjugate platform featuring high drug loading and a controlled bystander effect. Mol Cancer Ther. 2021;20(5):885–95. doi:10.1158/1535-7163.MCT-20-0166

31. Viricel W, Fournet G, Beaumel S, Perrial E, Papot S, Dumontet C, et al. Monodisperse polysarcosine-based highly-loaded antibody-drug conjugates. Chem Sci. 2019;10(14):4048–53. doi:10.1039/C9SC00285E

32. Conilh L, Fournet G, Fourmaux E, Murcia A, Matera EL, Joseph B, et al. Exatecan antibody drug conjugates based on a hydrophilic polysarcosine drug-linker platform. Pharmaceuticals. 2021;14(3):247. doi:10.3390/ph14030247

33. Yurkovetskiy AV, Yin M, Bodyak N, Stevenson CA, Thomas JD, Hammond CE, et al. A polymer-based antibody-vinca drug conjugate platform: Characterization and preclinical efficacy. Cancer Res. 2015;75(16):3365–72. doi:10.1158/0008-5472.CAN-15-0129

34. Wang R. Antibody-Drug Conjugates (ADCs): current and future perspectives. J Hematol OncolJ Hematol Oncol. 2025;18. doi:10.1186/s13045-025-01704-3

35. Udofa EA. Antibody drug conjugates in the clinic. Bioeng Transl Med. 2024. doi:10.1002/btm2.10677

36. Castaigne S, Pautas C, Terré C, Raffoux E, Bordessoule D, Bastie JN, et al. Effect of gemtuzumab ozogamicin on survival of adult patients with de-novo acute myeloid leukaemia (ALFA-0701): a randomised, open-label, phase 3 study. The Lancet. 2012;379(9825):1508–16. doi:10.1016/S0140-6736(12)60485-1

37. Kantarjian HM, DeAngelo DJ, Stelljes M, Martinelli G, Liedtke M, Stock W, et al. Inotuzumab Ozogamicin versus Standard Therapy for Acute Lymphoblastic Leukemia. N Engl J Med. 2016;375(8):740–53. doi:10.1056/NEJMoa1509277

38. Francisco JA, Cerveny CG, Meyer DL, Mixan BJ, Klussman K, Chace DF, et al. cAC10-vcMMAE, an anti-CD30–monomethyl auristatin E conjugate with potent and selective antitumor activity. Blood. 2003;102(4):1458–65. doi:10.1182/blood-2003-01-0039

39. Tilly H, Morschhauser F, Sehn LH, Friedberg JW, Trněný M, Sharman JP, et al. Polatuzumab Vedotin in Previously Untreated Diffuse Large B-Cell Lymphoma. N Engl J Med. 2022;386(4):351–63. doi:10.1056/NEJMoa2115304

40. Powles T, Rosenberg JE, Sonpavde GP, Loriot Y, Durán I, Lee JL, et al. Enfortumab Vedotin in Previously Treated Advanced Urothelial Carcinoma. N Engl J Med. 2021;384(12):1125–35. doi:10.1056/NEJMoa2035807

41. Coleman RL, Lorusso D, Gennigens C, González-Martín A, Randall L, Cibula D, et al. Efficacy and safety of tisotumab vedotin in previously treated recurrent or metastatic cervical

cancer (innovaTV 204/GOG-3023/ENGOT-cx6): a multicentre, open-label, single-arm, phase 2 study. Lancet Oncol. 2021;22(5):609–19. doi:10.1016/S1470-2045(21)00056-5

42. Verma S, Miles D, Gianni L, Krop IE, Welslau M, Baselga J, et al. Trastuzumab Emtansine for HER2-Positive Advanced Breast Cancer. N Engl J Med. 2012;367(19):1783–91. doi:10.1056/NEJMoa1209124

43. Modi S, Jacot W, Yamashita T, Sohn J, Vidal M, Tokunaga E, et al. Trastuzumab Deruxtecan in Previously Treated HER2-Low Advanced Breast Cancer. N Engl J Med. 2022;387(1):9–20. doi:10.1056/NEJMoa2203690

44. Tolaney SM, Cardillo TM, Chou CC, Dornan C, Faris M. The Mode of Action and Clinical Outcomes of Sacituzumab Govitecan in Solid Tumors. Clin Cancer Res. 2025;31(8):1390–9. doi:10.1158/1078-0432.CCR-24-1525

45. Tarantelli C, Wald D, Munz N, Spriano F, Bruscaggin A, Cannas E, et al. Targeting CD19-positive lymphomas with the antibodydrug conjugate loncastuximab tesirine: preclinical evidence of activity as a single agent and in combination therapy. Haematologica. 2024;109(10):3314–26. doi:10.3324/haematol.2023.284197

46. Smith JA, Medina P, Miao M, Moore KN. A review of mirvetuximab soravtansine-gynx in folate receptor alpha–expressing platinum-resistant ovarian cancer. Am J Health Syst Pharm. 2025;82(10):522–36. doi:10.1093/ajhp/zxaf011

47. Okajima D, Yasuda S, Maejima T, Karibe T, Sakurai K, Aida T, et al. Datopotamab Deruxtecan, a Novel TROP2-directed Antibody–drug Conjugate, Demonstrates Potent Antitumor Activity by Efficient Drug Delivery to Tumor Cells. Mol Cancer Ther. 2021;20(12):2329–40. doi:10.1158/1535-7163.MCT-21-0206

48. Camidge DR, Bar J, Horinouchi H, Goldman J, Moiseenko F, Filippova E, et al. Telisotuzumab Vedotin Monotherapy in Patients with Previously Treated c-Met Protein–Overexpressing Advanced Nonsquamous EGFR-Wildtype Non–Small Cell Lung Cancer in the Phase II LUMINOSITY Trial. J Clin Oncol. 2024;42(25):3000–11. doi:10.1200/JCO.24.00720

49. Kreitman RJ, Dearden C, Zinzani PL, Delgado J, Karlin L, Robak T, et al. Moxetumomab pasudotox in relapsed/refractory hairy cell leukemia. Leukemia. 2018;32(8):1768–77. doi:10.1038/s41375-018-0210-1

50. Behren Ketchum, PharmD E, Clarke, PharmD, Bcop A, B. Clemmons, PharmD, Bcop A. Belantamab Mafodotin-blmf: A Novel Antibody-Drug Conjugate for Treatment of Patients With Relapsed/Refractory Multiple Myeloma. J Adv Pract Oncol. 2022;13(1):77–85. doi:10.6004/jadpro.2022.13.1.7

51. Connors JM. Brentuximab vedotin with chemotherapy for stage III or IV Hodgkin's lymphoma. N Engl J Med. 2018;378:331–44. doi:10.1056/NEJMoa1708984

52. Ansell SM. Overall survival with brentuximab vedotin in stage III or IV Hodgkin's lymphoma. N Engl J Med. 2022;387:310–20. doi:10.1056/NEJMoa2206125

53. Okeley NM, Miyamoto JB, Zhang X. Development of an antibody-drug conjugate targeting CD30 for relapsed/refractory lymphoma. Clin Cancer Res. 2010;16(3):888–97. doi:10.1158/1078-0432.CCR-09-2069

54. Younes A. Results of a pivotal phase II study of brentuximab vedotin for patients with relapsed or refractory Hodgkin's lymphoma. J Clin Oncol. 2012;30(18):2183–9. doi:10.1200/JCO.2011.38.0410

55. Castaigne S. Effect of gemtuzumab ozogamicin on survival of adult patients with de-novo acute myeloid leukaemia (ALFA-0701): a randomised, open-label, phase 3 study. The Lancet. 2012;379(9825):1508–16. doi:10.1016/S0140-6736(12

56. Kantarjian HM. Inotuzumab ozogamicin versus standard therapy for acute lymphoblastic leukemia. N Engl J Med. 2016;375:740–53. doi:10.1056/NEJMoa1509277

57. Verma S, Miles D, Gianni L. Trastuzumab emtansine for HER2-positive advanced breast cancer. N Engl J Med. 2012;367(19):1783–91. doi:10.1056/NEJMoa1209124

58. Von Minckwitz G, Huang CS, Mano MS. Trastuzumab emtansine for residual invasive HER2-positive breast cancer. N Engl J Med. 2019;380(7):617–28. doi:10.1056/NEJMoa1814017

59. Tilly H. Polatuzumab vedotin in previously untreated diffuse large B-cell lymphoma. N Engl J Med. 2022;386:351–63. doi:10.1056/NEJMoa2115304

60. Cortés J. Trastuzumab deruxtecan versus trastuzumab emtansine for breast cancer. N Engl J Med. 2022;386:1143–54. doi:10.1056/NEJMoa2115022

61. Modi S, Jacot W, Yamashita T. Trastuzumab deruxtecan in previously treated HER2-low advanced breast cancer. N Engl J Med. 2022;387:9–20. doi:10.1056/NEJMoa2203690

62. Hurvitz SA. Updated results from DESTINY-Breast03: trastuzumab deruxtecan versus trastuzumab emtansine. The Lancet. 2023;401:1693–706. doi:10.1016/S0140-6736(22

63. Shitara K. Trastuzumab deruxtecan in previously treated HER2-positive gastric cancer. N Engl J Med. 2020;382:2419–30. doi:10.1056/NEJMoa2004413

64. Bardia A. Sacituzumab govitecan in metastatic triple-negative breast cancer. N Engl J Med. 2021;384:1529–41. doi:10.1056/NEJMoa2028485

65. Powles T. Enfortumab vedotin in previously treated advanced urothelial carcinoma. N Engl J Med. 2021;384:1125–35. doi:10.1056/NEJMoa2035807

66. Powles T. Enfortumab vedotin and pembrolizumab in untreated advanced urothelial cancer. N Engl J Med. 2024;390:875–88. doi:10.1056/NEJMoa2312117

67. Coleman RL. Efficacy and safety of tisotumab vedotin in previously treated recurrent or metastatic cervical cancer (innovaTV 204). Lancet Oncol. 2021;22(5):609–19. doi:10.1016/S1470-2045(21

68. Moore KN. Mirvetuximab soravtansine in FRα-positive, platinum-resistant ovarian cancer. N Engl J Med. 2023;389:2162–74. doi:10.1056/NEJMoa2309169

69. Yu HA, Goto Y, Hayashi H, Felip E, Chih-Hsin Yang J, Reck M, et al. HERTHENA-Lung01, a Phase II Trial of Patritumab Deruxtecan (HER3-DXd) in Epidermal Growth Factor Receptor–Mutated Non–Small-Cell Lung Cancer After Epidermal Growth Factor Receptor Tyrosine Kinase Inhibitor Therapy and Platinum-Based Chemotherapy. J Clin Oncol. 2023;41(35):5363–75. doi:10.1200/JCO.23.01476

70. Yamato M, Hasegawa J, Maejima T, Hattori C, Kumagai K, Watanabe A, et al. DS-7300a, a DNA Topoisomerase I Inhibitor, DXd-Based Antibody–Drug Conjugate Targeting B7-H3, Exerts Potent Antitumor Activities in Preclinical Models. Mol Cancer Ther. 2022;21(4):635–46. doi:10.1158/1535-7163.MCT-21-0554

71. Moore KN, Philipovskiy A, Sudo K, Harano K, Kitano S, Buscema J, et al. 77MO Raludotatug deruxtecan (R-DXd) monotherapy in patients (pts) with heavily pretreated platinum-sensitive ovarian cancer (PSOC): Subgroup analysis of a phase I study. ESMO Open. 2025;10. doi:10.1016/j.esmoop.2025.105206

72. Banerji U, Van Herpen CML, Saura C, Thistlethwaite F, Lord S, Moreno V, et al. Trastuzumab duocarmazine in locally advanced and metastatic solid tumours and HER2-expressing breast cancer: a phase 1 dose-escalation and dose-expansion study. Lancet Oncol. 2019;20(8):1124–35. doi:10.1016/S1470-2045(19)30328-6

73. Gazzah A, Bedard PL, Hierro C, Kang YK, Abdul Razak A, Ryu MH, et al. Safety, pharmacokinetics, and antitumor activity of the anti-CEACAM5-DM4 antibody–drug conjugate tusamitamab ravtansine (SAR408701) in patients with advanced solid tumors: first-in-human dose-escalation study. Ann Oncol. 2022;33(4):416–25. doi:10.1016/j.annonc.2021.12.012

74. Jang S, Powderly JD, Spira AI, Bakkacha O, Loo D, Bohac GC, et al. Phase 1 dose escalation study of MGC018, an anti-B7-H3 antibody-drug conjugate (ADC), in patients with advanced solid tumors. J Clin Oncol. 2021;39(15_suppl):2631–2631. doi:10.1200/JCO.2021.39.15_suppl.2631

75. Lyon RP, Jonas M, Frantz C, Trueblood ES, Yumul R, Westendorf L, et al. SGN-B6A: A New Vedotin Antibody–Drug Conjugate Directed to Integrin Beta-6 for Multiple Carcinoma Indications. Mol Cancer Ther. 2023;22(12):1444–53. doi:10.1158/1535-7163.MCT-22-0817

76. Wang ML, Barrientos JC, Furman RR, Mei M, Barr PM, Choi MY, et al. Zilovertamab Vedotin Targeting of ROR1 as Therapy for Lymphoid Cancers. NEJM Evid. 2022;1(1):EVIDoa2100001. doi:10.1056/EVIDoa2100001

77. Daver NG, Montesinos P, DeAngelo DJ, Wang ES, Papadantonakis N, Todisco E, et al. Pivekimab sunirine (IMGN632), a novel CD123-targeting antibody–drug conjugate, in relapsed or refractory acute myeloid leukaemia: a phase 1/2 study. Lancet Oncol. 2024;25(3):388–99. doi:10.1016/S1470-2045(23)00674-5

78. Hamadani M, Collins GP, Samaniego F, Spira AI, Davies A, Radford J, et al. Phase 1 Study of Adct-301 (Camidanlumab Tesirine), a Novel Pyrrolobenzodiazepine-Based Antibody Drug Conjugate, in Relapsed/Refractory Classical Hodgkin Lymphoma. Blood. 2018;132(Supplement 1):928–928. doi:10.1182/blood-2018-99-118198

79. Boni V, Fidler MJ, Arkenau HT, Spira A, Meric-Bernstam F, Uboha N, et al. Praluzatamab Ravtansine, a CD166-Targeting Antibody–Drug Conjugate, in Patients with Advanced Solid Tumors: An Open-Label Phase I/II Trial. Clin Cancer Res. 2022;28(10):2020–9. doi:10.1158/1078-0432.CCR-21-3656

80. Johnson M, El-Khoueiry A, Hafez N, Lakhani N, Mamdani H, Rodon J, et al. Phase I, First-in-Human Study of the Probody Therapeutic CX-2029 in Adults with Advanced Solid Tumor Malignancies. Clin Cancer Res. 2021;27(16):4521–30. doi:10.1158/1078-0432.CCR-21-0194

81. Wenham RM, Ghamande S, Oaknin A, Berek JS, Perez-Fidalgo JA, Sentís PG, et al. Open label, multicenter, phase 2 study of farletuzumab ecteribulin, a folate receptor alpha-targeting

antibody-drug conjugate, alone and in combination with lenvatinib in platinum-resistant ovarian cancer. Int J Gynecol Cancer. 2026;36(2). doi:10.1016/j.ijgc.2025.104404

82. Luveltamab tazevibulin (STRO-002), an anti-folate receptor alpha (FolRα) antibody drug conjugate (ADC), safety and efficacy in a broad distribution of FolRα expression in patients with recurrent epithelial ovarian cancer (OC): Update of STRO-002-GM1 phase 1 dose expansion cohort. J Clin Oncol. doi:10.1200/JCO.2023.41.16

83. Baird RD, Chung WP, Schmid P, Dongen MV, Jung KH, Naito Y, et al. 300MO Puxitatug samrotecan (P-Sam, AZD8205) in patients (pts) with HR+/HER2– breast cancer (BC): A first-in-human phase I/IIa dose escalation and expansion study. ESMO Open. 2025. doi:10.1016/j.esmoop.2025.104872

84. Hamilton EP, Han HS, Kalinsky K, Abuhadra N, McAndrew NP, Spira AI, et al. Initial phase 1 dose escalation data for emiltatug ledadotin (Emi-Le), a novel B7-H4-directed dolasynthen antibody-drug conjugate. J Clin Oncol. 2025; doi:10.1200/JCO.2025.43.

85. Capone E, Piccolo E, Fichera I, Ciufici P, Barcaroli D, Sala A, et al. Generation of a novel Antibody-Drug Conjugate targeting endosialin: potent and durable antitumor response in sarcoma. Oncotarget. 2017;8(36):60368–77. doi:10.18632/oncotarget.19499 PubMed PMID: 28947977; PubMed Central PMCID: PMC5601145.

86. Ma J, Lyu H, Huang J, Liu B. Targeting of erbB3 receptor to overcome resistance in cancer treatment. Mol Cancer. 2014;13:105. doi:10.1186/1476-4598-13-105

87. Lyu H, Han A, Polsdofer E, Liu S, Liu B. Understanding the biology of HER3 receptor as a therapeutic target in human cancer. Acta Pharm Sin B. 2018;8(4):503–10. doi:10.1016/j.apsb.2018.05.010

88. Jänne PA, Baik C, Su WC. Efficacy and safety of patritumab deruxtecan (HER3-DXd) in EGFR inhibitor-resistant, EGFR-mutated NSCLC. Cancer Discov. 2022;12(1):74–89. doi:10.1158/2159-8290.CD-21-0715

89. Sala G, Traini S, D'Egidio M. MP-RM-1 anti-ErbB3 antibody study. Oncogene. 2012. doi:10.1038/onc.2011.322

90. D'Agostino D. EV20-sss-vc/MMAF in hepatocellular carcinoma models. Oncol Rep. 2021. doi:10.3892/or.2020.7893

91. Chen Q, Jia G, Zhang X, Ma W. Targeting HER3 to overcome EGFR TKI resistance in NSCLC. Front Immunol. 2024;14. doi:10.3389/fimmu.2023.1332057

92. Sala G, Traini S. EV20 humanized anti-HER3 antibody study. Transl Oncol. 2013. doi:10.1593/tlo.13475

93. Yu HA. HERTHENA-Lung01 phase II trial of patritumab deruxtecan in EGFR-mutated NSCLC after EGFR TKI and platinum chemotherapy. J Clin Oncol. 2023. doi:10.1200/JCO.23.01476

94. Capone E, Lamolinara A, D'Agostino D. EV20-saporin immunotoxin: preclinical activity in melanoma models. Oncotarget. 2017. doi:10.18632/oncotarget.20728

95. Capone E, Lamolinara A, D'Agostino D. EV20-MMAF conjugate: targeted delivery of auristatin to HER3-expressing tumors. J Controlled Release. 2018. doi:10.1016/j.jconrel.2018.03.016

96. Capone E, Lamolinara A, D'Agostino D. EV20-based conjugate delivering NMS-P945 (HER3-targeted drug conjugate). Pharmaceutics. 2021. doi:10.3390/pharmaceutics13040483

97. Gandullo-Sánchez L, Capone E, Ocaña A, Iacobelli S, Sala G, Pandiella A. HER3 targeting with an antibody-drug conjugate bypasses resistance to anti-HER2 therapies. EMBO Mol Med. 2020;12(5):EMMM201911498. doi:10.15252/emmm.201911498

98. Soucek L, Whitfield J, Martins CP. Modelling MYC inhibition as a cancer therapy. Nature. 2008;455(7213):679–83. doi:10.1038/nature07260

99. Massó-Vallés D, Soucek L. Blocking MYC to treat cancer: reflecting on two decades of Omomyc. Cells. 2020;9(4):883. doi:10.3390/cells9040883

100. Garralda E. MYC targeting by OMO-103 in solid tumors: a phase 1 trial. Nat Med. 2024. doi:10.1038/s41591-024-02805-1

101. Beaulieu ME, Jauset T, Massó-Vallés D. Intrinsic cell-penetrating activity propels Omomyc from proof of concept to viable anti-MYC therapy. Sci Transl Med. 2019;11(484):5012. doi:10.1126/scitranslmed.aar5012

102. Maris JM, Hogarty MD, Bagatell R, Cohn SL. Neuroblastoma. The Lancet. 2007;369(9579):2106–20. doi:10.1016/S0140-6736(07

103. DuBois SG, Macy ME, Henderson TO. High-Risk and Relapsed Neuroblastoma: Toward More Effective Strategies. ASCO Educ Book. 2022;42:1–14. doi:10.1200/EDBK_349783

104. Johnsen JI, Dyberg C, Wickström M, Baryawno N. MYCN Impact on High-Risk Neuroblastoma: From Diagnosis and Prognosis to Targeted Treatment. Cancers. 2022;14(18):4421. doi:10.3390/cancers14184421

105. Otte J, Dyberg C, Pepich A, Johnsen JI. MYCN Function in Neuroblastoma Development. Front Oncol. 2020;10:624079. doi:10.3389/fonc.2020.624079

106. Westhoff MA, Karpel-Massler G, Brühl O. Targeting the PI3K/Akt/mTOR pathway in neuroblastoma. PLOS ONE. 2013;8(12):83128. doi:10.1371/journal.pone.0083128

107. Richards KN, Zweidler-McKay PA, Van Roy N. Signaling of ERBB receptor tyrosine kinases promotes neuroblastoma growth. Cancer. 2010;116(13):3233–43. doi:10.1002/cncr.25073

108. Wilzén A, Krona C, Sveinbjörnsson B. ERBB3 is a marker of a ganglioneuroblastoma/ganglioneuroma-like expression profile in neuroblastic tumours. Mol Cancer. 2013;12:70. doi:10.1186/1476-4598-12-70

109. Bibbò S. EV20/Omomyc immunoconjugate targeting HER3 with MYC inhibition for enhanced anticancer activity. J Transl Med. 2024. doi:10.1186/s12967-024-05535-y

110. Iacobelli S, Arno E, D'Orazio A, Coletti G. Measurement of a breast cancer associated antigen detected by a monoclonal antibody (90K) in serum. Cancer Res. 1988. doi:10.1007/BF01807554

111. Koths K, Taylor E, Halenbeck R, Casipit C, Wang A. Cloning and characterization of a human Mac-2-binding protein, a new member of the superfamily defined by the macrophage scavenger receptor cysteine-rich domain. J Biol Chem. 1993. doi:10.1016/S0021-9258(19)85233-X

112. Ullrich A, Sures I, D'Egidio M. The secreted tumor-associated antigen 90K is a potent immune stimulator. J Biol Chem. 1994;269(28):18401–7. doi:10.1016/S0021-9258(17

113. Calabrese G, Sures I, Pompetti F, Natoli C, Palka G, Iacobelli S, et al. The gene (LGALS3BP) encoding the serum protein 90K, associated with cancer and infection by the human immunodeficiency virus, maps at 17q25. Cytogenet Cell Genet. 1995. doi: 10.1159/000133969

114. Natoli C, Sures I, Mottolese M. The immune stimulatory protein 90K increases major histocompatibility complex class I expression and is regulated by hormones in breast cancer cells. J Details PubMed. 1996. doi: 10.1210/en.2004-0506

115. Tinari N, Iacobelli S, Natoli C. Identification of the tumor antigen 90K domains recognized by monoclonal antibodies. J Details PubMed. 1997. doi: 10.1016/S0021-9258(17)32322-0

116. Sasaki T, Brakebusch C, Engel J, Timpl R. Mac-2 binding protein is a cell-adhesive protein of the extracellular matrix which forms ring-like structures and binds β1 integrins. EMBO J. 1998. doi: 10.1093/emboj/17.6.1606

117. Fornarini, B., D'Ambrosio, C., Natoli, C., Tinari, N., Silingardi, V., & Iacobelli, S. (2000). Adhesion to 90K (Mac-2 BP) as a mechanism for lymphoma drug resistance in vivo. Blood, 96(9), 3282–3285. doi: 10.1182/V96.9.3282

118. Ozaki Y, Kontani K, Teramoto K, Fujita T, Tezuka N, Sawai S, Maeda T, Watanabe H, Fujino S, Asai T, Ohkubo I. Involvement of 90K/Mac-2 binding protein in cancer metastases by increased cellular adhesiveness in lung cancer. Involvement of 90K/Mac-2 binding protein in cancer metastases by increased cellular adhesiveness in lung cancer. doi: 10.3892/12.5.1071

119. Grassadonia A, Tinari N, Iurisci I, Piccolo E, Cumashi A, Innominato P, et al. 90K (Mac-2 BP) and galectins in tumor progression and metastasis. Glycoconj J. 2002;19(7–9):551–6. doi:10.1023/B:GLYC.0000014071.51205.6b

120. Laferté S, Loh LC, Keeler V. Monoclonal antibodies specific for human tumor-associated antigen 90K/Mac-2 binding protein: tools to examine protein conformation and function. J Cell Biochem. 2000;77(4):540–59. doi:10.1002/(SICI

121. Nonaka M, Ma BY, Murai R. Glycosylation-dependent recognition of Mac-2 binding protein by DC-SIGN and functional implications. J Biol Chem. 2011. doi: 10.1074/ M110.215301

122. White MJV, Roife D, Gomer RH. Galectin-3 binding protein secreted by breast cancer cells inhibits monocyte-derived fibrocyte differentiation using a DC-SIGN-dependent mechanism. J Immunol. 2015;195(4):1858–67. doi:10.4049/jimmunol.1500365

123. Läubli H, Pearce OMT, Schwarz F. Lectin galactoside-binding soluble 3 binding protein (LGALS3BP) is a tumor-associated immunomodulatory ligand for CD33-related Siglecs. J Biol Chem PMC Free Artic. 2014.

124. Lee JH, Bae JA, Lee JH. Glycoprotein 90K, downregulated in advanced colorectal cancer tissues, interacts with CD9/CD82 and suppresses the Wnt/β-catenin signal via ISGylation of β-catenin. Gut. 2010;59:907–17.

125. Piccolo E, Tinari N, D'Addario D. Prognostic relevance of LGALS3BP in human colorectal carcinoma. J Transl Med. 2015. doi: 10.1186/s12967-015-0606-x

126. Loimaranta V, Hepojoki J, Laaksoaho O, Pulliainen AT. Galectin-3-binding protein: A multitask glycoprotein with innate immunity functions in viral and bacterial infections. J Leukoc Biol. 2018. doi.org/10.1002/JLB.3VMR0118-036R

127. Hong CS, Park MR, Sun EG. Gal-3BP negatively regulates NF-κB signaling by inhibiting the activation of TAK1. Front Immunol. 2019;10:1760. doi:10.3389/fimmu.2019.01760

128. Xu G. Inducible LGALS3BP/90K activates antiviral innate immune signaling (TRAF-dependent) and promotes interferon responses. J Details PubMed. 2019. doi: 10.1371/journal.ppat.1008002

129. Piccolo E, Tinari N, Semeraro D. LGALS3BP secreted by breast cancer cells functions as a pro-angiogenic factor through induction of VEGF and stimulation of endothelial tubulogenesis. J Details PubMed. 2013. doi: 10.1007/s00109-012-0936-6

130. Traini S, Piccolo E, Tinari N. Inhibition of tumor growth and angiogenesis by SP-2, an anti-LGALS3BP antibody. Mol Cancer Ther. 2014;13(4):916–25. doi:10.1158/1535-7163.MCT-12-1117

131. Capone E, Iacobelli S, Sala G. Role of galectin 3 binding protein in cancer progression: a potential novel therapeutic target. J Transl Med. 2021;19(1):405. doi:10.1186/s12967-021-03085-w

132. Giansanti F. Secreted Gal-3BP is a novel promising target for non-internalizing antibody-drug conjugates (1959-based) and shows strong in vivo antitumor activity. J Details PubMed. 2019. doi: 10.1016/j.jconrel.2018.12.018

133. Dufrusine B. Extracellular LGALS3BP: vesicular biology, translational relevance, and targeting with 1959-sss/DM4 in glioblastoma models. J Details PubMed. 2023. doi: 10.1002/1878-0261.13453

134. Keinänen O, Sarrett SM, Delaney LJ. Visualizing galectin-3 binding protein expression with ImmunoPET. Mol Pharm. 2023;20(6):3241–8. doi:10.1021/acs.molpharmaceut.3c00241

135. Giansanti F, Capone E, Ponziani S, Piccolo E, Gentile R, Lamolinara A, et al. Secreted Gal-3BP is a novel promising target for non-internalizing Antibody–Drug Conjugates. J Controlled Release. 2019;294:176–84. doi:10.1016/j.jconrel.2018.12.018

136. Kennedy PT, Zannoupa D, Son MH, Dahal LN, Woolley JF. Neuroblastoma: an ongoing cold front for cancer immunotherapy. J Immunother Cancer. 2023;11(11):007798. doi:10.1136/jitc-2023-007798

137. Capone E, Iacobelli S, Sala G. Targeting vesicular LGALS3BP by an antibody-drug conjugate as novel therapeutic strategy for neuroblastoma. Cancers. 2020;12(10):2989. doi:10.3390/cancers12102989

138. Kepp O, Senovilla L, Vitale I. Consensus guidelines for the detection of immunogenic cell death. Oncoimmunology. 2014;3(9):955691. doi:10.4161/21624011.2014.955691

139. Bauzon M, Drake PM, Barfield RM, Cornali BM, Rupniewski I, Rabuka D. Maytansine-bearing antibody-drug conjugates induce in vitro hallmarks of immunogenic cell death selectively

in antigen-positive target cells. Oncoimmunology. 2019;8(4):1565859. doi:10.1080/2162402X.2019.1565859

140. Dosset M, Vargas TR, Lagrange A. PD-1/PD-L1 pathway: an adaptive immune resistance mechanism to immunogenic chemotherapy in colorectal cancer. Oncoimmunology. 2018;7(6):1433981. doi:10.1080/2162402X.2018.1433981

141. Hu Y, Manasrah BK, McGregor SM. Paclitaxel induces micronucleation and activates pro-inflammatory cGAS-STING signaling in triple-negative breast cancer. Mol Cancer Ther. 2021;20(12):2553–67. doi:10.1158/1535-7163.MCT-21-0195

142. Serpico AF, Pisauro C, Grieco D. cGAS-dependent proinflammatory and immune homeostatic effects of the microtubule-targeting agent paclitaxel. Front Immunol. 2023;14:1127623. doi:10.3389/fimmu.2023.1127623

143. Dondero A, Pastorino F, Della Chiesa M. PD-L1 expression in metastatic neuroblastoma as an additional mechanism for limiting immune surveillance. Oncoimmunology. 2015;5(1):1064578. doi:10.1080/2162402X.2015.1064578

144. Siebert N, Zumpe M, Jüttner M. PD-1 blockade augments anti-neuroblastoma immune response induced by anti-GD2 antibody ch14.18/CHO. Oncoimmunology. 2017;6(10):1343775. doi:10.1080/2162402X.2017.1343775

145. Cela I, Capone E, Pece A. LGALS3BP antibody-drug conjugate enhances tumor-infiltrating lymphocytes and synergizes with immunotherapy to restrain neuroblastoma growth. J Transl Med. 2025;23(1):431. doi:10.1186/s12967-025-06434-1

146. Ricci EM, Dainese E, De Laurenzi V, Lovato G, Sala G, Locatelli M. New analytical challenges in characterization of antibody-drug conjugates. J Chromatogr Open. 2025;8:100260. doi:10.1016/j.jcoa.2025.100260

147. Dixit T, Aswini A, Nikam H, Vaidya A, Ravindran S. Emerging trends in synthesis, characterization, and mechanism of action of antibody-drug and antibody-nanoparticle conjugates. Expert Rev Proteomics. 2025;22:170–99. doi:10.1080/14789450.2025.1781471

148. Wakankar A, Chen Y, Gokarn Y, Jacobson FS. Analytical methods for physicochemical characterization of antibody drug conjugates. mAbs. 2011;3(2):161–72. doi:10.4161/mabs.3.2.14960

149. Ducry L, Stump B. Antibody-drug conjugates: Linking cytotoxic payloads to monoclonal antibodies. Bioconjug Chem. 2010;21:5–13. doi:10.1021/bc9002019

150. Khan RMN, Zeng Y, Lanihun AA, Arisa OT, Horner JL, Figg WD. Recent advances in bioanalytical methods for quantification and pharmacokinetic analyses of antibody-drug conjugates. AAPS J. 2025;27:138. doi:10.1208/s12248-025-01115-9

151. Lu J. Analysis of antibody-drug conjugates by mass spectrometry. Anal Chem. 2015;87:571–9. doi:10.1021/ac504095e

152. Cahuzac H, Devel L. Analytical methods for the detection and quantification of ADCs in biological matrices. Pharmaceuticals. 2020;13(12):462. doi:10.3390/ph13120462

153. Gorovits B. Bioanalysis of antibody-drug conjugates: Assay challenges and strategies. Bioanalysis. 2013;5:997–1009. doi:10.4155/bio.13.38

154. Stumpp MT, Fuchs H. Applications of MALDI imaging mass spectrometry in pharmaceutical research. Bioanalysis. 2016;8:367–79. doi:10.4155/bio-2015-0016

155. Prideaux B, Stoeckli M. Mass spectrometry imaging for drug distribution studies. J Proteomics. 2012;75:4999–5013. doi:10.1016/j.jprot.2012.05.024

156. Tumey LN. Hydrophobic interaction chromatography for characterization of antibody-drug conjugates. Bioconjug Chem. 2014;25:1871–80. doi:10.1021/bc500372f

157. Sun X. Effects of drug-antibody ratio on pharmacokinetics and toxicity of antibody-drug conjugates. Bioconjug Chem. 2011;22:728–35. doi:10.1021/bc1004903

158. FDA. Bioanalytical method validation: Guidance for industry. U.S. Food and Drug Administration. 2020. Report No.

159. Sparidans RW, Beijnen JH. Bioanalytical LC-MS/MS of antibody-drug conjugates: Current status and future perspectives. Bioanalysis. 2016;8(4):335–48. doi:10.4155/bio-2015-0015

160. Lovato G, Ciriolo L, Perrucci M, Federici L, Ippoliti R, Iacobelli S, et al. HPLC-DAD validated method for DM4 and S-methyl-DM4 quantification in biological matrices. J Pharm Biomed Anal. 2023;235:115642. doi:10.1016/j.jpba.2023.115642

161. Lovato G, Perrucci M, Cela I, Lamolinara A, Mercatelli A, De Laurenzi V, et al. Evaluation of antibody-drug conjugate performances using a novel HPLC-DAD method for tumor-specific detection of DM4 and S-methyl-DM4. ACS Omega. 2025. doi:10.1021/acsomega.5c07693

162. Costa J, Pronto-Laborinho A, Pinto S, Gromicho M, Bonucci S, Tranfield E, et al. Investigating LGALS3BP/90K glycoprotein in the cerebrospinal fluid of patients with neurological diseases. Sci Rep. 2020;10(1):5649. doi:10.1038/s41598-020-62592-w

163. Rana R. Plasma-Derived Extracellular Vesicles Reveal Galectin-3 Binding Protein as Potential Biomarker for Early Detection of Glioma. Front Oncol. 2021;11:778754. doi:10.3389/fonc.2021.778754

164. Ghanta P. Lung cancer exosomal Gal3BP promotes osteoclastogenesis with potential connotation in osteolytic metastasis. Sci Rep. 2024;14(1):27201. doi:10.1038/s41598-024-79006-w

165. Grassadonia A. Circulating autoantibodies to LGALS3BP: a novel biomarker for cancer. Dis Markers. 2013;35(6):747–52. doi:10.1155/2013/214595

166. Hudson AL. CA9, CYFIP2 and LGALS3BP-A Novel Biomarker Panel to Aid Prognostication in Glioma. Cancers. 2024;16(5):1069. doi:10.3390/cancers16051069

167. Gontero, P., Birtle, A., Capoun, O., Compérat, E., Dominguez-Escrig, J. L., Liedberg, F., Mariappan, P., Masson-Lecomte, A., Mostafid, H. A., Pradere, B., Rai, B. P., van Rhijn, B. W. G., Seisen, T., Shariat, S. F., Soria, F., Soukup, V., Wood, R., & Xylinas, E. N. (2024). European Association of Urology Guidelines on Non-muscle-invasive Bladder Cancer (TaT1 and Carcinoma in Situ)-A Summary of the 2024 Guidelines Update. European urology, 86(6), 531–549. https://doi.org/10.1016/j.eururo.2024.07.027

168. Ferlay J, Ervik M, Lam F, Laversanne M, Colombet M, Mery L, et al. Global Cancer Cancer Today (Bladder cancer factsheet). Lyon, France: International Agency for Research on Cancer (IARC); 2024.

169. Rodriguez Pena MDC, Springer SU, Taheri D, Li L, Tregnago AC, Eich ML, et al. Performance of novel non-invasive urine assay UroSEEK in cohorts of equivocal urine cytology. Virchows Arch. 2020. doi:10.1007/s00428-019-02654-1

170. Yang Z, Song F, Zhong J. Urinary Biomarkers in Bladder Cancer: FDA-Approved Tests and Emerging Tools for Diagnosis and Surveillance. Cancers Basel. 2025;17(21):3425. doi:10.3390/cancers17213425

171. Maas M, Todenhöfer T, Black PC. Urine biomarkers in bladder cancer - current status and future perspectives. Nat Rev Urol. 2023;20(10):597–614. doi:10.1038/s41585-023-00773-8

172. Jeong IG, Yun SC, Ha HK, Kang SG, Lee S, Park S, et al. Urinary DNA Methylation Test for Bladder Cancer Diagnosis. JAMA Oncol. 2025;11(3):293–9. doi:10.1001/jamaoncol.2024.6160

173. Pece A, Lovato G, Cela I, Mercatelli A, Ferro B, Nikkola J, et al. Glycosylated LGALS3BP is highly secreted by bladder cancer cells and represents a novel urinary disease biomarker. Mol Oncol. 2025. doi:10.1002/1878-0261.70140

174. Ladenstein R, Pötschger U, Valteau-Couanet D, Luksch R, Castel V, Yaniv I, et al. Interleukin 2 with anti-GD2 antibody ch14.18/CHO (dinutuximab beta) in patients with high-risk neuroblastoma (HR-NBL1/SIOPEN): a multicentre, randomised, phase 3 trial. Lancet Oncol. 2018;19(12):1617–29. doi:10.1016/S1470-2045(18)30578-3

175. Ly S, Anand V, El-Dana F, Nguyen K, Cai Y, Cai S, et al. Anti-GD2 antibody dinutuximab inhibits triple-negative breast tumor growth by targeting GD2+ breast cancer stem-like cells. J Immunother Cancer. 2021;9(3). doi:10.1136/jitc-2020-001197 PubMed PMID: 10.1136/jitc-2020-001197.

176. Hein CD, Liu XM, Wang D. Click Chemistry, A Powerful Tool for Pharmaceutical Sciences. Pharm Res. 2008;25(10):2216–30. doi:10.1007/s11095-008-9616-1

ABBREVIATIONS AND ACRONYMS

Abbreviation	Full term
ADC	Antibody–Drug Conjugate
ADCC	Antibody-Dependent Cell-mediated Cytotoxicity
AKT	Protein Kinase B
APCs	Antigen-Presenting Cells
ATCC	American Type Culture Collection
BCA	Bicinchoninic Acid Assay
BSA	Bovine Serum Albumin
CQAs	Critical Quality Attributes
DAR	Drug-to-Antibody Ratio
DAD	Diode Array Detection
DAMPs	Damage-Associated Molecular Patterns
DAPI	4′,6-Diamidino-2-Phenylindole
DM1	Maytansinoid DM1
DM4	Maytansinoid DM4
DMA	Dimethylacetamide
DMSO	Dimethyl Sulfoxide
DNA	Deoxyribonucleic Acid
DTNB	5,5′-Dithiobis(2-nitrobenzoic acid)
DXd	Deruxtecan
ECL	Enhanced Chemiluminescence
EDTA	Ethylenediaminetetraacetic Acid
EGFR	Epidermal Growth Factor Receptor
ELISA	Enzyme-Linked Immunosorbent Assay
EVs	Extracellular Vesicles
Fc	Fragment crystallizable region
FcRn	Neonatal Fc Receptor
FBS	Fetal Bovine Serum
FMO	Fluorescence Minus One
GFP	Green Fluorescent Protein
GD2	Disialoganglioside GD2
HER	Human Epidermal Growth Factor Receptor
HER2	Human Epidermal Growth Factor Receptor 2
HER3	Human Epidermal Growth Factor Receptor 3
HIC	Hydrophobic Interaction Chromatography
HPLC	High-Performance Liquid Chromatography
HRP	Horseradish Peroxidase
HSP70	Heat Shock Protein 70
HSP90	Heat Shock Protein 90

Abbreviation	Full term
ICD	Immunogenic Cell Death
ICIs	Immune Checkpoint Inhibitors
ICI	Immune Checkpoint Inhibitor
IgG	Immunoglobulin G
IL-6	Interleukin 6
IR	Infrared Spectroscopy
kDa	Kilodalton
LC–MS	Liquid Chromatography–Mass Spectrometry
LGALS3BP	Galectin-3 Binding Protein
LLE	Liquid–Liquid Extraction
mAb	Monoclonal Antibody
MEM	Minimum Essential Medium
MMAE	Monomethyl Auristatin E
MMAF	Monomethyl Auristatin F
MSCs	Mesenchymal Stem Cells
mRNA	Messenger Ribonucleic Acid
MYC	MYC Proto-Oncogene
MYCN	MYC Neuroblastoma-derived oncogene
NB	Neuroblastoma
NEM	N-ethylmaleimide
NHS	N-Hydroxysuccinimide
OD	Optical Density
PAGE	Polyacrylamide Gel Electrophoresis
PBS	Phosphate Buffered Saline
PD-1	Programmed Death-1
PD-L1	Programmed Death-Ligand 1
PEG	Polyethylene Glycol
PI	Propidium Iodide
PI3K	Phosphoinositide 3-Kinase
PSAR	Polysarcosine
QC	Quality Control
RNA	Ribonucleic Acid
RT	Room Temperature
SDS	Sodium Dodecyl Sulfate
SDS-PAGE	Sodium Dodecyl Sulfate–Polyacrylamide Gel Electrophoresis
shRNA	Short Hairpin RNA
siRNA	Small Interfering RNA
SN-38	Active metabolite of Irinotecan
TBS	Tris-Buffered Saline
TCEP	Tris(2-carboxyethyl)phosphine
TMB	Tetramethylbenzidine

Abbreviation	Full term
TME	Tumor Microenvironment
TNF	Tumor Necrosis Factor
Tris	Tris(hydroxymethyl)aminomethane
UV	Ultraviolet